Optimization of a Human-Powered Aircraft using Fluid-Structure Interaction Simulations

Bob Vanderhoydonck

Supervisors: Prof. dr. ir. Joris Degroote, Prof. dr. ir. Jan Vierendeels
Counsellor: Gilberto Santo

Master's dissertation submitted in order to obtain the academic degree of
Master of Science in Electromechanical Engineering

Department of Flow, Heat and Combustion Mechanics
Chair: Prof. dr. ir. Jan Vierendeels
Faculty of Engineering and Architecture
Academic year 2015-2016

UNIVERSITEIT GENT

Optimization of a Human-Powered Aircraft using Fluid-Structure Interaction Simulations

Bob Vanderhoydonck

Supervisors: Prof. dr. ir. Joris Degroote, Prof. dr. ir. Jan Vierendeels
Counsellor: Gilberto Santo

Master's dissertation submitted in order to obtain the academic degree of
Master of Science in Electromechanical Engineering

Department of Flow, Heat and Combustion Mechanics
Chair: Prof. dr. ir. Jan Vierendeels
Faculty of Engineering and Architecture
Academic year 2015-2016

UNIVERSITEIT GENT

Acknowledgements

Throughout this entire work, I received the support and guidance of many people, who deserve a special word of gratitude.

First and foremost I would like to thank Prof. Joris Degroote for letting me propose my own thesis subject, which allowed me to explore the fascinating domain of human-powered aircrafts. Together with Prof. Jan Vierendeels and Gilberto Santo, they guided me the entire year, gave me the freedom to use new software packages and they carefully reviewed my paper. An additional word to my supervisor Gilberto; thank you for our weekly meetings and for your willingness to thoroughly review my work.

To Patrik Dahlin from CD-adapco, thank you for providing me with an academic license for STAR-CCM+. The CFD package includes many powerful tools, allowing to perform exiting simulations.

To Mark Drela from MIT, thank you for providing the links to some crucial data of the *Daedalus*, giving me a more detailed insight into the design of human-powered aircrafts.

To Thomas Hansen, thank you for sharing your STAR-CCM+ simulation of the Cirrus glider, allowing me to make great advancements and for your advice concerning the CFD simulations.

Finally I would like to thank a good friend Toon Demeester. He is the second pilot on which the optimization procedure is based and was willing to perform an exhausting test to measure his physical performance. Together we dream of building and flying one day a human-powered aircraft.

Permission for Usage

The author gives permission to make this master dissertation available for consultation and to copy parts of this master dissertation for personal use. In the case of any other use, the copyright terms have to be respected, in particular with regard to the obligation to state expressly the source when quoting results from this master dissertation.

— Bob Vanderhoydonck, *May 31th 2016*

Abstract

The special type of aircrafts in which the human power of the pilot is sufficient to take off and sustain flight, are known as human-powered aircrafts. In this work it is attempted to design and optimize a human-powered aircraft capable of winning the Kremer International Marathon Competition. This is a prestigious challenge set out specifically for human-powered aircrafts, in which a marathon distance is to be flown in less than 1 hour. Although the challenge has been announced in 1988, it remains unaccomplished up to date. Hence, the completion of this challenge would be a major accomplishment in the history of human powered flight. Additionally, the first successful team is rewarded with a monetary prize of £50 000. In the optimization procedure of our human-powered aircraft, Fluid-Structure Interaction simulations will be performed allowing to determine the deflection of the wing during flight. This deflection is crucial for the stability of the aircraft. To asses the feasibility of winning the competition with our optimized human-powered aircraft, the physical performance of candidate pilots is measured and compared with the predicted required power.

Keywords

Human-Powered Aircraft, Vortex Lattice Method, Computational Fluid Dynamics, Fluid-Structure Interaction, optimization

Optimization of a Human-Powered Aircraft using Fluid-Structure Interaction Simulations

Bob Vanderhoydonck

Supervisors: Prof. dr. ir. J. Degroote, Prof. dr. ir. J. Vierendeels, ir. G. Santo

Abstract— **The special type of aircrafts in which the human power of the pilot is sufficient to take off and sustain flight are known as Human-Powered Aircrafts (HPAs). To explore the peculiarities of these aircrafts, the aerodynamic performance of an existing design is evaluated first, using both the Vortex Lattice Method and Computational Fluid Dynamics. In a second step, it is attempted to design and optimize a new HPA capable of winning the Kremer International Marathon Competition. The design will be special in that it allows to include a second pilot on board of the aircraft. As the structural deflection of the wing is found to be a key aspect during design, Fluid-Structure Interaction simulations are performed and included in the optimization procedure. To asses the feasibility of winning the competition, the physical performance of candidate pilots is measured and compared with the predicted required power.**

Keywords— **Human-Powered Aircraft, Vortex Lattice Method, Computational Fluid Dynamics, Fluid-Structure Interaction, optimization**

I. Introduction

Imagine being able to take off and fly with your own human power. This may sound as a very futuristic idea, but history has already proven it to be possible. By careful design, the human power is found sufficient to propel an aircraft. These special aircrafts are extremely light, fly at very low speeds and are usually constructed for a single pilot. They are known as Human-Powered Aircrafts (HPAs) and will be studied in this work.

One of the most sophisticated HPAs is the *Daedalus* from MIT. It was built in an attempt to recreate the mythical escape of its namesake, said to have built himself wings of feathers and wax. After years of intensive design and testing with a prototype aircraft, the Daedalus was finally ready in 1988 for a legendary flight across the Aegean Sea from Crete to Santorini. The flight covered a distance of 74 miles (119 km), completed in 3 hours 54 minutes, the longest time and distance flown under human power up to date [1]. The Daedalus can be seen in Figure 1.

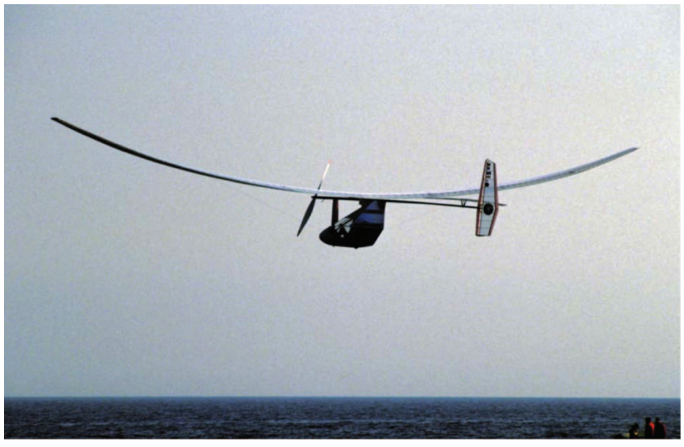

Fig. 1. The Daedalus

Given its outstanding performance, the first part of this work is devoted to analysing this HPA. More specifically, the Daedalus will be simulated in two different softwares. The first software is AVL [2], which performs aerodynamic analyses based on the Vortex Lattice Method (VLM). This software is developed by MIT and is publicly available. For the second simulation, the Computational Fluid Dynamics (CFD) software STAR-CCM+ is used, which will solve the Reynolds-Averaged Navier-Stokes equations. The main purpose of this first part is to have an idea of the capabilities of both softwares and to verify their accuracy by comparing the results with other data.

In the second part, it is attempted to design and optimize a HPA ourselves using AVL and MATLAB. The design will be special in that the HPA should be capable of winning the Kremer International Marathon Competition. This is a prestigious challenge set out by Henry Kremer in which a specific course is to be flown in less than 1 hour. The course is illustrated in Figure 2 and consists of two laps of the outer circuit, followed by a figure-of-eight and two more outer circuits. As such, the total distance is approximately the distance of a marathon. More details can be found in [3].

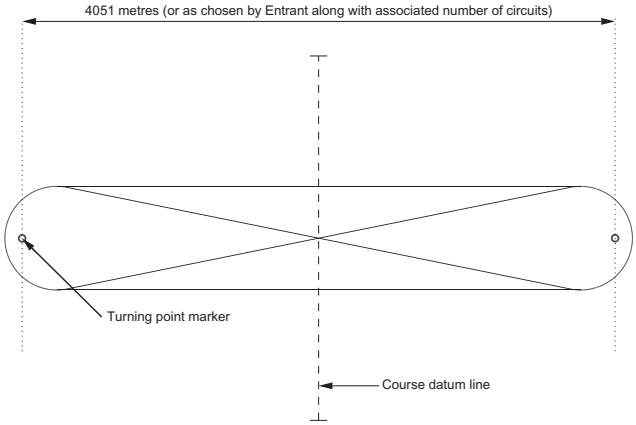

Fig. 2. The Kremer International Marathon Competition

As can be seen in Figure 1, the wing experiences a large deformation during flight. This deformation is actually desired for stability reasons and should therefore be carefully designed. To take this aspect into account during the optimization of our own HPA, Fluid-Structure Interaction (FSI) simulations of the wing will be performed coupling AVL and MATLAB.

Another special feature of our design is the possibility of adding a second pilot on board of the aircraft. As such, it will be investigated if powering a HPA by two pilots offers some advantages compared to a single pilot.

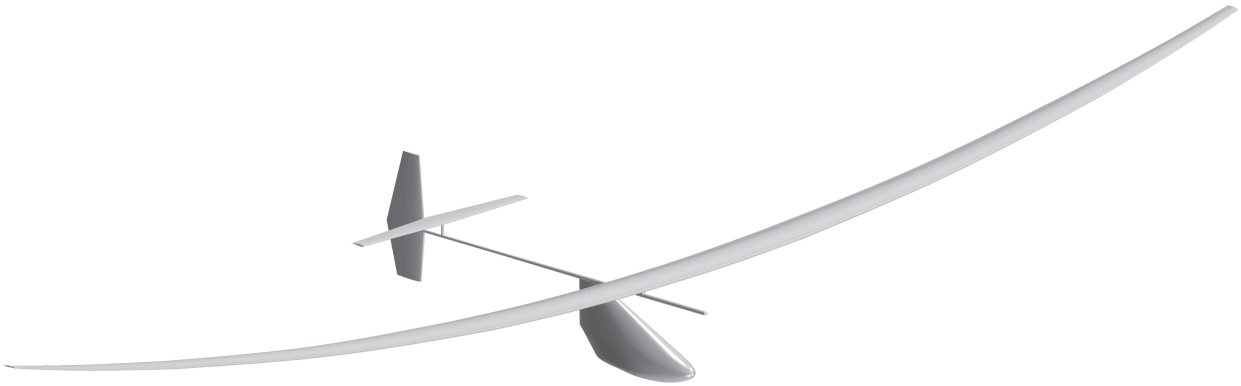

Fig. 3. CAD Model of the Daedalus

In the final part, a CFD simulation of the optimized design is performed in STAR-CCM+. Additionally, the physical performance of the candidate pilots for our HPA is measured. Using this data, it will be verified if sufficient human power can be generated in order to complete the Kremer International Marathon Course within time.

II. The Daedalus

As a first step, a 3D CAD model of the Daedalus is constructed, which will give a clear overview of its geometry. This CAD model is further used for the CFD simulation in STAR-CCM+. To perform the simulation in AVL, a second and simplified model will have to be constructed as further explained.

A. CAD Model

Most of the geometrical and structural data concerning the Daedalus is made publicly available by MIT [4]. Based on this data, a precise replicate was constructed which can be seen in Figure 3. The Daedalus has a wingspan of 112 ft (34 m), being as large as the wingspan of a Boeing 737-800. The corresponding wing area is 332 ft^2 (31 m^2), resulting in a mean chord length of 2.96 ft (0.90 m). For increased aerodynamic performance, the wing is highly tapered, the ratio of the chord length at the tip to root (c_{tip}/c_{root}) being equal to 1/3. Due to the tapering, there is a large variation in the chord Reynolds number Re_c, such that the wing is made up of four different airfoils (DAE11, DAE21, DAE31, DAE41), each optimized for a different Reynolds number [5]. During flight, the wing is designed to have a tip deflection of 2 m at a cruise speed of 6.7 m/s [6]. As only the tip deflection was specified, the deformation of the complete wing is assumed as parabolic. The fuselage is the aerodynamic structure surrounding the pilot and is located just underneath the wing. The airfoil used to construct the fuselage was not specifically given but is assumed to be the symmetrical $NACA65_4$-021. Since the Daedalus was designed for long, straight flights, it required no ailerons for its control, steering was accomplished by the all-moving rudder and elevator. These are respectively the

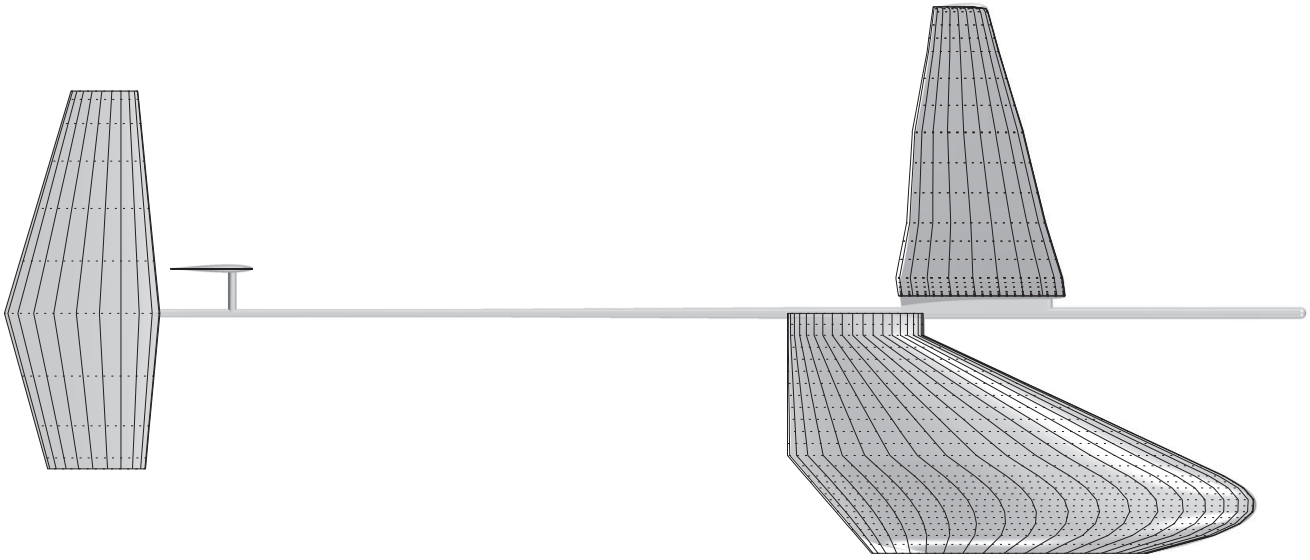

Fig. 4. AVL Model of the Daedalus plotted on top of its CAD Model

vertical and horizontal surface of the tail and are assumed to be constructed of the symmetrical NACA0010. The final structure is the tailboom, a carbon fiber tube going from the nose of the aircraft to its tail, used to connect the different parts of the aircraft. The propeller mounted in front of the aircraft will not be simulated in this work, but will be taken into account in the form of a propulsive efficiency.

B. AVL Model

To simulate the Daedalus using the Vortex Lattice Method, every aerodynamic structure (wing, fuselage, rudder and elevator) should first be represented as a thin surface, located along its camber lines. The different structures are defined in AVL by specifying a number of sections, each characterized by the type of airfoil, the chord length, the position of leading edge and the incidence. These sections are then linearly interpolated. By defining the structures in this way, the camber lines are easily determined together with the thin surfaces. These thin surfaces are now further divided into smaller elements, both in the spanwise and chordwise direction. Figure 4 shows the AVL model of the Daedalus plotted on top of its CAD model. Note that as the tailboom does not consist of airfoil sections, it cannot be included into the AVL model.

The Vortex Lattice Method [7], implemented into AVL, allows to calculate the lift and the induced drag of the aircraft. In order to take the profile drag (viscous + pressure drag) of the aircraft into account, AVL has the option to include the drag polar of every section used in defining the geometry. The drag polar is the relation between the profile drag coefficient C_D and lift coefficient C_L of an airfoil for different angles of attack. This relation also depends on the chord Reynolds number. The different drag polars were constructed using the panel code XFOIL [8].

Finally, to determine the equilibrium position of the Daedalus at a certain flight velocity, AVL requires its mass and Center of Gravity (CG). Based on the structural data provided by MIT, the mass and CG of the different structures were determined and are summarized in Table 1. Note that the empty weight of the Daedalus, so without pilot, is equal to just 30.60 kg. This means that the pilot (74.84 kg) was almost 2.5 times heavier than the aircraft itself. In equilibrium, the total lift should equal the weight of the Daedalus and the pitching moment around its CG should be zero. This can be accomplished by adjusting the Angle of Attack (AoA) of the aircraft and the local AoA of the elevator. These two angles will be a direct output of AVL, together with the induced and profile drag when the drag polars have been included.

	Mass (kg)	x_{CG} (m)	y_{CG} (m)	z_{CG} (m)
Wing	17.10	0	0	0.94
Fuselage	1.91	0.76	0	-0.85
Elevator	0.52	5.33	0	0.31
Rudder	0.52	6.10	0	0.26
Tailboom	1.49	1.55	0	0
Propeller	1.36	-1.98	0	0
Gearbox	0.91	-0.91	0	0
Crankset	1.36	-0.91	0	-1.52
Water	5.44	-0.06	0	-1.68
Pilot	74.84	0	0	-1.22
Daedalus	105.44	0.04	0	-0.83

Table 1. Mass and CG breakdown of the Daedalus

C. CFD Model

As HPAs fly at very low speeds (around 6.7 m/s in case of the Daedalus), their corresponding chord Reynolds numbers are mostly well below 1 million. The result is that the flow will remain laminar over a noticeable fraction of the airfoil and that the transition process laminar-turbulent will take place in the form of a so-called laminar separation bubble. This phenomenon is illustrated in Figure 6.

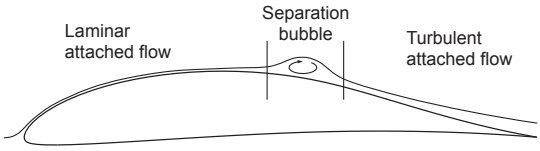

Fig. 5. Laminar Separation Bubble [9]

To predict this phenomenon in CFD, two models will be used; the k-ω SST turbulence model and the γ-Re$_\theta$ transition model. The γ-Re$_\theta$ transition model is based on a correlation and will predict the onset of transition. The objective is to simulate the entire Daedalus in CFD. However, using its symmetry, half of the aircraft will be sufficient. For this simulation, the fluid domain is constructed as a half-sphere with a radius of 100 m. The outer boundary is split into a velocity inlet and a pressure outlet. Using the trimmed hexahedral mesher of STAR-CCM+, the complete fluid domain is discretized and is shown in Figure 6. The boundary layer mesh consists of a 15-layer, 20 mm thick inflation layer, in which the first cell height is 0.01 mm, assuring a $y^+ < 1$. The maximal edge size of the elements on the geometry is 5 mm. By performing 2D simulations of an airfoil, this boundary layer mesh was found to produce sufficiently accurate results. The complete mesh consists of 52 million cells. The CFD simulation is performed steady, in which the flow is further modeled as incompressible, justified by the very low Mach numbers of HPAs. Additionally, the turbulent intensity is set to 0.07% together with a turbulent viscosity ratio of 10.

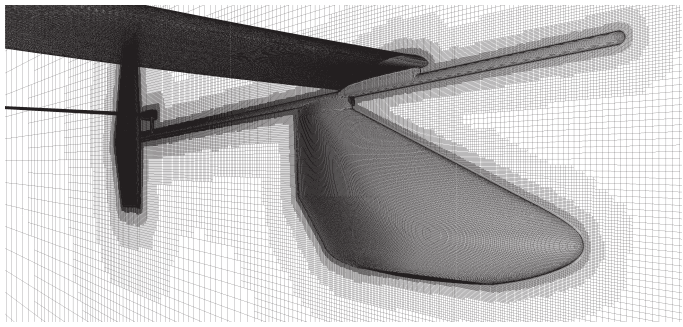

Fig. 6. Trimmed hexahedral mesh around the Daedalus

D. Results

The results of the AVL and CFD simulation of the Daedalus are given in Table 2. The simulations were performed at the design flight velocity of 15 mph (6.7 m/s). In AVL, the Daedalus was found to fly at an angle of attack of 2.76 degrees in order to generate sufficient lift. Additionally, for the pitching moment to be zero, the elevator had to be trimmed to a negative angle of -4.6 degrees. For the CFD simulation, the configuration of the aircraft was adjusted to be identical as in AVL. At this equilibrium position, the total drag was calculated together with its components. Note that this total drag corresponds with the so-called gliding drag of the aircraft, as no propulsion is simulated.

For the different drag components listed, it is important to know that the induced drag and profile drag only refer to the wing of the Daedalus and that the parasite drag is the difference between the gliding drag and the drag of the wing. Based on the gliding drag and the propulsive efficiency, consisting of the mechanical and propeller efficiency, the corresponding pilot power is determined. This is thus the actual power that the pilot will have to deliver to keep the aircraft up in the air.

At this point, a comparison can be made with the data from MIT, which is also included in Table 2. It is important to emphasize that the data from MIT are also estimates, but nevertheless, they provide an idea of the actual drag and its components. Comparing the gliding drag, AVL is found to predict a noticeable smaller value (18%), whereas the value of the CFD simulation is seen to agree within 5%. The underprediction in AVL was partly attributed to the drag polars generated by XFOIL, found to underpredict the profile drag.

The results of the CFD simulation can be seen in Figure 8, showing the turbulent kinetic energy close to the surface of the Daedalus together with the constrained streamlines. These help in visualizing the laminar separation bubble. At the position were the streamlines seem to be halted for the first time, the flow locally detaches and at the position of peak turbulent kinetic energy, the flow reattaches. The size of the laminar separation bubble on the wing is seen to be approximately constant along its span, except near to the wingtip. Note that the pressure side of the wing is completely laminar. The flow around the rudder is clearly influenced by the wake of the wing, in which the midsection is seen to be fully turbulent, whereas the upper section is largely laminar with transition occuring near the trailing edge.

	MIT [10]	**AVL**	**CFD**
Flight Velocity (m/s)	6.7	6.7	6.7
Gliding Drag (N)	27	22.2	26.2
Induced (N)	10.5 (35%)	11.2	–
Profile (N)	12.0 (40%)	9.7	–
Parasite (N)	4.5 (15%)	1.3	2.5
Lift (N)	1034.4	1034.4	1034.8
Propulsive Efficiency	0.90	0.90	0.90
Pilot Power (W)	201	165	195
AoA Aircraft (°)	–	2.76	2.76
AoA Elevator (°)	–	-4.6	-4.6
Calculation time	–	9.94 *s*	1 day

Table 2. Comparison estimated performance of the Daedalus

For the intended optimization of a HPA, it is interesting to compare the calculation time of both simulations (Table 2). For AVL, the calculation time is in the order of seconds, which is a major advantage when optimizing. Although the drag predictions are somewhat less accurate, as all designs are evaluated in the same software, a fair comparison can be made. On the other hand, CFD simulations allow to accurately predict the required pilot power, but require a large amount of computational time.

III. FSI Optimization

As the drag of the wing is the main contributor (90%) to the aircraft's total drag, the first step in designing our HPA for the Kremer International Marathon Competition will consist of optimizing a wing. To do so, the outer geometry of a wing is parameterized and described by its airfoil, span b, tip chord length c_{tip}, taper ratio λ $(c_{\text{tip}}/c_{\text{root}})$, twist angle θ and the relative position x/c of the spar's center. These design variables are indicated on half of a wing in Figure 7. By performing FSI simulations, it is possible to determine the material stresses and deformation of the wing during flight. These stresses should of course be limited to avoid structural failure. Further, the tip deflection of the wing during flight should equal a certain design value in order for the aircraft to be sufficiently stable. Designing a spar which fulfils these conditions and in addition minimizes the total mass of the wing is done in the FSI optimization. The spar is characterized by its wall thicknesses at the root and tip of the wing and it is assured that the spar will always fit into the wing. Additionally, a lift wire is included into the design, which will reduce the bending moments of the wing and help attain the desired tip deflection.

To find the optimal complete wing, a large Design of Experiments is be performed, in which a large set of different wing geometries is generated and individually structurally optimized. The optimal wing is then taken as the wing geometry with the lowest total drag and which is structurally feasible. As mentioned in the introduction, it is intended to investigate if powering a HPA by two pilots offers some advantages, such that two Design of Experiments were performed.

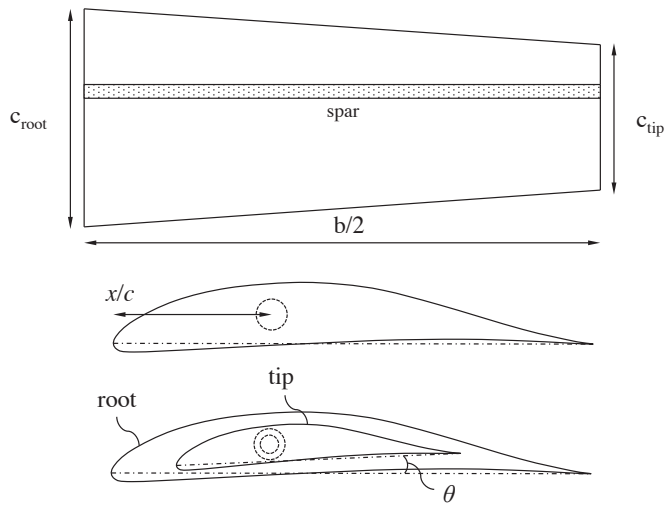

Fig. 7. Parameterized wing geometry

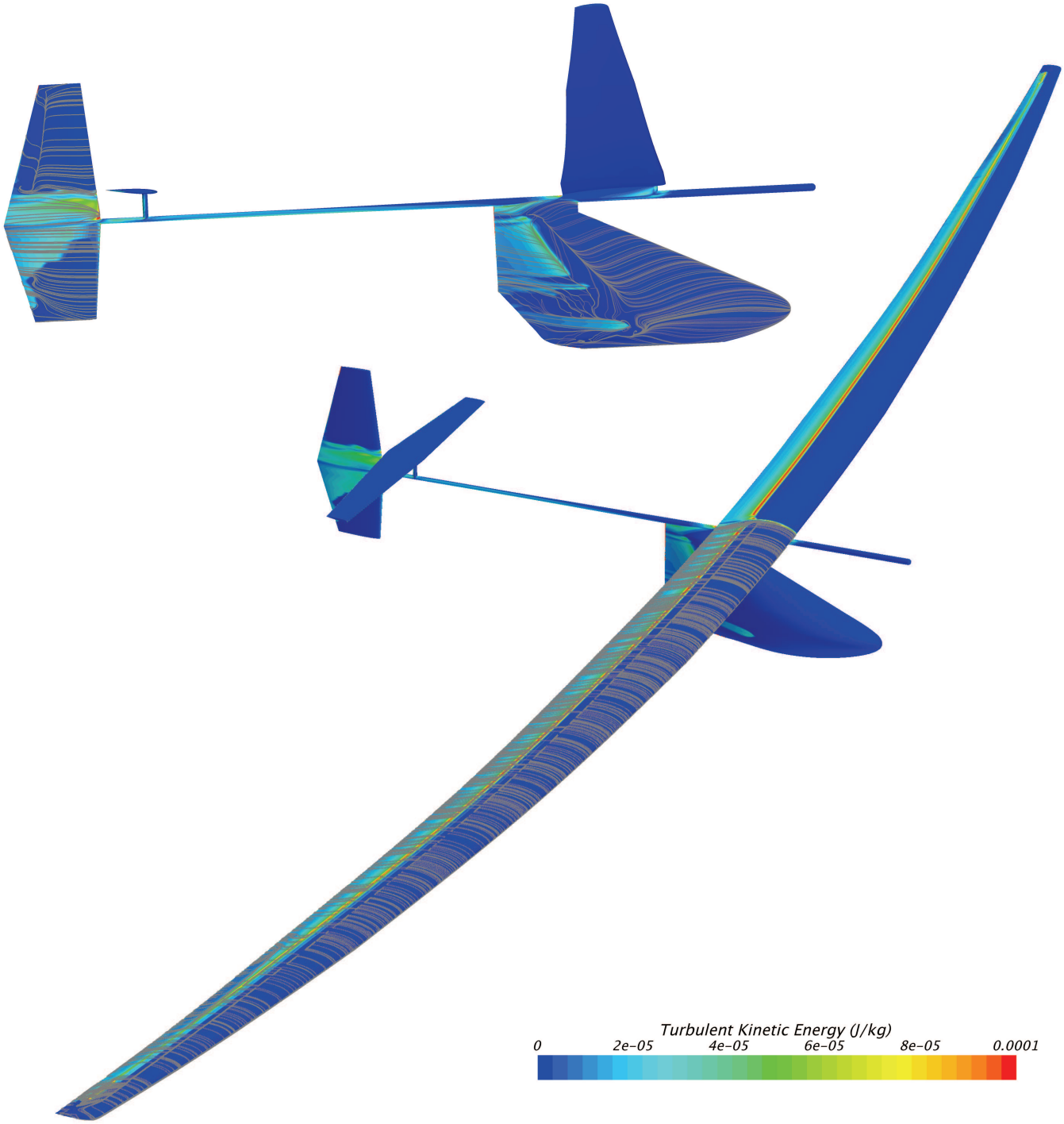

Fig. 8. Transition laminar-turbulent on the Daedalus visualized by the constrained streamlines and the turbulent kinetic energy

A. Results

The optimization proved the dual-pilot designs to be advantageous compared to the single-pilot designs, the reduction in required power per pilot ranging from 35 to 57 W. As such, only the results of the second Design of Experiments are included and shown in Table 3. In the Design of Experiments, 12 airfoils were investigated and for each airfoil type, the geometrical and structural data of the optimal design is given. Comparing the results for the different airfoils in Table 3, the E395 is seen to be the most optimal. Using this most optimal wing, our HPA will now be further constructed and designed for 2 pilots.

B. Complete Optimized Design

The idea consists of taking the Daedalus and replacing its wing by our own optimized wing and to adjust its fuselage to fit a second pilot. The position of the wing along the aircraft followed from a small optimization and the fuselage was extended

Dual-Pilot	b	c_{tip}	λ	Γ	t_{root}	t_{tip}	m_{spar}	σ_{spar}	σ_{LW}	AoA	D	P/pilot
Airfoil	(m)	(m)	–	(°)	(mm)	(mm)	(kg)	(MPa)	(MPa)	(°)	(N)	(W)
DAE11	27.50	0.35	0.47	6	1.21	1.21	8.01	284	388	4.50	25.72	154
DAE21	27.75	0.35	0.46	6	1.62	1.62	9.94	255	392	4.27	24.15	145
DAE31	27.25	0.35	0.46	6	1.89	1.89	10.52	253	392	3.79	23.42	141
E395	**28.75**	**0.35**	**0.46**	**6**	**1.65**	**1.65**	**10.94**	**239**	**388**	**2.88**	**22.47**	**135**
E396	28.75	0.35	0.46	6	1.36	1.36	9.68	250	392	2.79	23.04	138
E397	28.50	0.35	0.48	6	1.32	1.32	9.38	253	392	3.27	23.35	140
E398	29.25	0.35	0.47	6	1.20	1.20	9.32	250	392	2.98	23.86	143
E399	28.75	0.35	0.46	6	0.90	0.90	7.33	284	392	2.86	24.26	146
FX63-137	29.50	0.35	0.42	6	1.03	1.03	8.38	265	392	0.12	23.35	140
FX76MP120	26.25	0.35	0.55	6	1.93	1.93	10.20	255	392	2.17	24.99	150
FX76MP140	27.00	0.35	0.57	6	1.46	1.46	9.22	258	392	-1.17	24.75	149
L7769	27.25	0.35	0.43	6	1.64	1.64	9.45	266	391	7.49	26.72	160

Table 3. Geometrical and structural data of the dual-pilot designs

by 1.5 m, assuring sufficient space for the second pilot. Concerning the stability, both the Daedalus and our optimized HPA were found to be statically stable in AVL. The final simulation nows consist of performing a CFD calculation of our optimized HPA in STAR-CCM+. As for the Daedalus, the CFD simulation was performed steady, in which the flight velocity was set to 12 m/s (in order to complete the Marathon Course within 1 hour) and the angle of attack of the aircraft to 1.30 degrees. The results of the CFD simulation are given in Table 4 and are compared with the CFD results of the Daedalus. So, in case of our optimized HPA, each pilot should generate a power of 215 W. Note that the flight velocity is 80% higher compared to the Daedalus while the corresponding pilot power has only increased by 10%. An interesting result is that the total drag of the optimized wing is smaller compared to the Daedalus. However, the parasite drag has substantially increased. Further note that the generated lift is somewhat larger than the total weight, which is a small safety and allows to carry an additional 2.4 kg. The final step now consists of measuring the physical performance of our 2 pilots.

IV. Final Test

The physical performance was measured using a bicycle trainer with an adaptive resistive power. Starting at a low resistive power of 60 W, the power was gradually increased every 2 minutes by 20 W until the pilot reached total fatigue. Pilot 1 produced a maximal power output of 260 W, compared to 240 W for pilot 2. This is quite an exciting result as the maximal power output of both pilot together (500W) is definitely larger than the theoretical required power of 430 W. As such, the pilots can surely reach the design flight velocity of 12 m/s with our optimized dual-HPA. However, in order to win the Kremer International Marathon Competition, the pilots must sustain the aircraft at this 12 m/s during 1 hour. Dividing the theoretical required power over the 2 pilots based on their maximal power output, results in respectively 223.6 W for pilot 1 and 206.4 W for pilot 2. These values correspond with 86% of their maximal physical performance.

	Daedalus	**Optimized HPA**
Total Mass (kg)	105.4	147.0
Flight Velocity (m/s)	6.7	12
AoA Aircraft (°)	2.76	1.30
Gliding Drag (N)	26.2	32.3
Wing (N)	23.67	22.76
Parasite (N)	2.53	9.54
Lift (N)	1034.8	1465.5
Propulsive Efficiency	0.90	0.90
Total Power (W)	195	430
Pilot Power (W)	195	215

Table 4. Comparison performance Daedalus versus optimized dual-HPA

V. Conclusions

In our attempt to design and optimize a HPA capable of winning the Kremer International Marathon Competition, it was found that powering a HPA by 2 pilots is advantageous. From a final CFD simulation, the theoretical required power was estimated to be 430 W, which is lower than the maximal power output of both pilot together (500 W). Given this result, both pilots dream of constructing the aircraft and launching an attempt at winning the competition.

References

[1] J. McIntyre *Man's Greatest Flight*. AeroModeller, 1988.

[2] M. Drela and H. Youngren. *AVL (Athena Vortex Lattice)*. Massachusetts Institute of Technology, http://web.mit.edu/drela/Public/web/avl/, February 2016.

[3] RAeS. *Regulations and Conditions for the Kremer International Marathon Competition*. http://aerosociety.com/About-Us/specgroups/Human-Powered/Kremer, February 2016.

[4] M. Drela. *ASWING: Configuration Development System for Flexible Aircraft*. Massachusetts Institute of Technology, http://web.mit.edu/drela/Public/web/aswing/, February 2016.

[5] M. Drela. Low-Reynolds-Number Airfoil Design for the MIT Daedalus Prototype: A Case Study *Journal of Aircraft*, 25(8):724-732, 1988.

[6] J. R. Cruz and M. Drela. *Structural Design Conditions for Human Powered Aircraft*. OSTIV Conference, 1989.

[7] J. Katz and A. Plotkin. *Low-Speed Aerodynamics*, Cambridge University Press, second edition, 2001.

[8] M. Drela and H. Youngren. *XFOIL: Subsonic Airfoil Development System*. Massachusetts Institute of Technology, http://web.mit.edu/drela/Public/web/xfoil/, February 2016.

[9] T. Hansen. Modeling the Performance of the Standard Cirrus Glider using Navier-Stokes CFD *Technical Soaring*, 38(1):5-14, 2014.

[10] M. Drela. Aerodynamics of Human-Powered Flight *Annual Review of Fluid Mechanics*, 22(1):93-110, 1990.

Contents

1 Introduction **1**

1.1 Human-Powered Aircrafts . . . 2
1.2 Goal . . . 2
1.3 Outline . . . 3

2 Human Powered Flight **4**

2.1 Advancements in the early 1900s . . . 4
2.2 SUMPAC . . . 5
2.3 Toucan . . . 6
2.4 Gossamer Condor . . . 7
2.5 Gossamer Albatross . . . 8
2.6 Monarch B, Musculair I & II . . . 9
2.7 Daedalus . . . 10
2.8 The Kremer Prizes . . . 10
2.8.1 Kremer Marathon Competition . . . 11
2.8.2 Kremer Sporting Aircraft Competition . . . 11
2.9 Competitors . . . 13

3 Vortex Lattice Method **14**

3.1 General Equations . . . 14
3.2 Laplace's Equation . . . 15
3.3 Irrotational Vortex . . . 17
3.4 Basic Solution . . . 19
3.5 Biot-Savart Law . . . 20
3.6 Lifting-Line Solution . . . 22
3.7 Induced Drag . . . 24
3.8 Trefftz Plane . . . 25

4 Dynamics of Flight **30**

4.1 Static Stability . . . 30
4.1.1 Longitudinal Static Stability . . . 32
4.1.2 Directional Static Stability . . . 35
4.1.3 Roll Stability . . . 36
4.2 Equations of Motion . . . 37
4.3 Dynamic Stability . . . 42
4.3.1 Longitudinal Motion . . . 42
4.3.2 Lateral Motion . . . 43

5 Validation Case - Daedalus **46**
5.1 Reconstruction of the Daedalus . . . 46
5.1.1 Wing . . . 46
5.1.2 Fuselage . . . 55
5.1.3 Stab and Rudder . . . 57
5.1.4 Tailboom . . . 58
5.1.5 Pilot and miscellaneous . . . 59
5.1.6 Final CAD Model . . . 60
5.2 Specific Design Aspects . . . 62
5.2.1 Airfoil Design . . . 62
5.2.2 Specific Power . . . 64
5.2.3 Stability . . . 64
5.3 Lower-Order Analysis using VLM . . . 65
5.3.1 AVL Model . . . 65
5.3.2 Straight Level Flight . . . 70
5.3.3 Stability Analysis . . . 72
5.4 Higher-Order Analysis using CFD . . . 74
5.4.1 2D Simulation of the FX63-137 . . . 74
5.4.2 3D Simulation of the Daedalus . . . 83

6 FSI Optimization **87**
6.1 Optimization of a Wing . . . 87
6.1.1 Optimization Procedure . . . 87
6.1.2 Cases . . . 93
6.1.3 Wing Deflection . . . 94
6.1.4 Sensitivity Study . . . 97
6.1.5 Results . . . 103
6.2 Complete Optimized Design . . . 104

7 Final Test **108**
7.1 Physical Performance of Pilots . . . 108
7.2 Conclusions . . . 109

Appendix A **111**
A.1 Paper . . . 111
A.2 Detailed Overview Drawings . . . 132
A.3 Structural Data of the Daedalus . . . 136
A.4 AVL files of the Daedalus . . . 138

References **145**

List of Symbols

α	Angle of attack
b	Wing span
β	Sideslip angle
c	Chord length
C_D	Drag coefficient
C_L	Lift coefficient
C_l	Rolling moment coefficient
C_m	Pitching moment coefficient
C_n	Yawing moment coefficient
C_p	Pressure coefficient
D	Total drag
D_i	Induced drag
E	Young's modulus
g	Gravitational acceleration
Γ	Vortex strength
	Dihedral angle
γ	Intermittency
I	Inertia tensor
	Second moment of area
k	Turbulent kinetic energy
L	Lift
λ	Linear density
	Taper ratio
M	Bending moment
μ	Dynamic viscosity
p	Pressure
Φ	Velocity potential
Re	Reynolds number
ρ	Density
t	Spar's wall thickness
θ	Twist angle
	Deflection angle
σ	Material stress
u	Deflection
V	Shear force
v_∞	Free-stream velocity
ζ	Vorticity
	Damping ratio

List of Abbreviations

AoA	Angle of Attack
AVL	Athena Vortex Lattice
CAD	Computer-Aided Design
CFD	Computational Fluid Dynamics
CG	Center of Gravity
FSI	Fluid-Structure Interaction
HMCF	High Modulus Carbon Fiber
HPA	Human-Powered Aircraft
HR	Heart Rate
LSB	Laminar Separation Bubble
LW	Lift Wire
MBL	Minimum Breaking Load
MIT	Massachusetts Institute of Technology
NP	Neutral Point
PBA	Principal Bending Axis
RANS	Reynolds Averaged Navier-Stokes
RHS	Right-Hand Side
RP	Reference Point
SF	Safety Factor
SM	Static Margin
TKE	Turbulent Kinetic Energy
TS	Tensile Strength
UIUC	University of Illinois at Urbana-Champaign
VLM	Vortex Lattice Method

Chapter 1

Introduction

"Once you have tasted flight, you will forever walk the earth with your eyes turned skywards, for there you have been and there you will always long to return."

— Leonardo da Vinci

The dream of flying like a bird is as old as humanity itself. It was Leonardo da Vinci who around 1490 was the first person to study flight in a scientific manner. Inspired by nature, he spent years drawing designs for gliders, flying machines and ornithopters (flapping wings). A sketch of one of his most advanced ornithopters is shown in Figure 1.1, in which only the wing tips were to flap. Although no design was ever successful, the combined weight of machine and pilot simply being too heavy to be lifted by human power, still a first step had been made towards human-powered aircrafts.

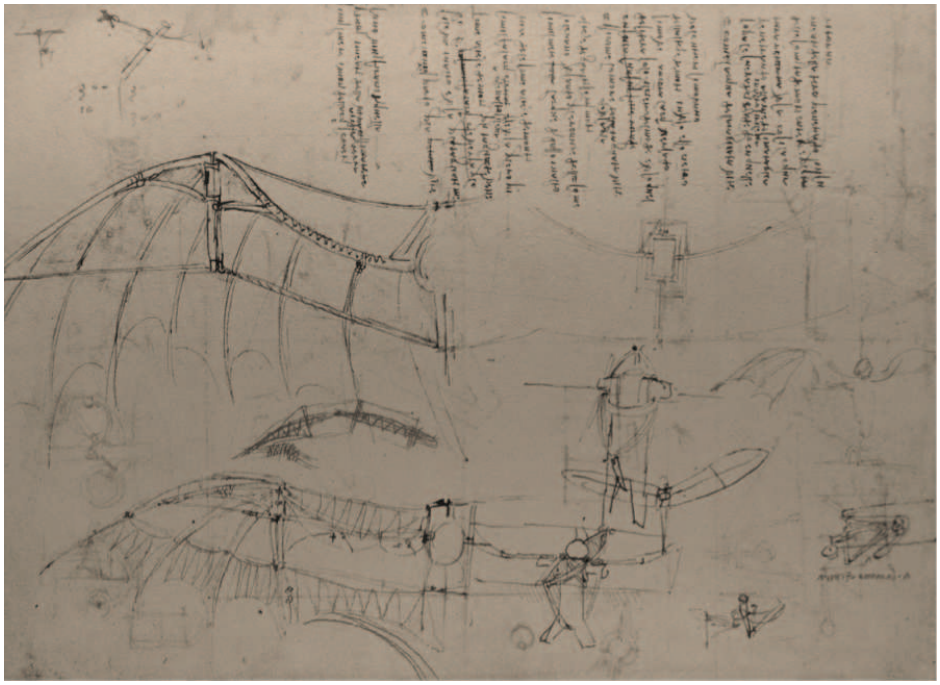

Figure 1.1: Sketch by Leonardo da Vinci

1.1 Human-Powered Aircrafts

It may sound impossible, but by careful design the human power is found sufficient to propel an aircraft. These special aircrafts, known as Human-Powered Aircrafts (HPAs), are extremely light, fly at very low speeds and are usually constructed for a single pilot. In many designs the aircraft is powered by the pedaling motion of the pilot, driving a propeller. This configuration is illustrated in Figure 1.2 and a complete human-powered aircraft can be seen in Figure 1.3. The challenging design and construction of these aircrafts have attracted the attention of research teams from all over the world. Combining new materials and more advanced analysis tools, these aircrafts are continuously further optimized allowing longer flights, higher flight velocities or increased maneuverability. There are many peculiarities involved in the aircraft's aerodynamics giving them a high educational value.

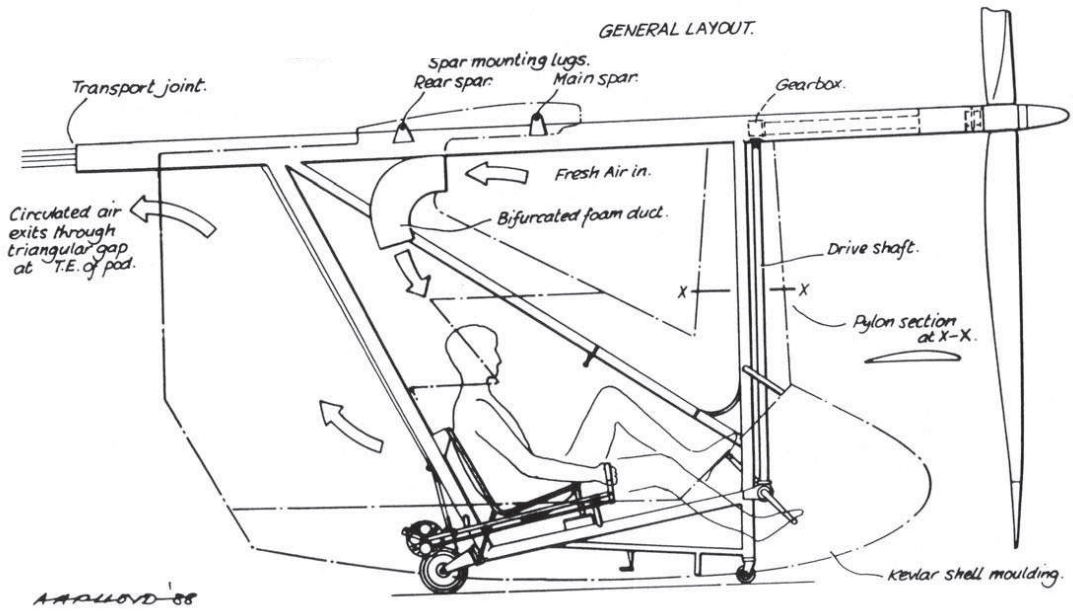

Figure 1.2: Typical configuration of a human-powered aircraft

1.2 Goal

The goal of the present work is to design and optimize a human-powered aircraft capable of winning the Kremer International Marathon Competition. This is a prestigious challenge set out specifically for human-powered aircrafts, in which a marathon distance is to be flown in less than 1 hour. Although the challenge has been announced in 1988, it remains unaccomplished up to date. Completing the challenge would be a major accomplishment in the history of human powered flight and in addition the team is rewarded with a monetary prize of £50 000. More details concerning the Kremer International Marathon Competition will be given in Chapter 2.

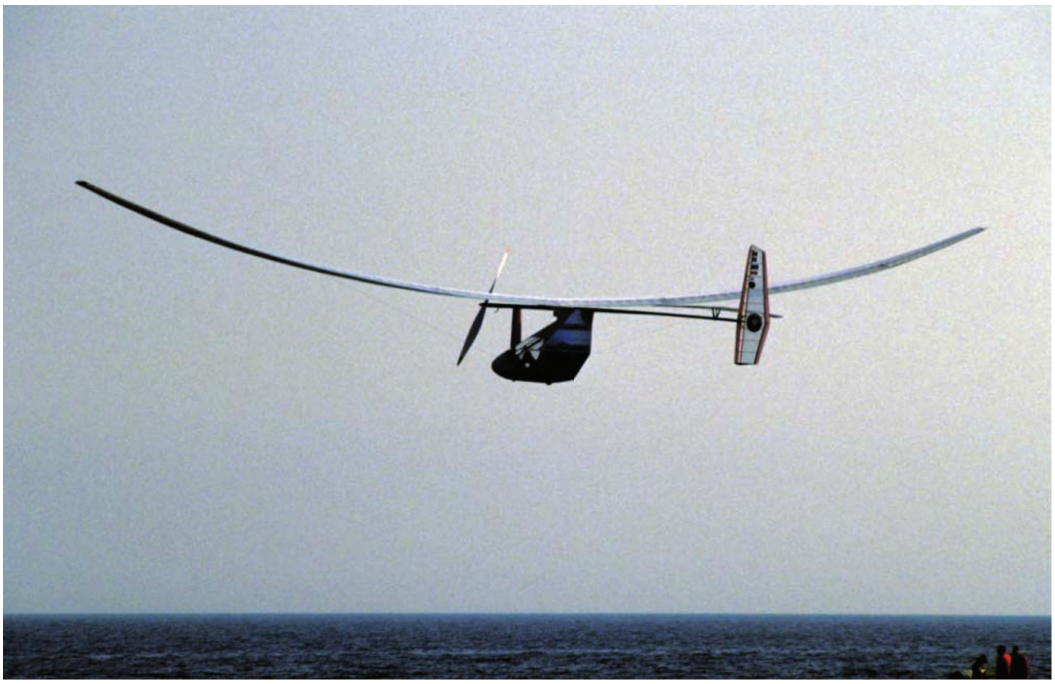

Figure 1.3: A human-powered aircraft in flight

1.3 Outline

In the attempt to design a new human-powered aircraft, we will first explore the history of human powered flight (Chapter 2), revealing some interesting designs, facts and achievements. With the intention of optimizing a complete human-powered aircraft, many different aircraft designs will have to be evaluated. In order to reduce the computational time needed to evaluate a single design, the *Vortex Lattice Method* will be used. For a good understanding, Chapter 3 explains the theory behind this method. In Chapter 4, we derive the conditions for an aircraft to be statically and dynamically stable which is an important aspect in aircraft design. With this theoretical background we will first analyze an existing design in some more detail (Chapter 5). The design we choose is the *Daedalus*, the most successful design built so far. The purpose is to gain additional insight into designing a human-powered aircraft and to verify the accuracy of the Vortex Lattice Method with *Computational Fluid Dynamics*. In Chapter 6, we present the optimization procedure of our own human-powered aircraft. As the deflection of the wing during flight is found to be a key aspect in the design, Fluid-Structure Interaction (FSI) simulations will be performed and included in the optimization. The final and possibly most exciting part is Chapter 7, where we verify if the pilot or pilots are able to generate the required power to win the Kremer International Marathon Competition.

A full research paper of this work has been written and submitted to the journal *Aerospace* for the special issue on Fluid-Structure Interactions. The submitted paper can be found in Appendix A.1.

Chapter 2

Human Powered Flight

The present chapter provides an overview of the history of human powered flight, including the most successful designs and their major achievements. The special challenges set out for human-powered aircrafts are introduced along with the different designs. One of these special challenges is the Kremer International Marathon Competition.

2.1 Advancements in the early 1900s

To encourage the development of human powered flight, the French *Peugeot Competition* was established in 1912. The purpose of the competition was to find out if a flying machine could be constructed, set into motion solely by the human power of the pilot and able to fly a distance of 10 m, further than anyone could jump. In order to eliminate the benefit of a possible wind, the pilot had to fly the distance of 10 m in both directions within 15 min. It was only in 1921 that Gabriel Poulain, a racing cyclist, claimed the Peugeot Prize with his aero-cycle after two consecutive flights of 10.54 m and 11.64 m with heights exceeding 1 m [1]. Poulain is seen in action on that specific day in Figure 2.1.

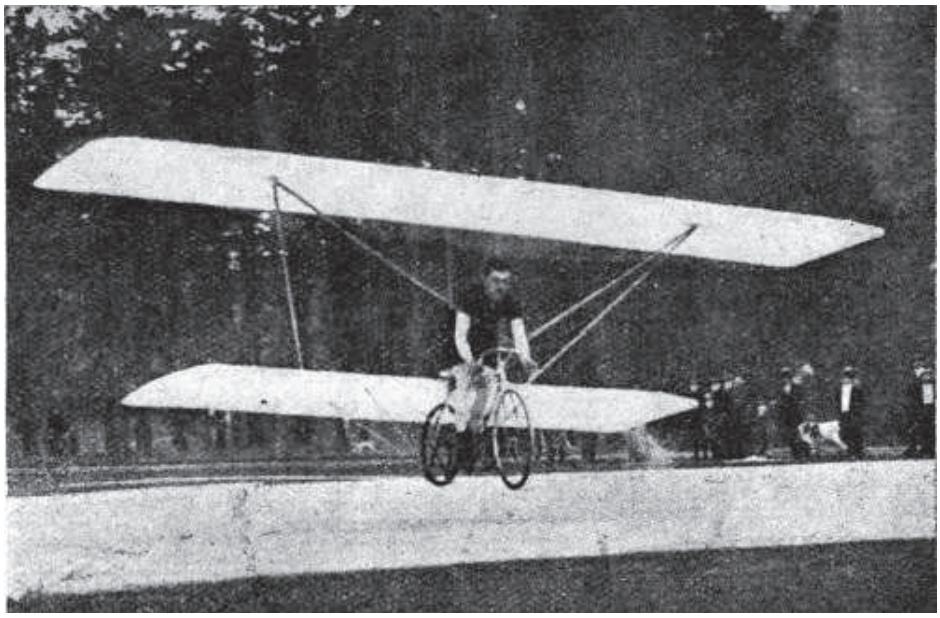

Figure 2.1: Poulain and his aero-cycle in 1921

In the 1930s, advancements were made in the human powered flight with the German *Mufli* and Italian *Pedaliante* (Figure 2.2). These designs resembled typical gliders of that period but were fitted with an additional propeller or in the case of the *Pedaliante* two contra-rotating propellers [1]. Although the flights involved a catapult or tension cables to assist in launch and the pilots could only make prolonged glides, these designs provided a basis for future human-powered aircrafts.

Figure 2.2: The *Pedaliante* (1936)

The development of Human-Powered Aircraft (HPA) technology was greatly stimulated when in 1959, the British industrialist Henry Kremer offered a prize of £5 000 for the first HPA to complete a figure-of-eight course around two markers 1/2 mile (803 m) apart. The aircraft had to take off and fly solely by human power and cross the start and finish line at an altitude of at least 10 ft (3.05 m). At that time, no HPA had ever been able to take off unaided and sustain the aircraft in straight level flight.

2.2 SUMPAC

The first major achievement was in 1961 when the Southampton University Man-Powered Aircraft *SUMPAC* made the first official human powered flight with no assistance during take-off [1]. The *SUMPAC* flew a distance of 64 m and was airborne for about 8 s. The design can be seen in Figure 2.3.

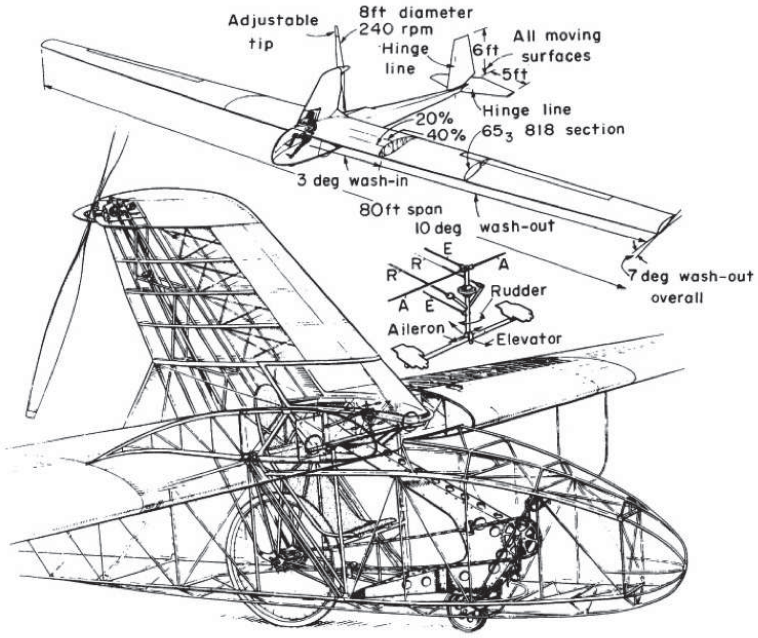

Figure 2.3: The *SUMPAC* (1961)

2.3 Toucan

In the years that followed, many different designs were tested. A particular design was the *Toucan* (Figure 2.4), one of the largest HPAs ever built and powered by 2 men. The anticipated advantages were a higher power to weight ratio and a more continuous power output, favorable during difficult manoeuvres such as turns. It was in 1972, that the *Toucan I* made the world's first flight of a two seat HPA covering a distance of 68 yards (62 m).

Figure 2.4: The *Toucan* (1972)

2.4 Gossamer Condor

After 18 years of unsuccessful attempts, the first Kremer Prize was finally won in 1977 by the American *Gossamer Condor*. A combination of novel ideas, numerous flight tests and modifications had made the seemingly unattainable Kremer Prize possible. The design was not based on a sailplane, but instead followed the hang-glider concept, as can be seen in Figure 2.5. A more detailed overview drawing can be found in Appendix A.2. Compared to previous HPAs, the *Gossamer Condor* had a very large wing area making it possible to fly at very low speeds of about 10 mph (16 km/h), requiring less power from the pilot [2]. The extensive external wire bracing needed for structural support and control were tolerable due to the very low speeds. The aircraft was fitted with a canard control surface, which in addition to pitch control could also be tilted sideways, leading the aircraft around by the nose. However, turning in a controlled manner remained a problem. It was after a crash, where the aircraft had to be rebuild, that a turn-control breakthrough occurred. By twisting the wings in opposite direction at the tips through external wires known as *wing warping*, the aircraft was able to make stable and gently banked turns. The Kremer course consisting of two turns of more than 180° was now possible.

Figure 2.5: The *Gossamer Condor* (Don Monroe, 1977)

2.5 Gossamer Albatross

In response to the achievement of the *Gossamer Condor*, Henry Kremer soon proposed a new challenge, known as the second Kremer Channel Prize. He offered a prize of £100 000 for the first human powered flight across the English Channel from England to France. The challenge would require further advancements in aerodynamic and structural efficiency and the ability to handle less ideal weather conditions. To everyone's surprise, the prize was won only two year later in 1979 by the American *Gossamer Albatross*, a refined version of the *Gossamer Condor*. The *Gossamer Albatross* can be seen in flight in Figure 2.6 and a more detailed overview drawing can be found in Appendix A.2. A major advancement was the use of carbon fibre and Styrofoam resulting in a reduction of the empty weight from 70 to 55 pounds (6.8 kg) while maintaining strength and rigidity [2]. Further adjustments included; a smaller chord (was designed to fly faster, 22-29 km/h), closely-spaced ribs and tensilized Mylar skin (giving a smoother and more consistent surface), an optimized propeller and the pilot in upright position (found to produce more power in this position). The official time for the cross over was 2 hours 49 minutes and a distance of 22 miles (35.4 km).

Figure 2.6: The *Gossamer Albatross* (Jim Harrison, 1979)

2.6 Monarch B, Musculair I & II

In the early 1980s, a new challenge was launched, known as the third Kremer Speed Prize. The first HPA to fly around a triangular course of 1500 m in under 3 minutes was awarded with £20 000. Additional prizes of £5 000 were rewarded for every improvement of the record time by at least 5%. The rules permitted the pilot to store his own energy over a period of 10 minutes prior to take-off, which could then be used during flight [3]. In 1984, the prize was won by MITs *Monarch B*, completing the course in 2 minutes 55 seconds. Successful improvements were made by the *Musculair I* (2'31"), *Bionic Bat* (2'23") and *Musculair II* (2'02"), in which the *Musculair* aircrafts did not store any energy. Assuming a flight distance of 1 mile, taking into account the increased distance due to the turnings, the *Musculair II* (Figure 2.7) flew at an average speed of about 48 km/h!

Figure 2.7: The *Musculair II* (Ernst Schoberl, 1985)

2.7 Daedalus

In an attempt to reconstruct the mythical escape of Daedalus from Crete, said to have built himself wings of feathers and wax, a new HPA was developed at MIT, named after Daedalus. The *Daedalus*, powered by fourteen-times Greek cyclist champion Kanellos, took off in 1988 from the island of Crete, across the Aegean Sea, to the mainland of Greece. The legendary flight covered a distance of 74 miles (119 km), completed in 3 hours 54 minutes [4] and can be seen in Figure 2.8. The long, straight flight required no ailerons for its control, steering was accomplished by the all-moving rudder and elevator. A more detailed analysis of the *Daedalus* will be given in Chapter 5. At present, the *Daedalus* still holds the world record for longest time and distance flown under human power.

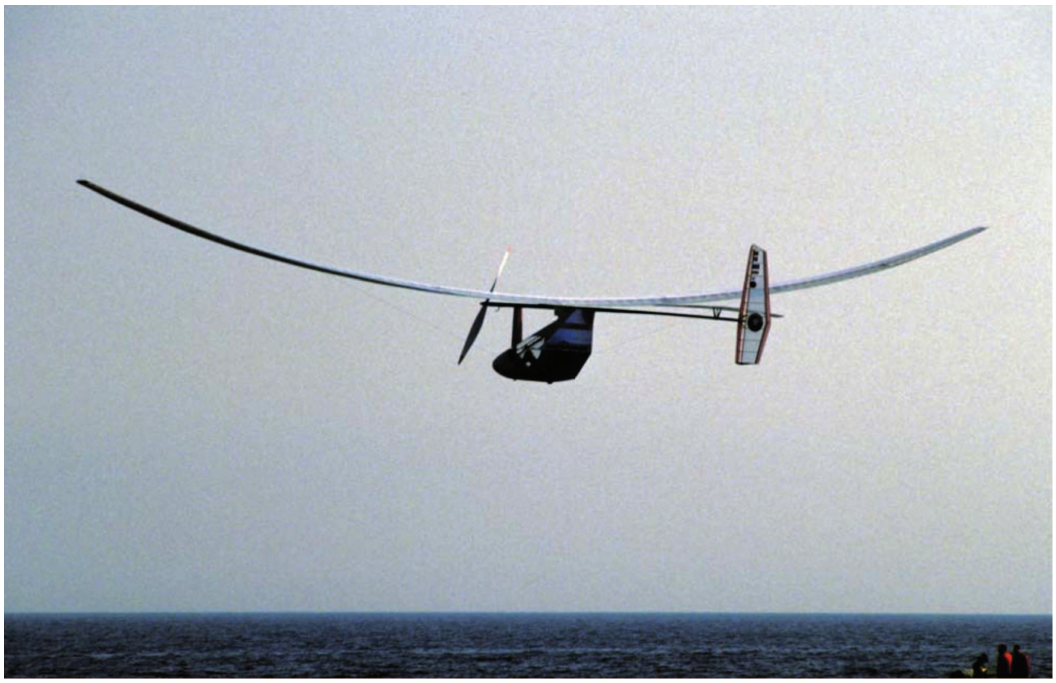

Figure 2.8: The *Daedalus* (John McIntyre, 1988)

2.8 The Kremer Prizes

At present, two Kremer challenges remain unaccomplished,

- the Kremer International Marathon Competition (£50 000)
- the Kremer International Sporting Aircraft Competition (£100 000)

2.8.1 Kremer Marathon Competition

The Marathon Prize will be awarded to the first HPA conforming to a number of rules, able of completing a specific course within the United Kingdom in 1 hour or less. The Marathon Course is shown in Figure 2.9. Starting from the *Course datum line*, the aircraft is to take off from rest, perform two laps of the outer circuit followed by a figure-of-eight and two more outer circuits. When passing the course datum line and turning point markers, the lowest point of the aircraft must be at least 5 m above the ground. The timing of the flight ends when the nose of the aircraft passes the course datum line but the aircraft must land safely to be valid. The turns around the markers can be of any radius, such that the minimal distance of the course is 40 510 m. Lately, some revisions have been made to the course, in which the entrant is now free to choose the distance between the turning points from a list (see Figure 2.9) with the corresponding number of circuits. Any one of the circuits should be a figure-of-eight. Some of the regulations and conditions dealing with the aircraft and competition are listed below [5],

- The aircraft shall be propelled entirely by human power. No device for the storage or supply of energy may be used.
- The crew shall be those in the aircraft during the takeoff and flight. There shall be no limit to their number and no member of the crew shall be permitted to leave the aircraft at any time of the flight.
- The aircraft shall be a heavier than air machine and the use of lighter than air gases shall be prohibited.
- Auto-stabilization, auto-speed-limiter and propeller-governing are allowed, but not an autopilot.

As outlined, it is attempted to design and optimize a human-powered aircraft with the goal of winning this Kremer International Marathon Competition.

2.8.2 Kremer Sporting Aircraft Competition

The Sport Prize will be awarded to the first HPA conforming to a number of rules, completing a triangular course within the United Kingdom under a mean ambient wind speed of no less than 5 m/s. The triangular course has side lengths of 500 m and a circuit in both directions is to be flown. The flying time of both flights together, should be no more than 7 minutes. Aiming at future athletic competition, the dismantled HPA is to fit in a container no longer than 8 m and shown to be assembled within 30 minutes. Upon successful completion of the two flights, the HPA is to be dismantled back and stowed in the container within 30 minutes.

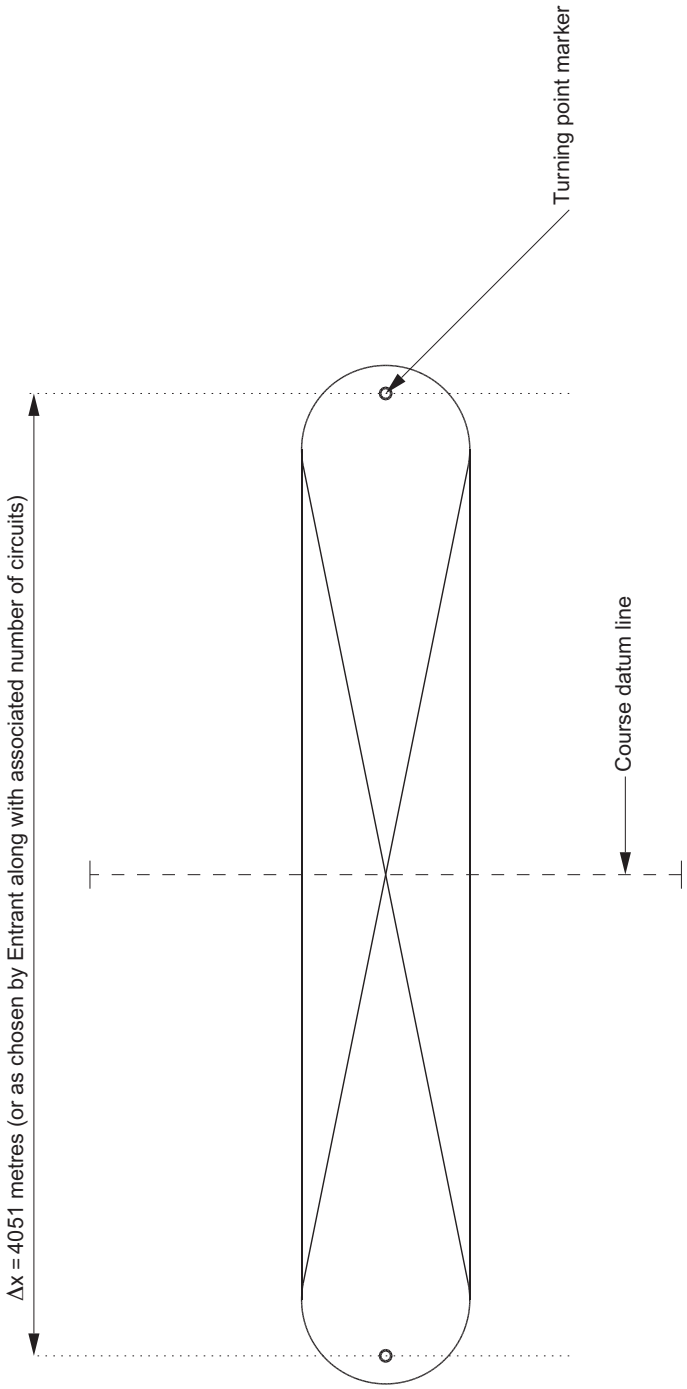

Δx (m)	Number of circuits
4051	5
3348	6
2846	7
2469	8
2176	9
1942	10
1750	11
1590	12
1455	13
1339	14
1238	15
1151	16
1073	17
1004	18
942	19
887	20
837	21
791	22
749	23

Figure 2.9: The Kremer Marathon Competition course

2.9 Competitors

At the time of writing, one group of young Aerospace Engineering students at Queen Mary University of London is known to attempt the Kremer International Marathon Competition. Their HPA *Queen Bee* can be seen in Figure 2.10 and is currently under construction.

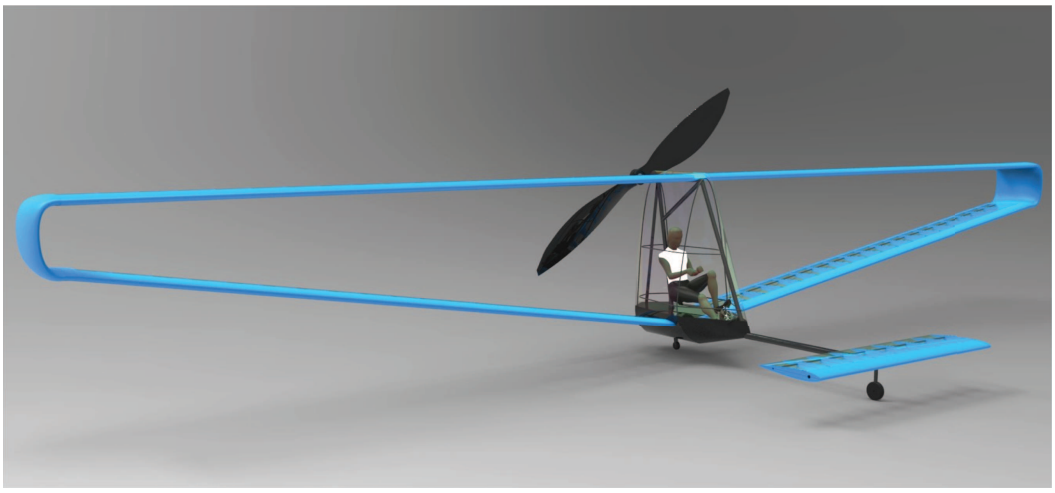

Figure 2.10: The *Queen Bee*

Chapter 3

Vortex Lattice Method

As outlined in Section 1.2, we will introduce the *Vortex Lattice Method* (VLM) for doing quick aerodynamic analyses of aircrafts. It will be shown that the Vortex Lattice Method leads to a system of linear equations which can easily be solved numerically. The resulting calculation times will be very short and ideal for doing optimization.

3.1 General Equations

To develop the simplified equations used in Vortex Lattice Methods, consider an arbitrary control volume (Figure 3.1) stationary with respect to an inertial reference frame, on which we express conservation of mass and momentum,

$$\frac{\partial}{\partial t}\int\limits_{c.v.} \rho \,\mathrm{d}V + \int\limits_{c.s.} \rho(\vec{v}\cdot\vec{n})\,\mathrm{d}S = 0 \tag{3.1}$$

$$\frac{\partial}{\partial t}\int\limits_{c.v.} \rho\vec{v} \,\mathrm{d}V + \int\limits_{c.s.} \rho\vec{v}(\vec{v}\cdot\vec{n})\,\mathrm{d}S = \int\limits_{c.v.} \rho\vec{f}\,\mathrm{d}V + \int\limits_{c.s.} \vec{n}\cdot\vec{\vec{\sigma}}\,\mathrm{d}S \tag{3.2}$$

where $\vec{\vec{\sigma}}$ is the stress tensor and $\rho\vec{f}$ the body forces per unit of volume. Using the *divergence theorem*, we can transform the surface integrals into volume integrals,

$$\int\limits_{c.v.} \left(\frac{\partial\rho}{\partial t} + \vec{\nabla}\cdot(\rho\vec{v})\right)\mathrm{d}V = 0 \tag{3.3}$$

$$\int\limits_{c.v.} \left(\frac{\partial}{\partial t}(\rho v_i) + \vec{\nabla}\cdot(\rho v_i\vec{v}) - \rho f_i - \frac{\partial\sigma_{ij}}{\partial x_j}\right)\mathrm{d}V = 0 \qquad i = 1,2,3 \tag{3.4}$$

where the time derivative is taken inside the integral since the control volume is stationary.

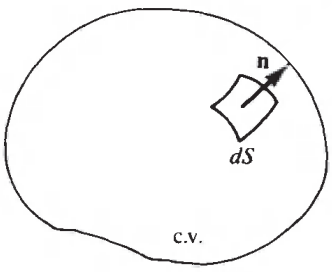

Figure 3.1: A control volume in the fluid [6]

As the equations (3.3),(3.4) hold for an arbitrary control volume, the integrands must be zero. We now obtain the general differential forms of the mass (continuity) and momentum equation

$$\frac{\partial \rho}{\partial t} + \vec{\nabla} \cdot (\rho \vec{v}) = 0 \tag{3.5}$$

$$\frac{\partial}{\partial t}(\rho v_i) + \vec{\nabla} \cdot (\rho v_i \vec{v}) = \rho f_i + \frac{\partial \sigma_{ij}}{\partial x_j} \qquad i = 1, 2, 3 \ . \tag{3.6}$$

For a Newtonian fluid (stress components σ_{ij} linear in the derivatives $\partial v_i / \partial x_j$), the momentum equations can be written as [6]

$$\rho \left(\frac{\partial v_i}{\partial t} + \vec{v} \cdot \vec{\nabla} v_i \right) = \rho f_i - \frac{\partial}{\partial x_i} \left(p + \frac{2}{3} \mu \vec{\nabla} \cdot \vec{v} \right) + \frac{\partial}{\partial x_j} \mu \left(\frac{\partial v_i}{\partial x_j} + \frac{\partial v_j}{\partial x_i} \right) \qquad i = 1, 2, 3 \tag{3.7}$$

which are known as the *Navier-Stokes equations*. Note that we have used Einstein's summation convention in (3.6) and (3.7).

3.2 Laplace's Equation

We will now introduce some simplifications, inherent to Vortex Lattice Methods. As human-powered aircrafts fly at very low Mach numbers, we may assume the flow to be incompressible. Further, in a first approximation, we will assume the flow to be inviscid ($\mu = 0$) and steady. Based on these assumptions, equations (3.5),(3.6) reduce to

$$\vec{\nabla} \cdot \vec{v} = 0 \tag{3.8}$$

$$\vec{v} \cdot \vec{\nabla} \vec{v} = \vec{f} - \frac{\vec{\nabla} p}{\rho} \ . \tag{3.9}$$

The arbitrary motion of a fluid element consists of translation, rotation and deformation, in which the angular velocity $\vec{\omega}$ is given by [6]

$$\vec{\omega} = \frac{1}{2} \vec{\nabla} \times \vec{v} \ . \tag{3.10}$$

For convenience, the *vorticity* $\vec{\zeta}$ is defined as twice the angular velocity,

$$\vec{\zeta} \equiv 2\vec{\omega} = \vec{\nabla} \times \vec{v} \ . \tag{3.11}$$

Now consider an open surface S with a closed curve C as its boundary. The *circulation* Γ is defined by

$$\Gamma \equiv \oint_C \vec{v} \cdot \vec{dl} \ . \tag{3.12}$$

Using *Stokes' theorem*, the circulation can be related to the vorticity on the surface S,

$$\oint_C \vec{v} \cdot \vec{dl} = \int_S (\vec{\nabla} \times \vec{v}) \cdot \vec{n} \, \mathrm{d}S = \int_S \vec{\zeta} \cdot \vec{n} \, \mathrm{d}S \ . \tag{3.13}$$

As a final simplification, we will assume the flow to be irrotational, $\vec{\nabla} \times \vec{v} = 0$. As a result, we can write the velocity field $\vec{v}$ as the gradient of a so-called *velocity potential* Φ,

$$\vec{v} = \vec{\nabla}\Phi \ . \tag{3.14}$$

Note that for a scalar field A, $\vec{\nabla} \times \vec{\nabla} A \equiv 0$. Substitution of (3.14) into the continuity equation (3.8) leads to

$$\vec{\nabla} \cdot \vec{v} = \vec{\nabla} \cdot \vec{\nabla}\Phi = \nabla^2 \Phi \equiv 0 \tag{3.15}$$

which is *Laplace's equation*. As we have neglected the fluid's viscosity, we cannot enforce the no-slip boundary condition on a solid-fluid boundary. Instead, we state that the normal component of the velocity on the solid boundaries must be zero,

$$\vec{\nabla}\Phi \cdot \vec{n} = 0 \ . \tag{3.16}$$

As a second boundary condition, we state that the disturbance caused by the object (e.g. a wing) should decay to zero at infinity,

$$\lim_{r \to \infty} \vec{\nabla}\Phi = \vec{v}_\infty \tag{3.17}$$

in which $\vec{v}_\infty$ is the free-stream velocity. At this point, we have reduced the problem to finding a velocity potential Φ satisfying (3.15) and the appropriate boundary conditions (3.16),(3.17). Note that Laplace's equation is linear, such that the solution can be obtained as a linear combination of elementary solutions.

Once the velocity field $\vec{v}$ is obtained, we can determine the pressure distribution on the body's surface using the momentum equation, which will allow us to calculate the aerodynamic forces and moments. The left-hand side of (3.9) can be rewritten as [6]

$$\vec{v} \cdot \vec{\nabla}\vec{v} = \vec{\nabla}\frac{v^2}{2} - \vec{v} \times (\vec{\nabla} \times \vec{v}) \tag{3.18}$$

where the last term is zero for irrotational flow. Assuming that gravity is the only body force acting, we can write

$$\vec{f} = -\vec{\nabla}E \tag{3.19}$$

with $E = -gz$.

As such, the momentum equation becomes

$$\begin{aligned} \vec{\nabla}\left(E+\frac{p}{\rho}+\frac{v^2}{2}\right)&=0 \\ \longrightarrow E+\frac{p}{\rho}+\frac{v^2}{2}&=cst \end{aligned} \tag{3.20}$$

known as the *Bernoulli equation* for potential flow. Comparing the quantities at two points; an arbitrary point and a reference point at infinity,

$$\left(E+\frac{p}{\rho}+\frac{v^2}{2}\right)=\left(E+\frac{p}{\rho}+\frac{v^2}{2}\right)_\infty \tag{3.21}$$

the pressure p at any point in the fluid is calculated from

$$\frac{p_\infty-p}{\rho}=(E-E_\infty)+\left(\frac{v^2}{2}-\frac{v_\infty^2}{2}\right). \tag{3.22}$$

3.3 Irrotational Vortex

We will now make a small sidestep and consider the steady flowfield of a two-dimensional rigid cylinder of radius R rotating in an incompressible viscous fluid at a constant angular velocity ω_y as shown in Figure 3.2. The continuity and momentum equations for a steady incompressible fluid in polar coordinates are respectively [6]

$$\frac{\partial v_r}{\partial r}+\frac{1}{r}\frac{\partial v_\theta}{\partial \theta}+\frac{v_r}{r}=0 \tag{3.23}$$

and

$$r-direction: \qquad -\rho\frac{v_\theta^2}{r}=\rho f_r-\frac{\partial p}{\partial r}+\mu\left(\nabla^2 v_r-\frac{v_r}{r^2}-\frac{2}{r^2}\frac{\partial v_\theta}{\partial \theta}\right) \tag{3.24}$$

$$\theta-direction: \qquad \rho\frac{v_r v_\theta}{r}=\rho f_\theta-\frac{1}{r}\frac{\partial p}{\partial \theta}+\mu\left(\nabla^2 v_\theta-\frac{v_\theta}{r^2}+\frac{2}{r^2}\frac{\partial v_r}{\partial \theta}\right) \tag{3.25}$$

As suggested by Figure 3.2, the motion of the cylinder results in a flow with circular streamlines, such that the radial velocity component v_r is zero. The continuity equation becomes

$$\frac{\partial v_\theta}{\partial \theta}=0 \tag{3.26}$$

which states that v_θ is only a function of r.

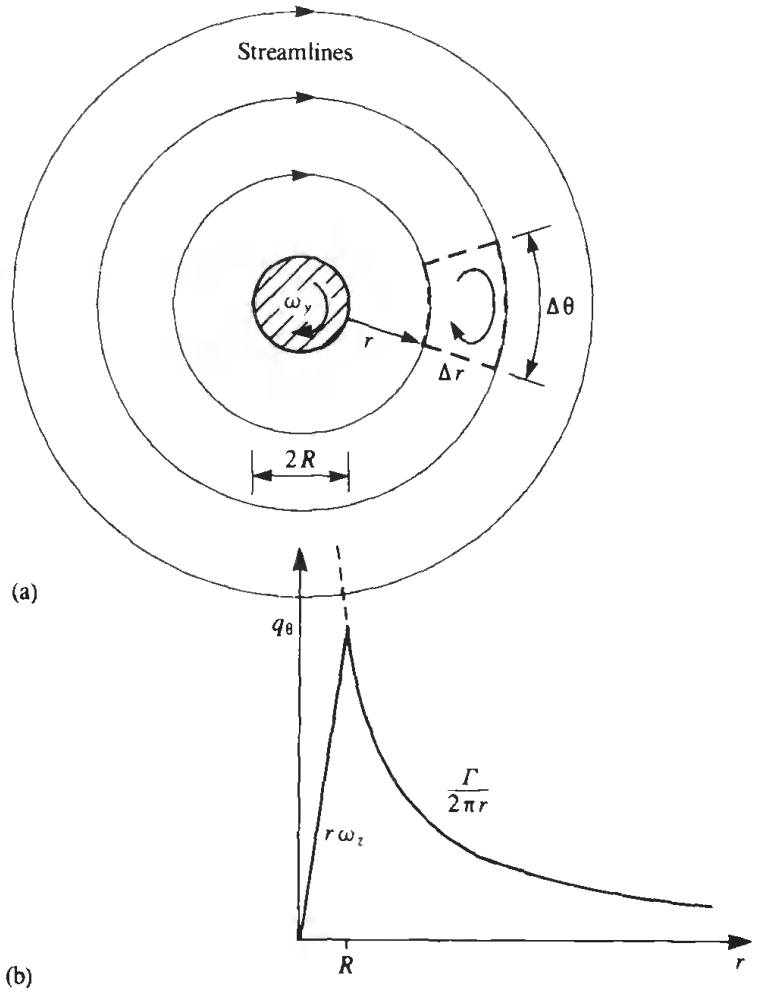

Figure 3.2: Two-dimensional flowfield around a cylinder core rotating as a rigid body [6]

Using the continuity equation and neglecting the body force terms, the momentum equations become

$$r - direction: \qquad -\rho\frac{v_\theta^2}{r} = -\frac{\partial p}{\partial r} \tag{3.27}$$

$$\theta - direction: \qquad 0 = \mu\left(\nabla^2 v_\theta - \frac{v_\theta}{r^2}\right) \ . \tag{3.28}$$

Since v_θ is a function of r only, (3.28) can be written as

$$0 = \frac{\mathrm{d}^2 v_\theta}{\mathrm{d}r^2} + \frac{\mathrm{d}}{\mathrm{d}r}\left(\frac{v_\theta}{r}\right) \tag{3.29}$$

with as boundary conditions,

$$\begin{aligned} v_\theta &= -R\omega_y \qquad at \quad r = R \\ v_\theta &= 0 \qquad\quad\ \ at \quad r = \infty \ . \end{aligned}$$

Performing the integration and using the above boundary conditions, we obtain the tangential velocity

$$v_\theta = -\frac{R^2 \omega_y}{r} \qquad (r \geq R) \ . \tag{3.30}$$

The circulation around a circle of radius r, concentric with the cylinder, is found to be constant,

$$\Gamma = \int_{2\pi}^{0} v_\theta r \, \mathrm{d}\theta = 2\omega_y \pi R^2 = cst \tag{3.31}$$

such that the tangential velocity can be rewritten as,

$$v_\theta = -\frac{\Gamma}{2\pi r} \qquad (r \geq R) \ . \tag{3.32}$$

To estimate the vorticity in the fluid, consider the integration path shown by the dashed lines in Figure 3.2. Integrating in clockwise direction results in,

$$\oint \vec{v} \cdot \vec{dl} = 0 \cdot \Delta r + \frac{\Gamma}{2\pi(r+\Delta r)}(r+\Delta r)\Delta\theta - 0 \cdot \Delta r - \frac{\Gamma}{2\pi r} r \Delta\theta \equiv 0 \ . \tag{3.33}$$

At this point, we make an important observation in that the flow is irrotational everywhere except at the core where all vorticity is concentrated. This flow is called an *irrotational vortex*.

3.4 Basic Solution

With the knowledge of previous section, we will now determine a basic solution to Laplace's equation. Consider a *point vortex* located at the origin which we model as a zero area point ($\mathrm{d}S = 0$) with infinite vorticity ($\zeta \to \infty$), such that the circulation $\Gamma = \zeta \mathrm{d}S$ is finite. In order to satisfy Laplace's equation, the flow must be irrotational. Based on the example, we know that the velocity field given by

$$\begin{aligned} v_r &= 0 \\ v_\theta &= -\frac{\Gamma}{2\pi r} \end{aligned} \tag{3.34}$$

fulfills this condition. Using (3.14), we can now determine the velocity potential Φ of a point vortex,

$$\begin{aligned} \vec{v} &= \vec{\nabla}\Phi \\ \left(\frac{\partial \Phi}{\partial r}, \frac{1}{r}\frac{\partial \Phi}{\partial \theta}\right) &= \left(0, -\frac{\Gamma}{2\pi r}\right) \end{aligned} \tag{3.35}$$

such that,

$$\Phi = -\frac{\Gamma}{2\pi}\theta + C \tag{3.36}$$

in which C is an arbitrary constant that can be set to zero. Note that the tangential velocity component decays to zero, such that the second boundary condition (3.17) is satisfied. Thus, the vortex point is a basic solution to Laplace's equation and results in an irrotational flow, except at the vortex point itself.

We can now extend the above reasoning. Given that Laplace's equation is linear, the *principle of superposition* holds. As such, a *vortex line* (which can be seen as een infinite number of vortex points), is also a basic solution to Laplace's equation.

3.5 Biot-Savart Law

In this section, we will derive the velocity induced by a segment of a straight vortex line with constant circulation Γ and which extends to infinity as shown in Figure 3.3. According to the *Biot-Savart Law*, the velocity induced by an infinitesimal segment $\mathrm{d}\vec{\ell}$ at a point P is [6],

$$\Delta\vec{v} = \frac{\Gamma}{4\pi}\frac{\mathrm{d}\vec{\ell}\times\vec{r}}{r^3} \ . \tag{3.37}$$

This may be rewritten as

$$\begin{aligned} \Delta v_r &= 0 \\ \Delta v_\theta &= \frac{\Gamma}{4\pi}\frac{\sin\beta}{r^2}\mathrm{d}\ell \ . \end{aligned} \tag{3.38}$$

Note that only a tangential velocity component is induced.

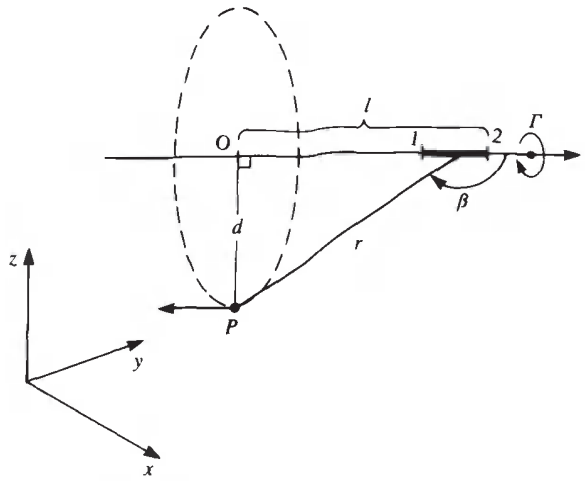

Figure 3.3: Velocity induced by a straight vortex segment [6]

Using the relations

$$\begin{aligned} d &= r\cos\beta \\ \ell &= d\tan\beta \rightarrow \mathrm{d}\ell = \frac{d}{\cos^2\beta}\mathrm{d}\beta \end{aligned} \tag{3.39}$$

we obtain

$$\Delta v_\theta = \frac{\Gamma}{4\pi}\frac{\cos^2\beta}{d^2}\sin\beta\frac{d}{\cos^2\beta}\mathrm{d}\beta = \frac{\Gamma}{4\pi d}\sin\beta\mathrm{d}\beta \ . \tag{3.40}$$

Integrating over a section $(1 \rightarrow 2)$, as shown schematically in Figure 3.4 results in

$$(\Delta v_\theta)_{1,2} = \frac{\Gamma}{4\pi d}\int_{\beta_1}^{\beta_2}\sin\beta\,\mathrm{d}\beta = \frac{\Gamma}{4\pi d}(\cos\beta_1 - \cos\beta_2) \ . \tag{3.41}$$

The induced velocity is thus a function of its strength Γ, the distance d and the two view angles β_1, β_2. For the two-dimensional case $(\beta_1 = 0, \beta_2 = \pi)$

$$v_\theta = \frac{\Gamma}{2\pi d} \tag{3.42}$$

a result in agreement with Section 3.4. For the general case shown in Figure 3.5, the induced velocity is given by [6]

$$\vec{v}_{1,2} = \frac{\Gamma}{4\pi}\frac{\vec{r}_1 \times \vec{r}_2}{|\vec{r}_1 \times \vec{r}_2|}(\vec{r}_2 - \vec{r}_1)\left(\frac{\vec{r}_1}{r_1} - \frac{\vec{r}_2}{r_2}\right) \tag{3.43}$$

and will be used in the Vortex Lattice Methods.

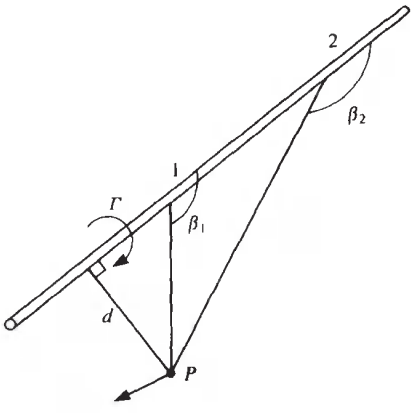

Figure 3.4: Definition of the view angles [6]

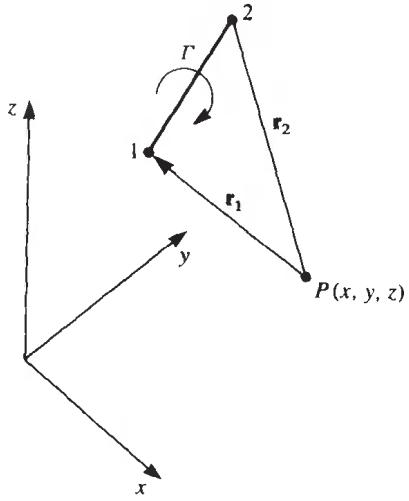

Figure 3.5: Nomenclature used for the velocity induced by a three-dimensional, straight vortex segment [6]

3.6 Lifting-Line Solution

We have seen that the *vortex line* is a basic solution of Laplace's equation, satisfying the boundary condition at infinity. The only boundary condition which remains is,

$$\vec{\nabla}(\Phi + \Phi_\infty) \cdot \vec{n} = 0 \tag{3.44}$$

in which we have split the free-stream velocity field $\vec{\nabla}\Phi_\infty$ from the induced velocity field $\vec{\nabla}\Phi$. In order to solve the problem, we will use *horseshoe vortices* as basic solutions. These consist of (see Figure 3.6) a straight bound vortex segment BC and two semi-infinite trailing vortex lines AB and CD. One of *Helmholtz's theorems* states that a vortex line cannot start or end in a fluid, such that a vortex segment AD must be added at infinity. The effect of this segment will be negligible.

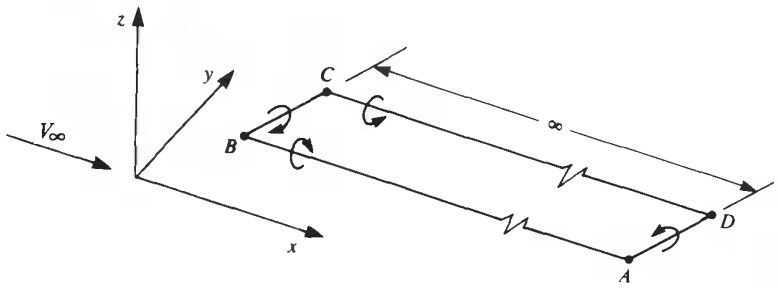

Figure 3.6: Horseshoe vortex [6]

We will now attempt a numerical solution of (3.44), which we will apply on a wing as an example. The method consists of dividing the wing into elements, both in the spanwise and chordwise direction as shown in Figure 3.7. For simplicity here, only one chordwise element is used, but the method can easily be extended to include more chordwise elements. Each element contains a horseshoe vortex where the bound vortex is placed at the panel's quarter chord, see Figure 3.8. We further define a *collocation point*, which will be used for expressing our boundary condition, placed at the panel's three-quarter chord line. This is known as the "*1/4 - 3/4 rule*". The circulation or strength Γ is assumed constant for the horseshoe element. Using the results of Section 3.5, we can determine the velocity induced by the bound vortex and trailing vortex lines at an arbitrary point. In order to express the boundary conditions at every collocation point, we determine the velocity induced by horseshoe vortex j with unit-strength ($\Gamma = 1$) at collocation point i denoted as $(u, v, w)_{ij}$. These terms are known as the *influence coefficients*. To find the actual induced velocity, we have to multiply the influence coefficient by the vortex strength Γ_j, which is still unknown.

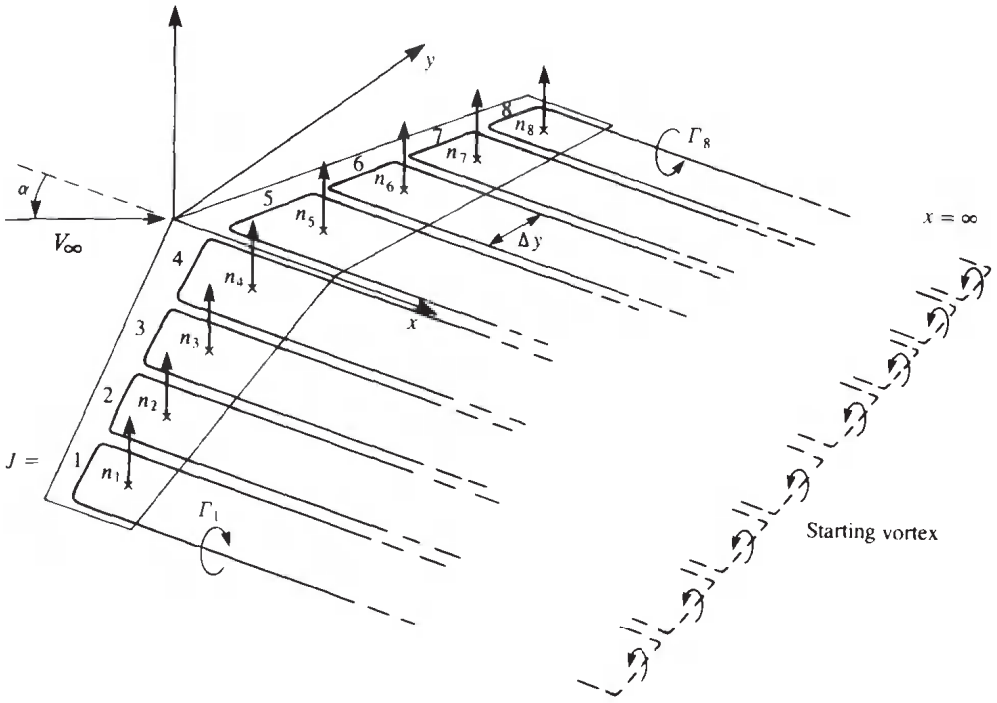

Figure 3.7: Horseshoe vortex lattice method for solving the lifting-line problem [6]

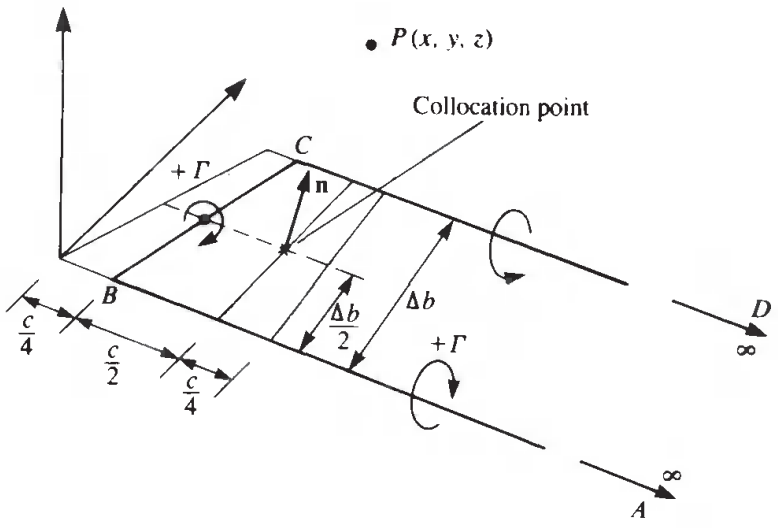

Figure 3.8: Position of bound vortex and collocation point [6]

Expressing the boundary condition at the first collocation point results in,

$$\left[(u,v,w)_{11}\Gamma_1 + (u,v,w)_{12}\Gamma_2 + \cdots + (u,v,w)_{1N}\Gamma_N + (u_\infty, v_\infty, w_\infty)\right] \cdot \vec{n}_1 = 0 \tag{3.45}$$

where $\vec{n}_1$ is the wing's normal vector at collocation point 1. Following a same procedure, the discretized form of the boundary condition becomes,

$$\begin{pmatrix} a_{11} & a_{12} & \cdots & a_{1N} \\ a_{21} & a_{22} & \cdots & a_{2N} \\ \vdots & \vdots & \ddots & \vdots \\ a_{N1} & a_{N2} & \cdots & a_{NN} \end{pmatrix} \begin{pmatrix} \Gamma_1 \\ \Gamma_2 \\ \vdots \\ \Gamma_N \end{pmatrix} = \begin{pmatrix} RHS_1 \\ RHS_2 \\ \vdots \\ RHS_N \end{pmatrix} \tag{3.46}$$

in which $a_{ij} = (u,v,w)_{ij} \cdot \vec{n}_i$ and $RHS_i = -(u_\infty, v_\infty, w_\infty) \cdot \vec{n}_i$. This is a set of N linear algebraic equations with N unknowns Γ_i.

3.7 Induced Drag

Given the solution of the vortex strenghts Γ_i of Section 3.6, the corresponding aerodynamic forces (lift, drag) and moments can be calculated in different ways. At this point, it might seem strange that there is a drag component as we have modeled the flow as inviscid and incompressible. To understand where the drag component comes from, consider the finite wing shown in Figure 3.9.

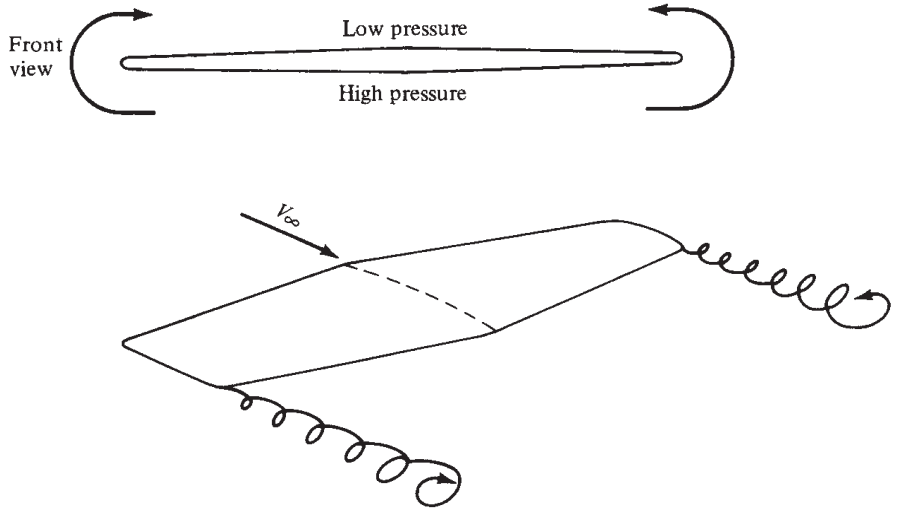

Figure 3.9: Wing-tip vortices of a finite wing [7]

Due to the wing's geometry, designed to generate lift, there exists a high pressure region underneath the wing and a low pressure region above the wing (Figure 3.10). As a result of this pressure difference, the flow near the wing tips tends to curl around the tips forming a trailing vortex. The effect of these wing-tip vortices is a small downward component of air

velocity w called *downwash*. As a result, the angle of attack seen by the local airfoil sections has changed. Although the wing is at a *geometric* angle of attack α, the local airfoil section sees a smaller angle of attack α_{eff}, defined as the *effective* angle of attack. The geometric and effective angle of attack differ by the angle α_i, called the *induced* angle of attack. For inviscid flow, the force acting on an airfoil section is perpendicular to the local relative wind direction. As a result, the lift vector is tilted by the angle α_i (Figure 3.10) creating a force component in the direction of V_∞, thus a drag component. This drag, denoted by D_i, is called the *induced drag*.

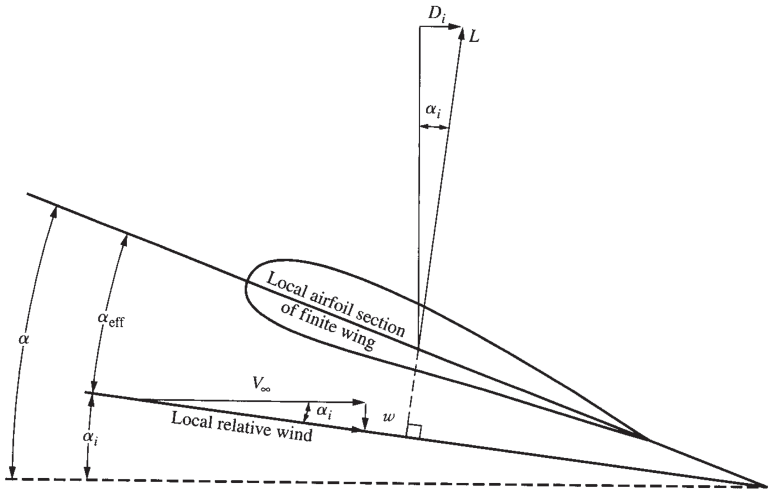

Figure 3.10: Effect of downwash on the flow over an airfoil section of a finite wing [7]

3.8 Trefftz Plane

Now that we know the origin of the induced drag, the question remains how to calculate the corresponding lift and induced drag from the strengths Γ_i. In a first method, the *Kutta-Joukowski theorem* is applied to each panel [6],

$$\Delta L_i = \rho V_\infty \Gamma_i \Delta y_i \tag{3.47}$$

which relates the lift ΔL_i of the bound vortex i to its strength Γ_i and the magnitude of the free-stream velocity V_∞. The induced drag of each panel is found by a similar expression,

$$\Delta D_i = -\rho w_{ind_i} \Gamma_i \Delta y_i \tag{3.48}$$

where the free-stream velocity V_∞ is replaced by the induced downwash w_{ind_i} at the collocation point of the panel. The induced downwash w_{ind_i} is found by adding up the velocity induced by every trailing vortex line, so without the influence of the bound vortex segments. The total lift L and induced drag D_i now follow from the sum of all ΔL_i respectively ΔD_i.

A second method is based on *Trefftz plane*. Consider the wing shown in Figure 3.11 which is surrounded by a large control volume. For incompressible, inviscid and steady flow without body forces, the integral form of the continuity and momentum equation (3.1),(3.2) reduces to

$$\int_{S_w+S_\infty} \vec{v} \cdot \vec{n} \, \mathrm{d}S = 0 \tag{3.49}$$

$$\int_{S_w+S_\infty} \rho \vec{v} (\vec{v} \cdot \vec{n}) \, \mathrm{d}S = -\int_{S_w+S_\infty} p \vec{n} \, \mathrm{d}S \tag{3.50}$$

where S_w is the wing's surface and S_∞ the outer surface of the control volume. Note that on a wall $\vec{v} \cdot \vec{n} = 0$, such that the equations simplify to

$$\int_{S_\infty} \vec{v} \cdot \vec{n} \, \mathrm{d}S = 0 \tag{3.51}$$

$$\int_{S_\infty} \rho \vec{v} (\vec{v} \cdot \vec{n}) \, \mathrm{d}S = \vec{F} - \int_{S_\infty} p \vec{n} \, \mathrm{d}S \tag{3.52}$$

in which,

$$-\vec{F} = \int_{S_w} p \vec{n} \, \mathrm{d}S \tag{3.53}$$

and represents the force acting on the wing. The x axis is taken parallel to the free-stream velocity such that the velocity $\vec{v}$ can be written as

$$\vec{v} = (V_\infty + u, v, w) \tag{3.54}$$

in which (u, v, w) represents the perturbation of the free-stream due to the wing. The pressure p can be found using Bernoulli's equation (3.22),

$$p = p_\infty + \frac{1}{2}\rho V_\infty^2 - \frac{1}{2}\rho \left((V_\infty + u)^2 + v^2 + w^2 \right) \ . \tag{3.55}$$

As such, the second term on the right-hand side of (3.52) can be written as

$$-\int_{S_\infty} p \vec{n} \, \mathrm{d}S = -(p_\infty + \frac{1}{2}\rho V_\infty^2) \cancel{\int_{S_\infty} \vec{n} \, \mathrm{d}S} + \int_{S_\infty} \frac{1}{2}\rho \left((V_\infty + u)^2 + v^2 + w^2 \right) \vec{n} \, \mathrm{d}S \tag{3.56}$$

in which $\int \vec{n} \, \mathrm{d}S = 0$ for a closed surface.

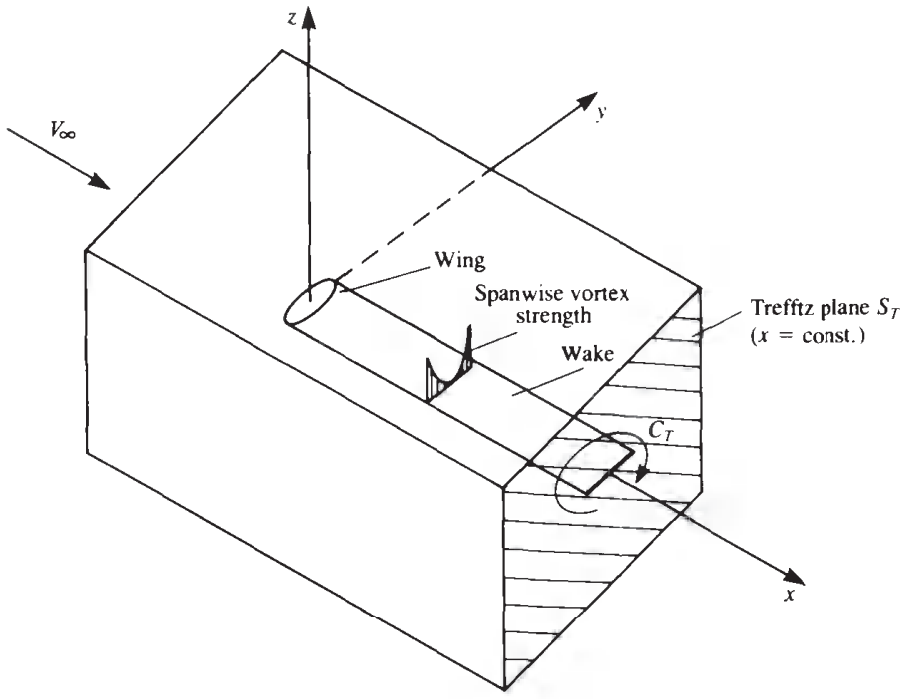

Figure 3.11: Control volume around finite wing [6]

We are now interested in the induced drag D_i of the wing (x component of the force), such that the left-hand side of (3.52) can be written as

$$\int_{S_\infty} \rho(V_\infty + u)(\vec{v} \cdot \vec{n})\,\mathrm{d}S = \rho V_\infty \cancel{\int_{S_\infty} \vec{v} \cdot \vec{n}\,\mathrm{d}S} + \int_{S_\infty} \rho u(\vec{v} \cdot \vec{n})\,\mathrm{d}S \tag{3.57}$$

where the first term on the right-hand side is zero due to the continuity equation (3.51). Taking the previous results into account, the momentum equation (3.52) reduces to

$$\int_{S_\infty} \rho u(\vec{v} \cdot \vec{n})\,\mathrm{d}S = -D_i + \int_{S_\infty} \frac{1}{2}\rho \left((V_\infty + u)^2 + v^2 + w^2\right) \vec{n} \cdot \vec{e_x}\,\mathrm{d}S \tag{3.58}$$

or

$$\begin{aligned} D_i = \frac{1}{2}\rho V_\infty^2 \cancel{\int_{S_\infty} \vec{n} \cdot \vec{e_x}\,\mathrm{d}S} + \rho V_\infty \int_{S_\infty} u\vec{n} \cdot \vec{e_x}\,\mathrm{d}S \\ + \int_{S_\infty} \frac{1}{2}\rho \left(u^2 + v^2 + w^2\right) \vec{n} \cdot \vec{e_x}\,\mathrm{d}S - \int_{S_\infty} \rho u(\vec{v} \cdot \vec{n})\,\mathrm{d}S\ . \end{aligned} \tag{3.59}$$

If we choose the control volume large enough, the perturbation velocity components will go to zero except in the wake.

As such,

$$\begin{aligned} D_i &= \rho V_\infty \cancel{\int_{S_T} u \, \mathrm{d}S} + \int_{S_T} \frac{1}{2}\rho(u^2 + v^2 + w^2)\,\mathrm{d}S - \int_{S_T} \rho u(\cancel{V_\infty} + u)\,\mathrm{d}S \\ &= \frac{1}{2}\rho \int_{S_T} (v^2 + w^2 - u^2)\,\mathrm{d}S \end{aligned} \tag{3.60}$$

in which S_T is the so-called *Trefftz plane*. The wake, made up of trailing vortices, is parallel to the free-stream (x-direction) far downstream. As a result, these trailing vortices will only induce a velocity in the y and z direction such that $u^2 \ll v^2, w^2$ in the Trefftz plane. The induced drag can now be written as

$$\begin{aligned} D_i &= \frac{1}{2}\rho \int_{S_T} (v^2 + w^2)\,\mathrm{d}S = \frac{1}{2}\rho \int_{S_T} \left[\left(\frac{\partial \Phi}{\partial y} \right)^2 + \left(\frac{\partial \Phi}{\partial z} \right)^2 \right] \mathrm{d}S \\ &= \frac{1}{2}\rho \int_{S_T} \left(\vec{\nabla}\Phi \cdot \vec{\nabla}\Phi \right) \mathrm{d}S \end{aligned} \tag{3.61}$$

where Φ is the perturbation velocity potential. Using the relation

$$\vec{\nabla}\Phi \cdot \vec{\nabla}\Phi = \vec{\nabla} \cdot (\Phi \vec{\nabla}\Phi) - \Phi \nabla^2 \Phi \tag{3.62}$$

in which $\nabla^2\Phi = 0$ in the Trefftz plane and applying the divergence theorem, (3.61) reduces to

$$D_i = \frac{1}{2}\rho \int_{S_T} \vec{\nabla} \cdot (\Phi \vec{\nabla}\Phi)\,\mathrm{d}S = \frac{1}{2}\rho \int_{C_T} \Phi \vec{\nabla}\Phi \cdot \vec{n}\,\mathrm{d}\ell = \frac{1}{2}\rho \int_{C_T} \Phi \frac{\partial \Phi}{\partial n}\,\mathrm{d}\ell \ . \tag{3.63}$$

Without going into further detail, it can be shown that the integral reduces to a single line integral along the span of the wake [6],

$$D_i = -\frac{1}{2}\rho \int_{-b_w/2}^{b_w/2} \Delta\Phi w_{ind}\,\mathrm{d}y = -\frac{1}{2}\rho \int_{-b_w/2}^{b_w/2} \Gamma(y) w_{ind}\,\mathrm{d}y \tag{3.64}$$

or in discretized form,

$$D_{ind} = -\frac{1}{2}\rho \sum_{i=1}^{N_w} w_{ind_i} \Gamma_i \Delta y_i \ . \tag{3.65}$$

Note that equation (3.65) is similar to (3.48), except for the factor 1/2. This results from the fact that (3.65) is evaluated at the Trefftz plane (where the trailing vortices seem two-dimensional), whereas (3.48) is evaluated at the bound vortex segments (where the trailing

vortices appear semi-infinite). Following a similar approach, the lift force can be derived as

$$L = \rho V_\infty \int_{-b_w/2}^{b_w/2} \Delta\Phi \, \mathrm{d}y = \rho V_\infty \int_{-b_w/2}^{b_w/2} \Gamma(y) \, \mathrm{d}y \ . \tag{3.66}$$

An important remark, the induced drag calculated in the Trefftz plane is usually more reliable than the drag obtained from surface force integration [8]. As such, the second method will be used in this work to determine the induced drag of an aircraft.

Chapter 4

Dynamics of Flight

In the present chapter we will start by introducing some specific terms related to aircrafts and which will be frequently used throughout this work. An important characteristic of an aircraft is its controllability. In order for the aircraft to be easily controllable, it should be statically and dynamically stable. These necessary conditions will be derived here and should provide some more insight into certain design aspects.

4.1 Static Stability

To describe the motion of an aircraft and the corresponding forces and moments acting on it, we choose a coordinate system fixed to the aircraft's center of gravity, as illustrated in Figure 4.1. X, Y, Z represent the aerodynamic force components; L, M, N the aerodynamic moment components; u, v, w the linear velocity components and p, q, r the angular velocity components. The moments L, M, N are defined as the rolling, pitching and yawing moments. Similarly, p, q, r are called the roll, pitch and yaw rates. We further define two angles (Figure 4.2), the *angle of attack* α and the *sideslip angle* β of the aircraft.

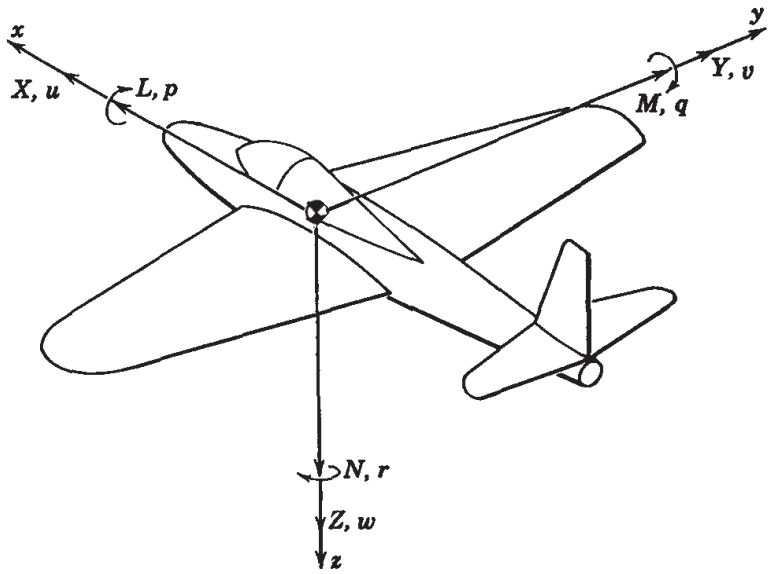

Figure 4.1: Body axis coordinate system [9]

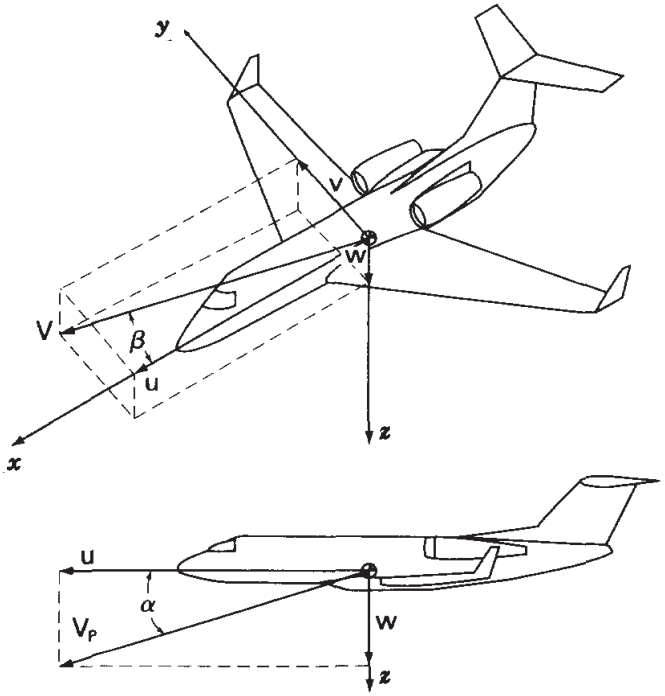

Figure 4.2: Definition of angle of attack and sideslip [10]

For an aircraft to be in equilibrium, the resultant force and moment about the aircraft's center of gravity must both be equal to zero. When the aircraft (in equilibrium) is now subjected to a small disturbance, the *static stability* describes the initial tendency of the aircraft to return to its equilibrium position. The various types of static stability are shown in Figure 4.3. So for an aircraft to be statically stable, a restoring force or moment must develop when subjected to a disturbance.

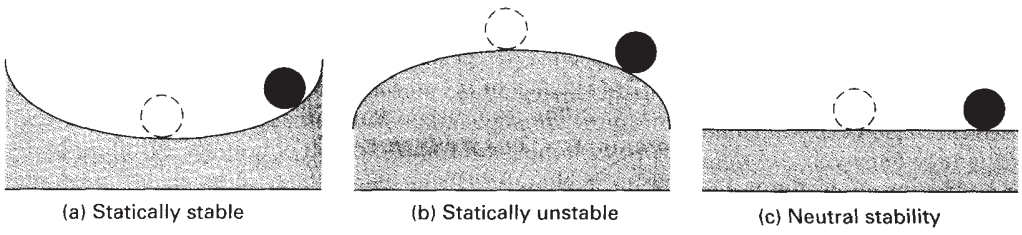

Figure 4.3: Various types of static stability [10]

4.1.1 Longitudinal Static Stability

In order for the aircraft to have static longitudinal stability (that is, around the y-axis), the aircraft's pitching moment curve must have a negative slope,

$$\frac{\mathrm{d}C_m}{\mathrm{d}\alpha} < 0 \ . \tag{4.1}$$

To see why, consider Figure 4.4 showing the pitching moment curves of two aircrafts. Point B corresponds to the equilibrium position where the pitching moment is zero. Now suppose that the aircrafts encounter a small disturbance, for instance an upward gust, such that the angle of attack increases to point C. At this angle of attack, aircraft 1 develops a negative (nose-down) pitching moment which tends to rotate the aircraft back to its equilibrium position. On the contrary, aircraft 2 develops a positive (nose-up) pitching moment which tends to rotate the aircraft away from its equilibrium position. A similar reasoning can be applied for a disturbance causing the angle of attack to decrease. Based on this simple analysis, we can confirm condition (4.1) for longitudinal static stability. In addition to (4.1), the pitching moment coefficient at zero angle of attack C_{m_0} should also be positive such that the equilibrium position corresponds to a positive angle of attack.

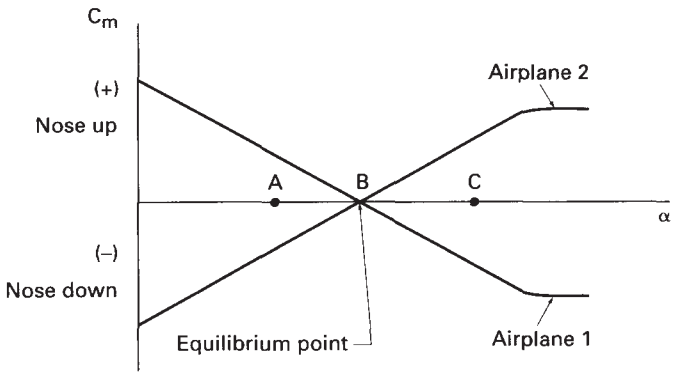

Figure 4.4: Pitching moment coefficient versus angle of attack [10]

We will now derive the contribution of the wing and horizontal tail surface (elevator) to the aircraft's longitudinal static stability. Consider Figure 4.5 in which the lifting surfaces are represented by their mean aerodynamic chord. The aerodynamic forces (lift L, drag D) act at the *aerodynamic center* (ac), where the pitching moments (M_{ac_w}, M_{ac_t}) are independent of the angle of attack (α_w, α_t). In order to obtain a simple expression for the resultant pitching moment about the aircraft's center of gravity, some simplifications will be made. We will neglect the contributions of the drag D_w, D_t and the tail's pitching moment M_{ac_t}. Further, we will neglect the vertical distances between the aerodynamic centers and the center of gravity ($z_{cg_w} \simeq 0$, $z_{cg_t} \simeq 0$) and using following approximations for small angles α,

$$\begin{aligned} \cos\alpha &\simeq 1 \\ \sin\alpha &\simeq \alpha \end{aligned} \tag{4.2}$$

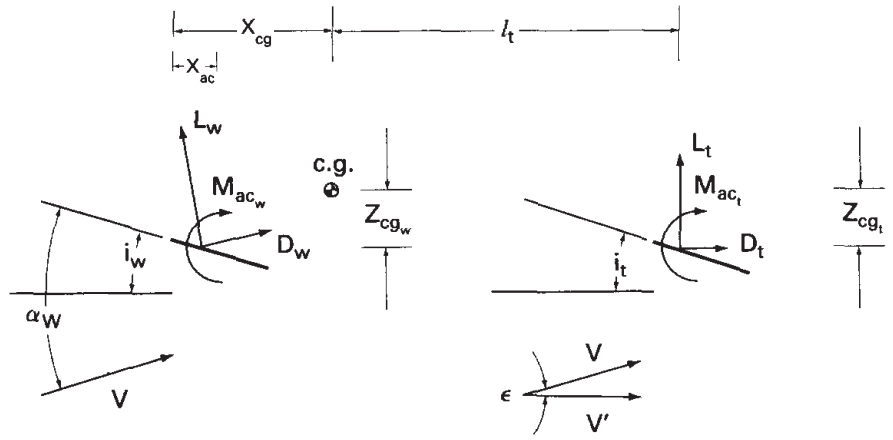

Figure 4.5: Contributions to the aircraft's pitching moment [10]

we obtain,

$$M_{cg} = M_{ac_w} + L_w(x_{cg} - x_{ac}) - \ell_t L_t \ . \tag{4.3}$$

Introducing the dimensionless force and moment coefficients,

$$\begin{aligned} C_{m_{ac_w}} &= \frac{M_{ac_w}}{\frac{1}{2}\rho V^2 S\overline{c}} \\ C_{L_w} &= \frac{L_w}{\frac{1}{2}\rho V^2 S} \\ C_{L_t} &= \frac{L_t}{\frac{1}{2}\rho {V_t}^2 S_t} \end{aligned} \tag{4.4}$$

(4.3) can be written as

$$\begin{aligned} C_{m_{cg}} &= C_{m_{ac_w}} + C_{L_w}\left(\frac{x_{cg}}{\overline{c}} - \frac{x_{ac}}{\overline{c}}\right) - \frac{\frac{1}{2}\rho {V_t}^2}{\frac{1}{2}\rho V^2}\frac{\ell_t S_t}{\overline{c}S}C_{L_t} \\ &= C_{m_{ac_w}} + C_{L_w}\left(\frac{x_{cg}}{\overline{c}} - \frac{x_{ac}}{\overline{c}}\right) - \eta V_H C_{L_t} \end{aligned} \tag{4.5}$$

where $V_H = \ell_t S_t/\overline{c}S$ is called the *horizontal tail volume* and η the *tail efficiency*. Depending on the location of the tail, η can be larger or smaller than unity. When located in the wake region of a wing or fuselage, η will be less than unity but when positioned in the slip stream of for instance a propeller, η will be greater than unity. From Figure 4.5, the angle of attack of the tail (with respect to V') is seen to be,

$$\alpha_t = \alpha_w - i_w - \epsilon + i_t \tag{4.6}$$

where ϵ is due to the downwash from the wing and where the angles i_w, i_t represent the incidence of the wing and tail with respect to the x-axis of the aircraft's coordinate system.

Defining the angle of attack of the aircraft as

$$\alpha \triangleq \alpha_w - i_w \tag{4.7}$$

we can express the downwash angle ϵ as follows,

$$\epsilon = \epsilon_0 + \frac{\mathrm{d}\epsilon}{\mathrm{d}\alpha}\alpha \tag{4.8}$$

where ϵ_0 is the downwash at zero angle of attack. Further, we write the lift coefficients C_{L_w}, C_{L_t} as

$$\begin{aligned} C_{L_w} &= C_{L_{0_w}} + C_{L_{\alpha_w}}\alpha_w \\ C_{L_t} &= \cancel{C_{L_{0_t}}} + C_{L_{\alpha_t}}\alpha_t \end{aligned} \tag{4.9}$$

where C_{L_0} is the lift coefficient at zero angle of attack and C_{L_α} is the slope of the lift curve. Note that $C_{L_{0_t}} = 0$, as usually a symmetric profile is used for the tail. Using the above relations, (4.5) is written as

$$C_{m_{cg}} = C_{m_0} + C_{m_\alpha}\alpha \tag{4.10}$$

where,

$$C_{m_0} = C_{m_{ac_w}} + \left(C_{L_{0_w}} - i_w C_{L_{\alpha_w}}\right)\left(\frac{x_{cg}}{\overline{c}} - \frac{x_{ac}}{\overline{c}}\right) + \eta V_H C_{L_{\alpha_t}}(\epsilon_0 - i_t) \tag{4.11}$$

$$C_{m_\alpha} = C_{L_{\alpha_w}}\left(\frac{x_{cg}}{\overline{c}} - \frac{x_{ac}}{\overline{c}}\right) - \eta V_H C_{L_{\alpha_t}}\left(1 - \frac{\mathrm{d}\epsilon}{\mathrm{d}\alpha}\right). \tag{4.12}$$

At this point, it is important to understand the function of the horizontal tail surface. By proper selection of V_H and $C_{L_{\alpha_t}}$ (both positive), it can be ensured that $C_{m_\alpha} < 0$, as the second term on the right-hand side of (4.12) contains a minus sign. Increasing V_H can be accomplished by increasing the tail moment arm ℓ_t or the tail surface area S_t, whereas increasing $C_{L_{\alpha_t}}$ is done by increasing the tail *aspect ratio* (ratio of the tail's span to mean chord). To further ensure that C_{m_0} is positive, the tail's incidence angle i_t can also be adjusted. Note that adjusting the tail plane to negative incidence angles results in a positive contribution to C_{m_0}. Finally, notice that (4.12) depends upon the position of the aircraft's center of gravity x_{cg}. To determine the sensitivity of x_{cg} to the aircraft's longitudinal static stability, we determine the position of x_{cg} which corresponds with $C_{m_\alpha} = 0$,

$$\begin{aligned} x_{NP} &\triangleq \left(x_{cg}\right)_{C_{m_\alpha}=0} \\ \longrightarrow \frac{x_{NP}}{\overline{c}} &= \frac{x_{ac}}{\overline{c}} + \eta V_H \frac{C_{L_{\alpha_t}}}{C_{L_{\alpha_w}}}\left(1 - \frac{\mathrm{d}\epsilon}{\mathrm{d}\alpha}\right). \end{aligned} \tag{4.13}$$

The position x_{NP} is called the aircraft's *neutral point* and if the center of gravity moves beyond this neutral point, the aircraft will become statically unstable.

4.1.2 Directional Static Stability

An aircraft possesses directional static stability if a restoring moment develops when the aircraft is subjected to a yawing disturbance. The condition can be expressed as

$$\frac{\mathrm{d}C_n}{\mathrm{d}\beta} > 0 \tag{4.14}$$

and is justified using Figure 4.6, showing the yawing moment coefficient C_n as a function of the sideslip angle β for two aircrafts. When both aircrafts are disturbed to a positive sideslip angle β, only aircraft 1 will develop a restoring yawing moment (positive in this case), causing the aircraft to rotate back to its equilibrium position (zero sideslip angle). As shown in Figure 4.6, the slope C_{n_β} must indeed be positive for directional static stability. Without going into detail, it is the vertical tail (rudder) which produces the restoring moment and should therefore be properly sized to ensure directional stability.

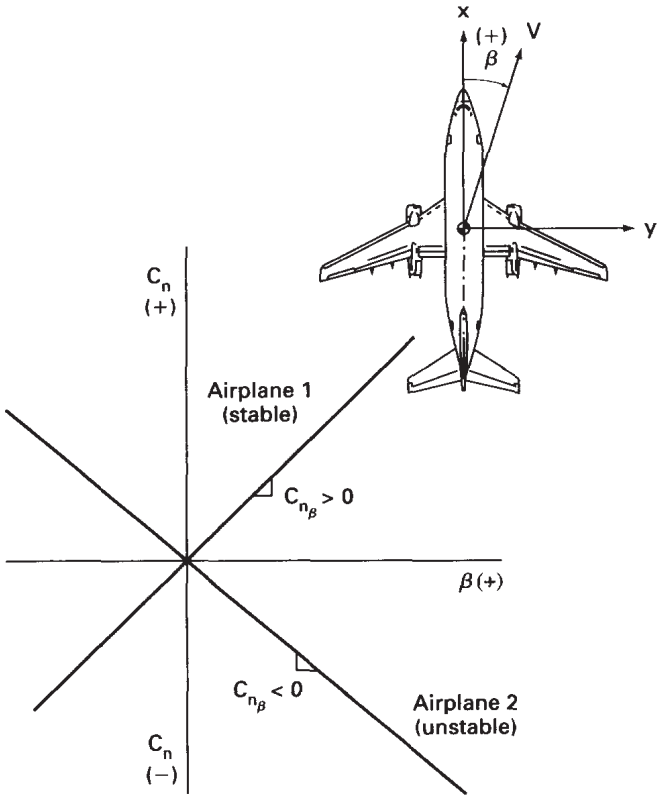

Figure 4.6: Static directional stability [10]

4.1.3 Roll Stability

As in the previous cases, it is desirable that the aircraft develops a restoring moment when disturbed in roll. Consider Figure 4.7 showing two responses of an aircraft disturbed in roll. Due to the initial roll disturbance, the lift generated by the aircraft will now contain a sideways component, causing the aircraft to sideslip. As seen on Figure 4.7, a positive roll disturbance leads to a positive sideslip β and the restoring rolling moment C_l should thus be negative (opposite direction). This leads to the following condition for roll stability,

$$\frac{\mathrm{d}C_l}{\mathrm{d}\beta} < 0 \ . \tag{4.15}$$

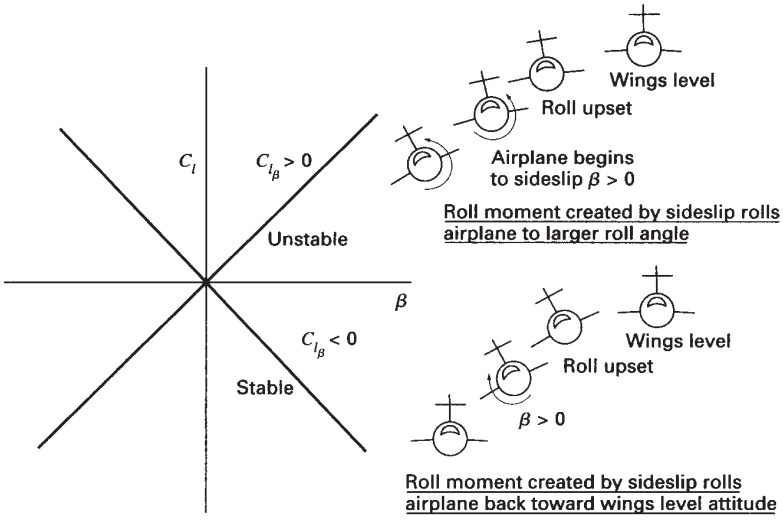

Figure 4.7: Static roll stability [10]

The major contribution to the restoring rolling moment (as a response to the sideslip), comes from the wing *dihedral angle* Γ. As shown in Figure 4.8, the dihedral angle is the spanwise inclination of the wing with respect to the horizontal. In Figure 4.8, the aircraft is seen to sideslip to the right, such that the aircraft experiences a wind component coming from that direction. The wind component is further resolved in a component normal and tangential to the wing. It is now the normal component which will increase the angle of attack experienced by wing section 1 and decrease the angle of attack experienced by wing section 2. As such, the lift of wing section 1 increases while the lift of wing section 2 decreases. The result is indeed a restoring rolling moment bringing the wing back to its horizontal position.

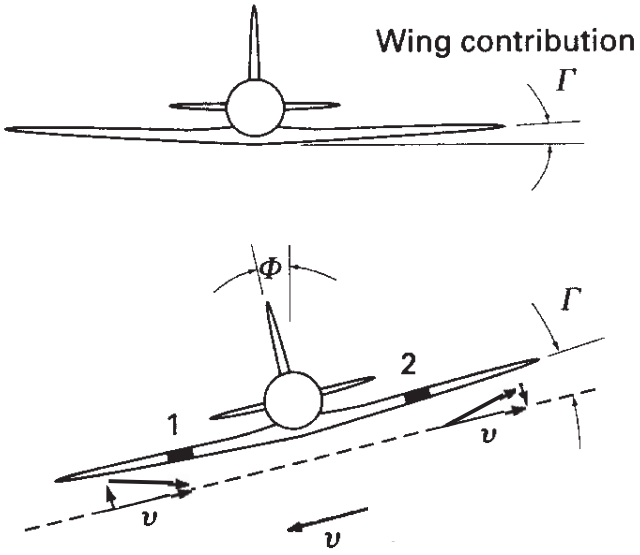

Figure 4.8: Wing dihedral [10]

4.2 Equations of Motion

The motion of a rigid body is described by *Euler's laws*,

$$\sum \vec{F} = \frac{\mathrm{d}}{\mathrm{d}t}(m\vec{v_c}) \tag{4.16}$$

$$\sum \vec{M} = \frac{\mathrm{d}}{\mathrm{d}t}(I\vec{\omega}) \tag{4.17}$$

which relates the external forces $\vec{F}$ and moments $\vec{M}$ acting on a body to the time rate of change of the body's momentum $m\vec{v_c}$ or angular momentum $\vec{H} = I\vec{\omega}$. Euler's laws in the above form, are expressed with respect to an inertial reference frame, where $\vec{v_c}$ represents the linear velocity of the aircraft's center of gravity and $\vec{\omega}$ the angular velocity of the aircraft. The *inertia tensor* I of a rigid body is defined as

$$I = \begin{bmatrix} I_x & -I_{xy} & -I_{xz} \\ -I_{xy} & I_y & -I_{yz} \\ -I_{xz} & -I_{yz} & I_z \end{bmatrix} \tag{4.18}$$

where,

$$\begin{aligned} I_x &= \int_V \rho(y^2+z^2)\,\mathrm{d}V & I_{xy} &= \int_V \rho xy\,\mathrm{d}V \\ I_y &= \int_V \rho(x^2+z^2)\,\mathrm{d}V & I_{xz} &= \int_V \rho xz\,\mathrm{d}V \\ I_z &= \int_V \rho(x^2+y^2)\,\mathrm{d}V & I_{yz} &= \int_V \rho yz\,\mathrm{d}V\ . \end{aligned} \tag{4.19}$$

Note that as the body rotates with respect to the inertial reference frame, the inertia tensor I will change. To avoid having to calculate the inertia tensor at every time instant, we choose a reference frame fixed to the aircraft as in Section 4.1. We must now rewrite Euler's laws with respect to this moving body frame of reference. The relationship between the derivatives of an arbitrary vector $\vec{A}$ with respect to an inertial and body reference frame is given by [10]

$$\left.\frac{\mathrm{d}\vec{A}}{\mathrm{d}t}\right|_I = \left.\frac{\mathrm{d}\vec{A}}{\mathrm{d}t}\right|_B + \vec{\omega} \times \vec{A} \tag{4.20}$$

where $\vec{\omega} = (p, q, r)$ and represents the angular velocity of the body expressed in B. Applying (4.20) to Euler's laws yields,

$$\sum \vec{F} = m \left.\frac{\mathrm{d}\vec{v_c}}{\mathrm{d}t}\right|_B + m(\vec{\omega} \times \vec{v_c}) \tag{4.21}$$

$$\sum \vec{M} = \left.\frac{\mathrm{d}\vec{H}}{\mathrm{d}t}\right|_B + (\vec{\omega} \times \vec{H}) \tag{4.22}$$

where $\vec{v_c}$ and $\vec{H}$ are expressed with respect to B. Assuming that the xz-plane of the body reference frame is a plane of symmetry (such that $I_{xy} = I_{yz} = 0$), the equations (4.21),(4.22) can be written in scalar form as

$$F_x = m(\dot{u} + q\dot{w} - rv) \tag{4.23a}$$

$$F_y = m(\dot{v} + ru - pw) \tag{4.23b}$$

$$F_z = m(\dot{w} + pv - qu) \tag{4.23c}$$

$$L = I_x\dot{p} - I_{xz}\dot{r} + qr(I_z - I_y) - I_{xz}pq \tag{4.24a}$$

$$M = I_y\dot{q} + rp(I_x - I_z) + I_{xz}(p^2 - r^2) \tag{4.24b}$$

$$N = -I_{xz}\dot{p} + I_z\dot{r} + pq(I_y - I_x) + I_{xz}qr\ . \tag{4.24c}$$

Knowing the forces and moments acting upon the aircraft, equations (4.23),(4.24) will allow us to determine the linear velocity $\vec{v_c}$ and angular velocity $\vec{\omega}$ with respect to B. If we are now interested in the position and orientation of the aircraft with respect to an absolute reference frame, we will have to introduce the so-called *Euler angles*. Figure 4.9 defines the Euler angles and it can be shown that [10]

$$\begin{bmatrix} p \\ q \\ r \end{bmatrix} = \begin{bmatrix} 1 & 0 & -\sin\theta \\ 0 & \cos\phi & \cos\theta\sin\phi \\ 0 & -\sin\phi & \cos\theta\sin\phi \end{bmatrix} \begin{bmatrix} \dot{\phi} \\ \dot{\theta} \\ \dot{\psi} \end{bmatrix} \tag{4.25}$$

where $(\dot{\phi}, \dot{\theta}, \dot{\psi})$ are called the *Euler rates*.

Similarly, we can derive an expression for the linear velocity components in the absolute frame as a function of the Euler angles and the linear velocity component in the body frame [10],

$$\begin{bmatrix} \frac{\mathrm{d}x}{\mathrm{d}t} \\ \frac{\mathrm{d}y}{\mathrm{d}t} \\ \frac{\mathrm{d}z}{\mathrm{d}t} \end{bmatrix} = \begin{bmatrix} c_\theta c_\psi & s_\phi s_\theta c_\psi - c_\phi s_\psi & c_\phi s_\theta c_\psi + s_\phi s_\psi \\ c_\theta s_\psi & s_\phi s_\theta s_\psi + c_\phi c_\psi & c_\phi s_\theta s_\psi - s_\phi c_\psi \\ -s_\theta & s_\theta c_\theta & c_\phi c_\theta \end{bmatrix} \begin{bmatrix} u \\ v \\ w \end{bmatrix} \tag{4.26}$$

where we have used the shorthand notations $s_\psi \triangleq \sin\psi$, $c_\psi \triangleq \cos\psi$, and so on. It is important to see that given p, q, r (known from the Euler equations), we can determine $\dot{\phi}, \dot{\theta}, \dot{\psi}$ using (4.25), which upon integration yield ϕ, θ, ψ. If we then substitute the known u, v, w and the just calculated ϕ, θ, ψ into (4.26), we can determine $\frac{\mathrm{d}x}{\mathrm{d}t}, \frac{\mathrm{d}y}{\mathrm{d}t}, \frac{\mathrm{d}z}{\mathrm{d}t}$. Performing a final integration yields the position of the aircraft's center of gravity as a function of time, expressed in the absolute frame.

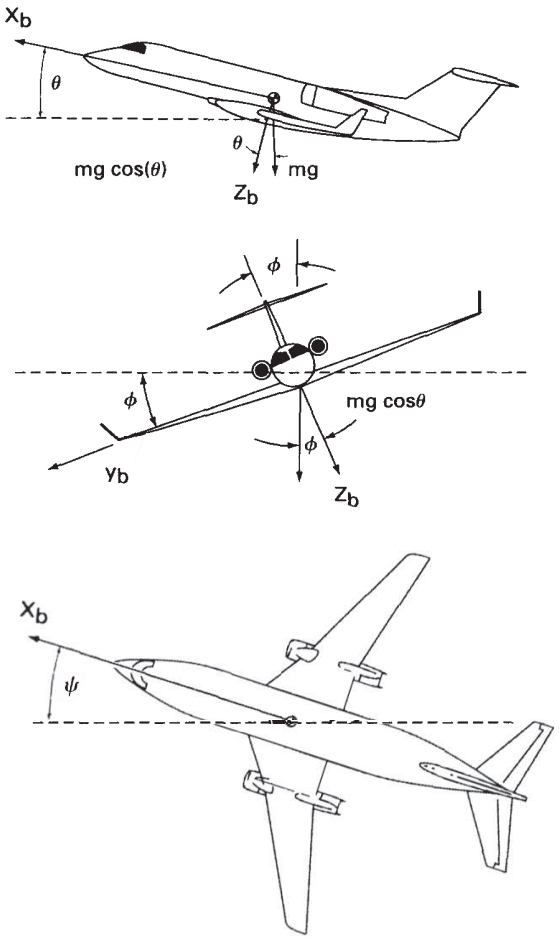

Figure 4.9: Definition of Euler angles [10]

We will now linearize the equations of motion (4.23),(4.24) using the *small-disturbance theory*. In this theory, it is assumed that the aircraft's motion consists of small deviations about a steady flight condition. As such, all variables appearing in the equations of motion can be replaced by a reference value plus a perturbation,

$$\begin{array}{lll} u = u_0 + \Delta u & v = v_0 + \Delta v & w = w_0 + \Delta w \\ p = p_0 + \Delta p & q = q_0 + \Delta q & r = r_0 + \Delta r \\ X = X_0 + \Delta X & Y = Y_0 + \Delta Y & Z = Z_0 + \Delta Z \\ L = L_0 + \Delta L & M = M_0 + \Delta M & N = N_0 + \Delta N \\ \phi = \phi_0 + \Delta\phi & \theta = \theta_0 + \Delta\theta & \psi = \psi_0 + \Delta\psi \ . \end{array} \tag{4.27}$$

Assuming the reference flight condition to be symmetric, implies

$$v_0 = p_0 = q_0 = r_0 = \phi_0 = \psi_0 = 0 \ . \tag{4.28}$$

If we further choose the x-axis of the body reference frame to coincide with the velocity vector of the steady symmetric reference flight, then w_0 is also zero. To further develop the linearized equations of motion, consider the X-force equation as an example,

$$X - mg\sin\theta = m(\dot{u} + q\dot{w} - rv) \tag{4.29}$$

where the contribution of the gravitational force has been already added. Substituting the small-disturbance variables (4.27) into (4.29) yields [10]

$$X_0 + \Delta X - mg(\sin\theta_0 + \Delta\theta\cos\theta_0) = m\Delta\dot{u} \tag{4.30}$$

where we have neglected products of perturbations and used the small angle approximations. In reference flight conditions, when all perturbation variables are zero,

$$X_0 - mg\sin\theta_0 = 0 \tag{4.31}$$

such that (4.30) reduces to

$$\Delta X - mg\Delta\theta\cos\theta_0 = m\Delta\dot{u} \ . \tag{4.32}$$

In general, the perturbation variable ΔX can be expressed as,

$$\begin{aligned} &\Delta X(u, v, w, \dot{u}, \dot{v}, \dot{w}, p, q, r, \dot{p}, \dot{q}, \dot{r}, \delta_e, \delta_r, \dot{\delta}_e, \dot{\delta}_r) \\ &\qquad \approx \frac{\partial X}{\partial u}\Delta u + \frac{\partial X}{\partial \dot{u}}\Delta\dot{u} + \cdots + \frac{\partial X}{\partial \dot{\delta}_r}\Delta\dot{\delta}_r \end{aligned} \tag{4.33}$$

where $\Delta\delta_e, \Delta\delta_r$ represent changes in elevator and rudder angle. Note that the higher order terms have already been neglected here, but many of the linear terms can also be neglected.

Below, we have summarized the most important contributions to a particular force or moment [10],

$$\begin{aligned}
&\Delta X(u, w, \delta_e) \\
&\Delta Y(v, p, r, \delta_r) \\
&\Delta Z(u, w, \delta_e) \\
&\Delta L(v, p, r, \delta_r) \\
&\Delta M(u, w, \dot{w}, q, \delta_e) \\
&\Delta N(v, p, r, \delta_r) \ .
\end{aligned} \tag{4.34}$$

Given (4.34) and following a similar approach as for the X-force equation, the linearized equations of motion can be written as [10]

$$\begin{bmatrix} \Delta\dot{u} \\ \Delta\dot{w} \\ \Delta\dot{q} \\ \Delta\dot{\theta} \end{bmatrix} = \begin{bmatrix} X_u & X_w & 0 & -g \\ Z_u & Z_w & u_0 & 0 \\ M_u + M_{\dot{w}} Z_u & M_w + M_{\dot{w}} Z_w & M_q + M_{\dot{w}} u_0 & 0 \\ 0 & 0 & 1 & 0 \end{bmatrix} \begin{bmatrix} \Delta u \\ \Delta w \\ \Delta q \\ \Delta\theta \end{bmatrix} + \begin{bmatrix} X_{\delta_e} \\ Z_{\delta_e} \\ M_{\delta_e} + M_{\dot{w}} Z_{\delta_e} \\ 0 \end{bmatrix} \Delta\delta_e \tag{4.35}$$

$$\begin{bmatrix} \Delta\dot{v} \\ \Delta\dot{p} \\ \Delta\dot{r} \\ \Delta\dot{\phi} \end{bmatrix} = \begin{bmatrix} Y_v & Y_p & -(u_0 - Y_r) & g\cos\theta_0 \\ L_v & L_p & L_r & 0 \\ N_v & N_p & N_r & 0 \\ 0 & 1 & 0 & 0 \end{bmatrix} \begin{bmatrix} \Delta v \\ \Delta p \\ \Delta r \\ \Delta\psi \end{bmatrix} + \begin{bmatrix} Y_{\delta_r} \\ L_{\delta_r} \\ N_{\delta_r} \\ 0 \end{bmatrix} \Delta\delta_r \tag{4.36}$$

where we have assumed $I_{xz} = 0$ in (4.36) and where we have used following notations,

$$\begin{aligned}
X_u &= \frac{\partial X/\partial u}{m} & L_u &= \frac{\partial L/\partial u}{I_x} \\
Y_u &= \frac{\partial Y/\partial u}{m} & M_u &= \frac{\partial M/\partial u}{I_y} \\
Z_u &= \frac{\partial Z/\partial u}{m} & N_u &= \frac{\partial N/\partial u}{I_z} \\
&\dots
\end{aligned} \tag{4.37}$$

in which the terms $\partial X/\partial u, \partial L/\partial u, \dots$ are called the *stability derivatives*.

At this point, we have derived the linearized equations of motion (4.35),(4.36) where the stability derivatives contained within these equations are still unknown. It is now that we can exploit the power of the Vortex Lattice Method. Recall (3.46) which allows us to determine the vortex strengths Γ_i and the corresponding aerodynamic forces and moments. For a given geometry of the aircraft, the matrix containing the influence coefficients is fixed, while the RHS (Right-Hand Side) depends upon the free-stream velocity. It can now be understood that for the stability derivatives to u, v or w we can apply an identical perturbation to u_∞, v_∞ or w_∞ at every collocation point and determine the corresponding forces and moments. Some

caution is needed for the stability derivatives to p, q, r as a perturbation to one of these variables will generally lead to a variation of each free-stream velocity component and where the variation will not be constant in space. To clarify, consider a perturbation to r (aircraft starts to yaw), it is now clear that the variation of $(u_\infty, v_\infty, w_\infty)$ will be larger at the tip of the wing than at the root. Summarizing, to calculate the stability derivatives, only the RHS of (3.46) is adjusted accordingly and by comparing the forces and moments in the reference and perturbed state, we can determine the derivatives. Note that the derivatives to δ_e, δ_r involve changing the geometry of the aircraft (adjusting the position of the elevator or rudder) while the free-stream velocity remains unchanged.

4.3 Dynamic Stability

In the study of dynamic stability, we are interested in the aircraft's motion after is has been disturbed from its equilibrium position. We usually quantify dynamic stability by the time is takes a disturbance to be damped to half of its initial amplitude or to double in amplitude in the case of unstable motion. Repeating the linearized equations of motion,

$$\begin{bmatrix} \Delta\dot{u} \\ \Delta\dot{w} \\ \Delta\dot{q} \\ \Delta\dot{\theta} \end{bmatrix} = \begin{bmatrix} X_u & X_w & 0 & -g \\ Z_u & Z_w & u_0 & 0 \\ M_u + M_{\dot{w}} Z_u & M_w + M_{\dot{w}} Z_w & M_q + M_{\dot{w}} u_0 & 0 \\ 0 & 0 & 1 & 0 \end{bmatrix} \begin{bmatrix} \Delta u \\ \Delta w \\ \Delta q \\ \Delta\theta \end{bmatrix} + \begin{bmatrix} X_{\delta_e} \\ Z_{\delta_e} \\ M_{\delta_e} + M_{\dot{w}} Z_{\delta_e} \\ 0 \end{bmatrix} \Delta\delta_e \tag{4.35}$$

$$\begin{bmatrix} \Delta\dot{v} \\ \Delta\dot{p} \\ \Delta\dot{r} \\ \Delta\dot{\phi} \end{bmatrix} = \begin{bmatrix} Y_v & Y_p & -(u_0 - Y_r) & g\cos\theta_0 \\ L_v & L_p & L_r & 0 \\ N_v & N_p & N_r & 0 \\ 0 & 1 & 0 & 0 \end{bmatrix} \begin{bmatrix} \Delta v \\ \Delta p \\ \Delta r \\ \Delta\psi \end{bmatrix} + \begin{bmatrix} Y_{\delta_r} \\ L_{\delta_r} \\ N_{\delta_r} \\ 0 \end{bmatrix} \Delta\delta_r \tag{4.36}$$

we notice that they have been split into two independent groups, where (4.35) represents the *longitudinal equations* and (4.36) the *lateral equations*. The separation follows from the assumptions (4.34) and will simplify our further analysis.

4.3.1 Longitudinal Motion

In this section, we analyze the longitudinal motion of an aircraft without control inputs, so $\Delta\delta_e = 0$. To determine the longitudinal *modes of motion*, we have to calculate the eigenvalues λ of the longitudinal stability matrix A. These can be found by solving the following characteristic equation,

$$|\lambda I - A| = 0 \tag{4.38}$$

where I is the identity matrix. The solution is generally two pair of complex eigenvalues,

$$\begin{aligned} \lambda_{1,2} &= -\zeta_p \omega_{n_p} \pm j\omega_{n_p}\sqrt{1-\zeta_p^2} &&= \sigma_p \pm j\omega_p \\ \lambda_{3,4} &= -\zeta_{sp} \omega_{n_{sp}} \pm j\omega_{n_{sp}}\sqrt{1-\zeta_{sp}^2} &&= \sigma_{sp} \pm j\omega_{sp} \end{aligned} \tag{4.39}$$

and corresponds to two oscillatory modes of motion as shown in Figure 4.10. We see that one mode has a long period and is lightly damped. This motion is called the *phugoid mode*. The second mode has a very short period and is heavily damped, which we call the *short-period mode*. To determine the period T of the oscillatory motion and the time for the amplitude to double t_2 or halve $t_{1/2}$, we can use following relations [10],

$$\begin{aligned} T &= \frac{2\pi}{\omega} \\ t_{1/2} = t_2 &= \frac{\ln 2}{|\sigma|} \ . \end{aligned} \tag{4.40}$$

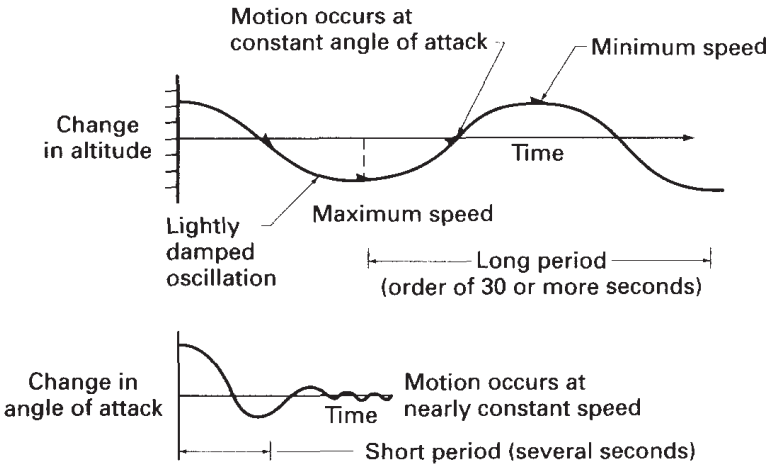

Figure 4.10: The phugoid and short-period motions [10]

Without going into further detail, it can be shown that the following approximations hold for the *natural frequency* ω_n and *damping ratio* ζ of the phugoid and short-period mode [10],

$$\begin{aligned} \omega_{n_p} &= \sqrt{\frac{-Z_u g}{u_0}} &\qquad \zeta_p &= \frac{-X_u}{2\omega_{n_p}} \\ \omega_{n_{sp}} &= \sqrt{\frac{Z_\alpha M_q}{u_0} - M_\alpha} &\qquad \zeta_{sp} &= -\frac{M_q + M_{\dot{\alpha}} + \frac{Z_\alpha}{u_0}}{2\omega_{n_{sp}}} \ . \end{aligned} \tag{4.41}$$

4.3.2 Lateral Motion

Following a similar approach as in Section 4.3.1, we can determine the lateral modes of motion by solving the characteristic equation (4.38) in which A is now the lateral stability matrix. In general, we will find two real eigenvalues and a pair of complex eigenvalues.

Spiral Mode

One of the real eigenvalues corresponds to the *spiral mode* and is illustrated in Figure 4.11. As shown, *spiral divergence* (a non-oscillatory motion) occurs when directional stability is large and lateral stability is small. In the case of *directional divergence*, the vertical tail surface produces an insufficient counteracting moment, such that the sideslip angle keeps on increasing. An approximation for the spiral eigenvalue is given by [10]

$$\lambda_{\text{spiral}} = \frac{L_\beta N_r - L_r N_\beta}{L_\beta}. \tag{4.42}$$

A stable spiral mode corresponds with $\lambda_{\text{spiral}} < 0$. As the stability derivatives L_β (dihedral effect) and N_r (yaw rate damping) are usually negative, the condition for stable spiral mode is,

$$L_\beta N_r > L_r N_\beta. \tag{4.43}$$

So, increasing the dihedral effect or yaw damping can make the spiral mode stable.

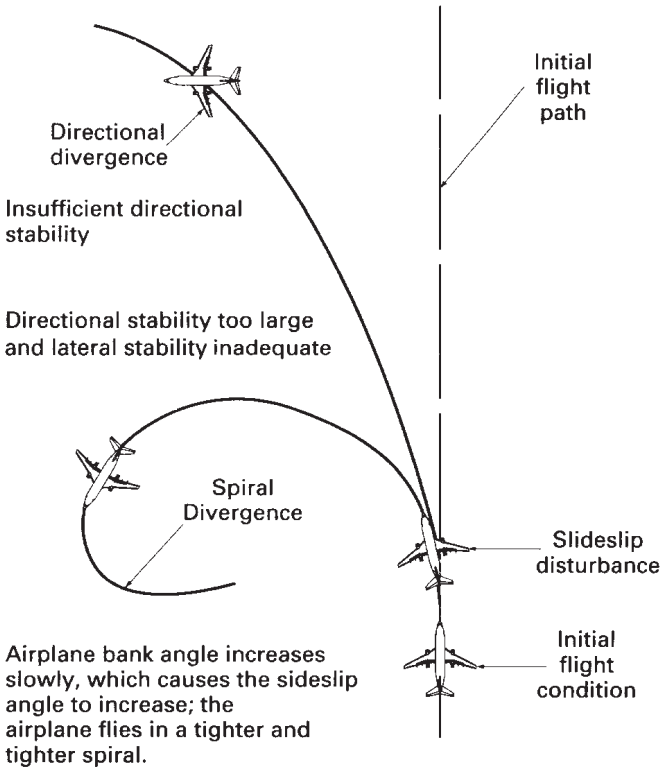

Figure 4.11: The spiral motion [10]

Rolling Mode

The second real eigenvalue corresponds to the *roll damping* and indicates how fast the aircraft approaches a new steady-state roll rate after being disturbed.

Dutch Roll Mode

The mode corresponding with the pair of complex eigenvalues is the *Dutch Roll Mode*. This motion, illustrated in Figure 4.12, is characterized by a combination of yawing and rolling oscillations that have the same frequency but are out of phase. This motion can be very unpleasant for pilot and passengers and should therefore be properly damped.

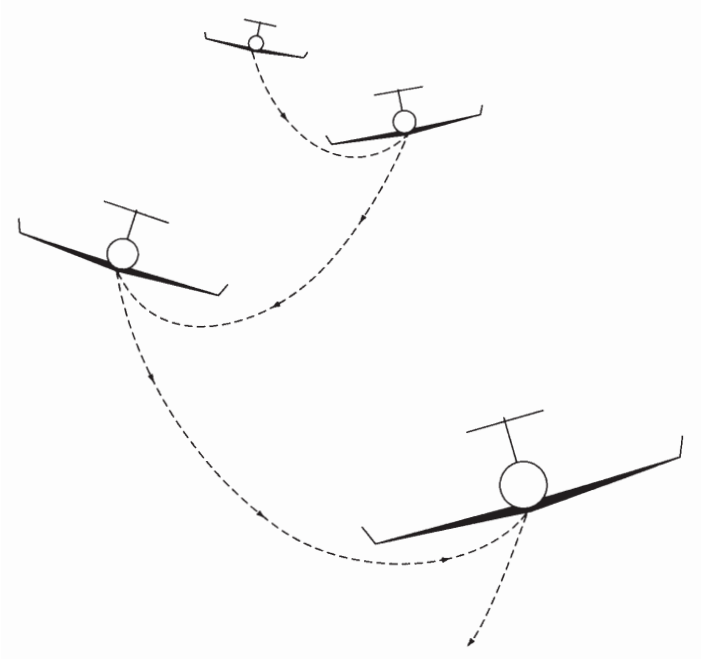

Figure 4.12: The Dutch roll motion [10]

To finalize, Figure 4.13 is a general plot showing the different eigenvalues and is called a *root locus plot*.

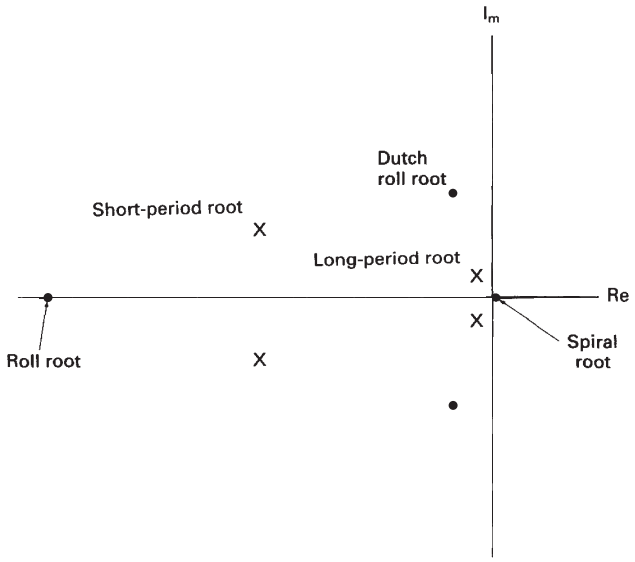

Figure 4.13: Root locus plot [10]

Chapter 5

Validation Case - Daedalus

With the knowledge obtained in Chapters 3 and 4, we will now analyze the *Daedalus* considered as the most successful design in the history of human powered flight. One of the goals of the present chapter is to get some feeling with the dimensions and mass of a HPA and to discuss some of the specific design aspects related to the Daedalus. However, the major goal is to simulate the entire Daedalus in two different softwares. The first is based on the *Vortex Lattice Method* while the second is a *CFD* package based on the finite volume method. As mentioned in Chapter 3, the VLM is characterized by very short calculation times and as such, the first software will also be used during the optimization in Chapter 6. In order to have an idea of the accuracy of both softwares, which is crucial when formulating conclusions, we will also compare the outputs of both softwares with data found in other work.

5.1 Reconstruction of the Daedalus

In our attempt to reconstruct the Daedalus as precise as possible, most of the geometrical and structural data was found in a public txt file provided by MIT [11]. Based on this txt file and the detailed overview drawing given in Appendix A.2, the Daedalus is now constructed piece by piece.

5.1.1 Wing

The Daedalus has an incredible wingspan of 112 ft (34 m) with a corresponding wing area of 332 ft^2 (31 m^2). As can be seen in Figure 5.1, four different airfoils (DAE11, DAE21, DAE31, DAE41) are indicated on the wing, such that each half of the wing can be virtually divided into four parts; center panel, mid panel, tip panel and wingtip. In reality, it is possible to disassemble the wing at the sections indicated by DAE11 and DAE21, such that the entire wing is actually made up of five different pieces. The same airfoil (DAE11) is used across the entire center panel whereas interpolated airfoils are used across the remaining three parts giving a smooth airfoil shape variation along the span of the wing. In Table 5.1 the *chord length* c of the wing is given as a function of its spanwise position s, going from root to tip [11].

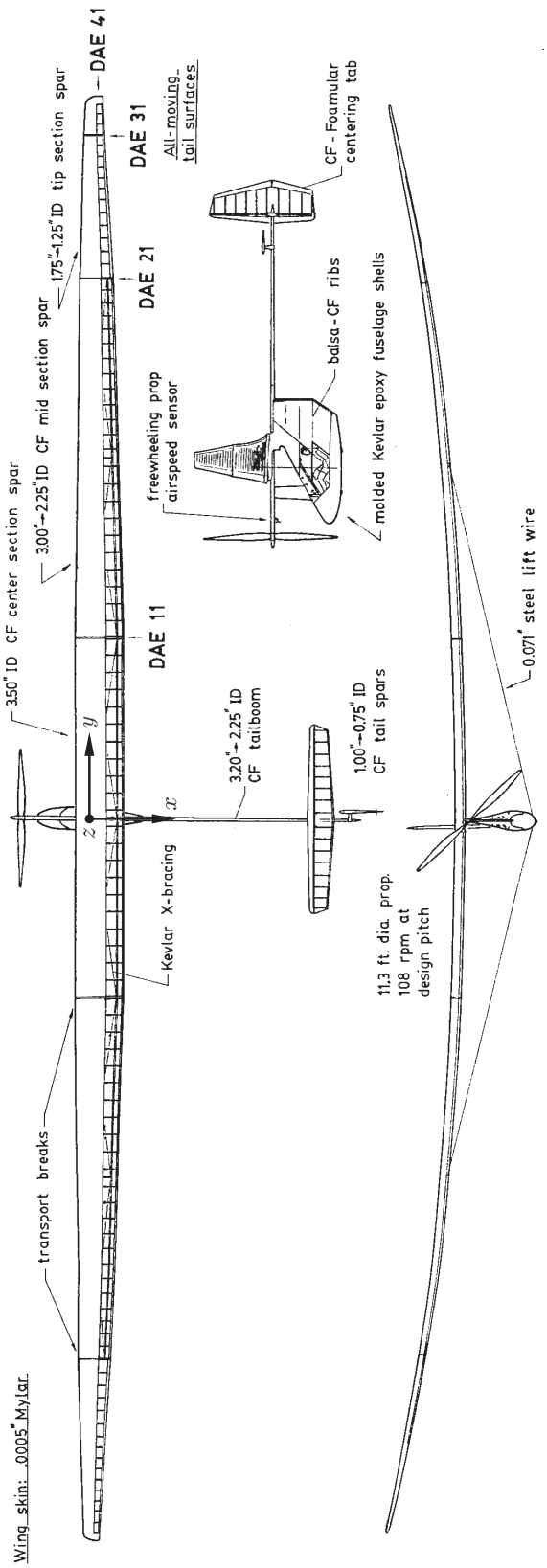

Figure 5.1: Part of detailed overview drawing Daedalus

s (ft)	s (m)	c (ft)	c (m)
0	0	3.750	1.143
14.00	4.27	3.750	1.143
42.00	12.80	2.500	0.762
55.42	16.89	1.250	0.381
56.00	17.07	0.625	0.191

Table 5.1: Chord lengths of wing Daedalus

The main structural element of a wing is its *spar*, in this case a thin-walled carbon fiber (CF) tube. The spar will provide the necessary strength to carry the bending and torsion loads acting on the wing during flight. A cross section of the center panel of the wing is shown in Figure 5.2 indicating the wing's main and rear spar.

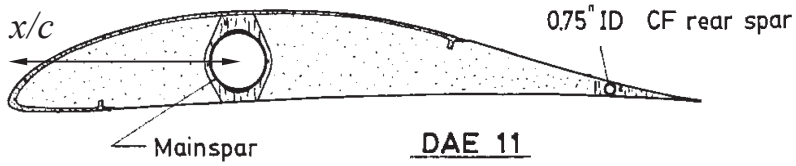

Figure 5.2: Cross section of center panel

In the remaining of this section we will make a consistent distinction between airfoil and profile coordinates. The airfoil coordinates are the coordinates as found in databases, i.e. a chord length of unity, leading edge at (0,0) and trailing edge at (1,0) in the x, y-plane. When any operation is performed on the airfoil coordinates (e.g. scaling, rotation, translation), we will refer to them as profile coordinates. In the txt file, the position and orientation of the wing was defined by the coordinates of the main spar's center together with its relative position x/c within the profile (see Figure 5.2). Note that with the description so far, the profiles are still free to rotate around the main spar. To fix their orientation, consider Figure 5.3 showing two wing sections with an identical orientation with respect to the aircraft axis. Knowing the *Principal Bending Axis* (PBA) of the section along with the so-called *twist angle* ϑ, it is possible to easily fix its orientation (see Representation 1). However, how do we determine the PBA? As somewhat suggested by Figure 5.3, the PBA goes through the centers of both the main and rear spar [12]. For the Daedalus, the relative position of the main spar is known ($x/c = 0.33$) but unfortunately the relative position of the rear spar was not specified, forcing us to make a small estimation. Based on Figure 5.2, the DAE11 airfoil coordinates and the chord length of the center panel, it is estimated that the rear spar is positioned at $x/c = 0.86$. At this position, it was verified that the inner diameter of the rear spar (indicated on the figure) fits into the profile with some additional margin.

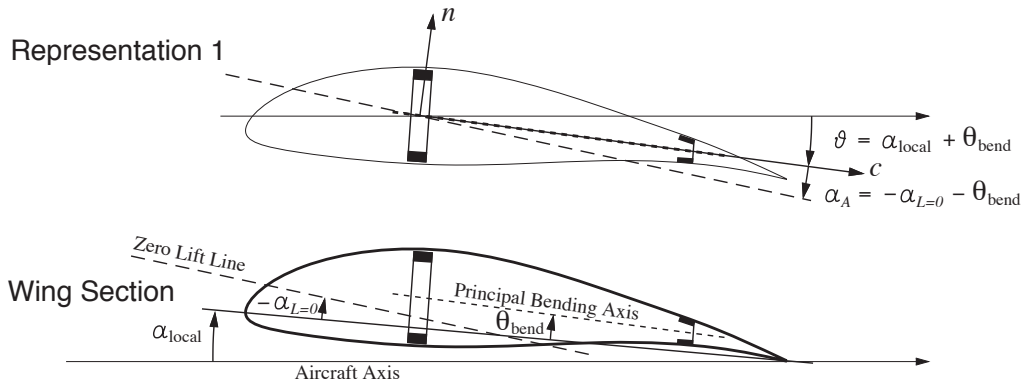

Figure 5.3: Defining the section's orientation

Now that we know the PBA, it is also possible to calculate the angle θ_{bend}. The procedure is as follows; using the airfoil coordinates, determine the points on the pressure and suction side of the airfoil at $x = 0.33c$ and $x = 0.86c$. Next, determine the midpoints between the pressure and suction side at these positions, which also correspond to the centers of the main and rear spar. With these two midpoints (defining the PBA), we can now easily determine the angle of the PBA with respect to the x-axis, which is θ_{bend}. Knowing ϑ and θ_{bend} also allows us to calculate the local incidence α_{local} of the wing's section using the relation

$$\alpha_{\text{local}} = \vartheta - \theta_{\text{bend}} \ . \tag{5.1}$$

In case of the Daedalus, the twist angle $\vartheta = 8.2°$ and is constant along the entire wing. Applying the above procedure to for instance the airfoil DAE11, results in $\theta_{\text{bend}} = 4.68°$ such that α_{local} of the center panel is equal to $3.52°$.

At this point, the geometry of the wing is fully defined. However, the data given in the txt file describes the geometry of the wing in undeformed state. In flight, the wing of the Daedalus is designed to have a tip deflection of 2 m, at a cruise speed of 6.7 m/s [13]. This desired tip deflection is obtained by proper selection of the spar's structural properties in combination with a lift wire. More details will follow in Chapter 6. Knowing the tip deflection and assuming a parabolic deformation of the wing, allows us to update the coordinates of the main spar's center. Note that the direction in which the main spar bends is not necessarily straight up. It is assumed that the wing bends around the section's PBA, which in case of the Daedalus is inclined with respect to the aircraft axis by the angle ϑ. As such, the wing will also experience a displacement along the aircraft axis when bent. Now that we have defined the deformed geometry of the wing, a small overview will be given on how the CAD model of the wing was constructed. As the cross section of a wing at a certain spanwise location is just a simple profile, we can try to draw some of these profiles with their correct position and orientation. In Figure 5.4, a set of well chosen sections is indicated on the wing together with a front view of the deformed spar and the set of profiles.

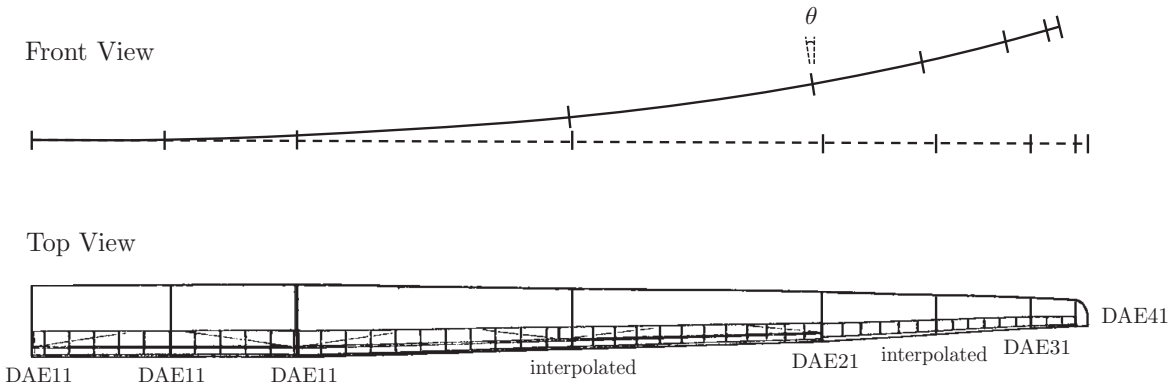

Figure 5.4: Overview of profiles used to construct the deformed wing

It is assumed that the length of the spar remains constant when the spar is bent to a parabolic shape, such that the tip of the spar will move somewhat closer to the symmetry plane of the aircraft. Further note that the profiles rotate around their PBA by the *deflection angle* θ (not to confuse with the twist angle ϑ), such that the profiles remain perpendicular to the spar. The final step consists of "skinning" the wing, in which we draw a smooth surface around the set of profiles. This smooth surface is now the outer geometry of the wing. The process of generating the different profiles of the deformed wing is explained in some more detail in the diagram of Figure 5.5. By using translation matrices T and rotation matrices R defined as

$$T_{(t_x,t_y,t_z)} \triangleq \left[\begin{array}{ccc|c} 1 & 0 & 0 & t_x \\ 0 & 1 & 0 & t_y \\ 0 & 0 & 1 & t_z \\ \hline 0 & 0 & 0 & 1 \end{array}\right] \tag{5.2}$$

$$R_{(x,\alpha)} \triangleq \left[\begin{array}{ccc|c} 1 & 0 & 0 & 0 \\ 0 & \cos\alpha & -\sin\alpha & 0 \\ 0 & \sin\alpha & \cos\alpha & 0 \\ \hline 0 & 0 & 0 & 1 \end{array}\right] \qquad R_{(z,\alpha)} \triangleq \left[\begin{array}{ccc|c} \cos\alpha & -\sin\alpha & 0 & 0 \\ \sin\alpha & \cos\alpha & 0 & 0 \\ 0 & 0 & 1 & 0 \\ \hline 0 & 0 & 0 & 1 \end{array}\right] \tag{5.3}$$

we will manipulate the airfoil coordinates x_p, y_p and z_p ($1 \times n$ matrices) until they correspond with a chosen cross section of the deformed wing. During the process, we will use the virtual position of the main spar's center, indicated by the Reference Point (RP). Note that in the end, this reference point should coincide with the center of the real deformed main spar.

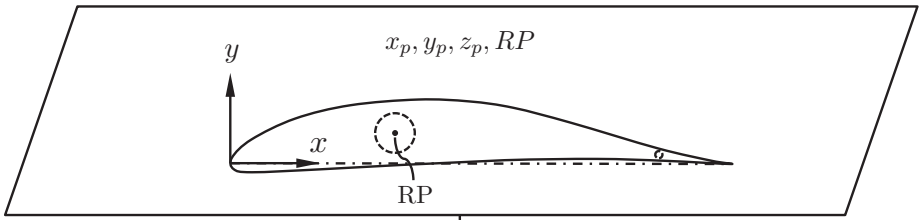

Multiply with the section's chord length c and define

$$P_1 \triangleq \begin{bmatrix} x_p \cdot c \\ y_p \cdot c \\ z_p \cdot c \\ \hline ones(1,n) \end{bmatrix} \qquad RP_1 \triangleq \begin{bmatrix} RP \cdot c \\ \hline 1 \end{bmatrix} .$$

Rotate the profile around its trailing edge by α_{local}.

$$A_1 = T^{-1}_{(-c,0,0)}\ R_{(z,-\alpha_{\text{local}})}\ T_{(-c,0,0)}$$

$$\longrightarrow \quad \begin{aligned} P_2 &= A_1 \cdot P_1 \\ RP_2 &= A_1 \cdot RP_1 \end{aligned}$$

Rotate the profile around its PBA by θ.

(1) Make the PBA coincide with the x-axis

$$A_2 = R_{(z,\vartheta)}\ T_{(-R\vec{P}_1)}$$

(2) Perform the rotation, note that θ depends on the spanwise location

$$A_3 = A_2^{-1}\ R_{(x,\theta)}\ A_2$$

$$\longrightarrow \quad \begin{aligned} P_3 &= A_3 \cdot P_2 \\ RP_3 &= A_3 \cdot RP_2 \end{aligned}$$

Perform a final translation T_f such that RP_3 coincides with the real position of the main spar's center.

$$P_f = T_f \cdot P_3$$

Draw a spline through the final profile coordinates x_{pf}, y_{pf}, z_{pf}.

$\longrightarrow$ smooth cross section of deformed wing

Figure 5.5: Process of generating a cross section of the deformed wing

Now that we have seen how the CAD model of the deformed wing is constructed (drawing a smooth surface around a set of profiles with the correct position and orientation), a final part will be devoted to the mass and inertia properties of the wing. For the mass and inertia properties, the wing is represented as a thin rod located along the main spar's center and characterized by a linear density distribution $\lambda(x)$. Using this distribution, we can easily calculate the mass and Center of Gravity (CG) of the wing. In the following, we will just analyze one half of the wing, which is sufficient to determine the properties of the complete wing due to its symmetry. The relations are

$$m = \int_0^{b/2} \lambda(x)\,\mathrm{d}x \tag{5.4}$$

$$x_{CG} = \frac{1}{m}\int_0^{b/2} x\lambda(x)\,\mathrm{d}x \tag{5.5}$$

where the values of the linear density distribution $\lambda(x)$ are provided in Appendix A.3. For the integrations in (5.4) and (5.5), the data in the table is interpolated using cubic splines. The mass of the entire wing is now $2m$ and equal to only 17.10 kg! From data provided in [4], the mass of the entire main spar is said to be 19 lb (8.62 kg). This means that the main spar accounts for about 50% of the wing's total mass. The other 50% is due to the additional structures as shown in Figure 5.6.

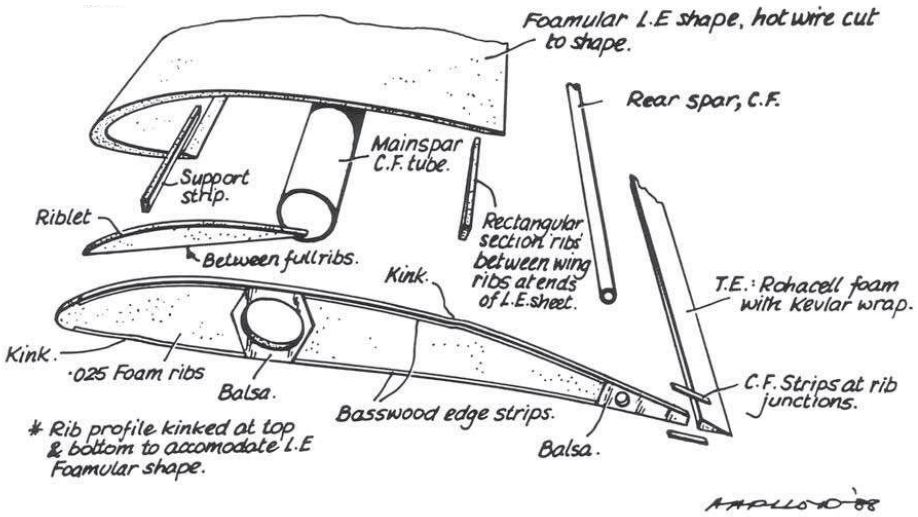

Figure 5.6: Structural decomposition of the wing

For the dynamic stability analysis of the Daedalus later on, the inertia tensor I of the wing must also be calculated. Referring to Figure 5.7, the inertia tensor of half of the wing around its own CG is given by

$$I = \begin{bmatrix} 0 & 0 & 0 \\ 0 & I_{CG} & 0 \\ 0 & 0 & I_{CG} \end{bmatrix} \tag{5.6}$$

in which

$$I_{CG} = I - m x_{CG}^2 \tag{5.7}$$

$$I = \int_0^{b/2} x^2 \lambda(x)\, \mathrm{d}x \ . \tag{5.8}$$

Note that we have used the *parallel-axis theorem* in (5.7) and that the mass moment of inertia around the x-axis is zero for the thin rod shown in Figure 5.7.

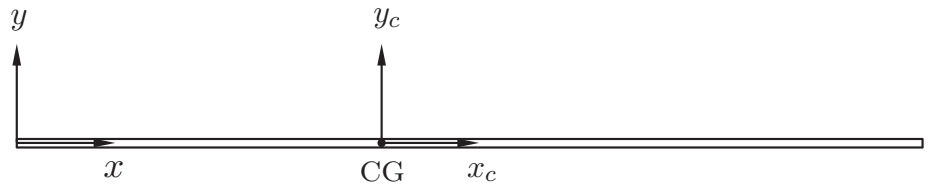

Figure 5.7: Half of the wing represented as a thin rod

A small difficulty arises when the wing is deformed as shown in Figure 5.8. Although the wing is assumed to deform according to a parabolic shape, for the mass and inertia properties we will assume the deformation to be linear as suggested in Figure 5.8. This will somewhat simplify the calculations to determine the CG in the x'', y''-frame and the inertia tensor expressed in the x', y'-frame (which is just rotated with respect to the x_c, y_c-frame).

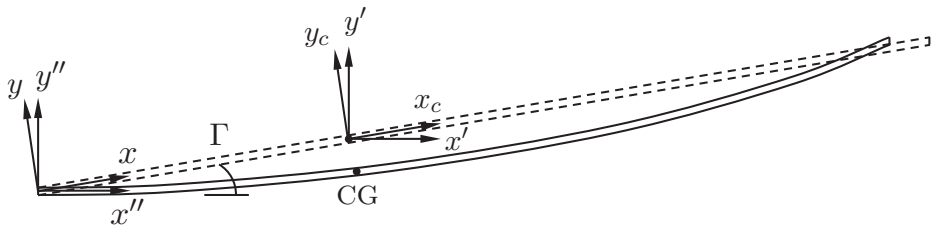

Figure 5.8: Simplification of the deformed thin rod

The relations are [14]

$$x''_{CG} = x_{CG} \cos\Gamma \tag{5.9}$$

$$y''_{CG} = x_{CG} \sin\Gamma \tag{5.10}$$

$$I' = \begin{bmatrix} \cos\Gamma & -\sin\Gamma & 0 \\ \sin\Gamma & \cos\Gamma & 0 \\ 0 & 0 & 1 \end{bmatrix} \begin{bmatrix} 0 & 0 & 0 \\ 0 & I_{CG} & 0 \\ 0 & 0 & I_{CG} \end{bmatrix} \begin{bmatrix} \cos\Gamma & \sin\Gamma & 0 \\ -\sin\Gamma & \cos\Gamma & 0 \\ 0 & 0 & 1 \end{bmatrix} \tag{5.11}$$

in which Γ is the dihedral angle calculated from the tip deflection. Using the reference frame as indicated in Figure 5.1, the result of the mass and inertia analysis of half of the deformed wing is

$$\begin{aligned} m &= 8.55 \text{ kg} \\ CG &= (0, 6.618, 0.943) \text{ m} \\ I' &= \begin{bmatrix} 156.92 & 0 & 0 \\ 0 & 2.13 & -18.14 \\ 0 & -18.14 & 154.80 \end{bmatrix} \text{ kg.m}^2 \end{aligned} \tag{5.12}$$

in which the inertia tensor I' is expressed in a frame with the origin in CG and with the same orientation as the reference frame. The reason for doing so is that this data can now be directly used for the dynamic stability analysis of the Daedalus in Section 5.3.3. For the other half of the wing, the only difference is its CG, in which we have to add a minus sign to the y-coordinate.

Note that a lot of effort has been put into reconstructing the wing as accurate as possible. This is necessary as the performance of a HPA is mainly determined by the performance of the wing as will be shown.

5.1.2 Fuselage

The fuselage is a streamlined structure surrounding the pilot of the aircraft as schematically shown in Figure 5.9.

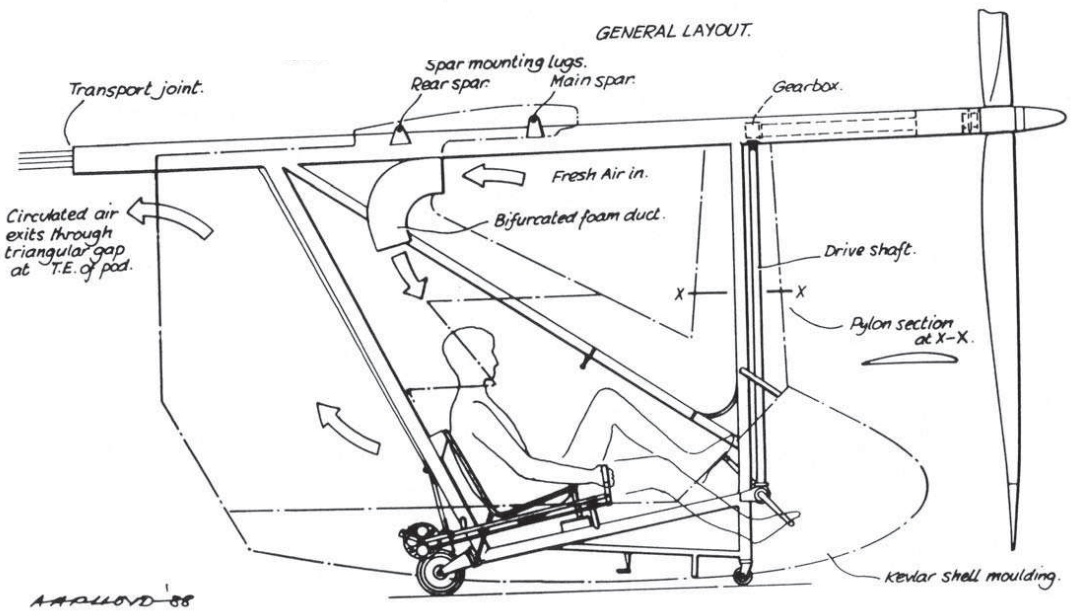

Figure 5.9: Fuselage of the Daedalus

For most HPAs, the geometry of the fuselage can be described by a symmetric airfoil and a certain chord length distribution. For the Daedalus, the type of airfoil was not specifically mentioned, but based on data provided in [15], it is assumed to be the symmetrical NACA65_4-021. To give an idea of its shape, the airfoil is shown in Figure 5.10.

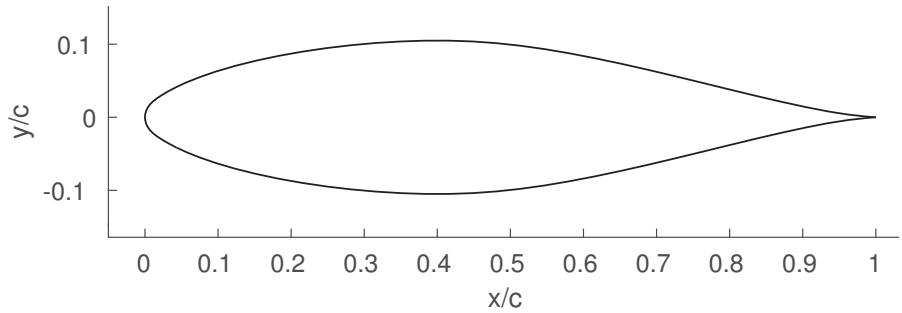

Figure 5.10: NACA65_4-021

In the txt file, the chord lengths are given as a function of the vertical position z. However, this data was slightly modified resulting in a fuselage geometry in closer agreement with some of the photographs of the Daedalus. In Table 5.2, the modified chord length distribution is given together with the position of the profile's leading edge x_{LE}.

z (m)	c (m)	x_{LE} (m)
0	0.9305	0.4411
−0.1500	0.9305	0.4411
−0.9754	2.6962	−1.3246
−1.1156	2.8754	−1.6246
−1.1973	2.9404	−1.7599
−1.2789	2.9392	−1.8290
−1.3606	2.8632	−1.8233
−1.4423	2.7041	−1.7346
−1.5240	2.4536	−1.5545
−1.6459	1.5545	−1.0973

Table 5.2: Chord lengths of fuselage Daedalus

For the construction of the CAD model of the fuselage, a similar approach is applied as in Section 5.1.1. We will draw a set of well chosen profiles with the correct position and orientation within the reference frame of Figure 5.1. These profiles will then be skinned, giving a smooth and streamlined geometry. The set of well chosen profiles is shown in Figure 5.11 and corresponds with the data given in Table 5.2.

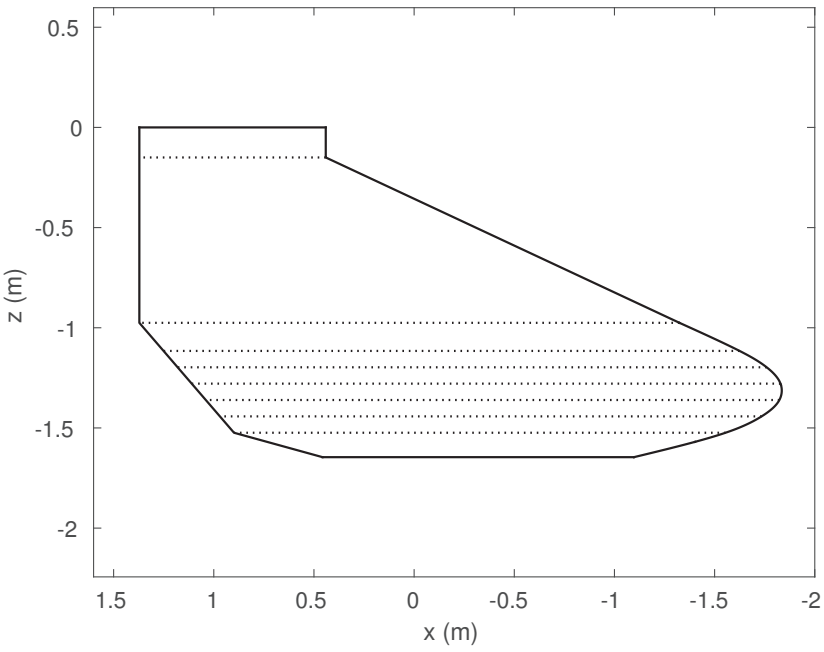

Figure 5.11: Sections used for constructing the fuselage

As for the wing, we can also determine the mass, CG and inertia tensor of the fuselage structure by representing it as a thin rod. The linear density distribution can be found in Appendix A.3. The results are summarized below.

$$\begin{aligned} m &= 1.91 \text{ kg} \\ CG &= (0.762, 0, -0.853) \text{ m} \\ I' &= \begin{bmatrix} 0.463 & 0 & 0 \\ 0 & 0.463 & 0 \\ 0 & 0 & 0 \end{bmatrix} \text{ kg.m}^2 \end{aligned} \tag{5.13}$$

Note that the representation as a thin rod is not very accurate here, but as the mass and inertias of the fuselage structure are very small, it will have a minor effect on the dynamic stability analysis.

5.1.3 Stab and Rudder

The tail of the Daedalus consists of an elevator or stab (horizontal surface) and a rudder (vertical surface) as shown in Figure 5.12. These two all-moving surfaces play an important roll in controlling the aircraft. As seen in Figure 5.12, the geometry of the stab and rudder is quite similar. Both structures contain a single spar positioned at $x/c = 0.25$ within the profiles and the chord length distributions are given in Table 5.3 [11]. The airfoil of both surfaces is symmetric and assumed to be a NACA0010.

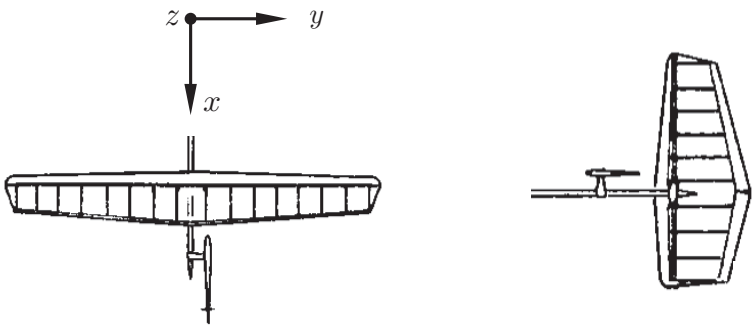

Figure 5.12: Tail surfaces of the Daedalus

Stab				**Rudder**			
y (ft)	y (m)	c (ft)	c (m)	z (ft)	z (m)	c (ft)	c (m)
0	0	1.85	0.564	−3.5	−1.067	2.2	0.671
7.5	2.286	1.05	0.320	0	0	3.5	1.067
				5.0	1.524	1.5	0.457

Table 5.3: Chord lengths of stab and rudder Daedalus

As for the wing, the stab can be divided into two symmetric parts, such that the data given in Table 5.3 only describes one symmetry part. Further, we will make a small simplification concerning the position of the rudder. Note that the rudder in not located within the x, z-plane of the aircraft but contains a little offset, facilitating its steering. However, for the CFD simulations later on, it is useful if the aircraft is completely symmetric. As such, we only have to simulate half of the aircraft, greatly reducing the computational time for the simulations. In order to have this advantage, we will move the rudder to the x, z-plane, making the aircraft symmetric. Note that this simplification will have almost no effect on the drag and stability of the aircraft.

Using the linear density distributions of the stab and rudder given in Appendix A.3, we can determine the mass, CG and inertia tensor as in the previous sections. For half of the stab, the results are

$$\begin{aligned} m &= 0.26 \text{ kg} \\ CG &= (5.334, 1.018, 0.305) \text{ m} \\ I' &= \begin{bmatrix} 0.107 & 0 & 0 \\ 0 & 0 & 0 \\ 0 & 0 & 0.107 \end{bmatrix} \text{ kg.m}^2 \end{aligned} \tag{5.14}$$

and for the rudder

$$\begin{aligned} m &= 0.52 \text{ kg} \\ CG &= (6.096, 0, 0.259) \text{ m} \\ I' &= \begin{bmatrix} 0.237 & 0 & 0 \\ 0 & 0.237 & 0 \\ 0 & 0 & 0 \end{bmatrix} \text{ kg.m}^2 \text{ .} \end{aligned} \tag{5.15}$$

5.1.4 Tailboom

The tailboom is a CF tube going from the nose of the aircraft to its tail and is used to connect the different parts of the aircraft (wing, fuselage, stab, rudder, propeller, ...). In Table 5.4, the outer diameter of the tube is given as a function of the x-position (see Figure 5.1) together with its linear density.

x (ft)	x (m)	d_o (in)	d_o (m)	λ (lb/ft)	λ (kg/m)
−6.5	1.981	6.5	0.165	0.15	0.223
4.0	1.219	6.5	0.165	0.15	0.223
12.0	3.658	4.5	0.114	0.11	0.164
20.0	6.096	4.5	0.114	0.06	0.089

Table 5.4: Dimensions and linear density of tailboom Daedalus

Using this data, we can determine the tailboom's mass, CG and inertia tensor.

$$\begin{aligned} m &= 1.49 \text{ kg} \\ CG &= (1.550, 0, 0) \text{ m} \\ I' &= \begin{bmatrix} 0 & 0 & 0 \\ 0 & 7.149 & 0 \\ 0 & 0 & 7.149 \end{bmatrix} \text{ kg.m}^2 \text{ .} \end{aligned} \tag{5.16}$$

5.1.5 Pilot and miscellaneous

Some of the additional components of the Daedalus are listed in Table 5.5 together with their mass and CG. Note that even the nutrition for the pilot is taken into account. These components are modeled as point masses such that the inertia tensors are zero.

	mass (kg)	x_{CG} (m)	y_{CG} (m)	z_{CG} (m)
propeller	1.36	−1.981	0	0
gearbox	0.91	−0.914	0	0
crankset	1.36	−0.914	0	−1.524
water	5.44	−0.061	0	−1.676

Table 5.5: Mass and CG of additional structures Daedalus

At this point, the complete structure of the Daedalus has been described and analyzed in detail, allowing us to calculate its empty weight. By simply adding up the different masses, we find that its empty weight is equal to just 30.60 kg, an impressive result! It is even more impressive if we compare its empty weight with the mass of the pilot (74.84 kg). So, the pilot was almost 2.5 times heavier than the aircraft itself. As a result, the CG of the Daedalus (when the pilot is included) is largely determined by the CG of the pilot itself as shown in Table 5.6.

	mass (kg)	CG (m)
pilot	74.84	(0, 0, -1.219)
Daedalus + pilot	105.44	(0.043, 0, -0.831)

Table 5.6: Mass and CG of pilot and Daedalus

Summarizing, although the wingspan of the Daedalus (34 m) is as large as the wingspan a Boeing 737-800, its complete structure only weighs 30.60 kg. This extremely low weight is mainly due to the usage of very light but strong materials such as carbon fiber and Kevlar. Including the pilot of 74.84 kg, the total mass of the Daedalus is now 105.44 kg. This total mass will have to be lifted up in the air and this by the sole human power of the pilot.

5.1.6 Final CAD Model

In this section, some figures are included showing the final CAD model of the Daedalus.

Figure 5.13: CAD model Daedalus

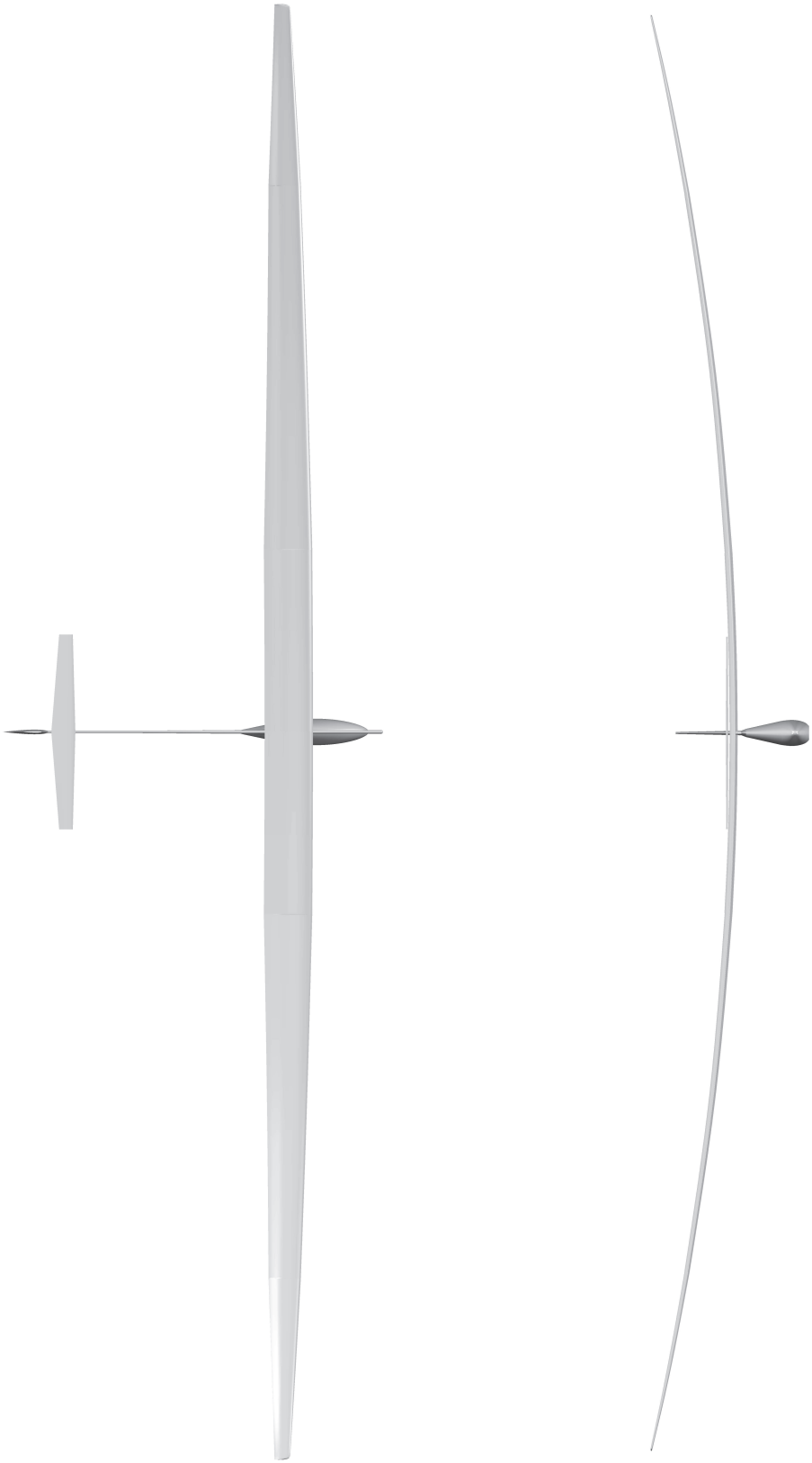

Figure 5.14: CAD model Daedalus

5.2 Specific Design Aspects

The purpose of this section is to discuss some of the interesting design aspects related to the Daedalus. We will start with the airfoil design of the wing and explain some of the challenges encountered during design and how they were solved. Next, we will show why the Daedalus is so ideal for making long-duration flights and we end with a small word concerning its stability and control.

5.2.1 Airfoil Design

To understand why the wing is made up of different airfoil types, note that the wing is highly tapered, the ratio of the chord length at the tip to root (c_{tip}/c_{root}) being equal to 1/3. A tapered wing has aerodynamic and structural advantages as will be seen in Chapter 6. The result of this tapering is a large variation in the chord *Reynolds number* Re_c along the span of the wing (180 000 - 540 000), in which

$$Re_c = \frac{\rho v_\infty c}{\mu} \tag{5.17}$$

and where ρ and μ are respectively the density and dynamic viscosity of air, v_∞ the free-stream velocity and c the chord length of a section of the wing. At these low Reynolds numbers, the flow will remain laminar over a noticeable fraction of the airfoil. However, a peculiar phenomenon occurs during the transition from laminar to turbulent flow as illustrated in Figure 5.15. When the laminar boundary layer fails to withstand the adverse pressure gradient at some point around the airfoil, it will separate. The adverse pressure gradient is due to local deceleration of the flow around the airfoil, resulting in a local pressure buildup. Once detached, the laminar flow will become unstable and transition into turbulent flow. If the adverse pressure gradient is not too high, this turbulent flow can reattach and form a so-called *laminar separation bubble* (LSB). Associated with the LSB are mixing losses which increase with increasing bubble size. The Reynolds number will have an important effect on the transition phenomenon, in that the instabilities will grow less fast at lower Reynolds numbers, increasing the bubble size. So the challenge consists of designing a set of airfoils, optimized for different Reynolds numbers, which minimize the bubble losses and contain a large fraction of laminar flow for minimal drag.

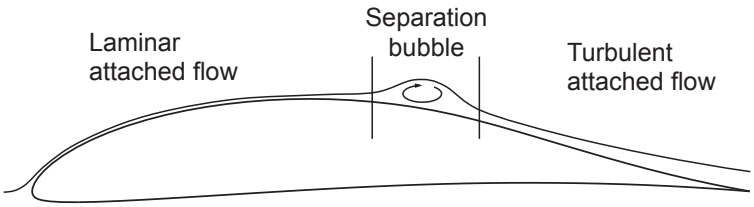

Figure 5.15: Laminar separation bubble [16]

For the Daedalus, a new set of airfoils were designed (DAE11, DAE21, DAE31) and optimized for a Reynolds number of respectively 500 000, 375 000 and 250 000 [17]. The strategy for minimizing the bubble losses was to destabilize the laminar boundary layer already before the actual point of separation. This resulted in a more rapid transition and hence a smaller LSB. To explain how the destabilization was done, consider Figure 5.16 showing the inviscid pressure distributions around the optimized airfoils at their design Re and lift coefficient. On the suction side, the destabilization resulted from the long but weak adverse pressure gradient (pressure buildup) after the leading edge. This region is denoted as the *transition ramp*. Note that the y-axis has been flipped in the figure and that the suction side corresponds with the upper parts of the pressure curves. Now, for decreasing Re, the basic design strategy was to increase the length of the transition ramp and to steepen the pressure curve near the end of destabilization [17, 18]. This compensates for the slower growth of instabilities and avoids long separation bubbles with high mixing losses. This strategy can be seen in Figure 5.16, also showing the corresponding airfoil shape. Concerning the pressure side, these were designed with only a small amount of loading, resulting in a nearly flat bottom surface of the airfoil. As such, the pressure side can be kept completely laminar and there is a reduction in the pitching moment of the airfoil. The main advantages of a lower pitching moment are the reduced loads acting on the wing, allowing a lighter wing structure and smaller tail surfaces [17–19].

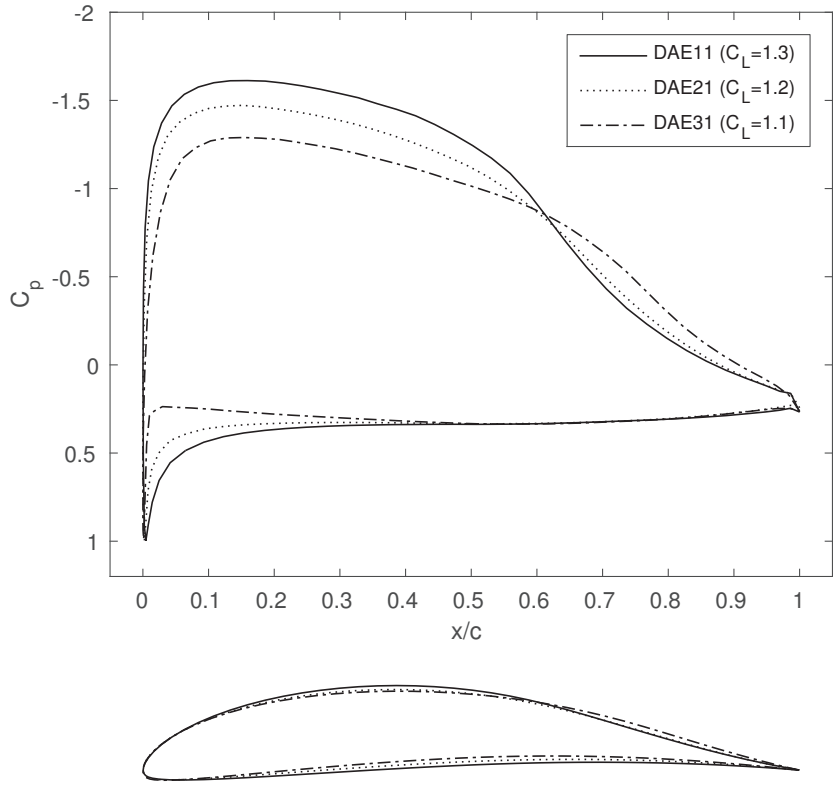

Figure 5.16: Design inviscid pressure distributions

5.2.2 Specific Power

To give an idea of the performance of the Daedalus compared with other HPAs, consider Figure 5.17 showing the specific power (W/kg pilot weight) as a function of flight speed. The Daedalus clearly shows the lowest aircraft specific power. Remarkable is that the Daedalus can fly at a higher speed compared to the Gossamer Albatross and requires less power. This is mainly due to its high aspect ratio (ratio of the wing's span to mean chord), being more than double compared to the Albatross [3]. As will be shown in Chapter 6, a larger aspect ratio is beneficial for reducing the induced drag. Further, only 55 ft (17 m) of external wire bracing was used compared to the 800 ft (244 m) of the Albatross, reducing the parasite drag. Other factors are improved surface quality and a slightly lower empty weight. All these measures resulted in the very low specific power, allowing to make long-duration flights.

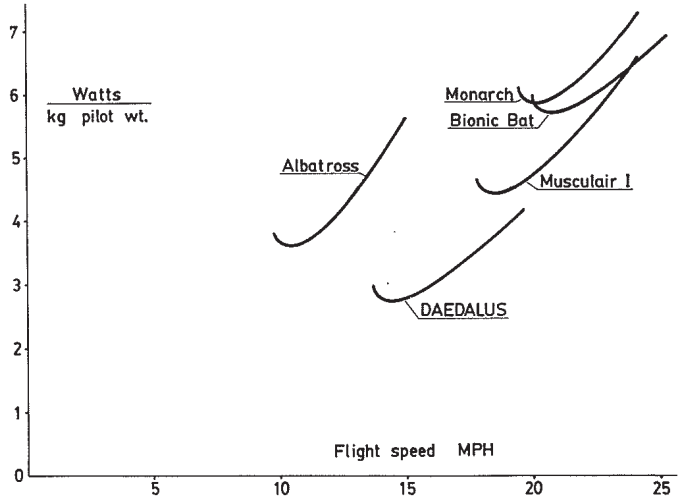

Figure 5.17: Specific power for various HPAs [3]

5.2.3 Stability

As seen in Section 5.1.3, the Daedalus has a conventional tail-aft configuration, found to give the lowest overall power requirement [3]. By proper design of the stab and the pilot's CG within the aircraft, the Daedalus was assured to have longitudinal static stability (Section 4.1.1) and outstanding pitch damping (Section 4.3.1). As such, the stab had to be trimmed only once during flight and required no further attention by the pilot. However, during one of the initial flight tests, the Daedalus experienced a bad spiral divergence (Section 4.3.2), resulting in quite some damage. The Daedalus was found to have insufficient dihedral at that time. Simply doubling of the dihedral appeared to give sufficient roll stability, avoiding any further occurrence of spiral divergence. This also explains the desired 2 m tip deflection. Although many more aspects were thoroughly investigated by MIT, it is quite clear that a tremendous amount of effort and time has been spent into designing the Daedalus, making it the most optimized design (both aerodynamically and structurally) up to date.

5.3 Lower-Order Analysis using VLM

As outlined, the major goal is to simulate the entire Daedalus in two different softwares. In this section, the Daedalus is analyzed using the Vortex Lattice Method. To do so, we will use the software *AVL* (Athena Vortex Lattice), which was developed by MIT and is publicly available [8]. It is however not possible to directly use the CAD model of the Daedalus into AVL, such that a new model will have to be created. The Daedalus will be simulated at its design flight velocity and in addition, its stability will be analyzed both static and dynamic.

5.3.1 AVL Model

The method of constructing the Daedalus in AVL is similar to the CAD model. For every aerodynamic structure (wing, fuselage, stab and rudder), a number of profile sections have to be defined which are then linearly interpolated. The profile sections are characterized by the type of airfoil, the position of the leading edge, the chord length and the incidence. In order to apply the Vortex Lattice Method, every aerodynamic structure must first be represented as a thin surface which can then be further divided into smaller elements as seen in Section 3.6. The thin surfaces are created by connecting the camber lines of the different sections, in which the camber line is formed by points located halfway between the pressure and suction side of the profile (Figure 5.18). For the AVL model, the same profile sections will be used as for the CAD model. In Figures 5.19, 5.20, 5.21 a comparison is made between the CAD and AVL model of the Daedalus. These models are seen to be nearly identical, except for the tailboom which is left out in the AVL model as it does not consist of profile sections.

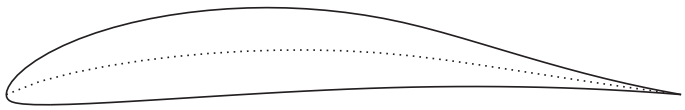

Figure 5.18: Camber line of a profile

To allow steering of the aircraft in AVL, a number of control surfaces will have to be defined. In case of the Daedalus, steering is accomplished by the all-moving stab and rudder. To define these surfaces as control surfaces, the hinge points should be specified together with the rotation axis. For the stab and rudder, the hinge points are taken along their spar and the entire surface is free to rotate about this spar. For the aircraft to be in equilibrium during straight level flight, the generated lift must equal its weight but also the pitching and yawing moment around its Center of Gravity must be zero. This is achieved by changing the angle of attack of the complete aircraft and by rotating the stab and rudder. Note that as the Daedalus was modelled as perfectly symmetric, no yawing moment will occur during straight level flight and as such no rotation of the rudder will be necessary.

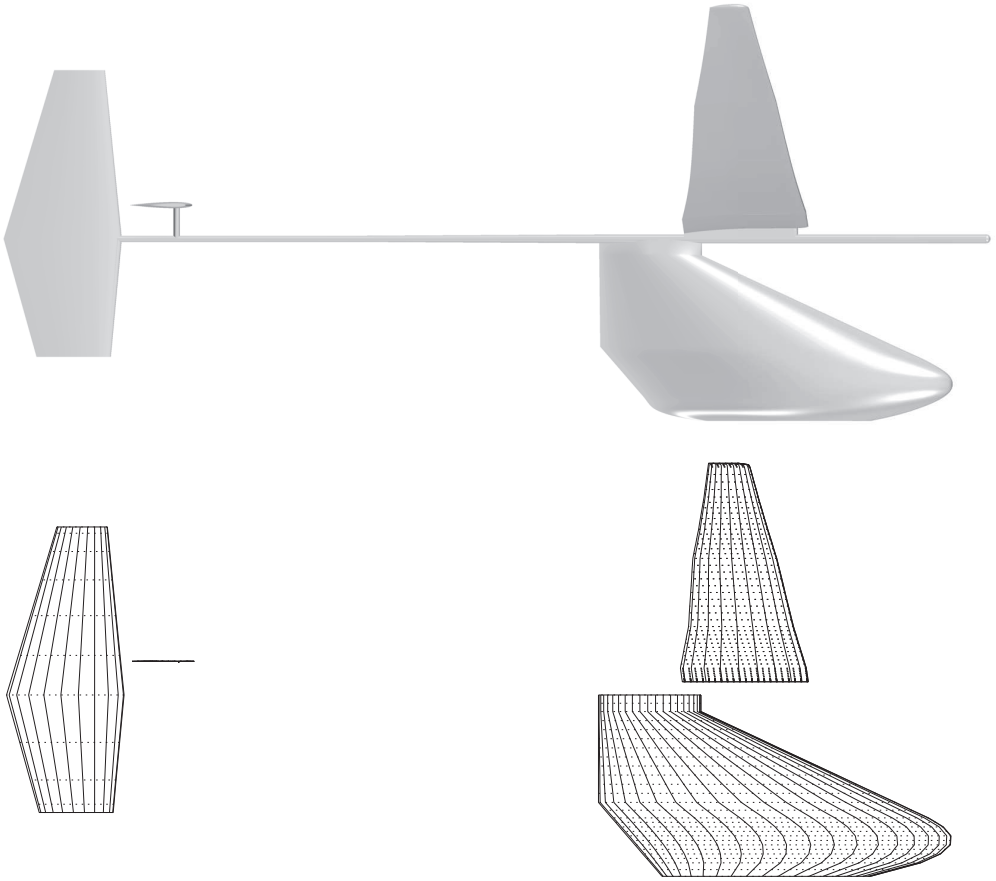

Figure 5.19: Comparison CAD and AVL model - side view

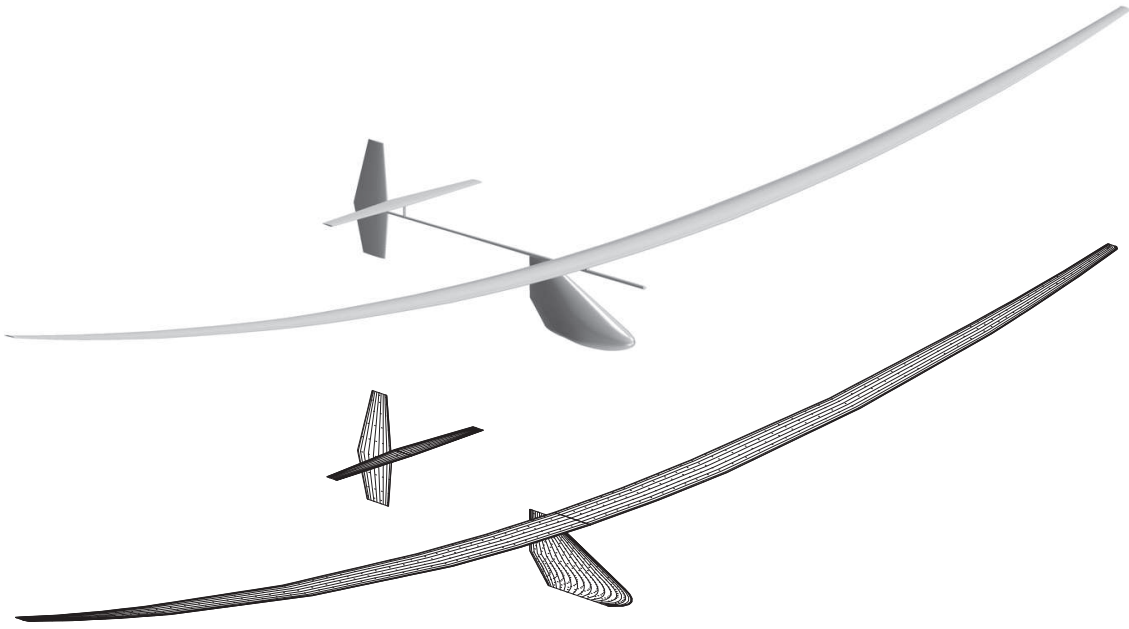

Figure 5.20: Comparison CAD and AVL model - general view

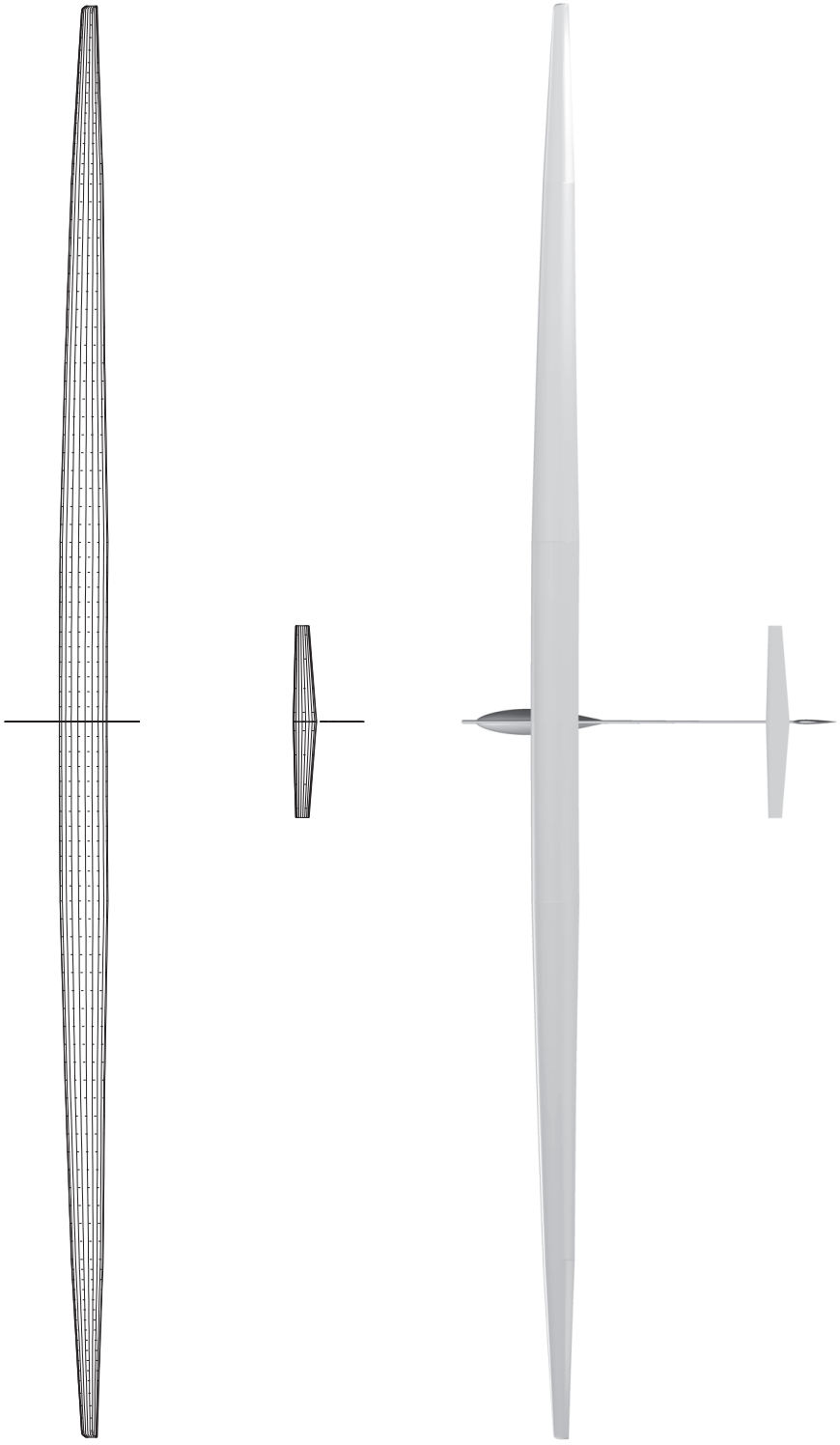

Figure 5.21: Comparison CAD and AVL model - top view

As seen in Chapter 3, applying the Vortex Lattice Method only allows to calculate the induced drag of the aircraft. However, the total drag of the aircraft consists of the induced, viscous and pressure drag. In order to take the viscous and pressure drag into account, AVL has the option to include the drag polar of every section used in defining the geometry of the aircraft. The drag polar is the relation between the drag coefficient C_D and lift coefficient C_L of a profile for different angles of attack. The drag and lift coefficients are defined as

$$C_D = \frac{D}{\frac{1}{2}\rho v^2 c} \tag{5.18}$$

$$C_L = \frac{L}{\frac{1}{2}\rho v^2 c} \tag{5.19}$$

where ρ is the density of air, v the free-stream velocity and c the chord length of the profile. This relation will be a function of the chord Reynolds number defined in (5.17). So, for a certain airfoil type and free-stream velocity, the drag polar will be different depending on the chord length. As the AVL model of the Daedalus contains a large number of sections, many of which have a different airfoil and chord length, a lot of drag polars will have to be determined. In order to generate a drag polar in just a few seconds, we will use the program *XFOIL*, developed at MIT and publicly available [20]. The program is based on boundary layer theory and is capable of simulating the low-Reynolds number phenomena discussed in Section 5.2.1. An example of a drag polar generated by XFOIL is shown in Figure 5.22, being the dotted line, in this case for the airfoil DAE11 at a Reynolds number of 500 000.

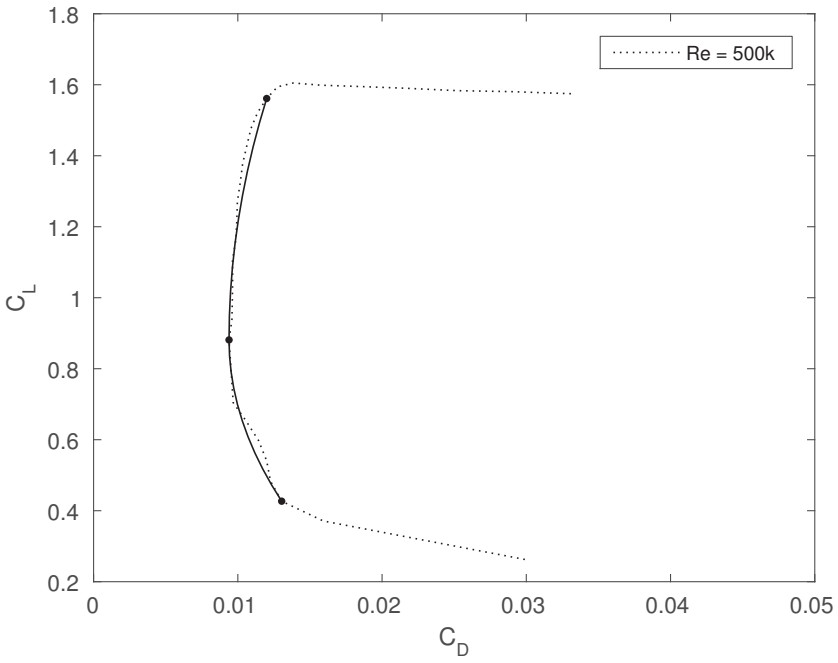

Figure 5.22: Drag polar of DAE11

However, to define this drag polar into AVL, three specific points should be determined; negative stall, minimal drag and positive stall. These three points are indicated in Figure 5.22 and should be given to AVL. Based on these points, AVL will now construct two parabolic curves, each starting in the point of minimal drag. As such, the actual drag polar is slightly approximated as shown. Concerning the points of negative and positive stall, these were mostly determined visually and sometimes slightly adjusted for a closer agreement with the actual drag polar. Figure 5.23 shows the influence of the Reynolds number on the drag polar for the airfoil DAE11. These drag polars, which will be stored in a database, can now be used to determine the drag polars at slightly different Reynolds numbers by linear interpolation of the three specific points. As such, we avoid having to generate a drag polar for every Reynolds number which will be useful in Chapter 6 when optimizing.

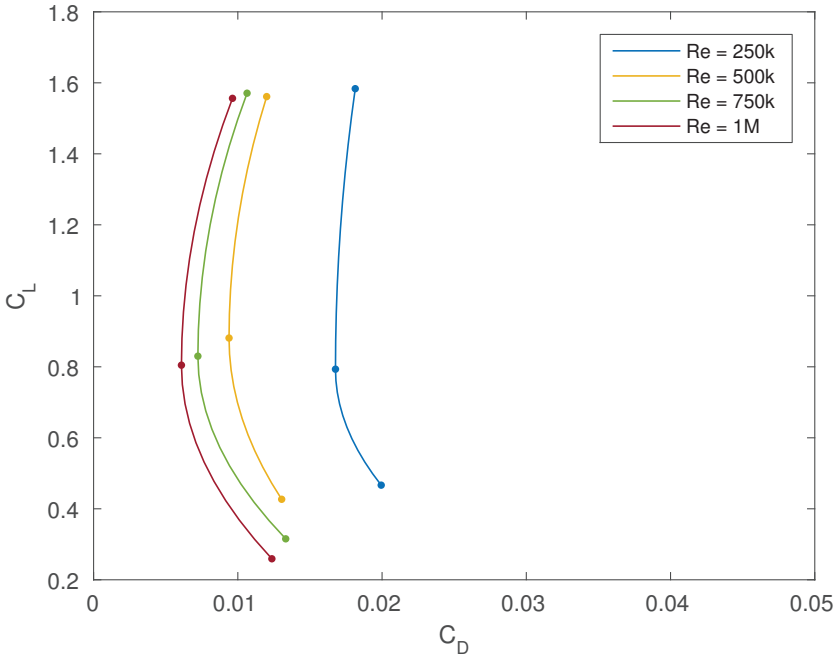

Figure 5.23: Drag polar of DAE11 for different Reynolds numbers

In order to determine the equilibrium position of the Daedalus at a certain flight velocity, its mass and Center of Gravity (CG) must be known. In Section 5.1, the mass, CG and inertia tensor of the different structures were determined and can now be given to AVL. Based on these individual structures, AVL will determine the total mass of the aircraft and its CG. To perform a dynamic stability analysis, the inertia tensor of the complete aircraft should also be known. This is obtained from the inertia tensors of the different structures.

The complete AVL model of the Daedalus, can be found in Appendix A.4 and is just a set of two txt-files, one for the geometry and one for the mass and inertia. These contain the appropriate data and in the correct format to be read-in by AVL.

5.3.2 Straight Level Flight

The simulation is performed at the design flight velocity of 15 mph (6.7 m/s), in which the Daedalus is found to fly at an angle of attack of 2.76 degrees in order to generate sufficient lift. Additionally, for the pitching moment to be zero, the stab is trimmed to a negative angle of -4.6 degrees. As expected, the angle of the rudder is found to be zero. Figure 5.24 visualizes the loading of the Daedalus in AVL. Note that the loading of the stab is pointed downwards as its angle with respect to the free-stream velocity is negative. Further note that as the fuselage and rudder are constructed of symmetric profiles, no lift or sideways force is being generated. These structures will only increase the drag of the aircraft, but are necessary for stability and to carry the pilot. At this equilibrium position, the total drag and its component can be calculated. As no propulsion is simulated in AVL, this total drag corresponds with the so-called gliding drag of the aircraft. The results are given in Table 5.7. For the different drag components listed, it is important to know that the induced drag and profile drag (viscous + pressure drag) only refer to the wing of the Daedalus and that the parasite drag is the difference between the gliding drag and the total drag of the wing. Based on the gliding drag and the propulsive efficiency, consisting of the mechanical and propeller efficiency, the corresponding pilot power can be determined. This is thus the actual power that the pilot will have to deliver to keep the aircraft up in the air.

	MIT [3]	**AVL Model**
Flight Velocity (m/s)	6.7	6.7
Gliding Drag (N)	27	22.2
Induced (N)	10.5 (35%)	11.2
Profile (N)	12.0 (40%)	9.7
Parasite (N)	4.5 (15%)	1.3
Lift (N)	1034.4	1034.4
Propulsive Efficiency	0.90	0.90
Pilot Power (W)	201	165
AoA Aircraft (°)	–	2.76
AoA Elevator (°)	–	-4.6
Calculation time	–	9.94 s

Table 5.7: Comparison estimated performance of the Daedalus

At this point a comparison can be made with the data from MIT, which is also included in Table 5.7. It is important to emphasize that the data from MIT are also estimates, but nevertheless they provide an idea of the actual drag and its components. Comparing the induced drag, AVL is found to predict a somewhat larger value (7%), but is still a reasonable prediction. However, comparing the profile and parasite drag, these are seen to be substantially underpredicted. In case of the profile drag, the underprediction is found to be 19%. Recall that AVL determines the profile drag based on the local lift coefficients of the

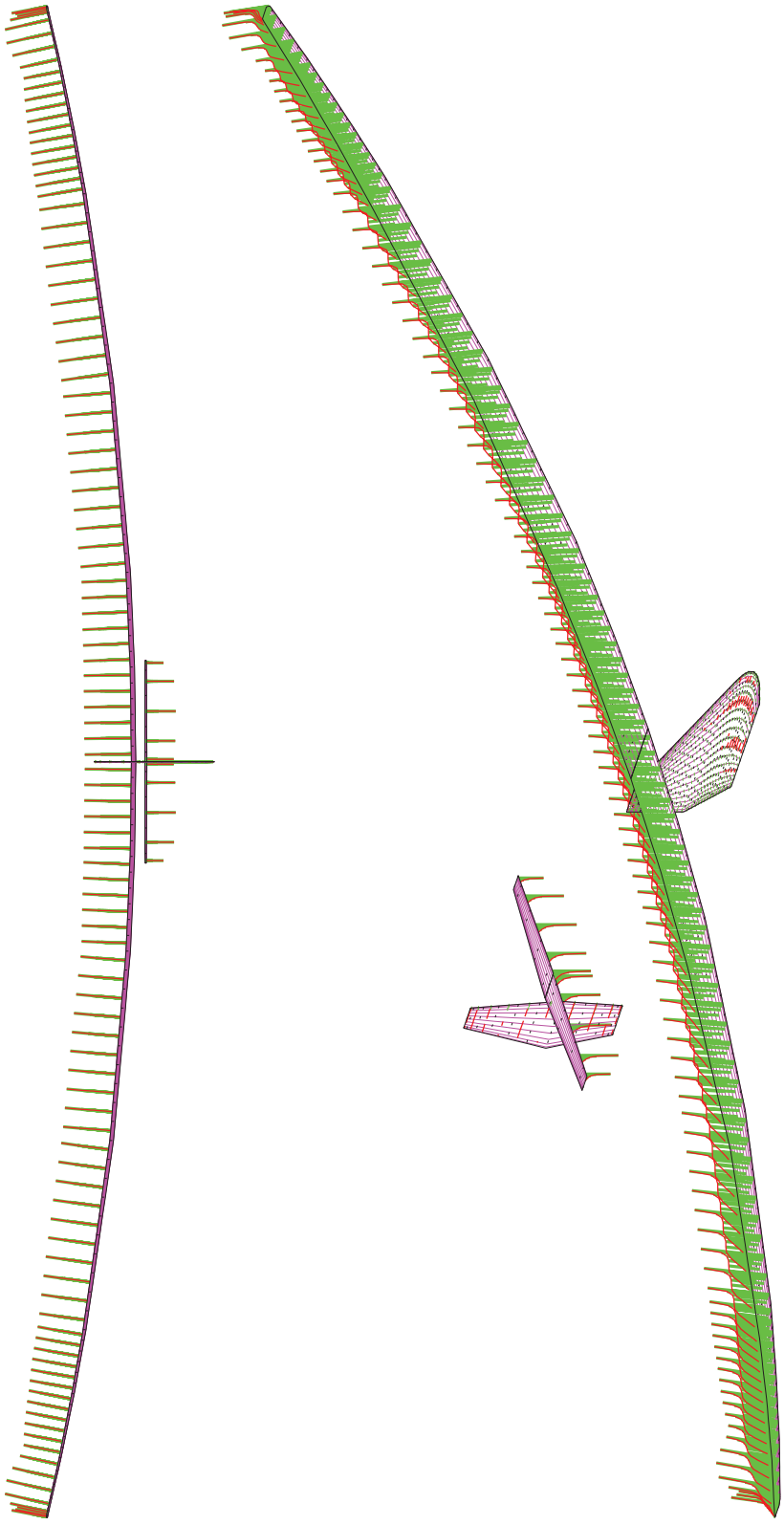

Figure 5.24: Loading of the Daedalus in AVL at design conditions

different sections and their corresponding drag polar. The lift coefficients are calculated by the Vortex Lattice Method, whereas the drag polars are generated by XFOIL. The accuracy of XFOIL's drag polars will be investigated in Section 5.4, such that we will wait with formulating conclusions.

5.3.3 Stability Analysis

In this section we will analyze the static and dynamic stability of the Daedalus in its previously determined equilibrium position. For the Daedalus to be statically stable, we must verify the conditions derived in Section 4.1. These conditions are repeated below

$$\frac{\mathrm{d}C_m}{\mathrm{d}\alpha} < 0 \tag{5.20}$$

$$\frac{\mathrm{d}C_n}{\mathrm{d}\beta} > 0 \tag{5.21}$$

$$\frac{\mathrm{d}C_l}{\mathrm{d}\beta} < 0 \tag{5.22}$$

and correspond to respectively longitudinal, directional and roll stability. Additionally we can verify if the aircraft's neutral point lays beyond its center of gravity

$$x_{CG} < x_{NP} \ . \tag{5.23}$$

The derivates are directly calculated by AVL together with the aircraft's neutral point and are given below.

$$\begin{aligned} \frac{\mathrm{d}C_m}{\mathrm{d}\alpha} &= -3.5164 \\ \frac{\mathrm{d}C_n}{\mathrm{d}\beta} &= 0.0042 \\ \frac{\mathrm{d}C_l}{\mathrm{d}\beta} &= -0.1922 \\ x_{NP} &= 0.5587 \text{ m} \\ x_{CG} &= 0.0431 \text{ m} \end{aligned} \tag{5.24}$$

Verifying all conditions, the Daedalus is found to be statically stable. A common way of quantifying the longitudinal static stability is by calculating the *static margin*

$$SM = \frac{x_{NP} - x_{CG}}{\overline{c}} \tag{5.25}$$

in which $\overline{c}$ is the wing's mean aerodynamic chord. In case of the Daedalus, the static margin is found to be 57%. The lower limit is usually taken as 5% [9], such that the Daedalus is definitely longitudinal statically stable.

Concerning the dynamic stability, as explained in Section 4.2 the Vortex Lattice Method easily allows to calculate the stability derivatives occurring in the linearized equations of motion (4.35),(4.36). As such, AVL is also capable of determining the aircraft's modes of motion. Figure 5.25 shows the root locus plot of the Daedalus generated by AVL and in Table 5.8 the different modes are listed together with the corresponding eigenvalue, period and damping ratio.

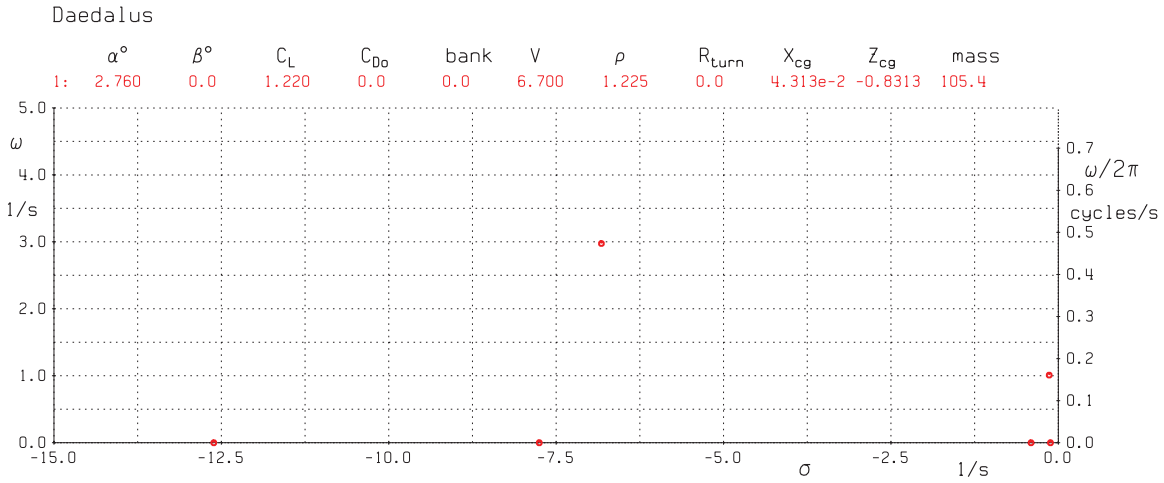

Figure 5.25: Root locus plot - Daedalus at design equilibrium position

The short-period mode is indeed heavily damped with a period of 2.11 s, while the phugoid mode is only lightly damped and has a larger period. The Daedalus was said to be spirally stable (assured by the 2 m tip deflection), which is indeed confirmed by the negative spiral eigenvalue. However, no Dutch Roll mode was present, the reason is still unclear.

Mode	Eigenvalue	Period (s)	Damping Ratio
Short-Period	$-6.82 \pm j2.98$	2.11	0.92
Phugoid	$-0.14 \pm j1.01$	6.22	0.13
Spiral	-0.116	–	–
Roll Damping	-12.61	–	–
Dutch Roll	–	–	–

Table 5.8: Modes of motion - Daedalus at design equilibrium position

5.4 Higher-Order Analysis using CFD

For the second simulation of the Daedalus, we will use the Computational Fluid Dynamics (CFD) software STAR-CCM+. This software will solve the Reynolds-Averaged Navier-Stokes (RANS) equations based on the finite volume method. To investigate the accuracy of the CFD software, some 2D simulations of an airfoil will be performed first and compared with experimental data. The Daedalus will be analyzed in a final simulation, which will also allow to formulate a small conclusion concerning the capabilities and accuracy of the softwares AVL and STAR-CCM+.

5.4.1 2D Simulation of the FX63-137

To simulate the laminar-turbulent transition process in CFD, two models will be used; the k-ω SST turbulence model and the γ-Re$_\theta$ transition model. We will mainly focus on the results of the CFD simulations, but for a better understanding, the concept of both models is now briefly explained. The k-ω SST model actually combines two models, the k-ϵ and k-ω model, using two blending functions. The k-ϵ model is used for free-stream calculations whereas the k-ω model is used in near wall regions. Each model uses two extra transport equations, containing the turbulent properties of the flow, needed to solve the RANS equations. In case of the k-ϵ model, the two variables are the turbulent kinetic energy k and the turbulent dissipation rate ϵ. For the k-ω model, the specific rate of dissipation ω is used instead of ϵ. To predict the onset of transition laminar-turbulent, the γ-Re$_\theta$ transition model is run on top of the k-ω SST model in STAR-CCM+. The γ-Re$_\theta$ model is a correlation-based transition model which also uses two extra transport equations, one for intermittency γ and one for the local transition onset momentum thickness Reynolds number Re$_{\theta_t}$. The intermittency is the fraction of time the boundary layer is turbulent in transitional flow. When the local momentum thickness Reynolds number Re$_\theta$ now exceeds a critical value Re$_{\theta_c}$, the intermittency production is switched on, which will generate turbulent kinetic energy.

The investigated airfoil is the FX63-137, specifically designed for low Reynolds numbers and used in some early HPA designs. For the 2D simulations, a circular fluid domain is considered, with a radius of 50 chord lengths and the airfoil located in the center. The outer boundary is cut at $+45$ and -45 degrees starting from the trailing-edge side, allowing to define a velocity inlet and a pressure outlet as schematically illustrated in Figure 5.26. The fluid domain is now discretized, in which we will compare two different meshes. The first mesh is a structured mesh generated in GAMBIT, whereas the second mesh is generated in STAR-CCM+ and is actually derived from a 3D mesh. More specifically, using the trimmed hexahedral mesher of STAR-CCM+, a 3D mesh is first constructed around a wing. This wing has a chord length of unity and is made up of the airfoil FX63-137. By now considering a specific section of this 3D mesh, the 2D mesh is obtained. The advantage of this 2D mesh, is that it will allow to directly evaluate the quality of the 3D mesh. This is useful as a trimmed hexahedral mesh will later on be constructed around the complete Daedalus. In Figures 5.27, 5.28, 5.29 a comparison is made between both meshes. At first they might look

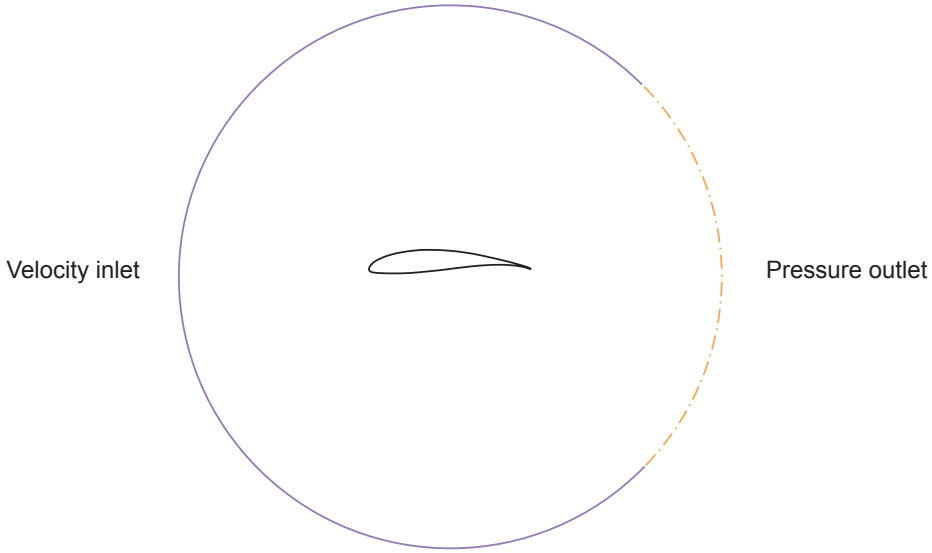

Figure 5.26: Boundary conditions on circular fluid domain [21]

completely different, but when zooming-in, both meshes are seen to have a nearly identical boundary layer mesh around the profile. In order to explore the full capability of the γ-Re$_\theta$ transition model, the boundary layer meshes were constructed extremely fine and consist of a 30-layer, 30 mm thick inflation layer. The first cell height is 0.01 mm, assuring a $y^+ < 1$, which is needed in order to properly resolve the boundary layer. To determine the precise location of transition, a chordwise spacing of 1 mm is applied. Comparing the meshes at the trailing edge, it is clear that the structured mesh will be more suited for capturing the wake of the profile. To see if this has a noticeable effect on the lift and drag of the profile, we will have to wait for the results. The structured mesh consists of 169 000 cells and the cartesian mesh (STAR-CCM+) of 93 000 cells. All simulations will be performed at a Reynolds number of 500 000. The flow is further modeled as incompressible, justified by the very low Mach numbers of HPAs and additionally, the turbulent intensity is set to 0.07% together with a turbulent viscosity ratio of 10.

The results of the two-dimensional CFD simulations performed on the structured mesh can be seen in Figures 5.30 and 5.31. In addition to the experimental data from wind tunnel tests performed at UIUC (University of Illinois at Urbana-Champaign) and the CFD simulations using the γ-Re$_\theta$ transition model, results have been added of CFD simulations using the k-ω SST turbulence model without transition together with the results of the panel code XFOIL. The 2D CFD simulations were performed transient, in which the solution was found to be steady after approximately 10 s in all of the cases considered. The time step was taken as 0.01 s.

Figure 5.30a shows the lift coefficient C_L versus the angle of attack α. The CFD simulations using the transition model are seen to agree the closest with the experimental data and show a slight overprediction for positive angles of attack. The results of CFD without transition

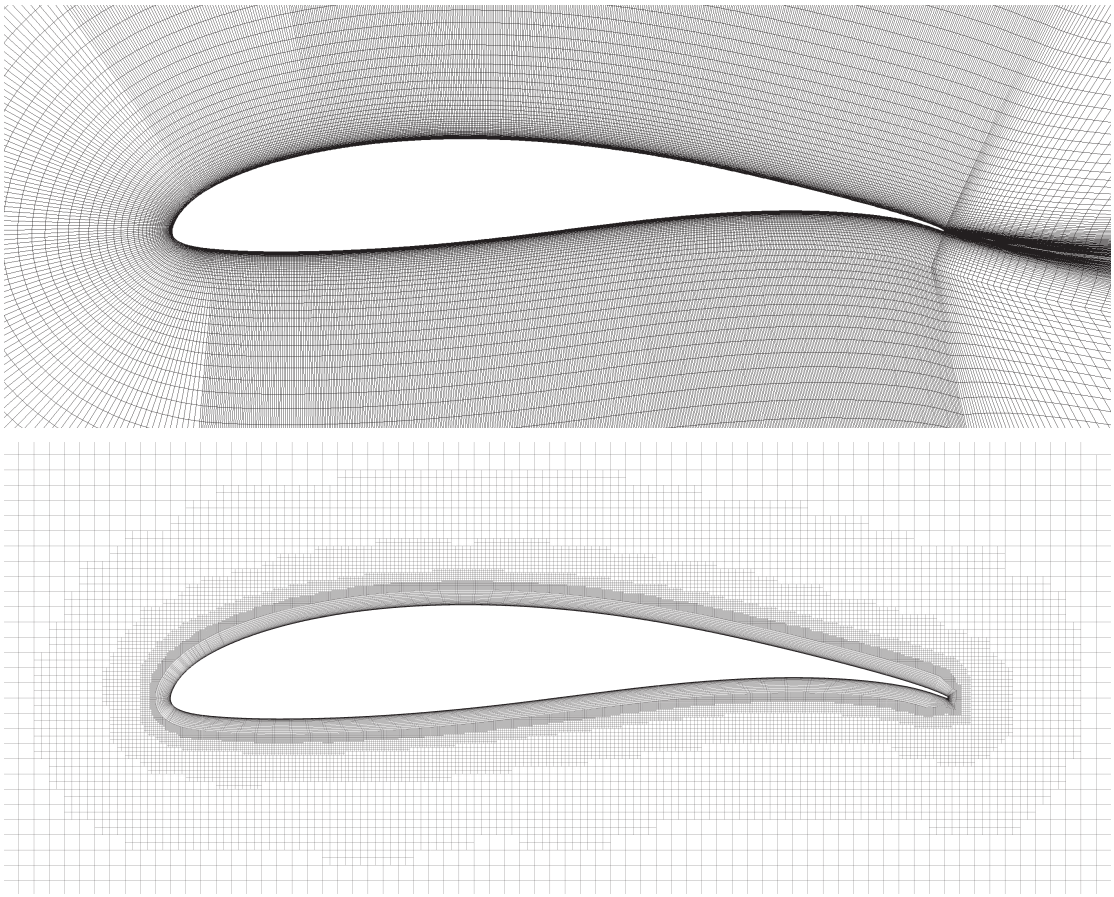

Figure 5.27: Comparison mesh (top: structured, bottom: cartesian)

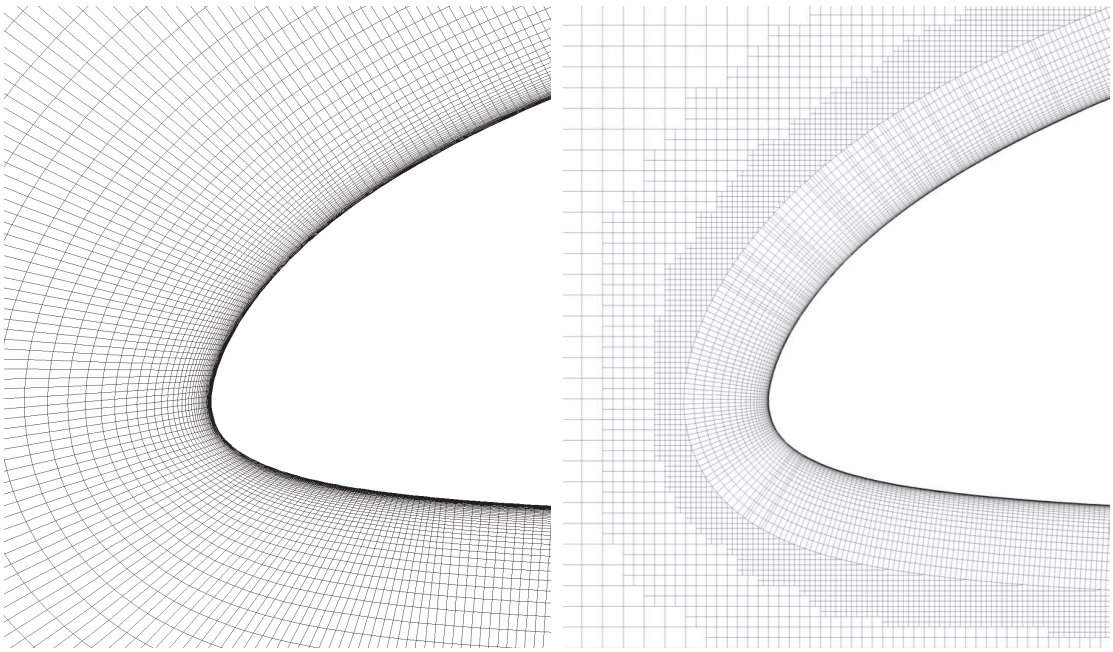

Figure 5.28: Comparison mesh at leading edge (left: structured, right: cartesian)

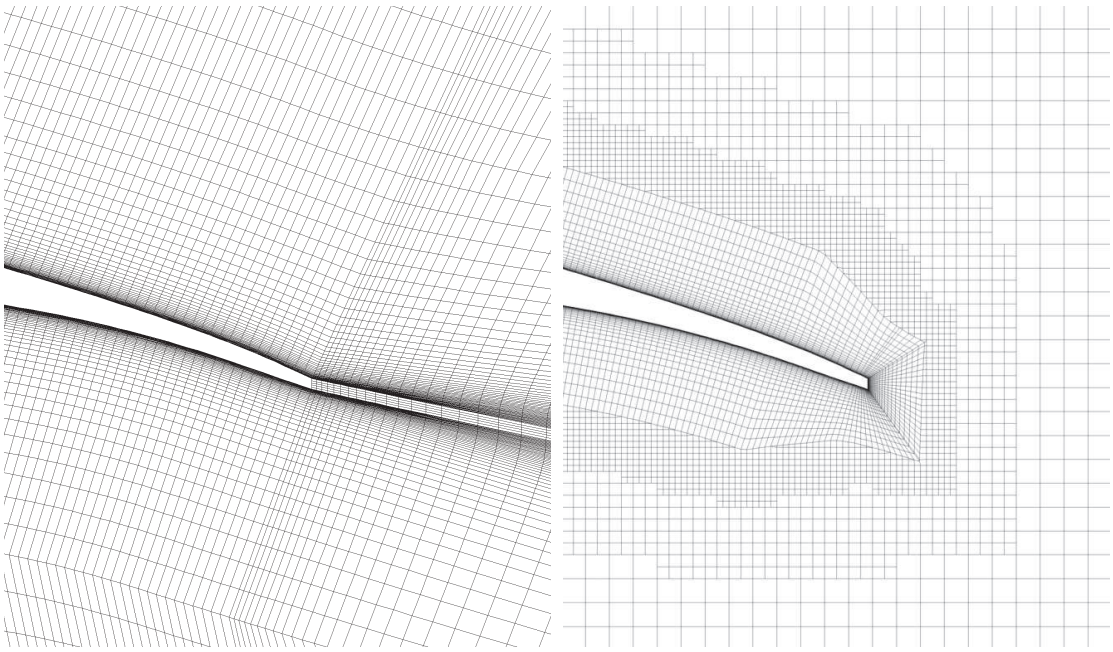

Figure 5.29: Comparison mesh at trailing edge (left: structured, right: cartesian)

and XFOIL are seen to respectively underestimate and overestimate the lift for all angles of attack considered. Further, in Figure 5.30b, the drag coefficient C_D is shown as a function of the angle of attack. CFD with transition and XFOIL show a comparable accuracy, in which CFD with transition is found to be slightly more accurate for angles of attack between 0 and 6 degrees while XFOIL is slightly more accurate beyond this range. Note that there is a consistent overprediction by CFD with transition and underprediction by XFOIL. Neglecting the transition phenomenon results in a heavy overprediction of the drag. For positive angles of attack, this overprediction is found to be more than 50%. It is clear that the Daedalus will have to be simulated using a transition model, in order to obtain accurate results. Using the previous two figures, the drag polar can now be constructed which is shown in Figure 5.31a. CFD with transition is seen to agree extremely well with the experimental data, especially for positive angles of attack. Due to the consistent overprediction of the lift and underprediction of the drag made by XFOIL, the corresponding drag polar is seen to have the same shape as the experimental data, but is shifted upwards. For positive angles of attack, this leads to an underestimation of the drag coefficient as a function of the lift coefficient. As an example, for a lift coefficient of 1.4, the underprediction with respect to the experimental data is found to be 14%. This observation here partly explains the underprediction of the profile drag seen in the AVL model (Section 5.3.2). Although the airfoil FX63-137 was not specifically used to construct the Daedalus, this underprediction is also observed in similar work for different airfoils [16, 22]. As such, the underprediction was to be expected. Figure 5.31b shows the lift-to-drag ratio versus the angle of attack. CFD with transition is seen to agree very well but predicts a slightly lower maximal value of L/D.

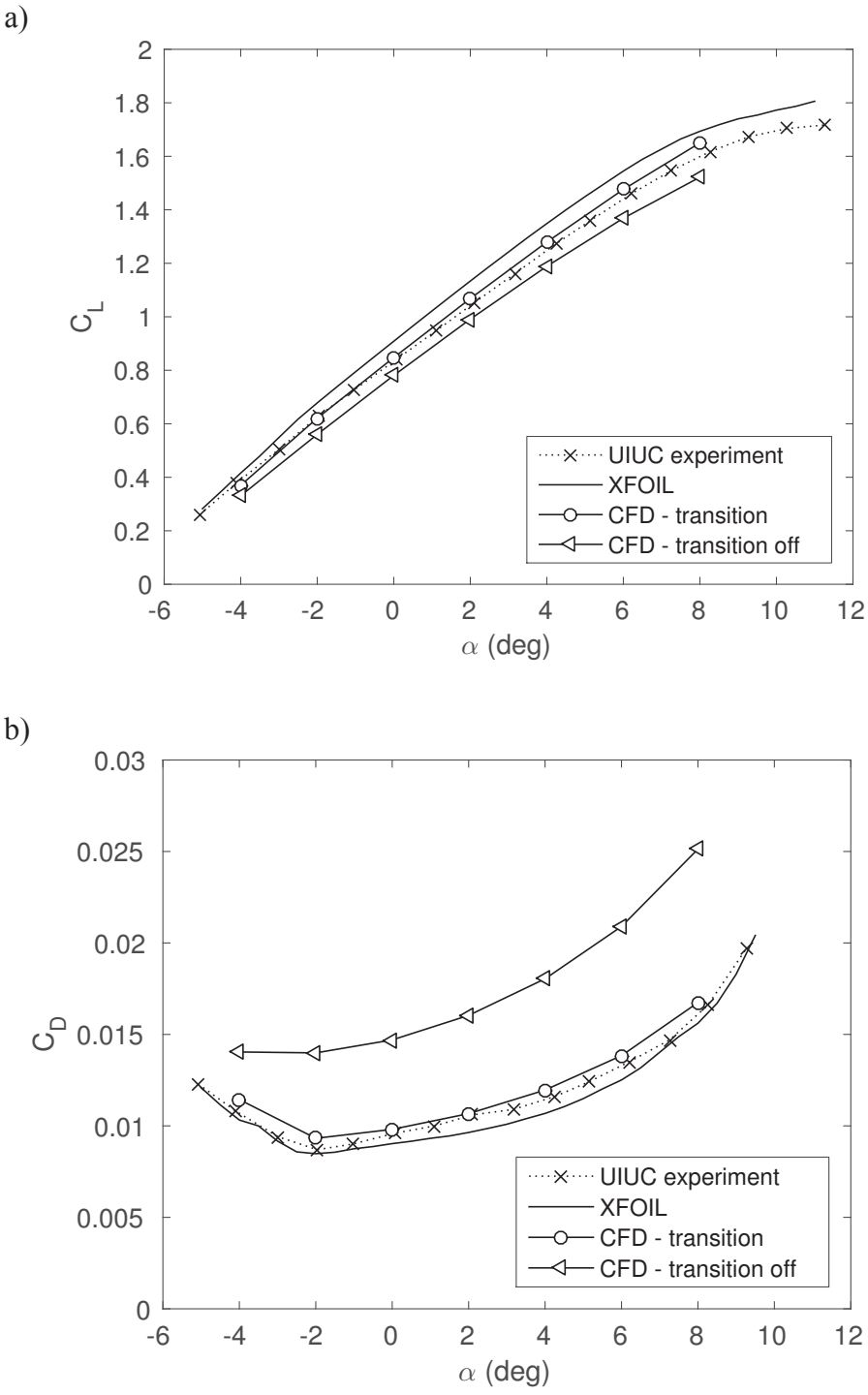

Figure 5.30: Two dimensional results of the airfoil FX63-137; (**a**) lift coefficient versus angle of attack, (**b**) drag coefficient versus angle of attack.

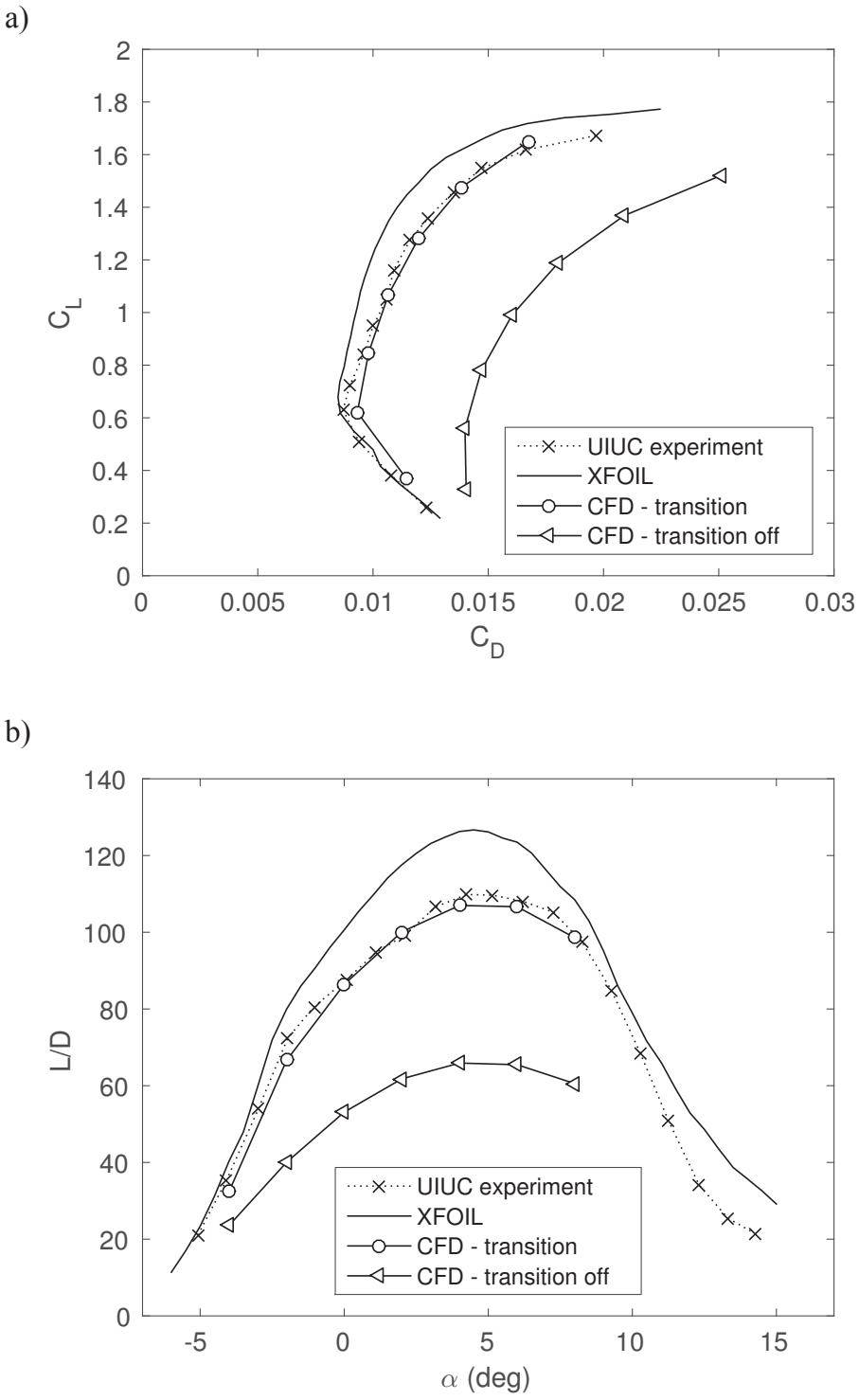

Figure 5.31: Two dimensional results of the airfoil FX63-137; (**a**) drag polar, (**b**) lift-to-drag ratio versus angle of attack.

In Figure 5.32a, the pressure coefficient C_p around the airfoil is given at zero degrees angle of attack. The pressure distributions predicted by CFD with transition and XFOIL clearly show the presence of a laminar separation bubble on both the suction and pressure side of the airfoil. When comparing the enclosed surfaces of the different pressure distributions, a clear difference is observed. XFOIL is seen to have the largest enclosed surface, followed by CFD with transition and CFD without transition. However, this observation is in agreement with the lift predictions at zero degrees angle of attack shown in Figure 5.30a. To see the key difference between the two CFD models, consider Figure 5.32b, showing the turbulent kinetic energy around the airfoil. In CFD without transition (upper airfoil), the production of turbulent kinetic energy is directly initiated at the leading edge of the airfoil and increases towards the trailing edge. In CFD with transition (lower airfoil), the production is only initiated after the laminar flow has locally detached (Figure 5.15). From the moment the detached flow becomes sufficiently turbulent, it will reattach, corresponding with a peak in turbulent kinetic energy.

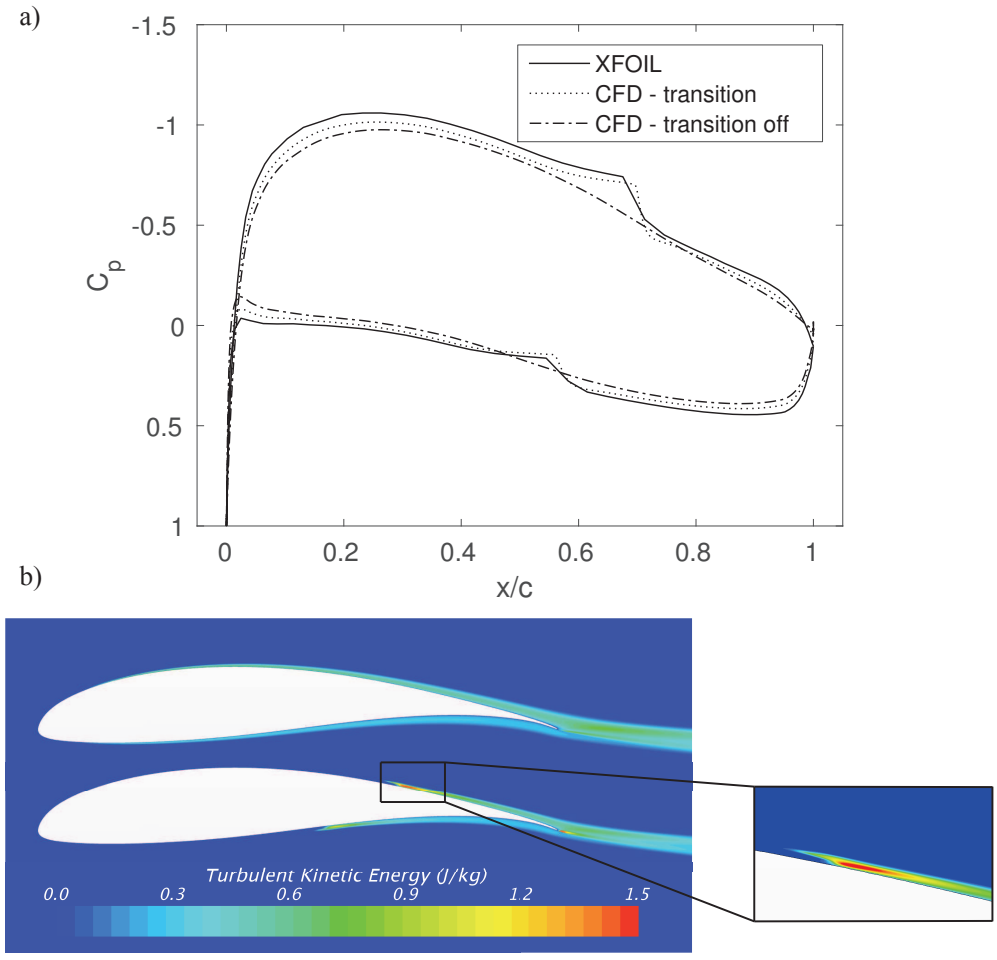

Figure 5.32: Two dimensional results of the airfoil FX63-137; (**a**) pressure coefficient distribution at zero degrees angle of attack, (**b**) turbulent kinetic energy (upper airfoil: CFD - transition off, lower airfoil: CFD - transition)

In Figure 5.33, the influence of the angle of attack on the turbulent kinetic energy around the airfoil is shown for both CDF models. Note how in the case of CFD with transition, the reattachment point on the pressure and suction side of the airfoil moves towards respectively the trailing and leading edge as the angle of attack increases. The pressure side is seen to be fully laminar for an angle of attack of 8 degrees.

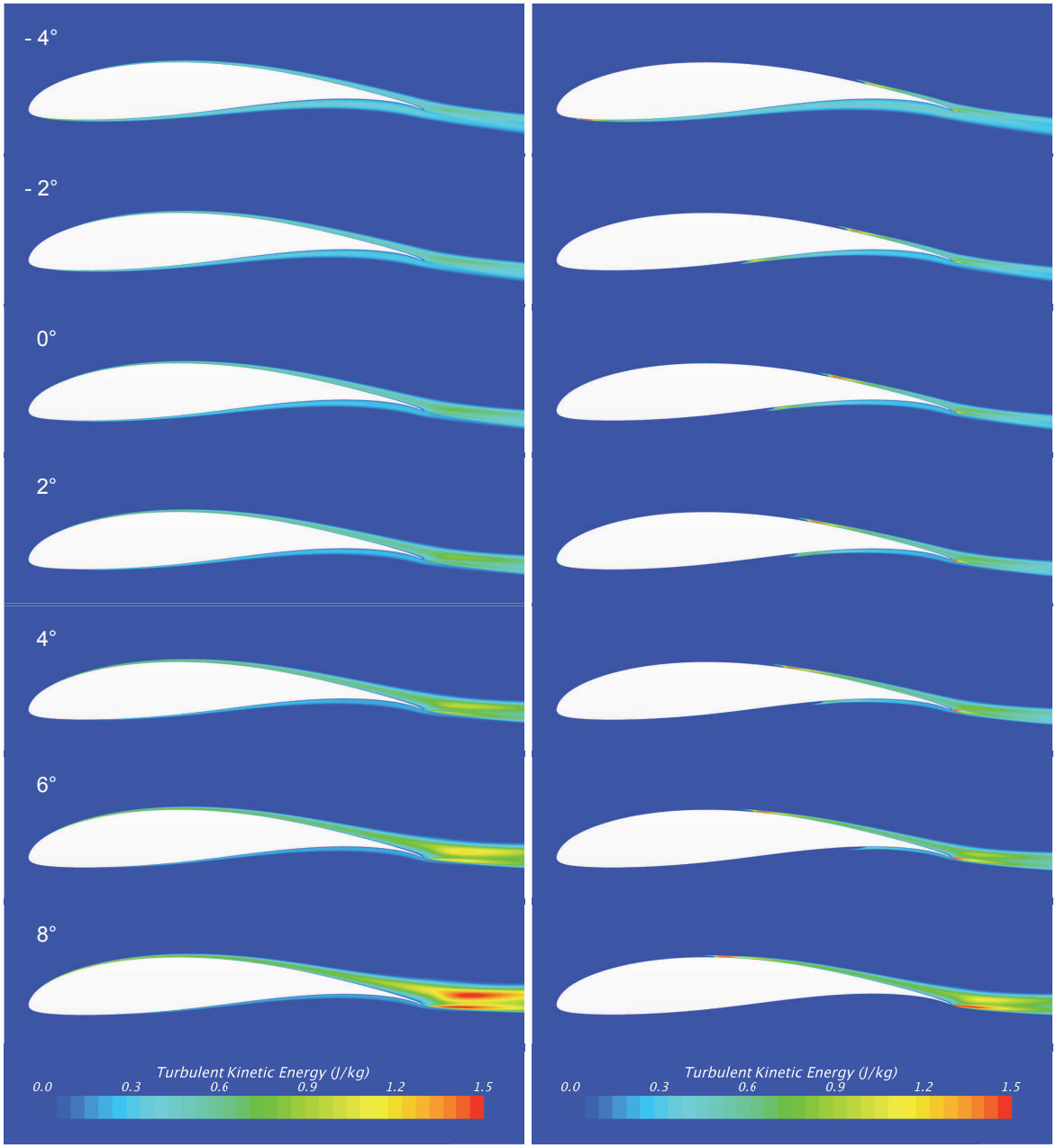

Figure 5.33: TKE as a function of the angle of attack (left: CFD - no transition, right: CFD - transition)

Finally, Figure 5.34 shows the comparison between the drag polars obtained with the structured mesh (GAMBIT) and the cartesian mesh (STAR-CCM+), using the transition model. The drag polar of the cartesian mesh is seen to be shifted slightly to the right, predicting a slightly higher drag but the lift is identical. The trimmed hexahedral mesher of STAR-CCM+ has the major advantage of being highly automated, such that with little effort, a wide variety of geometries can be meshed and solved. Although the mesh is somewhat less capable of capturing the wake, it produces accurate results and as such, the trimmed hexahedral mesher is definitely a good option for the Daedalus.

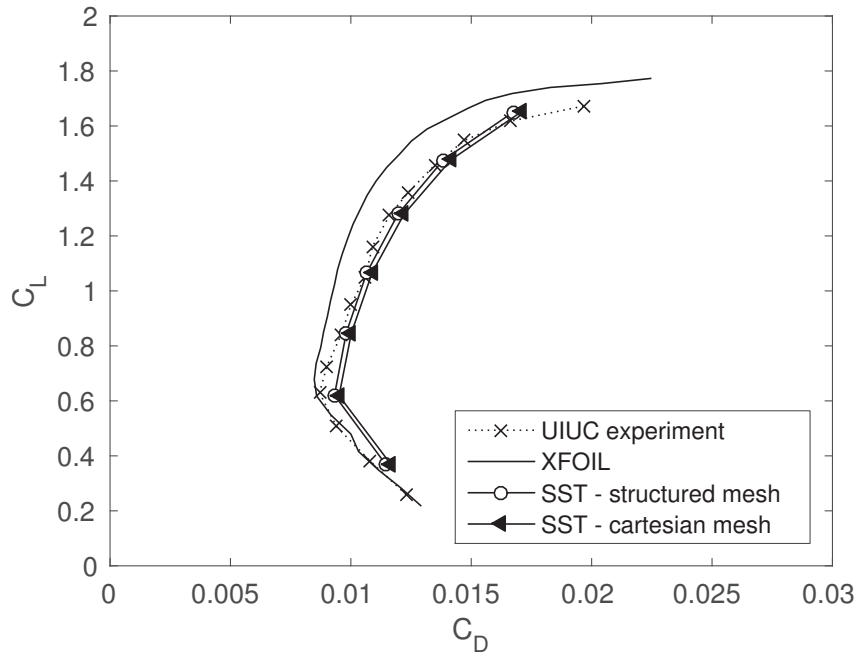

Figure 5.34: Comparison drag polar of structured and cartesian mesh

5.4.2 3D Simulation of the Daedalus

The objective of this section is to simulate the entire Daedalus in CFD. However, using its symmetry, half of the aircraft will be sufficient. For this simulation, the fluid domain is constructed as a half-sphere with a radius of 100 m. The outer boundary is split in a velocity inlet, a pressure outlet and a symmetry plane as illustrated in Figure 5.35. Using the trimmed hexahedral mesher of STAR-CCM+, the complete fluid domain is discretized which can be seen in Figure 5.36.

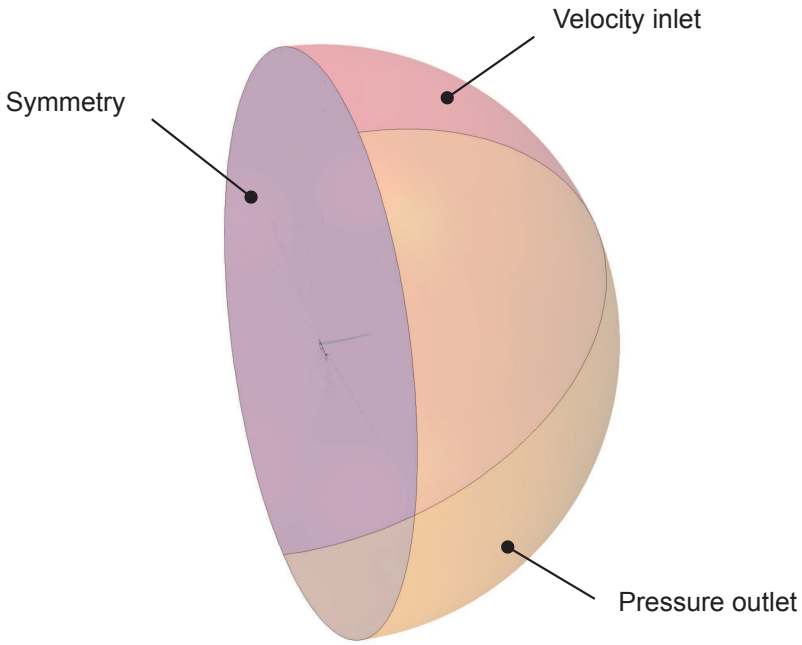

Figure 5.35: Boundary conditions of 3D fluid domain [21]

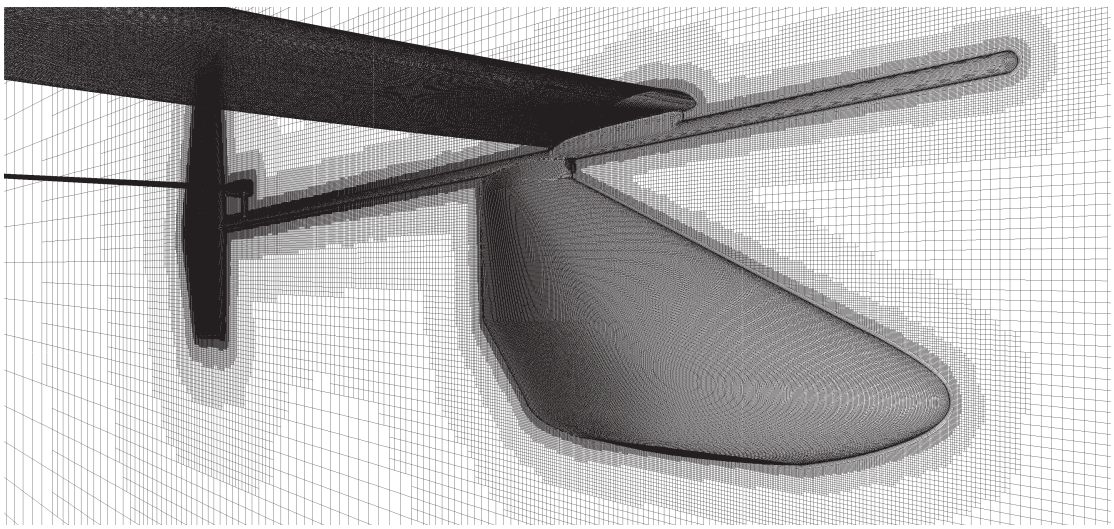

Figure 5.36: Trimmed hexahedral mesh around the Daedalus

The boundary layer mesh is somewhat coarser here, to limit the total number of cells. It consists of a 15-layer, 20 mm thick inflation layer, in which the maximal edge size of the elements on the geometry is 5 mm. Although the boundary layer mesh has been substantially coarsened, the complete 3D mesh still contains 52 million cells. To prove that the boundary layer mesh still provides sufficient accuracy, we can generate a second cartesian mesh applying the coarser boundary layer mesh settings and determine the corresponding drag polar. Recall that the cartesian mesh is generated by the trimmed hexahedral mesher of STAR-CCM+. The resulting drag polar can then be compared with the results of the extremely fine cartesian mesh of Section 5.4.1. Both drag polars are shown in Figure 5.37 and were determined using the transition model. The drag predicted by the coarser cartesian mesh is seen to be only slightly larger, but is definitely acceptable.

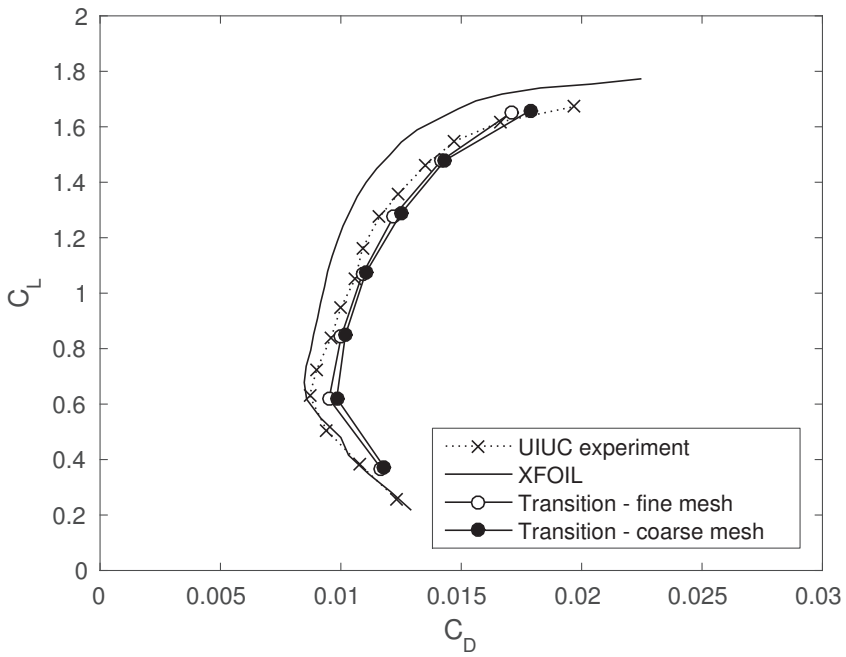

Figure 5.37: Comparison drag polar of FX63-137 with an extremely fine and coarser boundary layer mesh

The CFD simulation of the Daedalus was performed steady in which its configuration was adjusted to be identical as in AVL. As such, the angle of attack of the aircraft and elevator were the same in both simulations. The results of the CFD simulation can be found in Table 5.9. The generated lift is seen to agree extremely well, such that the Daedalus is also in equilibrium in the CFD simulation. Comparing the total drag of the wing, being 23.7 N in the CFD simulation versus 22.5 N estimated by MIT, the value is seen to agree within 5%. Note that 90% of the gliding drag is due to the wing. As for the AVL simulation, the parasite drag is strongly underpredicted. However, some simplifications were made to both models of the Daedalus, resulting in a somewhat lower parasite drag. In both models, the external lift wires of the Daedalus (Figure 5.38) were not included and the fuselage was made slightly more aerodynamic. In reality, the fuselage contained a ventilation opening to

Figure 5.38: Lift wires of the Daedalus

draw in air for the pilot and had an additional structure mounted on its nose to drive the propeller (can be seen in Figure 5.9). Recall that in the AVL model, also the tailboom is left out. Comparing the pilot power, the CFD simulation is seen to agree within 3% with the value of MIT. So, although there is a slight overprediction of the total drag of the wing and a noticeable underprediction of the parasite drag, the CFD simulation provides a very reasonable estimate of the pilot power.

	MIT [3]	**AVL Model**	**CFD Model**
Flight Velocity (m/s)	6.7	6.7	6.7
Gliding Drag (N)	27	22.2	26.2
Induced (N)	10.5 (35%)	11.2	–
Profile (N)	12.0 (40%)	9.7	–
Parasite (N)	4.5 (15%)	1.3	2.5
Lift (N)	1034.4	1034.4	1034.8
Propulsive Efficiency	0.90	0.90	0.90
Pilot Power (W)	201	165	195
AoA Aircraft (°)	–	2.76	2.76
AoA Elevator (°)	–	-4.6	-4.6
Calculation time	–	9.94 s	1 day

Table 5.9: Comparison estimated performance of the Daedalus

In Figure 5.39, the turbulent kinetic energy is shown close to the surface of the Daedalus together with the constrained streamlines. These help in visualizing the laminar separation bubble. At the position were the streamlines seem to be halted for the first time, the flow locally detaches and at the position of peak turbulent kinetic energy, the flow reattaches. The size of the laminar separation bubble on the wing is seen to be approximately constant along its span, except near to the wingtip. Note that the pressure side of the wing is completely laminar. The flow around the rudder is clearly influenced by the wake of the wing, in which the midsection is seen to be fully turbulent, whereas the upper section is largely laminar with transition occuring near the trailing edge.

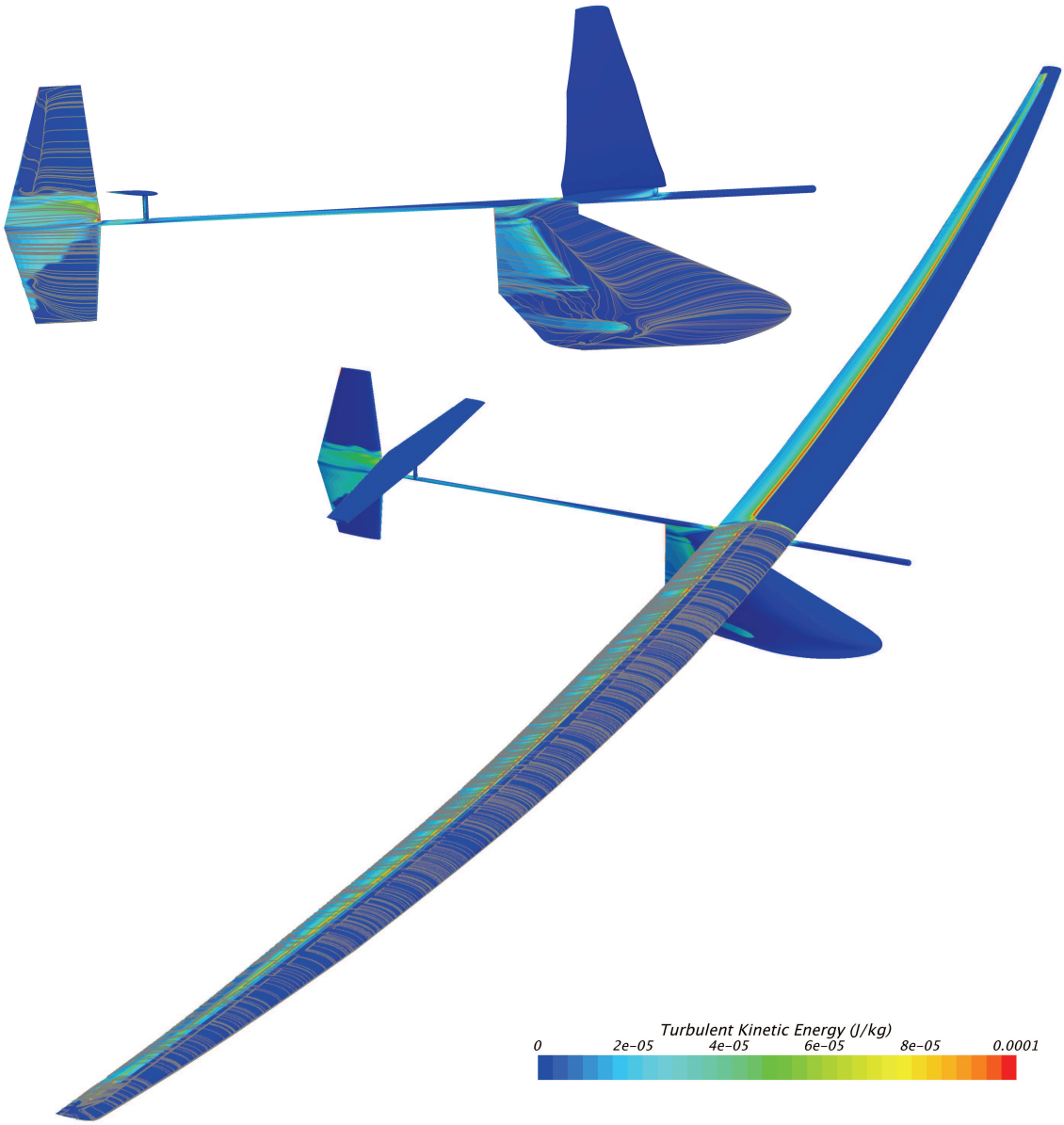

Figure 5.39: Transition laminar-turbulent on the Daedalus visualized by the constrained streamlines and the turbulent kinetic energy

For the intended optimization of our own HPA, it is interesting to compare the calculation time of both simulations (Table 5.9). It is clear that AVL will be an ideal tool for evaluating a lot of different designs. To conclude, the CFD simulation was seen to predict the pilot power very accurately, but needs a large amount of computational power and time for a single simulation. On the other hand, the AVL simulation was found to underpredict the pilot power by about 18%, in which the underprediction was partly attributed to the drag polars of XFOIL. However, the power of AVL lays in its very short calculation times which is essential when optimizing and as all designs will be evaluated in the same softwares (XFOIL and AVL), a fair comparison can be made.

Chapter 6

FSI Optimization

In this chapter it is attempted to design and optimize a HPA capable of winning the prestigious Kremer International Marathon Competition (Section 2.8.1). A special feature of our design will be the possibility of adding a second pilot on board of the aircraft. As such, it will be investigated if powering a HPA by two pilots offers some advantages compared to a single pilot. In the analysis of the Daedalus it was shown that the drag of the wing is the main contributor (around 90%) to the aircraft's total drag. Given this fact, the first step in designing our HPA will consist of optimizing a wing. In a second step, a complete HPA is constructed using the optimized wing. Depending on the results of the optimization, this wing could be for a single- or dual-pilot design. In the final step, the optimized HPA is simulated in STAR-CCM+ allowing to estimate the human power needed to complete the Kremer International Marathon Course within time.

6.1 Optimization of a Wing

As the structural deflection of the wing during flight is found to be a key aspect in the design, Fluid-Structure Interaction (FSI) simulations are performed coupling AVL and MATLAB. These FSI simulations will be included in the optimization procedure, which is explained first. Two optimization cases will be defined, corresponding to a single- and dual-pilot design. However, before analyzing the results of these two cases, we will have a closer look at the FSI simulations. Additionally, a sensitivity study is performed, showing the influence of the different design variables on the aerodynamic performance of the wing.

6.1.1 Optimization Procedure

The outer geometry of a wing will be parameterized allowing to generate any wing geometry. However, not every wing geometry will be structurally feasible with regard to strength and desired deformation. By performing FSI simulations it is possible to determine the material stresses and deformation of the wing during flight. These stresses and deformation will entirely depend upon the wing's structural parameters as the flight conditions will be kept constant. So it must be verified if a set of structural parameters can be found, which result in allowable material stresses and a certain design tip deflection. This design tip deflection is mostly determined from stability requirements (Section 5.2.3). As can be expected, in most cases multiple feasible sets will exist. So the challenge is to find a feasible set, which in addition minimizes the mass of the wing. This structural optimization procedure is schematically shown in Figure 6.1 and will now be explained in some more detail.

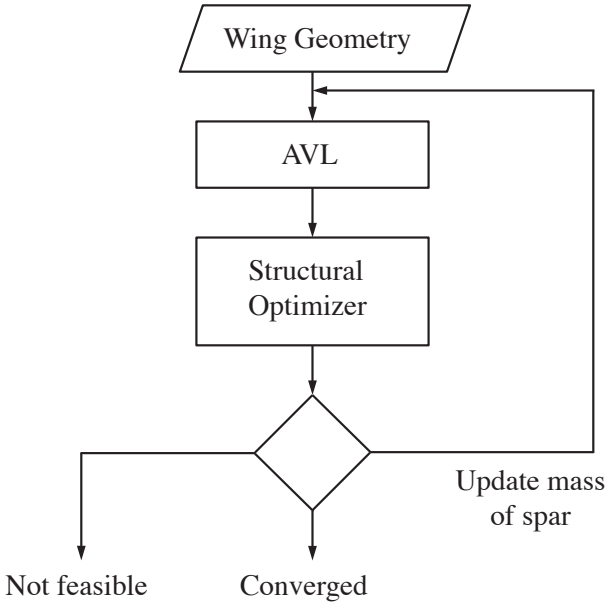

Figure 6.1: Structural optimization procedure

Wing Geometry

In undeformed state, the outer geometry of the wing is described by its airfoil, span b, tip chord length c_{tip}, taper ratio λ ($c_{\text{tip}}/c_{\text{root}}$), twist angle θ and the relative position x/c of the spar's center. These design variables are indicated on half of a wing in Figure 6.2. Note that the relative position x/c fixes the position of the leading edge with respect to the straight spar. In our model this relative position is assumed constant along the wing. Further note that only one type of airfoil is used for the entire wing and that the variation in chord length is linear from root to tip. The input for the structural optimizer is now a single wing geometry described by the appropriate values of the design variables.

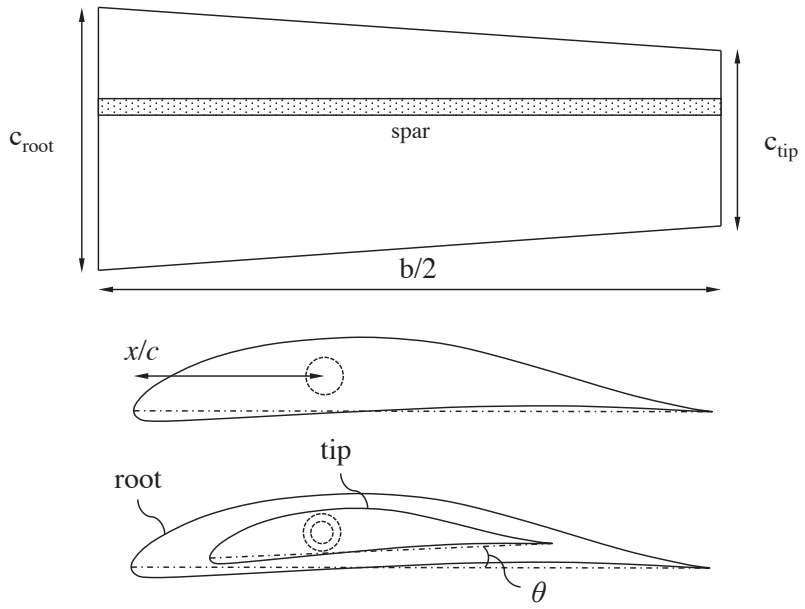

Figure 6.2: Parameterized wing geometry

AVL

Now that the geometry of the wing is defined, an initial simulation can be performed in AVL. In order to perform the simulation, two conditions will have to be defined; the flight velocity and the desired lift. The flight velocity follows from the challenge of completing a marathon distance (42 195 m) in less than 1 hour. This results in a minimal flight velocity of 11.72 m/s. However, to build in some safety margin, the flight velocity is set to 12 m/s, giving more than 1 minute spare-time. Although only the wing of our HPA is being simulated, it is assumed that the wing must generate just enough lift to carry the mass of the pilot(s) and the mass of the complete aircraft structure. At this moment the mass of the aircraft is still unknown, such that the mass of the Daedalus (30.60 kg) is taken as an initial guess for a HPA for 1 pilot and an additional 10 kg is added in case of a HPA for 2 pilots. Once both conditions are specified, AVL will determine the angle of attack of the wing, such that the needed lift is being generated. The results of interest are now, the total drag (induced + profile drag) of the wing and the so-called strip forces, being the resultant forces acting on every spanwise strip of the wing. These are schematically illustrated in Figure 6.3.

Structural Optimizer

The wing's mechanical structure is composed of two main parts. The first part is the wing's internal structure, consisting of a main spar (a thin-walled circular tube) and closely spaced ribs. This internal structure is also the basis for the wing's outer geometry, which is obtained by wrapping a Mylar sheet around the different ribs of the wing. The second mechanical structure is an external lift wire. This lift wire will offer some structural advantages as will be seen. In order to properly design the wing's mechanical structure, the process is started by fixing the outer diameters of the main spar. Consider the cross sections of the wing at root and tip (Figure 6.2), as the relative position x/c will be known and constant along the span, it is possible to determine the section's thickness at this position. Note that this thickness is proportional to the chord length of the section. The outer diameter will now be chosen as a fraction of this thickness. For the root and tip section, the outer diameter is taken as respectively 65% and 80%. These fractions are in close agreement with the values of the Daedalus. In addition, when the diameter at the root is found to be smaller than at the tip, e.g. when the wing is not tapered, both fractions are set to 65%. As such, the outer diameter at the root is always larger or equal to the outer diameter at the tip. It is now assumed that the outer diameters vary linearly from root to tip, which agrees with the linear variation of the chord lengths. The advantage of fixing the outer diameters geometrically is the guarantee that the spar will always fit into the wing.

At this point, it is important to know that the final result of the structural optimization will be a set of two wall thicknesses. These correspond with the thickness of the spar's wall at the root and tip. The procedure of finding the optimal set of wall thicknesses will now be further explained. Note that "optimal" again refers to minimizing the mass of the spar while maintaining sufficient strength and the desired tip deflection during flight. Consider an

arbitrary set of wall thicknesses. As the outer diameters of the spar are fixed for a given wing geometry, these thicknesses immediately allow to calculate the inner diameters of the spar at the root and tip. To determine the inner diameter at an intermediate position, a similar approach is applied as for the outer diameters in which the inner diameters are assumed to vary linearly from root to tip. The geometry of the spar is now fully defined. By specifying the spar's material properties it is possible to determine its bending stiffness EI, in which E is Young's modulus and I the second moment of area (not to confuse with the inertia tensor). For a hollow cylinder, the second moment of area is given by

$$I = \frac{\pi}{64}(d_o^4 - d_i^4) \tag{6.1}$$

in which d_i and d_o are respectively the inner and outer diameter of the hollow cylinder. Note that in most cases the bending stiffness EI will not be constant along the span of the wing, as the inner and outer diameters are allowed to vary. The next step consists of calculating the wing's deformation during flight. For these structural calculations the entire wing is simply represented by its main spar. To determine the deformation only half of the spar is considered and modelled as a cantilevered beam. In this simplified model, only the vertical deformation due to the lift forces will be calculated. Note that the lift-to-drag ratio of the wing is usually very high for HPAs, being in the order of 45 for the Daedalus, such that the horizontal deformation will be much smaller and therefore neglected. Also note that the torsion of the wing is not taken into account here. This simplified model is shown in Figure 6.3.

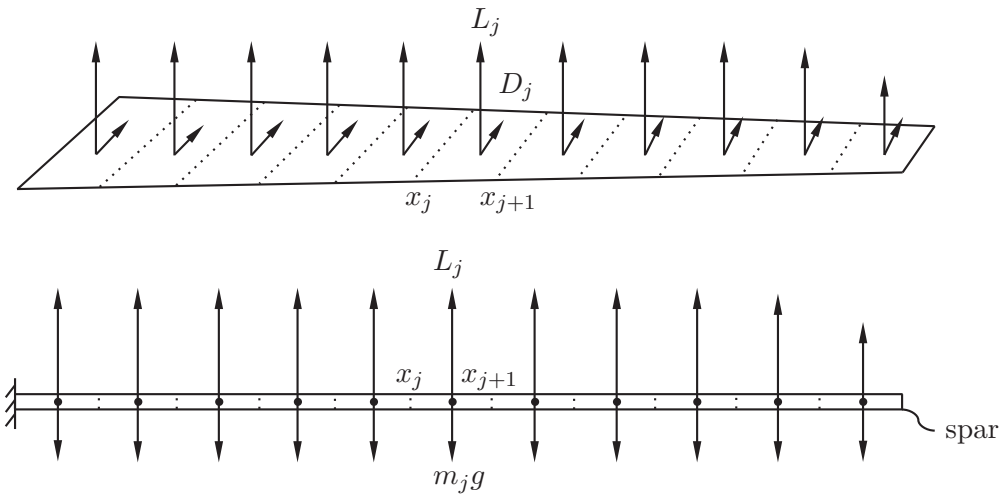

Figure 6.3: Simplified model to determine vertical deformation of the wing

Based on the *Euler-Bernoulli* beam theory and finite differencing, the deformation of the wing can now be easily determined numerically as follows

$$\begin{aligned} V_{j+1} - V_j &= f_j \\ M_{j+1} - M_j &= \left(\frac{V_{j+1} + V_j}{2}\right)(x_{j+1} - x_j) \\ \theta_{j+1} - \theta_j &= \left(\frac{(M/EI)_{j+1} + (M/EI)_j}{2}\right)(x_{j+1} - x_j) \\ u_{j+1} - u_j &= \left(\frac{\theta_{j+1} + \theta_j}{2}\right)(x_{j+1} - x_j) \end{aligned} \tag{6.2}$$

in which $f_j = L_j - m_j g$ and where V represents the shear force, M the bending moment, θ the deflection angle and u the deflection. The lift forces L_j follow from the initial AVL simulation. The boundary conditions for the fixed and free end can be expressed as

$$\begin{aligned} x = 0: \quad & u = 0 \\ & \theta = 0 \\ x = b/2: \quad & V = 0 \\ & M = 0\ . \end{aligned} \tag{6.3}$$

At this moment, the tip deflection of the wing can be calculated for a certain set of wall thicknesses. It is now that the purpose of the external lift wire can be understood. If the actual tip deflection is found to be larger than the desired one, it is calculated which amount of vertical force the lift wire must exert onto the wing in order to achieve the desired tip deflection. This is schematically illustrated in Figure 6.4.

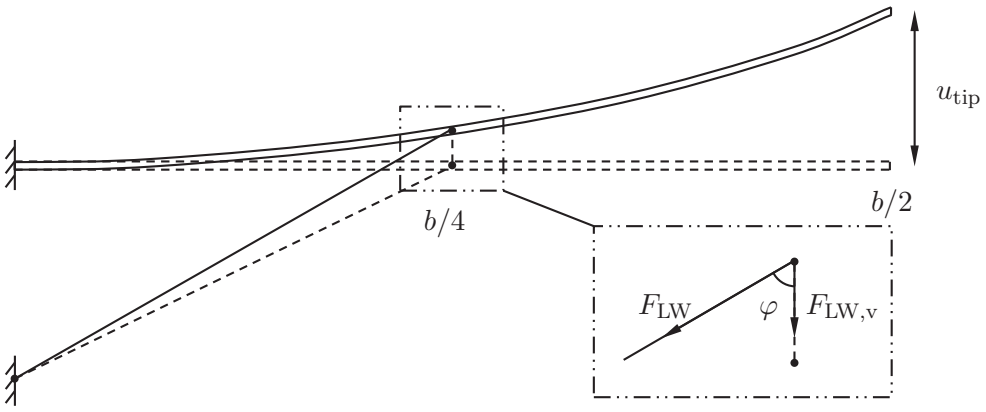

Figure 6.4: Force exerted by lift wire

Adjusting the lift wire's vertical force is easily achieved by changing its length, making it more tight or loose. The desired tip deflection will actually follow from a desired dihedral angle Γ,

$$\tan(\Gamma) = \frac{u_{\text{tip}}}{b/2} \tag{6.4}$$

and as such depends upon the span of the wing. In the calculations the lift wire is assumed to be connected underneath the fuselage and halfway between the root and tip of the wing. Note that if the initial tip deflection is smaller than desired, that the use of an external lift wire becomes irrelevant. Besides obtaining the desired tip deflection or dihedral, the lift wire has an additional advantage as it will reduce the bending moments acting on the wing. As such, there is a possibility of making the wing's structure lighter for the same level of material stresses. However, the lift wire will cause some additional parasite drag. At this point a number of important conditions must be verified in order for the set of wall thicknesses to be feasible. First, the stresses occurring within the wing's spar and lift wire should be below a certain maximal limit to avoid structural failure. For the spar, the maximal bending stress in every discrete point x_j is given by

$$\sigma_j = \left(\frac{Md_o/2}{I}\right)_j . \tag{6.5}$$

The shear stress will not be taken into account, as its contribution is negligible. This will be shown in Section 6.1.3. For the lift wire, the tension is given by

$$\sigma_{\text{LW}} = \frac{F_{\text{LW}}}{A_{\text{LW}}} \tag{6.6}$$

in which A_{LW} represents the cross-sectional area of the lift wire. To determine the force acting along its axis F_{LW}, the following relation is used (Figure 6.4)

$$F_{\text{LW}} = \frac{F_{\text{LW,v}}}{\cos\varphi} \tag{6.7}$$

where φ is determined based on the deflection at $x = b/4$ and the geometry of the wing in undeformed state. As a second condition, the deflection of the wing may nowhere be negative. This second condition might need some further clarification. It is possible that the force exerted by the lift wire is so strong, that the spar will deform negatively (downwards direction) near the root, but still achieves the desired tip deflection due to extreme bending towards the tip of the wing. Such a case is illustrated in Figure 6.5 and will not be considered as valid. The challenge now consists of finding a feasible set of wall thicknesses (if possible) and which in addition minimize the mass of the spar. This optimization procedure was implemented in MATLAB.

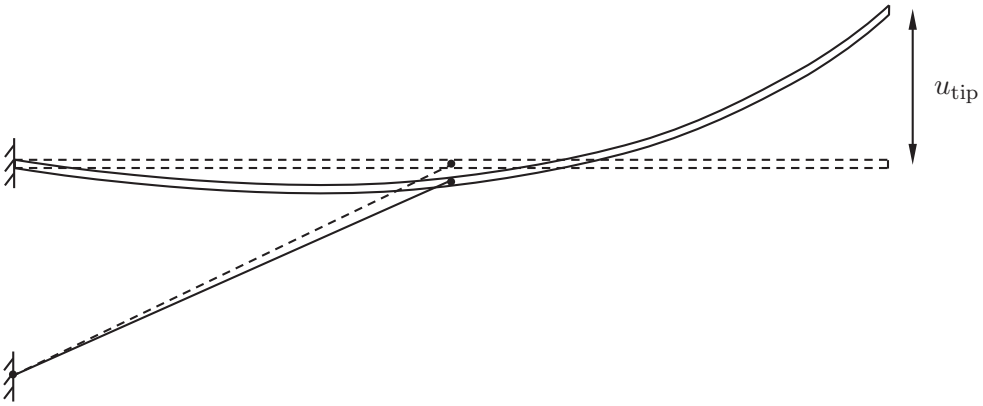

Figure 6.5: Invalid design

Decision Block

If no valid set of wall thicknesses was found, the wing geometry is considered as infeasible. If on the other hand an optimal set was found, the mass of the main spar can now be updated. The initial mass of the spar is taken as 8.62 kg, which corresponds with the spar of the Daedalus [4]. Once the mass has been updated, a new simulation is performed in AVL, resulting in a new angle of attack, total drag and strip forces. The process of optimizing the set of wall thicknesses is rerun and the complete loop is repeated until the relative change in the spar's mass is less than 1%.

6.1.2 Cases

To find the optimal complete wing, a large Design of Experiments will be performed, in which a large set of different wing geometries is generated and individually structurally optimized. The optimal wing is then taken as the wing geometry with the lowest total drag and which is also structurally feasible. As mentioned, it is intended to investigate if powering a HPA by two pilots offers some advantages, such that two Design of Experiments will be performed. The first corresponds to a single-pilot design, whereas the second corresponds to a dual-pilot design. The details of the Design of Experiments are given in Tables 6.1 and 6.2. The two pilots included in the optimization process correspond to two young engineering students, being the author of this work and a good friend. Their physical performance will be measured in Chapter 7. Table 6.1 contains the lower and upper boundary of every geometrical design variable together with its step size. Note that the relative position x/c of the spar's center has been set to 0.33 and that the desired dihedral angle Γ is taken as 6 degrees. These two values closely agree with the Daedalus. Further, 12 different airfoil types will be investigated, in which each airfoil is specifically designed for low-Reynolds number flows. The twist angle is set to zero degrees as its influence will only be investigated on the complete optimized HPA. Table 6.2 contains the structural properties of both the main spar and the lift wire. The main spar is constructed from High Modulus Carbon Fiber (HMCF), whereas the lift wire is a stainless steel wire rope. The material limits are indicated by the tensile strength (TS) in case of the spar and by the minimum breaking load (MBL) in case

of the lift wire (LW). For both structures a safety factor (SF) of 4 is chosen. Note that a different diameter of lift wire is used in case of the dual-pilot and that the minimal thickness of the main spar is set to 0.8 mm (Table 6.1).

	Lower Boundary	**Upper Boundary**	**Step Size**
x/c	0.33	–	–
Γ (°)	6	–	–
b (m)	15	40	0.25
c_{tip} (m)	0.35	0.5	0.01
λ	0.25	1	0.01
θ (°)	0	–	–
t_{spar} (mm)	0.8	10	–

Table 6.1: Design of Experiments - Geometrical design variables

	Single-Pilot	**Dual-Pilot**
$m_{\text{pilot(s)}}$ (kg)	56.4	56.4 + 50.2
ρ_{spar} (kg/m^3)	1600	1600
E_{spar} (GPa)	200	200
TS_{spar} (MPa)	1600	1600
SF_{spar}	4	4
MBL_{LW} (MPa)	1570	1570
SF_{LW}	4	4
d_{LW} (mm)	18	25

Table 6.2: Structural properties of spar and lift wire

6.1.3 Wing Deflection

In this section the accuracy of the finite differencing method for solving linear beam problems is investigated. Additionally, it will be shown that no iterations are required in the FSI simulations in order to determine the deflection of the wing during flight.

Finite Differencing

The theoretical deflection of a cantilevered beam under a uniformly distributed load q is given by

$$u(x) = \frac{qx^2}{24EI}(x^2 - 4\ell x + 6\ell^2) \tag{6.8}$$

in which ℓ is the length of the beam and $x = 0$ corresponds to the fixed end. To investigate the accuracy of the finite differencing method, the bending stiffness EI, the length of the beam ℓ and the distributed load q are all set to one. Figure 6.6 illustrates how the beam is divided into different elements, in which the force f_j is equal to the length of the element as the distributed load q was set to one. Note that a sinusoidal distribution has been used to divide the beam into different elements. This distribution is also used in AVL to divide the thin surfaces into smaller elements, both in the spanwise and chordwise direction. The advantage of this sinusoidal distribution in the spanwise direction is a higher accuracy near the root and tip of the wing, where most changes are expected to occur, while limiting the total number of spanwise elements. Using the equations (6.2) and boundary conditions (6.3), the deflection can now be determined using finite differencing. The number of spanwise elements was set to 20. Comparing the deflections at the discrete points x_j, the maximal difference was found to be smaller than $8.9 \cdot 10^{-5}$. As such, we may conclude that using the finite differencing method will yield sufficiently accurate results.

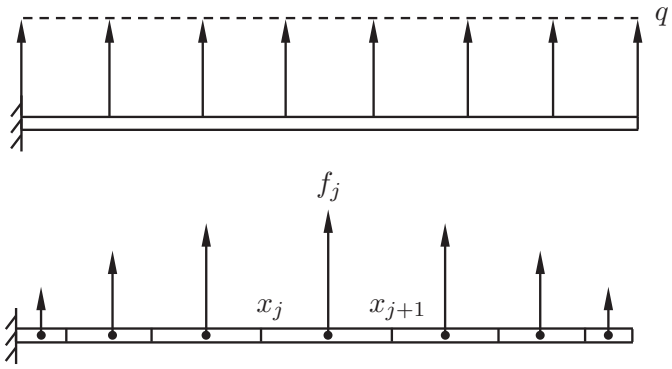

Figure 6.6: Uniformly distributed load

FSI Simulations

The Fluid-Structure Interaction simulations consist of coupling AVL and MATLAB, considered as respectively the flow and structural solver. Figure 6.7 schematically illustrates the FSI procedure in which the different steps are now explained in some more detail. The use of a lift wire will not be considered here. Starting from a perfectly straight wing (Figure 6.7a) and a set of flight conditions (velocity and lift), AVL will determine the wing's angle of attack, drag and strip forces. The strip forces are then given to MATLAB, which will determine the deflection of the wing using the finite differencing method (Figure 6.7b). We can now update the geometry of the wing. Since only two sections (root and tip) are used to define the wing geometry, the actual deflection is simplified by a linear deflection in which the tip deflection is identical. This deformed wing geometry is then simulated back again in AVL, resulting in a new angle of attack, drag and strip forces (Figure 6.7c). To calculate the new deflection of the wing, the vertical components of the strip forces are determined and applied to the undeformed spar (Figure 6.7d). As such, the sum of the forces in Figure 6.7d is equal to the specified lift needed to carry the pilot and the aircraft structure. The

deflection can now be determined, allowing to update the wing geometry once more. This procedure is repeated until the relative change of the wing geometry is found to be small enough. We will now perform such an FSI simulation.

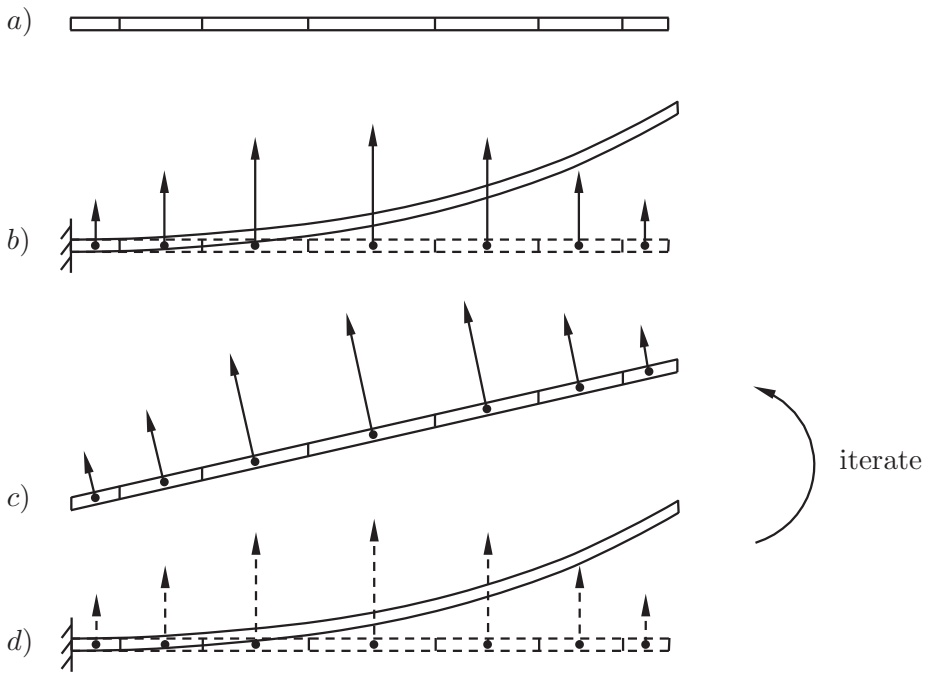

Figure 6.7: Procedure FSI simulation - half of the wing

The wing's geometrical data (airfoil, span b, tip chord length c_{tip} and taper ratio λ) together with the structural data (total mass of pilot and aircraft, spar's density ρ_{spar}, Young's modulus E_{spar} and wall thickness t_{spar}) is given in (6.9). Further, the flight velocity is set to 12 m/s.

$$\begin{array}{ll} DAE11 & mass = 56.4 + 30.6 \text{ kg} \\ b = 20 \text{ m} & \rho_{\text{spar}} = 1600 \text{ kg/m}^3 \\ c_{\text{tip}} = 0.5 \text{ m} & E_{\text{spar}} = 200 \text{ GPa} \\ \lambda = 0.5 & t_{\text{spar}} = 1 \text{ mm} \end{array} \tag{6.9}$$

The results of the simulation can be seen in Table 6.3. The relative change in tip deflection u_{tip} after the first iteration is found to be 0.2%. As such, no iterations are actually required to determine the final deflection of the wing. This important observation was used when outlining the structural optimization procedure (Section 6.1.1). Recall that the deflection of the wing was indeed directly calculated using the strip forces determined by AVL and the finite differencing method. Table 6.3 also contains the maximal bending and shear stress occurring in the wing's spar. The contribution of the shear stress is found to be 1% and as such will be neglected. Figure 6.8 visualizes the shear force, bending moment, deflection angle and deflection for half of the wing in its final deformed state.

Iteration	L (N)	u_{tip} (m)	Γ (°)	σ_{max} (MPa)	τ_{max} (MPa)
0	426.72	1.1720	6.6843	324.38	3.05
1	426.70	1.1694	6.6699	323.77	3.04
2	426.70	1.1694	6.6701	323.78	3.04
3	426.70	1.1694	6.6701	323.78	3.04
4	426.70	1.1694	6.6701	323.78	3.04
5	426.70	1.1694	6.6701	323.78	3.04

Table 6.3: Results of an example FSI simulation

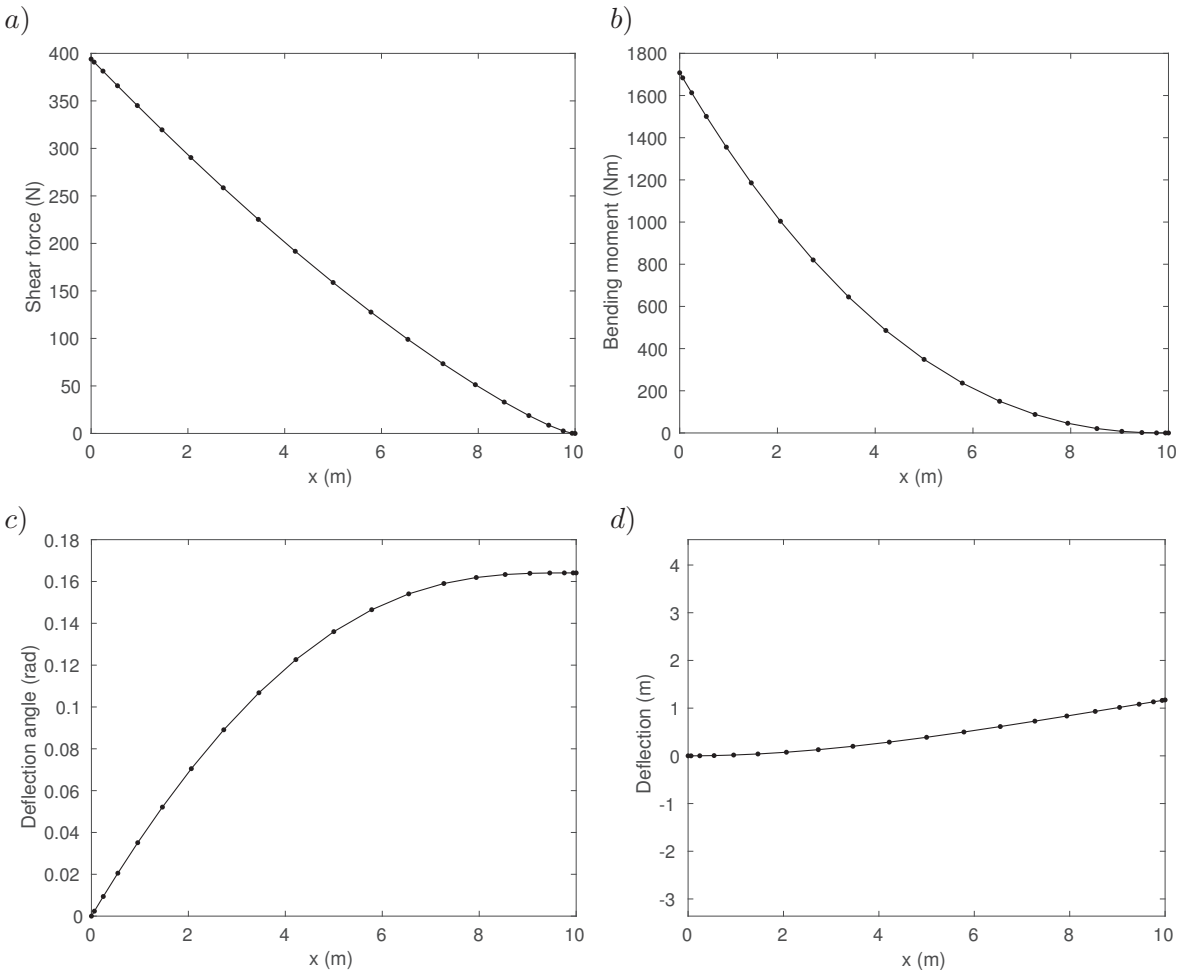

Figure 6.8: Results of an example FSI simulation

6.1.4 Sensitivity Study

In the sensitivity study, every geometric design variable will be varied independently. This results in a specific set of wing geometries for every geometric design variable. For most sets, every wing geometry will be analyzed in three different ways. We will start by performing an inviscid and viscous analysis of the wing in its undeformed state, allowing to calculate the corresponding induced and total drag. This analysis is performed in AVL. As previously explained, not every wing geometry will be structurally feasible. As such, the different wing

geometries will also be structurally optimized (if possible) for a certain design dihedral angle. Table 6.4 gives an overview of the different studies. The values indicated with an asterisk correspond to the desired value during flight. The flight velocity is set to 12 m/s and the structural properties of the spar and lift wire are identical to the values listed in Table 6.2 for the single-pilot case. The results of each study will now be analyzed in separate sections.

	Study 1	**Study 2**	**Study 3**	**Study 4**	**Study 5**
Airfoil	DAE11	DAE11	DAE11	DAE11	DAE11
x/c	0.33	0.33	0.33	0.33	0.33
Γ (°)	$0-10$	6*	6*	6*	6*
b (m)	20	$15-30$	20	20	20
c_{tip} (m)	0.5	0.5	$0.35-0.75$	0.5	0.5
λ	1	1	0.5	$0.25-1$	1
θ (°)	0	0	0	0	$0-5$

Table 6.4: Overview sensitivity study

Dihedral Angle

In the first study it is proven that the dihedral angle Γ has no influence on the aerodynamic performance of the wing (Figure 6.9). As mentioned, the desired dihedral angle during flight is actually determined from stability requirements and is set to 6 degrees in the following studies.

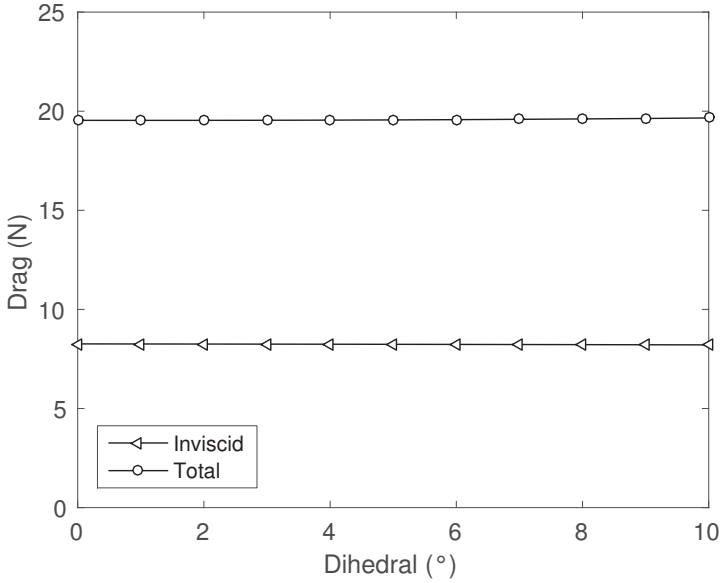

Figure 6.9: Sensitivity study - dihedral angle

Span

In the second study the span of the wing b is increased from 15 to 30 m in steps of 1 m. Increasing the span of the wing is found to be beneficial for decreasing the induced drag of the wing (Figure 6.10a). However, as the span increases, the surface area of the wing increases, causing additional viscous drag. As such, the total drag of the wing will exhibit a minimum for a certain wing span, in this case around 22 m. Every wing geometry of this study is now structurally optimized. The mass of the spar as a function of the span can be seen in Figure 6.10c and Figure 6.10d shows the corresponding maximal stress occurring in the spar and lift wire. For a wing span up to 24 m, the spar can be made lighter than initially assumed. Recall that the initial mass of the spar was taken as 8.62 kg, corresponding to the spar of the Daedalus. The result is a lighter aircraft structure, such that the wing must generate less lift. This is accomplished by decreasing the angle of attack compared to the unoptimized wing (Figure 6.10b) and is seen to reduce the total drag of the wing. The lift wire reaches its full potential at a wing span of around 21 m. To limit the tip deflection for a larger span, this can now only be accomplished by making the spar itself stiffer. This is done by increasing its wall thicknesses, resulting in a heavier spar but lower bending stresses. For a wing span larger than 28 m the wing geometries are found infeasible.

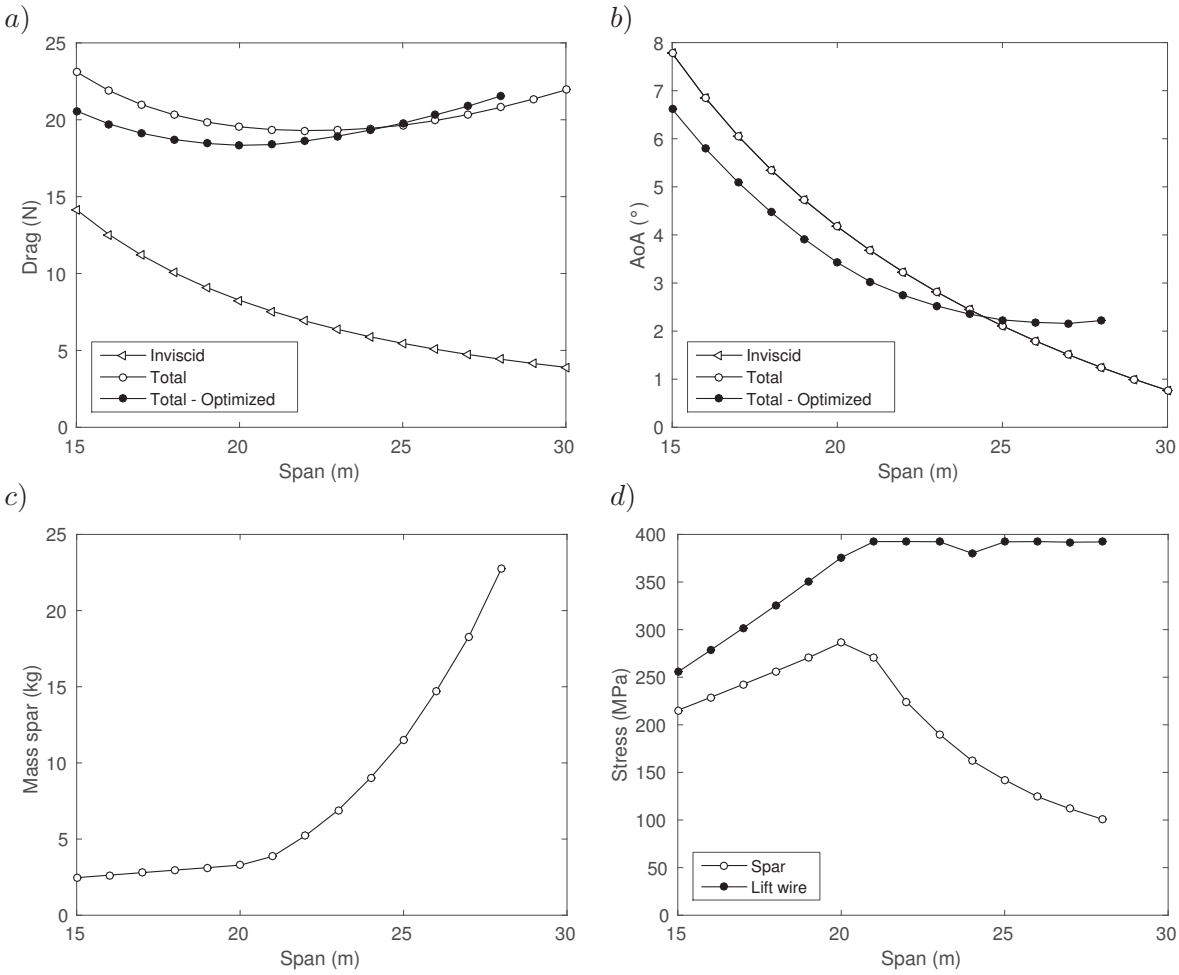

Figure 6.10: Sensitivity study - wing span

Tip Chord Length

In the third study, the tip chord length c_{tip} is increased from 0.35 to 0.75 m in steps of 0.05 m. Note that the wing is also given some tapering ($\lambda = 0.5$). As the wing span is rather small in this study, the wall thicknesses of all structurally optimized wing geometries are found to correspond to their lower boundary. The result is a linear increase in the mass of the spar as the tip chord length increases (Figure 6.11c). Further, with increasing tip chord length, the surface area of the wing increases. To obtain the necessary lift, the angle of attack of the wing is seen to decrease and even becomes negative for tip chord lengths larger than 0.6 m (Figure 6.11b). As the spar becomes heavier and stiffer for increasing tip chord length, no lift wire is used for values larger than 0.55 m and as such, the tip deflection during flight will be small than desired (Figure 6.11d). Analysing the total drag of the wing, a smaller tip chord length is seen to be beneficial (Figure 6.11a).

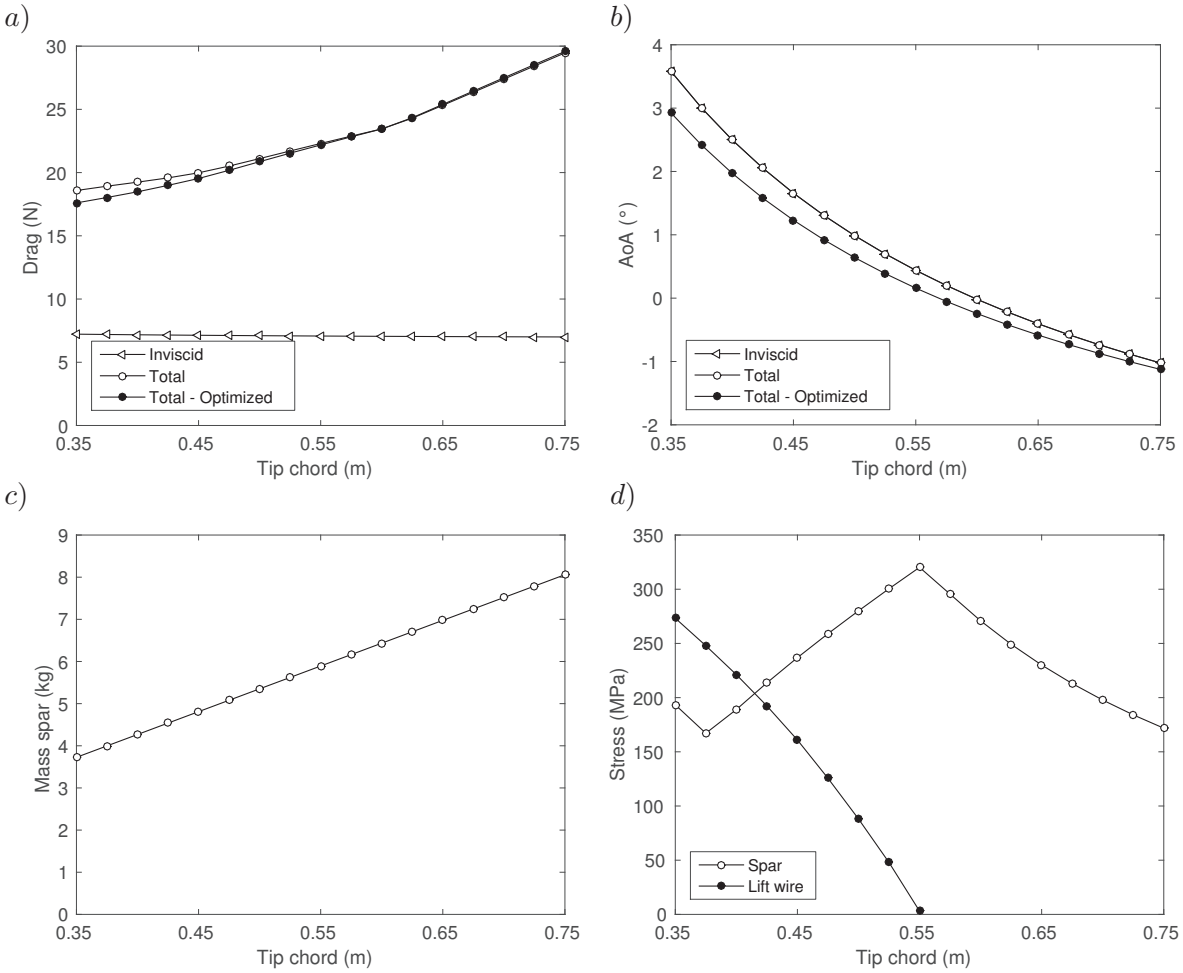

Figure 6.11: Sensitivity study - tip chord length

Taper Ratio

In the fourth study, the taper ratio λ ($c_{\text{tip}}/c_{\text{root}}$) is increased from 0.25 to 1 in steps of 0.05. Similar to study 3, the wall thicknesses of all structurally optimized wing geometries are found to correspond to their lower boundary. As the taper ratio increases, the chord length at the root decreases, causing the outer diameter of the spar at the root to decrease. Recall that the outer diameters were geometrically fixed. Since the wall thicknesses are constant, this results in a lighter spar, which can be seen in Figure 6.12c. Additionally, for a decreasing outer diameter of the spar at the root, the second moment of area I will decrease, causing the bending stresses (6.5) to increase. For taper ratios smaller than 0.5 no lift wire is used, such that the tip deflection during flight will be smaller than desired. The lift wire is seen to reduce the bending stresses of the spar for a taper ratio between 0.5 and 0.75, but for a larger value the bending stresses increase back again (Figure 6.12d). Concerning the total drag of the wing, a weak minimum is found for a taper ratio of about 0.8 (Figure 6.12a).

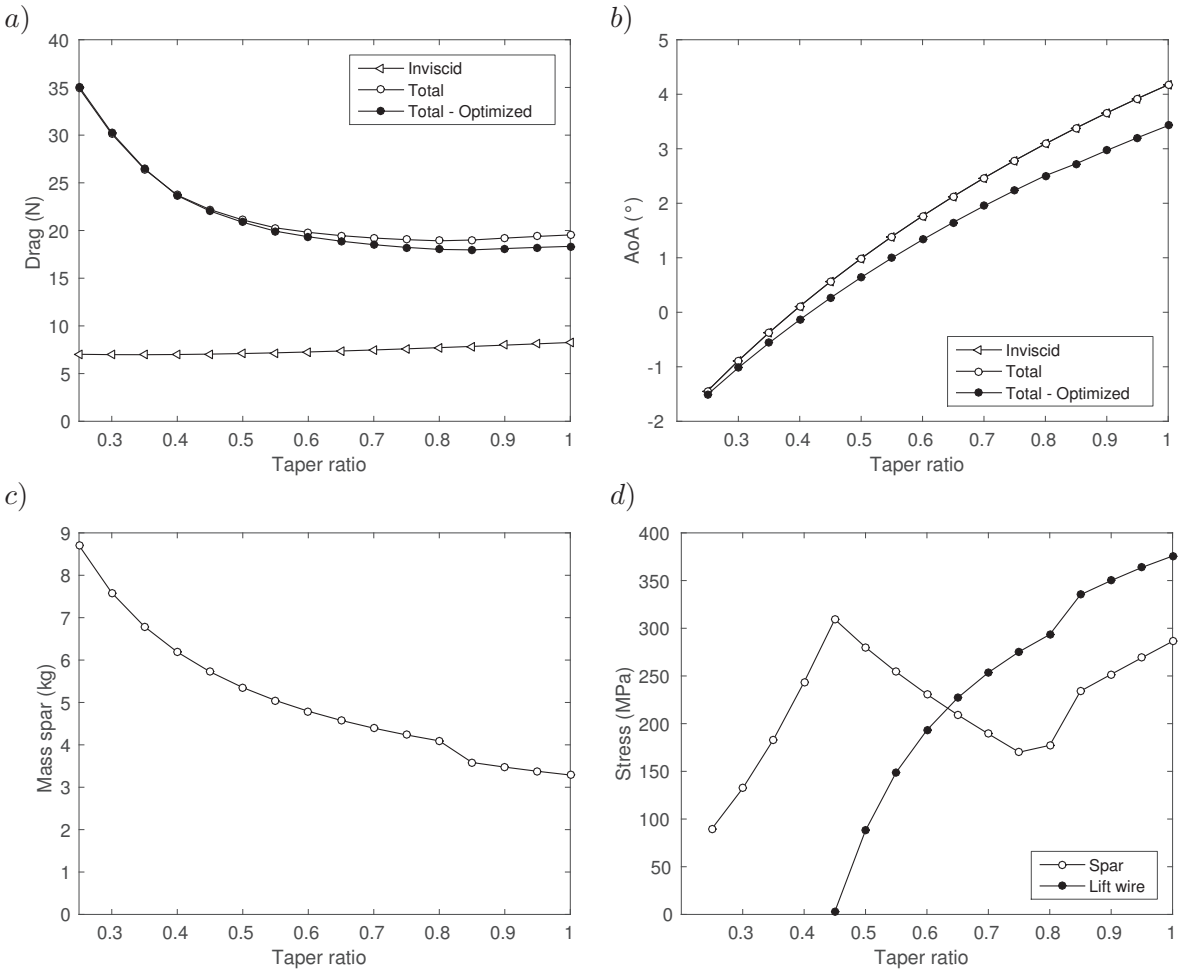

Figure 6.12: Sensitivity study - taper ratio

Twist Angle

In the final study, the twist angle θ is increased from 0 to 5 degrees in steps of 0.5 degrees. Note that increasing the twist angle causes the incidence of the tip profile to be smaller than the root profile (Figure 6.2). Compared to the case of no twist, the wing will generate less lift, which is compensated by increasing its angle of attack (Figure 6.13b). Although the angle of attack of the complete wing has increased, the local angle of attack near the tip has decreased, since the slope in Figure 6.13b is smaller than one. As such, less lift is being generated near the tip, resulting in lower bending moments and stresses (Figure 6.13d). Note that the angle of attack of the structurally optimized wing geometries is smaller compared to the unoptimized designs. This is due to the lower mass of the spar, resulting in a lighter aircraft structure and less required lift. As the loading is smaller near the tip, the tip deflection will also be smaller, such that the stress in the lift wire is seen to decrease. The influence on the total drag of the wing is found to be small, but twisting the wing is slightly advantageous up to a twist angle of 3 degrees (Figure 6.13a).

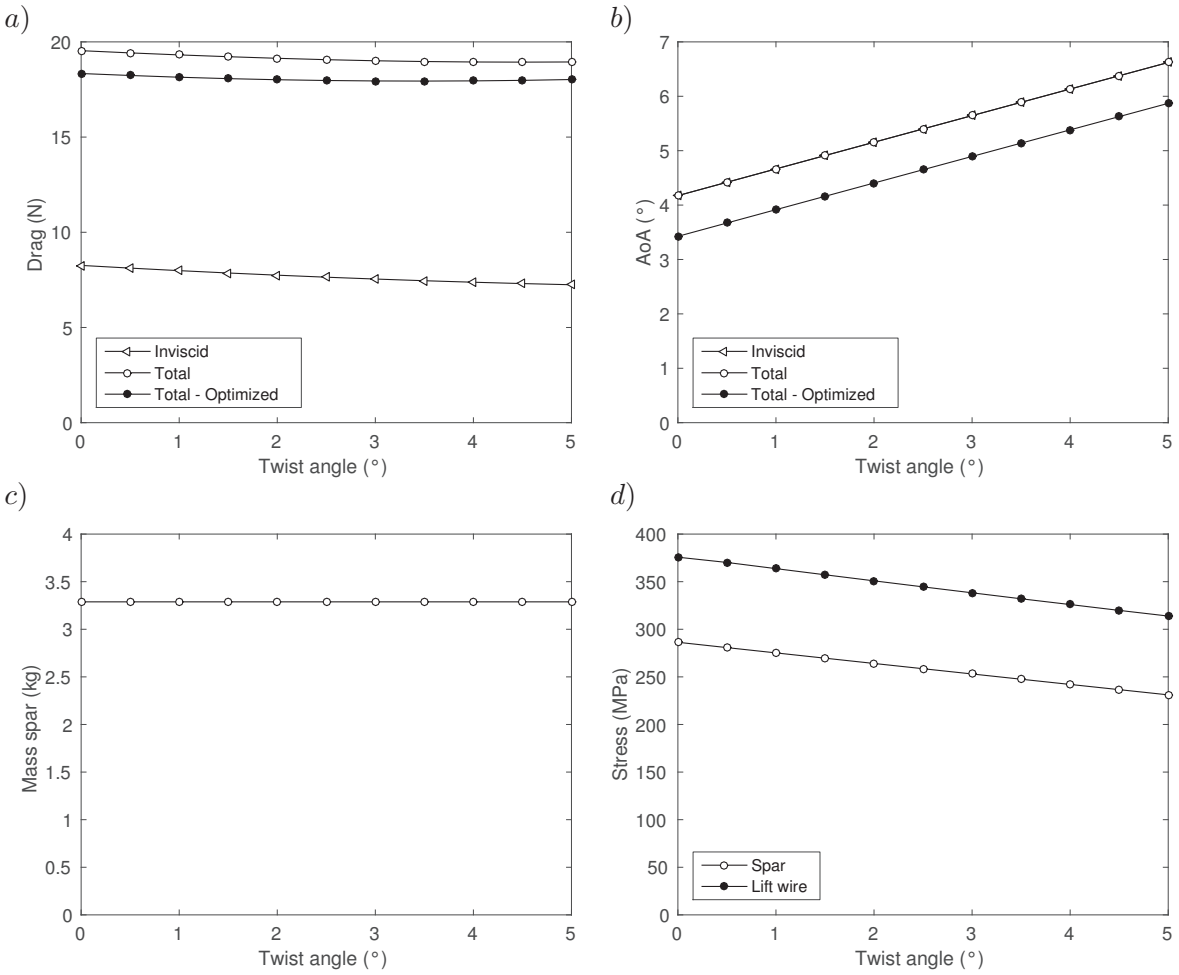

Figure 6.13: Sensitivity study - twist angle

6.1.5 Results

The results of both Design of Experiments defined in Section 6.1.2, are given in Tables 6.5 and 6.6. Structurally optimizing one specific wing geometry took about $8-15$ s and mostly required 2 to 6 iterations. For each airfoil type the geometrical and structural data of the optimal design is given. In every optimal design the wing is found to be tapered, in which the optimal tip chord length corresponds to its lower boundary. This result is in agreement with the observations made in the sensitivity study (Figure 6.11). The wings are somewhat more tapered in the dual-pilot case, the taper ratio λ being smaller compared to the single-pilot case. The higher lift needed in the dual-pilot case results in a larger optimal wing span b, a larger angle of attack AoA compared to the optimal designs in the single-pilot case with the same airfoil and a heavier spar (m_{spar}). The optimal wall thicknesses of the spar at root and tip (t_{root}, t_{tip}) were found to be identical in each optimal wing design. Note that all designs make use of a lift wire (LW), in which most of the lift wires are exploited to their maximum allowable stress. The maximal stress occurring within the main spar (σ_{spar}) is seen to be comparable in both cases. However, the most interesting result is the drag of the wing. Although the drag is larger in the dual-pilot cases, when dividing the corresponding required power over 2 pilots, there clearly seems to be an advantage. The reduction in required power per pilot is seen to range from 35 to 57 W. The most optimal wing is thus found to be for 2 pilots. Comparing the results for the different airfoils in Table 6.6, the E395 is seen to be the most optimal. Using this most optimal wing, our HPA will now be further constructed and designed for 2 pilots.

Single-Pilot Airfoil	b (m)	c_{tip} (m)	λ –	Γ (°)	$t_{\text{root,tip}}$ (mm)	m_{spar} (kg)	σ_{spar} (MPa)	σ_{LW} (MPa)	AoA (°)	D (N)	P/pilot (W)
DAE11	20.75	0.35	0.58	6	0.80	3.53	249	334	3.38	16.85	202
DAE21	21.00	0.35	0.58	6	0.81	3.31	298	367	3.11	15.58	187
DAE31	20.25	0.35	0.62	6	1.09	3.83	274	359	3.20	15.22	183
E395	22.00	0.35	0.64	6	1.00	4.18	273	388	2.21	14.18	170
E396	22.50	0.35	0.62	6	0.81	3.77	287	392	1.79	14.62	175
E397	22.75	0.35	0.63	6	0.80	3.89	277	391	1.92	14.92	179
E398	23.25	0.35	0.64	6	0.80	4.13	264	392	1.95	15.05	181
E399	23.50	0.35	0.66	6	0.80	4.30	252	391	2.00	15.44	185
FX63-137	23.50	0.35	0.60	6	0.80	4.18	264	392	-0.49	14.65	176
FX76MP120	18.75	0.35	0.70	6	0.89	3.00	295	342	1.35	17.10	205
FX76MP140	19.50	0.35	0.70	6	0.80	3.28	250	329	-2.22	17.15	206
L7769	20.25	0.35	0.58	6	0.98	3.52	285	355	7.00	16.93	203

Table 6.5: Geometrical and structural data of optimal designs for the single-pilot case

Dual-Pilot Airfoil	b (m)	c_{tip} (m)	λ –	Γ (°)	$t_{\text{root,tip}}$ (mm)	m_{spar} (kg)	σ_{spar} (MPa)	σ_{LW} (MPa)	AoA (°)	D (N)	P/pilot (W)
DAE11	27.50	0.35	0.47	6	1.21	8.01	284	388	4.50	25.72	154
DAE21	27.75	0.35	0.46	6	1.62	9.94	255	392	4.27	24.15	145
DAE31	27.25	0.35	0.46	6	1.89	10.52	253	392	3.79	23.42	141
E395	**28.75**	**0.35**	**0.46**	**6**	**1.65**	**10.94**	**239**	**388**	**2.88**	**22.47**	**135**
E396	28.75	0.35	0.46	6	1.36	9.68	250	392	2.79	23.04	138
E397	28.50	0.35	0.48	6	1.32	9.38	253	392	3.27	23.35	140
E398	29.25	0.35	0.47	6	1.20	9.32	250	392	2.98	23.86	143
E399	28.75	0.35	0.46	6	0.90	7.33	284	392	2.86	24.26	146
FX63-137	29.50	0.35	0.42	6	1.03	8.38	265	392	0.12	23.35	140
FX76MP120	26.25	0.35	0.55	6	1.93	10.20	255	392	2.17	24.99	150
FX76MP140	27.00	0.35	0.57	6	1.46	9.22	258	392	-1.17	24.75	149
L7769	27.25	0.35	0.43	6	1.64	9.45	266	391	7.49	26.72	160

Table 6.6: Geometrical and structural data of optimal designs for the dual-pilot case

6.2 Complete Optimized Design

To construct a complete HPA, the idea consists in taking the Daedalus and replacing its wing by our own optimized wing and to adjust its fuselage to fit a second pilot. The incidence of the optimized wing with respect to the aircraft is taken as the angle of attack determined in Table 6.6. To determine its optimal position along the aircraft, a small Design of Experiments is performed, in which the position of the main spar is varied from $x = 0\,\text{m}$ to $x = 1\,\text{m}$. The reference frame is shown in Figure 5.1. In the Design of Experiments, the total drag of the aircraft will be determined together with its static margin. Recall that the static margin, defined as (5.25), was used to quantify the aircraft's longitudinal static stability. The results of the Design of Experiments can be seen in Figure 6.14. Based on Figure 6.14a, the optimal position of the wing's spar is seen to be 0.6 m for which the static margin of the aircraft is 94%. This value is larger than previously determined for the Daedalus (57%), but this is due to the smaller mean aerodynamic chord of the optimized aircraft (0.55 m compared to 0.90 m for the Daedalus). Using the mean aerodynamic chord of the Daedalus, the static margin of the optimized aircraft is found to be 58%. Besides the static margin, we will also verify if the optimized aircraft is completely statically stable. The conditions are repeated once more below

$$\frac{\mathrm{d}C_m}{\mathrm{d}\alpha} < 0 \tag{6.10}$$

$$\frac{\mathrm{d}C_n}{\mathrm{d}\beta} > 0 \tag{6.11}$$

$$\frac{\mathrm{d}C_l}{\mathrm{d}\beta} < 0 \tag{6.12}$$

and correspond to respectively longitudinal, directional and roll stability. The derivates were calculated by AVL and are given in (6.13).

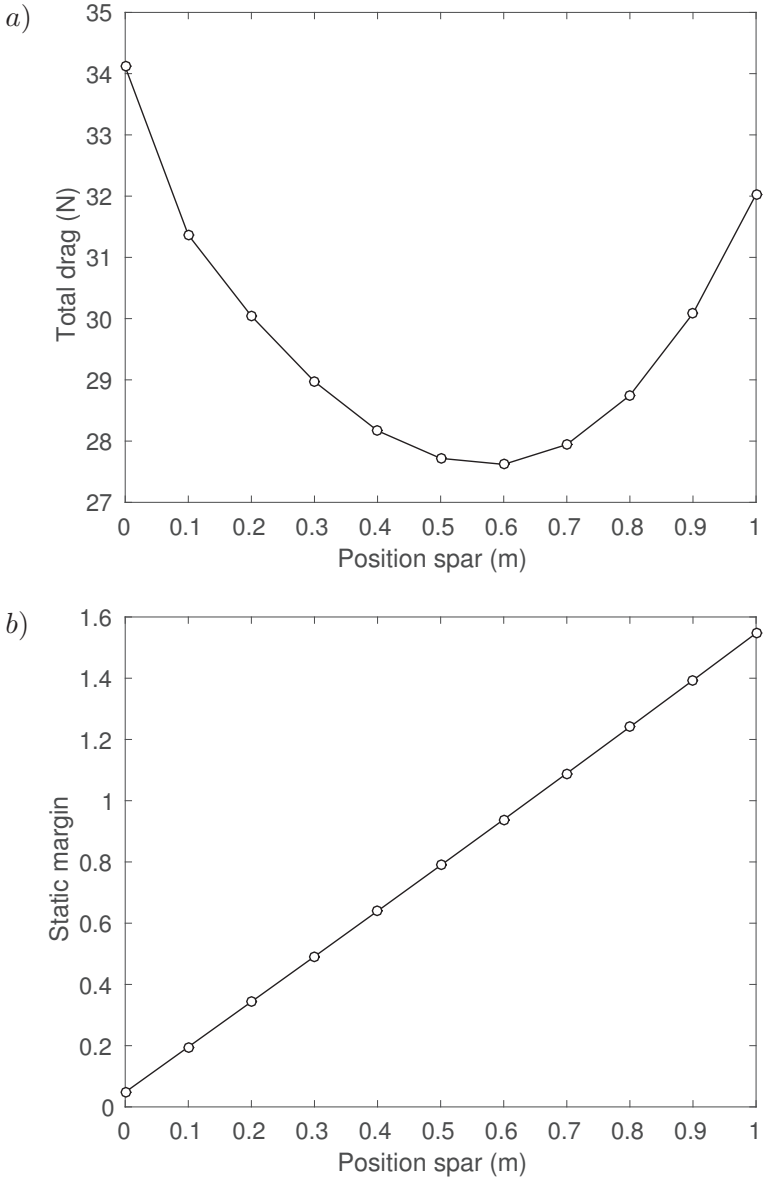

Figure 6.14: Optimal position of optimized wing

$$\begin{aligned} \frac{\mathrm{d}C_m}{\mathrm{d}\alpha} &= -6.1402 \\ \frac{\mathrm{d}C_n}{\mathrm{d}\beta} &= 0.0454 \\ \frac{\mathrm{d}C_l}{\mathrm{d}\beta} &= -0.1549 \end{aligned} \tag{6.13}$$

Verifying all conditions, also our optimized dual-HPA is found to be statically stable. The optimized wing was further given a twist of 1 degree, slightly improving its performance. Concerning the fuselage, it was extended by 1.5 m assuring sufficient space for the second pilot. The CAD model of the complete optimized dual-HPA is shown in Figure 6.15 together

with the Daedalus. Also a close-up of the fuselages is added for comparison. The optimized HPA is now simulated in STAR-CCM+, being the final simulation. As for the Daedalus, the CFD simulation was performed steady, in which the flight velocity was set to 12 m/s and the angle of attack of the aircraft to 1.30 degrees. The results of the CFD simulation are given in Table 6.7 and are compared with the CFD results of the Daedalus. So in case of our optimized HPA, each pilot should generate a power of 215 W in order to obtain a flight velocity of 12 m/s. Note that this flight velocity is 80% higher compared to the Daedalus while the corresponding pilot power has only increased by 10%. An interesting result is that the total drag of the optimized wing is smaller compared to the Daedalus. However, the parasite drag has substantially increased. The drag of the fuselage has increased with a factor 4, which is mainly due to the higher frictional surface. Further note that the generated lift is somewhat larger than the total weight, which is a small safety and allows to carry an additional 2.4 kg. The final step now consists of measuring the physical performance of our 2 pilots, which is done in the following chapter.

	Daedalus	**Optimized Dual-HPA**
Total Mass (kg)	105.4	147.0
Flight Velocity (m/s)	6.7	12
AoA Aircraft (°)	2.76	1.30
Gliding Drag (N)	26.2	32.3
Wing (N)	23.67	22.76
Fuselage (N)	1.05	4.24
Elevator (N)	0.44	2.36
Rudder (N)	0.53	1.60
Tailboom (N)	0.47	1.32
Lift (N)	1034.8	1465.5
Propulsive Efficiency	0.90	0.90
Total Power (W)	195	430
Pilot Power (W)	195	215

Table 6.7: Comparison performance Daedalus versus optimized dual-HPA in STAR-CCM+

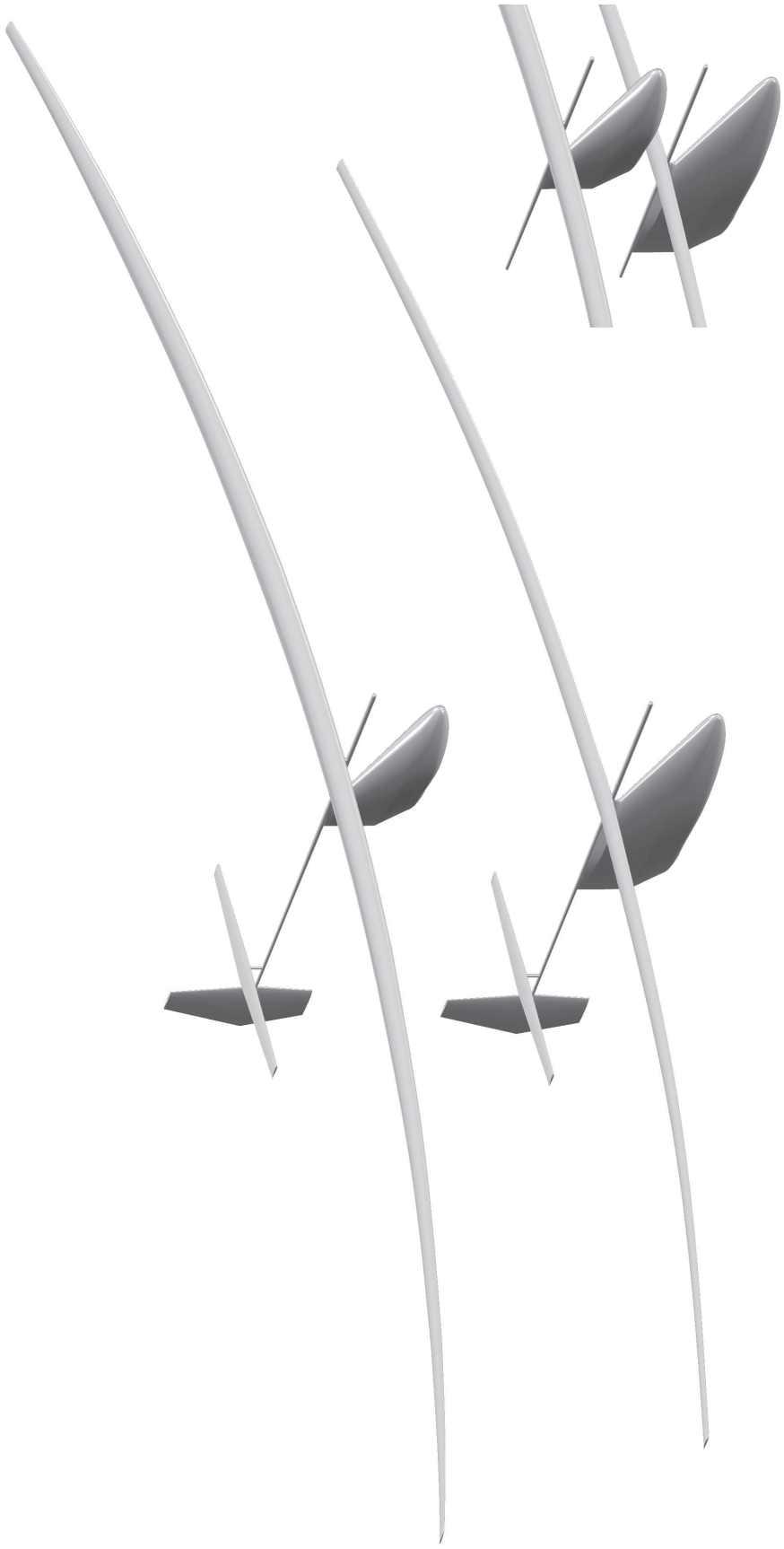

Figure 6.15: Comparison of CAD model (upper: Daedalus, lower: optimized dual-HPA)

Chapter 7

Final Test

In this final chapter, we will measure the physical performance of our two pilots, which will allow to verify the feasibility of winning the Kremer International Marathon Competition with our optimized dual-HPA. Some final thoughts can be found back in the conclusion of this work.

7.1 Physical Performance of Pilots

The physical performance was measured using a bicycle trainer with an adaptive resistive power. Starting at a low resistive power of 60 W, the power was gradually increased every 2 minutes by 20 W until the pilot reached total fatigue. The results of the Power Test are shown in Figure 7.1, in which the heart rates (HR) of both pilots are given as a function of time together with the resistive power. Pilot 1 (author of this work) is seen to produce a maximal power output of 260 W, compared to 240 W for pilot 2 (Toon Demeester). However, pilot 2 (50.2 kg) is somewhat lighter than pilot 1 (56.4 kg). The maximal power output of both pilots together is thus 500 W. This is definitely an exciting result as the theoretical power required to obtain a flight velocity of 12 m/s with our optimized dual-HPA is 430 W.

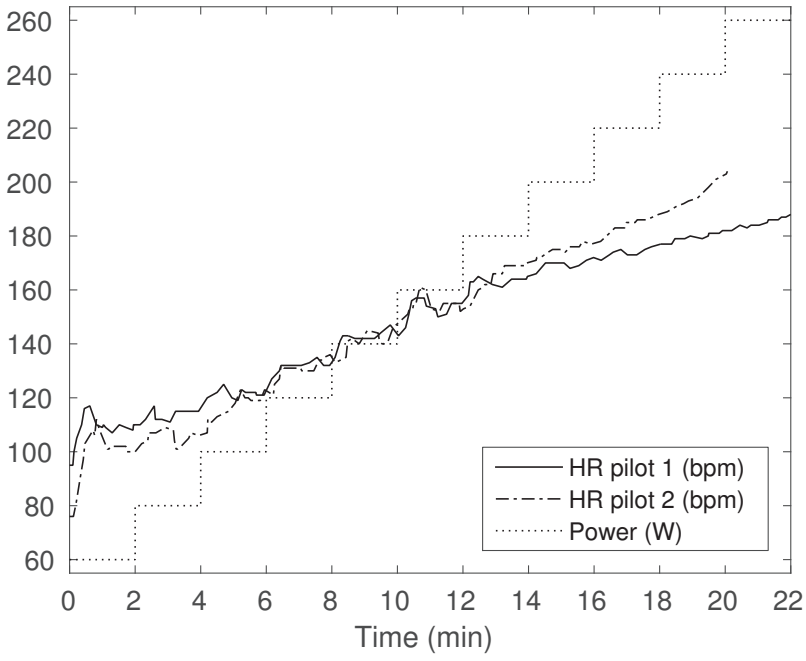

Figure 7.1: Power test of pilots

As such, the pilots can surely reach the required flight velocity of 12 m/s in order to win the Kremer International Marathon Competition. However, the pilots must sustain the aircraft at this 12 m/s during approximately 1 hour. Dividing the theoretical required power over the 2 pilots based on their maximal power output results in respectively 223.6 W for pilot 1 and 206.4 W for pilot 2. These values correspond with 86% of their maximal physical performance. To find out if the pilots are capable of sustaining this power output during 1 hour, a second physical test would have to be performed.

7.2 Conclusions

The goal of this work was to design and optimize a HPA capable of winning the Kremer International Marathon Competition. As a first step, the *Daedalus* from MIT was analysed in great detail and simulated in two different softwares; AVL and STAR-CCM+. The calculation times in AVL were found to be very short (order of seconds), making it an ideal tool for evaluating lots of different designs. However, the drag prediction was somewhat less accurate but still resulted in a reasonable first estimate. The 2D CFD simulations of the airfoil FX63-137 in STAR-CCM+ proved the γ-Re_θ transition model to provide very accurate results at low Reynolds numbers. When the transition phenomenon was neglected, the drag was seen to be heavily overpredicted by more than 50%. As such the entire Daedalus was simulated using a transition model. This resulted in an "expensive" simulation with more than 52 million cells and took about 1 day to solve. However, the drag prediction was found to closely agree with the value estimated by MIT (within 3%). The analysis of the Daedalus learned that for the intended optimization of a HPA, AVL is the most suited tool. But to obtain an accurate drag prediction of the final optimized HPA, it must also be simulated in STAR-CCM+.

For the optimization of our own HPA a full parametric model was constructed, allowing to generate any wing geometry. To verify the feasibility of every geometric design, AVL and MATLAB were coupled, allowing to perform FSI simulations. Using these simulations, the mechanical structure of the wing was further optimized (when feasible), resulting in a minimal mass of the wing while assuring sufficient strength and the desired tip deflection. The most interesting result of the optimization was that adding a second pilot on board of the aircraft was found to be beneficial compared to a single-pilot design. As such, a complete HPA was constructed for 2 pilots, which was then simulated in STAR-CCM+. The theoretical power required to obtain a flight velocity of 12 m/s was found to be 430 W. To verify the feasibility of winning the Kremer International Marathon Competition with the optimized dual-HPA, the physical performance of the two pilots was measured. They produced a maximal power output of 500 W, which is definitely sufficient to attain the required flight velocity of 12 m/s. However, the question remains if the pilots can sustain the required power output of 430 W during 1 hour.

In this thesis the optimized dual-HPA is entirely based upon simulations and only exists as a CAD model. Nevertheless, both pilots dream of constructing and flying one day their optimized dual-HPA. Knowing that first some additional aspects would have to be worked out, such as the steering of the aircraft and the design of a propeller, winning the Kremer International Marathon Competition would be the ultimate proof of the performance of their optimized dual-HPA.

Appendix A

A.1 Paper

The following paper has been submitted to the journal *Aerospace* for the special issue on Fluid-Structure Interactions.

MDPI

Article

Optimization of a Human-Powered Aircraft using Fluid-Structure Interaction Simulations

Bob Vanderhoydonck [1], Gilberto Santo [1], Jan Vierendeels [1] and Joris Degroote [1,*]

[1] Department of Flow, Heat and Combustion Mechanics, Sint-Pietersnieuwstraat 41, 9000 Ghent, Belgium; {Bob.Vanderhoydonck, Gilberto.Santo, Jan.Vierendeels, Joris.Degroote}@UGent.be

* Correspondence: Joris.Degroote@UGent.be; Tel.: +32-9-264-9522

Academic Editor: name

Version May 26, 2016 submitted to Aerospace; Typeset by LaTeX using class file mdpi.cls

Abstract: The special type of aircrafts in which the human power of the pilot is sufficient to take off and sustain flight are known as Human-Powered Aircrafts (HPAs). To explore the peculiarities of these aircrafts, the aerodynamic performance of an existing design is evaluated first, using both the Vortex Lattice Method and Computational Fluid Dynamics. In a second step, it is attempted to design and optimize a new HPA capable of winning the Kremer International Marathon Competition. The design will be special in that it allows to include a second pilot on board of the aircraft. As the structural deflection of the wing is found to be a key aspect during design, Fluid-Structure Interaction simulations are performed and included in the optimization procedure. To asses the feasibility of winning the competition, the physical performance of candidate pilots is measured and compared with the predicted required power.

Keywords: Human-Powered Aircraft; Vortex Lattice Method; Computational Fluid Dynamics; Fluid-Structure Interaction; optimization

1. Introduction

By careful design, the human power is found sufficient to propel an aircraft. These special aircrafts, known as Human-Powered Aircrafts (HPAs), are extremely light, fly at very low speeds and are usually constructed for a single pilot.

One of the most sophisticated HPAs is the *Daedalus* from MIT. It was built in an attempt to recreate the mythical escape of its namesake, said to have built himself wings of feathers and wax. After years of intensive design and testing with a prototype aircraft, the Daedalus was finally ready in 1988 for a legendary flight across the Aegean Sea from Crete to Santorini. The flight covered a distance of 74 miles (119 km), completed in 3 hours 54 minutes, the longest time and distance flown under human power up to date [1]. The Daedalus can be seen in Figure 1.

Given its outstanding performance, the first part of this work is devoted to analysing this HPA. More specifically, the Daedalus will be simulated in two different softwares. The first software is AVL [2], which performs aerodynamic analyses based on the Vortex Lattice Method (VLM). This software is developed by MIT and is publicly available. For the second simulation, the Computational Fluid Dynamics software (CFD) STAR-CCM+ is used, which will solve the Reynolds-Averaged Navier-Stokes equations. The main purpose of this first part is to have an idea of the capabilities of both softwares and to verify their accuracy by comparing the results with other data.

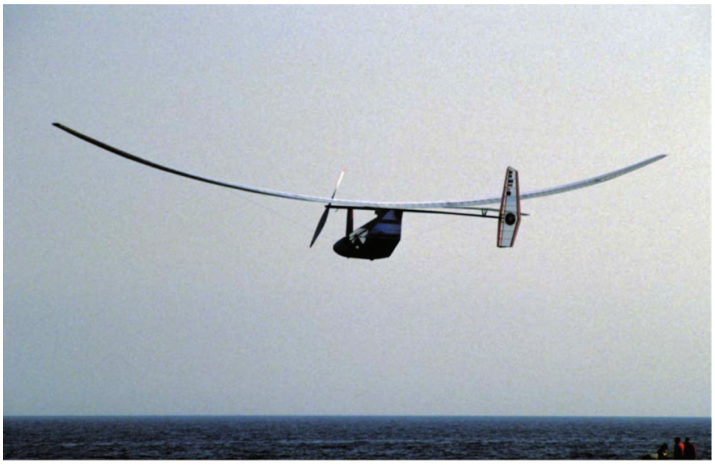

Figure 1. The Daedalus

In the second part, it is attempted to design and optimize a HPA ourselves using AVL and MATLAB. The design will be special in that the HPA should be capable of winning the Kremer International Marathon Competition. This is a prestigious challenge set out by Henry Kremer in which a specific course is to be flown in less than 1 hour. The course is illustrated in Figure 2 and consists of two laps of the outer circuit, followed by a figure-of-eight and two more outer circuits. As such, the total distance is approximately the distance of a marathon. More details can be found in [3].

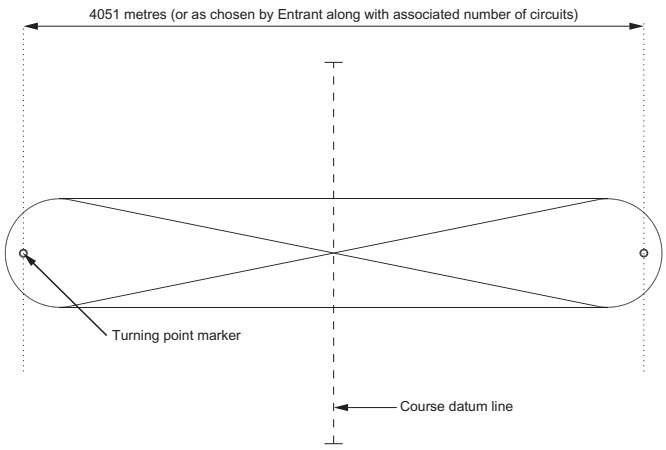

Figure 2. The Kremer International Marathon Competition

As can be seen in Figure 1, the wing experiences a large deformation during flight. This deformation is actually desired for stability reasons and should therefore be carefully designed. To take this aspect into account during the optimization of our own HPA, Fluid-Structure Interaction (FSI) simulations of the wing will be performed coupling AVL and MATLAB. Simulations [4,5] and experiments [6] of FSI are currently also used to optimize commercial aircrafts. Furthermore, the deflection of a wing can be used to reduce its sensitivity to wind gusts [7].

Another special feature of our design is the possibility of adding a second pilot on board of the aircraft. As such, it will be investigated if powering a HPA by two pilots offers some advantages compared to a single pilot.

In the final part, a CFD simulation of the optimized design is performed in STAR-CCM+. Additionally, the physical performance of the candidate pilots for our HPA is measured. Using this data, it will be verified if sufficient human power can be generated in order to complete the Kremer International Marathon Course within time.

2. The Daedalus - Models

As a first step, a 3D CAD model of the Daedalus is constructed, which will give a clear overview of its geometry. This CAD model is further used for the CFD simulation in STAR-CCM+. To perform the simulation in AVL, a second and simplified model will have to be constructed as further explained.

2.1. CAD Model

Most of the geometrical and structural data concerning the Daedalus is made publicly available by MIT [8]. Based on this data, a precise replicate was constructed which can be seen in Figure 3. The Daedalus has a wingspan of 112 ft (34 m), being as large as the wingspan of a Boeing 737-800. The corresponding wing area is 332 ft^2 (31 m^2), resulting in a mean chord length of 2.96 ft (0.90 m). For increased aerodynamic performance, the wing is highly tapered, the ratio of the chord length at the tip to root $(c_{\text{tip}}/c_{\text{root}})$ being equal to 1/3. Due to the tapering, there is a large variation in the chord Reynolds number Re_c, such that the wing is made up of four different airfoils (DAE11, DAE21, DAE31, DAE41), each optimized for a different Reynolds number [9]. During flight, the wing is designed to have a tip deflection of 2 m at a cruise speed of 6.7 m/s [10]. As only the tip deflection was specified, the deformation of the complete wing is assumed as parabolic. The fuselage is the aerodynamic structure surrounding the pilot and is located just underneath the wing. The airfoil used to construct the fuselage was not specifically given but is assumed to be the symmetrical NACA65$_4$-021. Since the Daedalus was designed for long, straight flights, it required no ailerons for its control, steering was accomplished by the all-moving rudder and elevator. These are respectively the vertical and horizontal surface of the tail and are assumed to be constructed of the symmetrical NACA0010. The final structure is the tailboom, a carbon fiber tube going from the nose of the aircraft to its tail, used to connect the different parts of the aircraft. The propeller mounted in front of the aircraft will not be simulated in this work, but will be taken into account in the form of a propulsive efficiency.

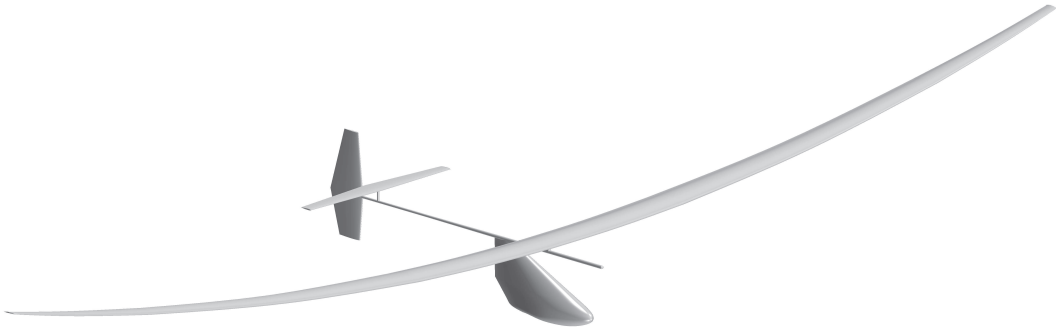

Figure 3. CAD Model of the Daedalus

2.2. AVL Model

When the flow is considered as steady, incompressible, inviscid and irrotational, it can be described by Laplace's equation

$$\nabla^2\Phi = 0 \tag{1}$$

in which $\vec{v} = \nabla\Phi$ and where $\vec{v}$ represents the velocity field. As boundary condition on a wall it holds

$$\nabla\Phi \cdot \vec{n} = 0 \tag{2}$$

which states that the normal component of the velocity on the wall must be zero. To solve Laplace's equation numerically, the Vortex Lattice Method can be applied. In this method, every aerodynamic structure (wing, fuselage, rudder and elevator) should first be represented as a thin surface, located along its camber lines. In AVL, the different structures are defined by specifying a number of sections, each characterized by the type of airfoil, the chord length, the position of leading edge and the incidence, which are then linearly interpolated. By defining the structures in this way, the camber lines are easily determined together with the thin surfaces. These thin surfaces are now further divided into smaller elements, both in the spanwise and chordwise direction. Figure 4 shows the AVL model of the Daedalus plotted on top of its CAD model. Note that as the tailboom does not consist of airfoil sections, it cannot be included into the AVL model.

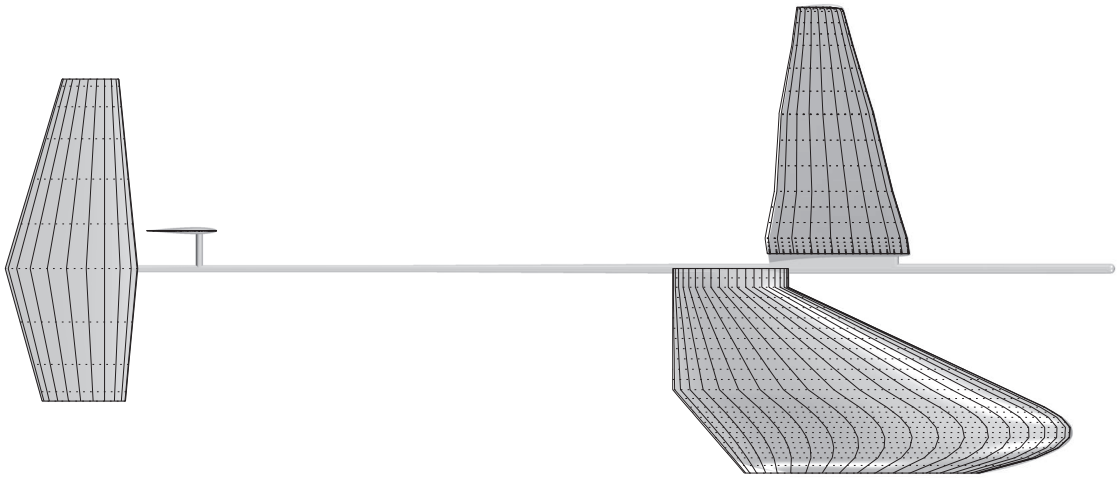

Figure 4. AVL Model of the Daedalus plotted on top of its CAD Model

The principle of the Vortex Lattice Method is now briefly explained and the reader is referred to [11] for more details. In every element, a horseshoe vortex is defined, which is characterized by certain a strength. The horseshoe vortices will each induce a velocity field according to the Biot-Savart Law and which is proportional to their strength. The problem now consists of finding the strengths of every horseshoe vortex, such that the boundary condition (2) is fulfilled. Once the strengths are known, it is possible to calculate the lift and induced drag of every element.

In order to take the profile drag (viscous + pressure drag) into account, AVL has the option to include the drag polar of every section used in defining the geometry. To see how it is done, consider Figure 5, showing the drag polar of the airfoil DAE11, in this case for a chord Reynolds number of 500 000. This drag polar was constructed using the panel code XFOIL [12]. To define this drag polar into AVL, three specific points should be determined; negative stall, minimal drag and positive stall. These points are indicated in the figure and should be given to AVL. Based on these three points, AVL will now construct two parabolic curves, each starting in the point of minimal drag. As such, the actual drag polar is slightly approximated as shown in the figure. Note that a specific drag polar will have to be defined for every section, which will depend on its type of airfoil and its chord Reynolds number.

Finally, to determine the equilibrium position of the Daedalus at a certain flight velocity, AVL requires its mass and Center of Gravity (CG). Based on the structural data provided by MIT, the mass and CG of the different structures were determined and are summarized in Table 1. Note that the empty weight of the Daedalus, so without pilot, is equal to just 30.60 kg. This means that the pilot (74.84 kg) was almost 2.5 times heavier than the aircraft itself. In equilibrium, the total lift should equal the weight of the Daedalus and the pitching moment around its CG should be zero. This can be

accomplished by adjusting the Angle of Attack (AoA) of the aircraft and the local AoA of the elevator. These two angles will be a direct output of AVL, together with the induced and profile drag when the drag polars have been included.

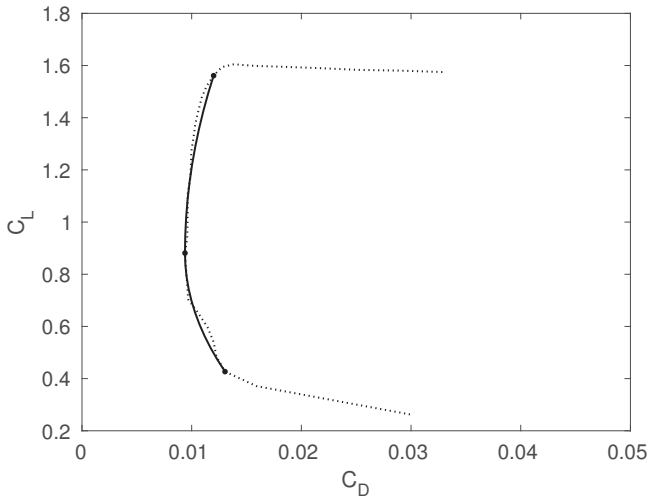

Figure 5. Drag polar of DAE11 at a Reynolds number of 500 000

Table 1. Mass and CG breakdown of the Daedalus

	Mass (kg)	x_{CG} (m)	y_{CG} (m)	z_{CG} (m)
Wing	17.10	0	0	0.94
Fuselage	1.91	0.76	0	-0.85
Elevator	0.52	5.33	0	0.31
Rudder	0.52	6.10	0	0.26
Tailboom	1.49	1.55	0	0
Propeller	1.36	-1.98	0	0
Gearbox	0.91	-0.91	0	0
Crankset	1.36	-0.91	0	-1.52
Water	5.44	-0.06	0	-1.68
Pilot	74.84	0	0	-1.22
Daedalus	105.44	0.04	0	-0.83

2.3. Two-dimensional CFD Model

As HPAs fly at very low speeds (around 6.7 m/s in the case of the Daedalus), their corresponding chord Reynolds numbers are mostly well below 1 million. The result is that the flow will remain laminar over a noticeable fraction of the airfoil and that the transition process from laminar to turbulent will take place in the form of a so-called laminar separation bubble. This phenomenon is illustrated in Figure 6.

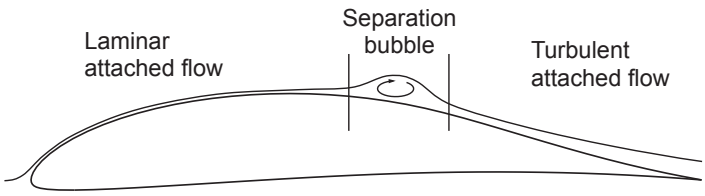

Figure 6. Laminar Separation Bubble [13]

To predict this phenomenon in CFD, two models will be used; the k-ω SST turbulence model and the γ-Re$_\theta$ transition model. The γ-Re$_\theta$ transition model is based on a correlation and will predict the onset of transition. In order to investigate the accuracy of the γ-Re$_\theta$ transition model, some 2D simulations of an airfoil will be performed first and compared with experimental data from wind tunnel tests performed at the University of Illinois at Urbana-Champaign (UIUC). The investigated airfoil is the FX63-137, specifically designed for low Reynolds numbers and used in some early HPA designs. For the 2D simulations, a circular fluid domain is considered, with a radius of 50 chord lengths and the airfoil located in the center. The outer boundary is cut at $+45$ and -45 degrees starting from the trailing-edge side, allowing to define a velocity inlet and pressure outlet. All simulations are performed at a Reynolds number of 500 000. The fluid domain is now discretized, in which the 2D mesh is actually derived from a 3D mesh. More specifically, using the trimmed hexahedral mesher of STAR-CCM+, a 3D mesh is first constructed around a wing. This wing has a chord length of unity and is made up of the airfoil FX63-137. By now considering a specific section of this 3D mesh, the 2D mesh is obtained. The advantage of this 2D mesh, is that it will allow to evaluate the quality of the 3D mesh. This is useful as a trimmed hexahedral mesh will later on be constructed around the complete Daedalus. In order to explore the full capability of the γ-Re$_\theta$ transition model, the trimmed hexahedral mesh was constructed with an extremely fine boundary layer mesh, shown in Figure 7.

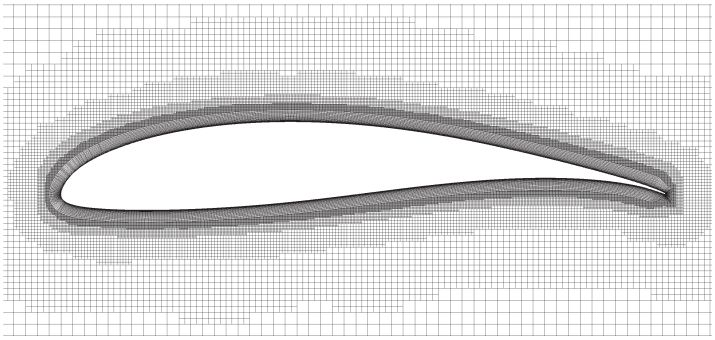

Figure 7. 2D section of trimmed hexahedral mesh (FX63-137)

This boundary layer mesh consists of a 30-layer, 30 mm thick inflation layer, hyperbolically extruded. Its first cell height is 0.01 mm, assuring a $y^+ < 1$, which is needed in order to properly resolve the boundary layer. To determine the precise location of transition, a chordwise spacing of 1 mm is applied. The complete 2D mesh consists of 93 000 cells. The flow is further modeled as incompressible, justified by the very low Mach numbers of HPAs and additionally, the turbulent intensity is set to 0.07% together with a turbulent viscosity ratio of 10.

2.4. Three-dimensional CFD Model

As outlined, the objective is to simulate the entire Daedalus in CFD. However, using its symmetry, half of the aircraft will be sufficient. For this simulation, the fluid domain is constructed as a half-sphere with a radius of 100 m. The outer boundary is again split into a velocity inlet and a pressure outlet. Using the trimmed hexahedral mesher, the complete fluid domain is discretized and is shown in Figure 8. The boundary layer mesh is somewhat coarser, to limit the number of cells, but still provides sufficient accuracy. It consists of a 15-layer, 20 mm thick inflation layer, in which the maximal edge size of the elements on the geometry is 5 mm. The complete mesh consists of 52 million cells.

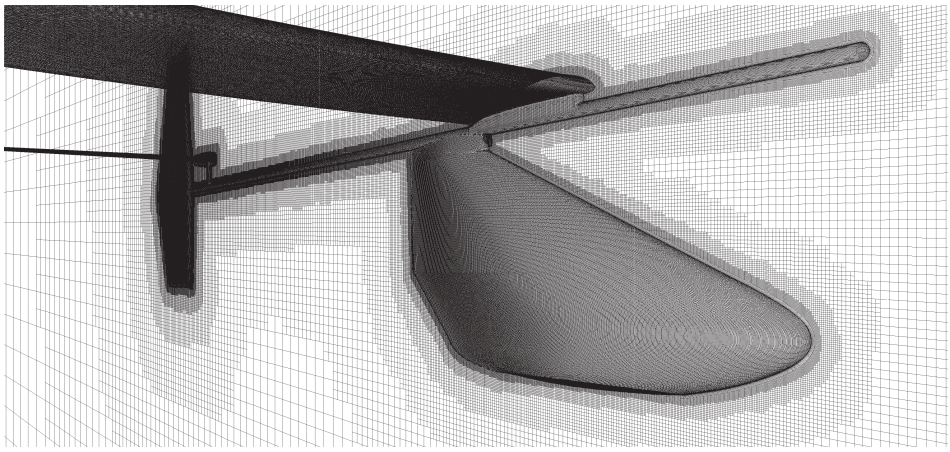

Figure 8. Trimmed hexahedral mesh around the Daedalus

3. The Daedalus - Results

For a clear overview, the results of the different models are discussed in separate sections. The two dimensional CFD simulations are analysed first and will provide additional insight when later on analysing the three dimensional simulations of the Daedalus in AVL and STAR-CCM+.

3.1. Results two-dimensional CFD

The results of the 2D CFD simulations can be seen in Figure 9. In addition to the experimental data and CFD simulations using the γ-Re$_\theta$ transition model, results have been added of CFD simulations using the k-ω SST turbulence model without transition together with the results of the panel code XFOIL. The 2D CFD simulations were performed transient, in which the solution was found to be steady after approximately 10 s in all of the cases considered. The time step was taken as 0.01 s. Figure 9a shows the lift coefficient C_L versus the angle of attack α. The CFD simulations using the transition model are seen to agree the closest with the experimental data and show a slight overprediction for positive angles of attack. The results of CFD without transition and XFOIL are seen to respectively underestimate and overestimate the lift for all angles of attack considered. Further, in Figure 9b, the drag coefficient C_D is shown as a function of the angle of attack. CFD with transition and XFOIL show a comparable accuracy for angles of attack between 0 and 6 degrees, in which XFOIL is found to be more accurate beyond this range. Note that there is a consistent overprediction by CFD with transition and underprediction by XFOIL. Neglecting the transition phenomenon results in a heavy overprediction of the drag. For positive angles of attack, this overprediction is found to be more than 50%. It is clear that the Daedalus will have to be simulated using a transition model, in order to obtain accurate results. Using the top two figures, the drag polar can now be constructed which is shown in Figure 9c. CFD with transition is seen to agree well with the experimental data, especially for positive angles of attack. Due to the consistent overprediction of the lift and underprediction of the drag made by XFOIL, the corresponding drag polar is seen to have the same shape as the experimental data, but is shifted upwards. For positive angles of attack, this leads to an underestimation of the drag coefficient as a function of the lift coefficient. As an example, for a lift coefficient of 1.4, the underprediction with respect to the experimental data is found to be 14%. Finally, Figure 9d shows the lift-to-drag ratio versus the angle of attack. CFD with transition is seen to agree well but predicts a somewhat lower maximal value of L/D.

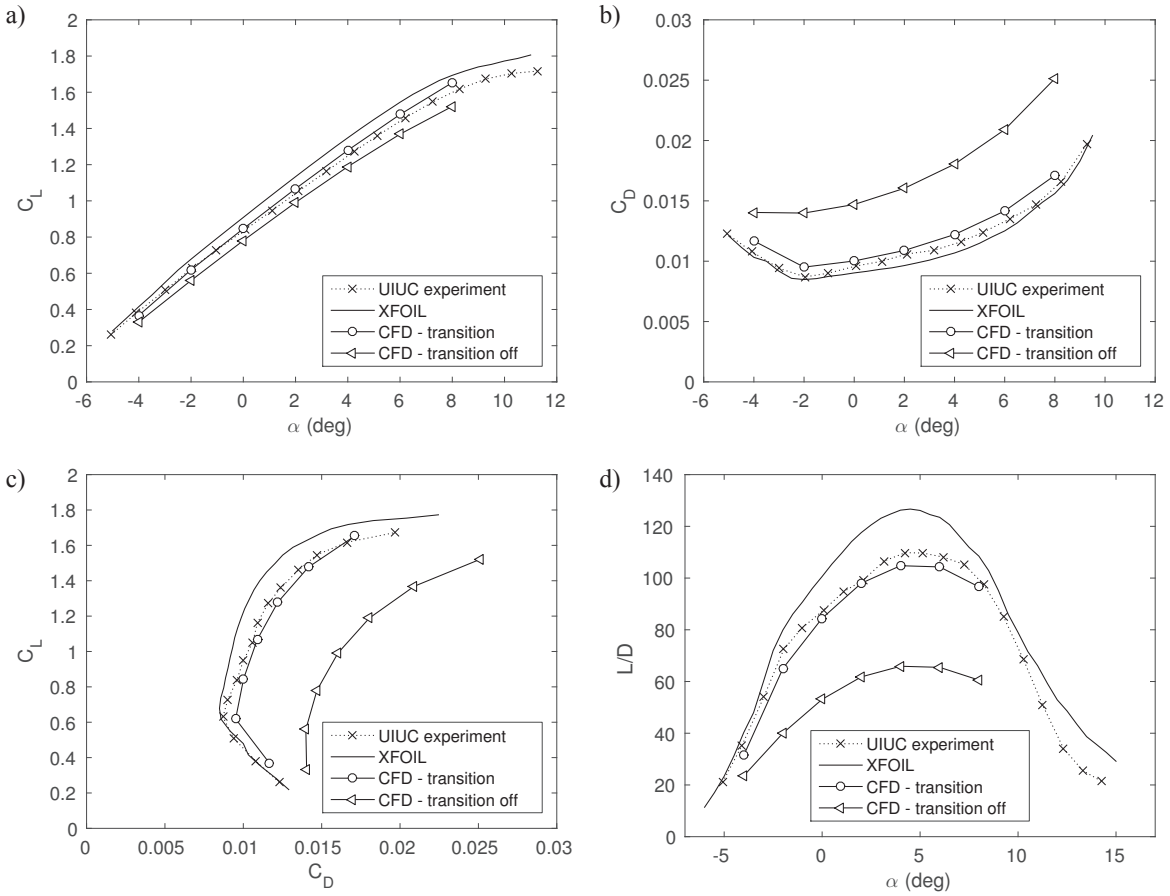

Figure 9. Two dimensional results of the airfoil FX63-137; (**a**) lift coefficient versus angle of attack, (**b**) drag coefficient versus angle of attack, (**c**) drag polar, (**d**) lift-to-drag ratio versus angle of attack.

In Figure 10a, the pressure coefficient around the airfoil is given at zero degrees angle of attack. The pressure distributions predicted by CFD with transition model and XFOIL clearly show the presence of a laminar separation bubble on both the suction and pressure side of the airfoil. When comparing the enclosed surfaces of the different pressure distributions, a clear difference is observed. XFOIL is seen to have the largest enclosed surface, followed by CFD with transition and CFD without transition. However, this observation is in agreement with the lift predictions at zero degrees angle of attack shown in Figure 9a. To see the key difference between the two CFD models, consider Figure 10b, showing the turbulent kinetic energy around the airfoil. In CFD without transition (upper airfoil), the production of turbulent kinetic energy is directly initiated at the leading edge of the airfoil and increases towards the trailing edge. In CFD with transition (lower airfoil), the production is only initiated after the laminar flow has locally detached (Figure 6). From the moment the detached flow becomes sufficiently turbulent, it will reattach, corresponding with a peak in turbulent kinetic energy.

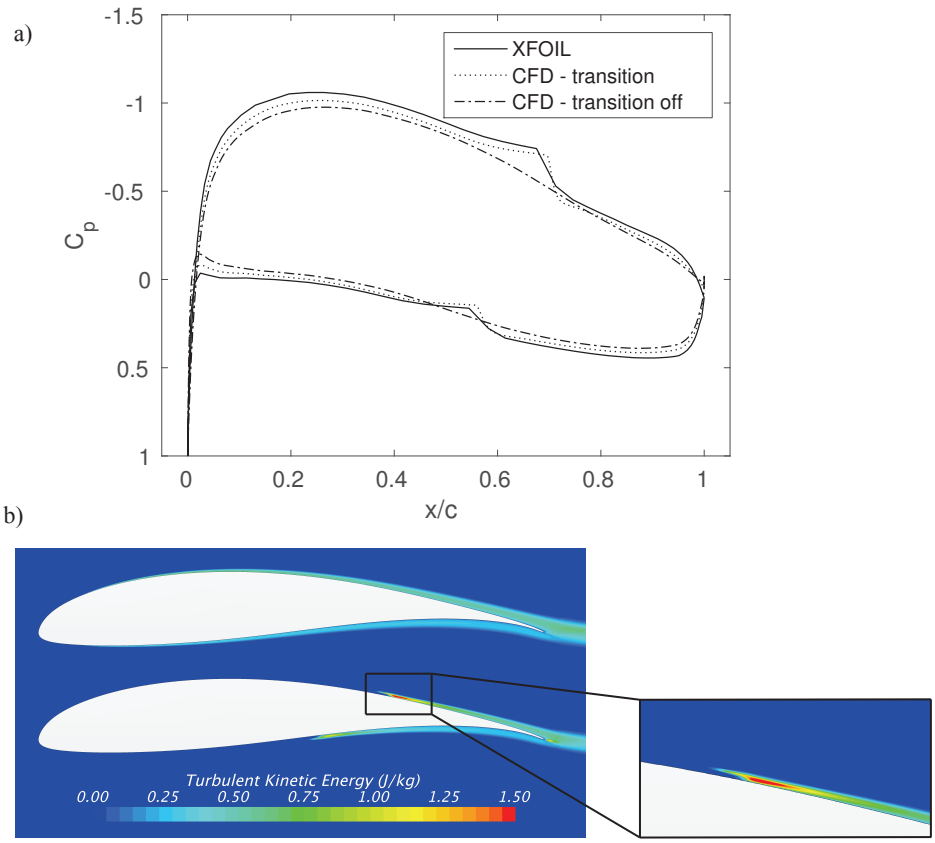

Figure 10. Two dimensional results of the airfoil FX63-137; (**a**) pressure coefficient distribution at zero degrees angle of attack, (**b**) comparison of turbulent kinetic energy (upper airfoil: CFD without transition, lower airfoil: CFD with transition)

3.2. *Results AVL*

The results of the AVL simulation of the Daedalus are given in Table 2. The simulation was performed at the design flight velocity of 15 mph (6.7 m/s), in which the Daedalus was found to fly at an angle of attack of 2.76 degrees in order to generate sufficient lift. Additionally, for the pitching moment to be zero, the elevator had to be trimmed to a negative angle of -4.6 degrees. At this equilibrium position, the total drag was calculated together with its components. Note that this total drag corresponds with the so-called gliding drag of the aircraft, as no propulsion is simulated in AVL.

For the different drag components listed, it is important to know that the induced drag and profile drag only refer to the wing of the Daedalus and that the parasite drag is the difference between the gliding drag and the drag of the wing. Based on the gliding drag and the propulsive efficiency, consisting of the mechanical and propeller efficiency, the corresponding pilot power is determined. This is thus the actual power that the pilot will have to deliver to keep the aircraft up in the air.

At this point, a comparison can be made with the data from MIT, which is also included in Table 2. It is important to emphasize that the data from MIT are also estimates, but nevertheless, they provide an idea of the actual drag and its components. Comparing the induced drag, AVL is found to predict a somewhat larger value (7%), but is still a reasonable prediction. However, comparing the profile and parasite drag, these are seen to be substantially underpredicted. In case of the profile drag, the underprediction is found to be 19%. Recall that AVL determines the profile drag based on the local lift coefficients of the different sections and the corresponding drag polars generated by XFOIL. In the 2D results, the drag polar of XFOIL was seen to underestimate the profile drag of the airfoil FX63-137.

This airfoil was not used to construct the Daedalus, but contains similar characteristics. Moreover, this underprediction is also observed for different airfoils [13,14]. Before making any conclusions on the performance of AVL, let us first examine the results of the CFD simulation.

Table 2. Comparison estimated performance of the Daedalus

	MIT [15]	**AVL Model**	**CFD Model**
Flight Velocity (m/s)	6.7	6.7	6.7
Gliding Drag (N)	27	22.2	26.2
Induced (N)	10.5 (35%)	11.2	–
Profile (N)	12.0 (40%)	9.7	–
Parasite (N)	4.5 (15%)	1.3	2.5
Lift (N)	1034.4	1034.4	1034.8
Propulsive Efficiency	0.90	0.90	0.90
Pilot Power (W)	201	165	195
AoA Aircraft (°)	–	2.76	2.76
AoA Elevator (°)	–	-4.6	-4.6
Calculation time	–	9.94 *s*	1 day

3.3. Results three-dimensional CFD

The CFD simulation of the Daedalus was performed steady in which its configuration was adjusted to be identical as in AVL. As such, the angle of attack of the aircraft and elevator were the same in both simulations. The results of the CFD simulation can be found in Table 2. The generated lift is seen to agree extremely well, such that the Daedalus is also in equilibrium in the CFD simulation. Comparing the total drag of the wing, being 23.7 N in the CFD simulation versus 22.5 N estimated by MIT, the value is seen to agree within 5%. Note that 90% of the gliding drag is due to the wing. As for the AVL simulation, the parasite drag is strongly underpredicted. However, some simplifications were made to both models of the Daedalus, resulting in a somewhat lower parasite drag. In both models, the external lift wires of the Daedalus (Figure 11) were not included and the fuselage was made slightly more aerodynamic. In reality, the fuselage contained a ventilation opening to draw in air for the pilot and had an additional structure mounted on its nose to drive the propeller (can be seen in Figure 1). Recall that in the AVL model, also the tailboom is left out. Comparing the pilot power, the CFD simulation is seen to agree within 3% with the value of MIT. So, although there is a slight overprediction of the total drag of the wing and a noticeable underprediction of the parasite drag, the CFD simulation provides a very reasonable estimate of the pilot power.

Figure 11. Lift wires of the Daedalus

In Figure 12, the turbulent kinetic energy is shown close to the surface of the Daedalus together with the constrained streamlines which help in visualizing the laminar separation bubble. At the position were the streamlines seem to be halted for the first time, the flow locally detaches and at the position of peak turbulent kinetic energy, the flow reattaches. The size of the laminar separation bubble on the wing is seen to be approximately constant along its span, except near the wingtip. Note that the pressure side of the wing is completely laminar. The flow around the rudder is clearly influenced by the wake of the wing, in which the midsection is seen to be fully turbulent, whereas the upper section is largely laminar with transition occurring near the trailing edge.

For the intended optimization of a HPA, it is interesting to compare the calculation time of both simulations (Table 2). It is clear that AVL will be an ideal tool for evaluating a lot of different designs. As a small conclusion, the CFD simulation was seen to predict the pilot power very accurately, but needs a large amount of computational power and time for a single simulation. On the other hand, the AVL simulation was found to underpredict the pilot power by about 18%, in which the underprediction was partly attributed to the drag polars of XFOIL. However, the power of AVL lays in its very short calculation times which is essential when optimizing and as all designs are evaluated in the same software, a fair comparison can be made.

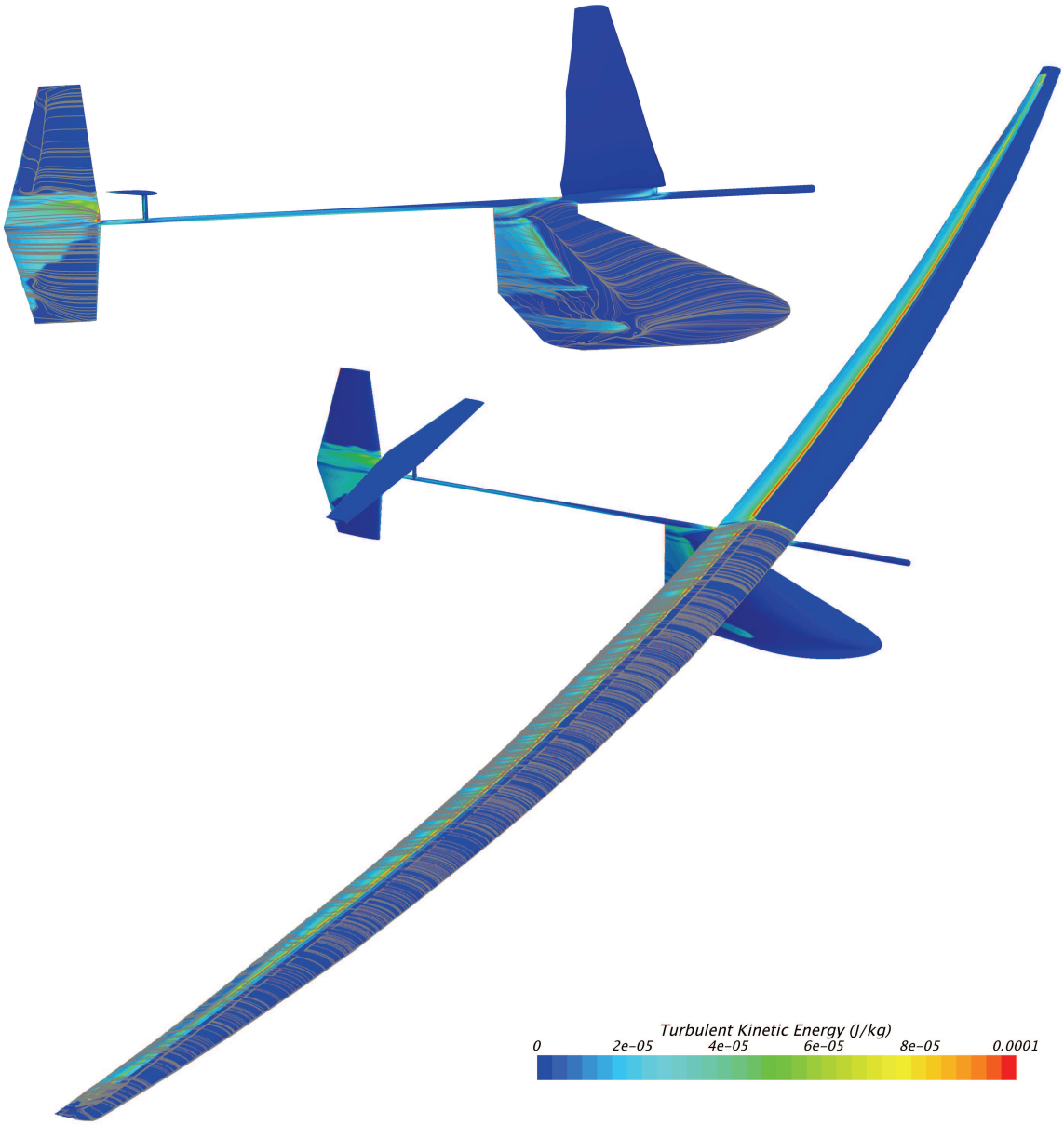

Figure 12. Transition from laminar to turbulent on the Daedalus visualized by the constrained streamlines and the turbulent kinetic energy

4. FSI Optimization

It was shown in Table 2 that the drag of the wing is the main contributor to the aircraft's total drag. As such, the first step in designing our HPA for the Kremer International Marathon Competition will consist of optimizing a wing. To do so, both the outer geometry and mechanical structure of a wing will be parameterized. Using this parametric model, it will be possible to generate any wing geometry. However, not every wing geometry will be structurally feasible with regard to strength and desired deformation. More specific, by performing FSI simulations, it is possible to determine the material stresses and deformation of the wing during flight. These stresses and deformation will entirely depend upon the wing's structural parameters as the flight conditions will be kept constant. So, it must be verified if a set of structural parameters can be found, which result in allowable material stresses and a certain design tip deflection. This design tip deflection is mostly determined from stability requirements. As can be expected, in most cases, multiple feasible sets will exist. So, the challenge is to find a feasible set, which in addition minimizes the mass of the wing. This structural optimization procedure is schematically shown in Figure 13 and will now be explained in some more detail.

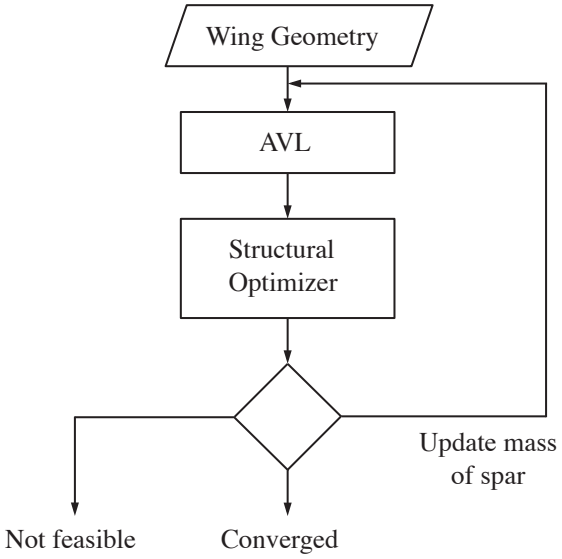

Figure 13. Structural optimization procedure

4.1. Wing Geometry

In undeformed state, the outer geometry of the wing is described by its airfoil, span b, tip chord length c_{tip}, taper ratio λ $(c_{\text{tip}}/c_{\text{root}})$, twist angle θ and the relative position x/c of the spar's center. These design variables are indicated on half of a wing in Figure 14. Note that the relative position x/c fixes the position of the leading edge with respect to the straight spar. In our model, this relative position is assumed constant along the wing. Further note that only one type of airfoil is used for the entire wing and that the variation in chord length is linear from root to tip. The input for the structural optimizer is now a single wing geometry described by the appropriate values of the design variables.

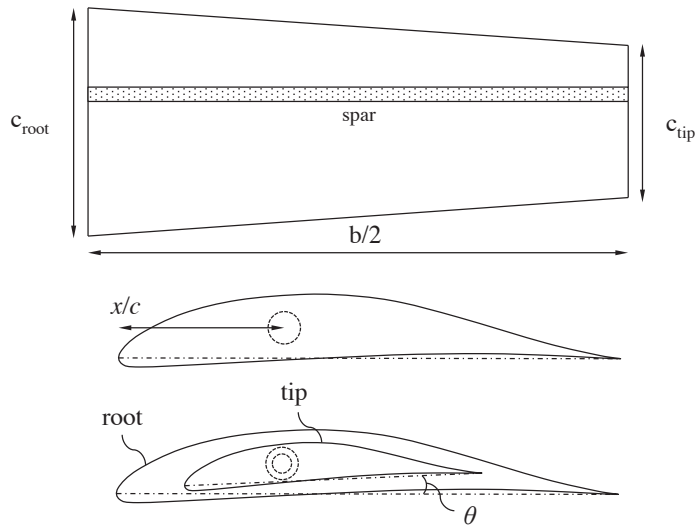

Figure 14. Parameterized wing geometry

4.2. AVL

Now that the geometry of the wing is defined, an initial simulation can be performed in AVL. In order to perform the simulation, two conditions will have to be defined; the flight velocity and the desired lift. The flight velocity follows from the challenge of completing a marathon distance (42 195 m) in less than 1 hour. This results in a minimal flight velocity of 11.72 m/s. However, the flight velocity is safely rounded to 12 m/s. Although only the wing of our HPA is being simulated, it is assumed that the wing must generate just enough lift to carry the mass of the pilot(s) and the mass of the complete aircraft structure. At this moment, the mass of the aircraft is still unknown, such that the mass of the Daedalus (30.60 kg) is taken as an initial guess for a HPA for 1 pilot and an additional 10 kg is added in case of a HPA for 2 pilots. Once both conditions are specified, AVL will determine the angle of attack of the wing, such that the needed lift is being generated. The results of interest are now, the total drag (induced + profile drag) of the wing and the so-called strip forces, being the resultant forces acting on every spanwise strip of the wing. These are schematically illustrated in Figure 15.

4.3. Structural Optimizer

The wing's mechanical structure is composed of two main parts. The first part is the wing's internal structure, consisting of a main spar (a thin-walled circular tube) and closely spaced ribs. This internal structure is also the basis for the wing's outer geometry, which is obtained by wrapping a Mylar sheet around the different ribs of the wing. The second mechanical structure is an external lift wire. This lift wire will offer some structural advantages as will be seen. In order to properly design the wing's mechanical structure, the process is started by fixing the outer diameters of the main spar. Consider the cross sections of the wing at root and tip, shown in Figure 14. As the relative position x/c will be known and constant along the span, it is possible to determine the section's thickness at this position. Note that this thickness is proportional to the chord length of the section. The outer diameter will now be chosen as a fraction of this thickness. For the root and tip section, the outer diameter is taken as respectively 65% and 80%. These fractions are in close agreement with the values of the Daedalus. In addition, when the diameter at the root is found to be smaller than at the tip, e.g. when the wing is not tapered, both fractions are set to 65%. As such, the outer diameter at the root is always larger or equal to the outer diameter at the tip. It is now assumed that the outer diameters vary linearly from root to tip, which agrees with the linear variation of the chord lengths. The advantage of fixing the outer diameters geometrically, is the guarantee that the spar will always fit into the wing.

At this point, it is important to know that the final result of the structural optimization will be a set of two wall thicknesses. These correspond with the thickness of the spar's wall at the root and tip. The procedure of finding the optimal set of wall thicknesses will now be further explained. Note that optimal again refers to minimizing the mass of the spar while maintaining sufficient strength and the desired tip deflection during flight.

Consider an arbitrary set of wall thicknesses. As the outer diameters of the spar are fixed for a given wing geometry, these thicknesses immediately allow to calculate the inner diameters of the spar at the root and tip. To determine the inner diameter at an intermediate position, a similar approach is applied as for the outer diameters, in which the inner diameters are assumed to vary linearly from root to tip. At this point, the geometry of the spar is fully defined. By now specifying the spar's material properties, it is possible to determine its bending stiffness EI, in which E is Young's modulus and I the second moment of area. Note that in most cases, the bending stiffness will not be constant along the span of the wing, as the inner and outer diameters are allowed to vary. The next step consists of calculating the wing's deformation during flight. For these structural calculations, the entire wing is simply represented by its main spar. To determine the deformation, only half of the spar is considered and modelled as a cantilevered beam. In this simplified model, only the vertical deformation due to the lift forces will be calculated. Note that the lift-to-drag ratio of the wing is usually very high for HPAs, being in the order of 45 for the Daedalus, such that the horizontal deformation will be much smaller and therefore neglected. Also note that the torsion of the wing is not taken into account here. This simplified model is shown in Figure 15.

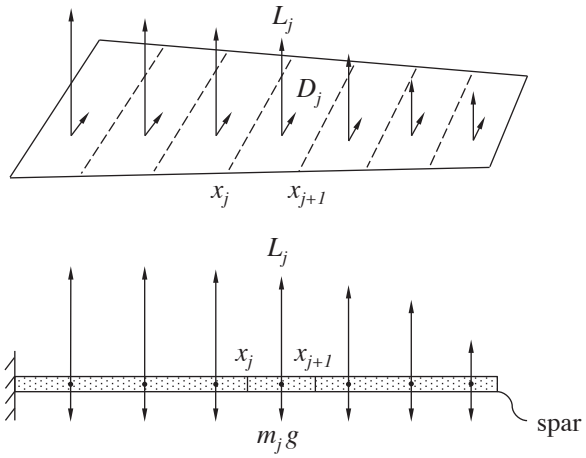

Figure 15. Simplified model to determine vertical deformation of the wing

Based on the Euler-Bernoulli beam theory and finite differencing, the deformation of the wing can now be easily determined numerically as follows

$$\begin{aligned} V_{j+1} - V_j &= f_j \\ M_{j+1} - M_j &= \left(\frac{V_{j+1} + V_j}{2}\right)(x_{j+1} - x_j) \\ \theta_{j+1} - \theta_j &= \left(\frac{(M/EI)_{j+1} + (M/EI)_j}{2}\right)(x_{j+1} - x_j) \\ u_{j+1} - u_j &= \left(\frac{\theta_{j+1} + \theta_j}{2}\right)(x_{j+1} - x_j) \end{aligned} \tag{3}$$

in which $f_j = L_j - m_j g$ and where V represents the shear force, M the bending moment, θ the deflection angle and u the deflection. The lift forces L_j follow from the initial AVL simulation. At this moment, the tip deflection of the wing can be calculated for a certain set of wall thicknesses. It is now

that the purpose of the external lift wire can be understood. If the actual tip deflection is found to be larger than the desired one, it is calculated which amount of vertical force the lift wire must exert onto the wing in order to achieve the desired tip deflection. Adjusting the lift wire's vertical force is easily achieved by changing its length, making it more tight or loose. The desired tip deflection will actually follow from a desired dihedral angle Γ,

$$\tan(\Gamma) = \frac{u_{\text{tip}}}{b/2} \tag{4}$$

and as such depends upon the span of the wing. In the calculations, the lift wire is assumed to be connected underneath the fuselage and halfway between the root and tip of the wing. Note that if the initial tip deflection is smaller than desired, that the use of an external lift wire becomes irrelevant. Besides obtaining the desired tip deflection or dihedral, the lift wire has an additional advantage as it will reduce the bending moments acting on the wing. As such, there is a possibility of making the wing's structure lighter for the same level of material stresses. However, there will also be some additional parasite drag.

At this point, a number of important conditions must be verified in order for the set of wall thicknesses to be feasible. First, the stresses occurring within the wing's spar and lift wire should be below a certain maximal limit to avoid structural failure. Second, the deflection of the wing may nowhere be negative. This second condition might need some further clarification. It is possible that the force exerted by the lift wire is so strong, that the spar will deform negatively (downwards direction) near the root, but still achieves the desired tip deflection due to extreme bending towards the tip of the wing. These designs will not be considered as valid. The challenge now consists of finding a feasible set of wall thicknesses (if possible) and which in addition minimizes the mass of the spar. This optimization procedure was implemented in MATLAB.

4.4. Decision Block

If no valid set of wall thicknesses was found, the wing geometry is considered as infeasible. If on the other hand, an optimal set was found, the mass of the main spar can now be updated. The initial mass of the spar is taken as 8.62 kg, which corresponds with the spar of the Daedalus [1]. Once the mass has been updated, a new simulation is performed in AVL, resulting in a new angle of attack, total drag and strip forces. The process of optimizing the set of wall thicknesses is rerun and the complete loop is repeated until the relative change in the spar's mass is less than 1%.

4.5. Cases

To find the optimal complete wing, a large Design of Experiments will be performed, in which a large set of different wing geometries is generated and individually structurally optimized. The optimal wing is then taken as the wing geometry with the lowest total drag and which is structurally feasible. As mentioned in the introduction, it is intended to investigate if powering a HPA by two pilots offers some advantages, such that two Design of Experiments were performed. The first corresponds to a single-pilot design, whereas the second corresponds to a dual-pilot design. The details of the Design of Experiments are given in Tables 3 and 4. The two pilots are no professional athletes, but rather two young engineering students, whose physical performance will be measured in the final part. Table 3 contains the lower and upper boundary of every geometrical design variable, together with its step size. Note that the relative position x/c of the spar's center has been set to 0.33 and that the desired dihedral angle Γ is taken as 6 degrees. These two values closely agree with the Daedalus. Further, 12 different airfoil types were investigated, in which each airfoil is specifically designed for low-Reynolds number flows. To avoid evaluating uninteresting regions in our Design of Experiments, a coarser scan was done first, which allowed to adjust the lower and upper boundaries given in Table 3. The twist angle was set to zero degrees as its influence will only be investigated on the complete optimized HPA. Table 4 contains the structural properties of both the main spar and the

lift wire. The main spar is constructed from High Modulus Carbon Fiber (HMCF), whereas the lift wire is a stainless steel wire rope. The material limits are indicated by the tensile strength (TS) in case of the spar and by the minimum breaking load (MBL) in case of the lift wire (LW). For both structures, a safety factor (SF) of 4 was chosen. Note that a different diameter of lift wire is used in case of the dual-pilot and that the minimal thickness of the main spar is set to 0.8 mm (Table 3).

Table 3. Design of Experiments - Geometrical design variables

	Lower Boundary	**Upper Boundary**	**Step Size**
x/c	0.33	–	–
Γ (°)	6	–	–
b (m)	15	40	0.25
c_{tip} (m)	0.35	0.5	0.01
λ	0.25	1	0.01
θ (°)	0	–	–
t_{spar} (mm)	0.8	10	–

Table 4. Structural properties of spar and lift wire

	Single-Pilot	**Dual-Pilot**
$m_{\text{pilot(s)}}$ (kg)	56.4	56.4 + 50.2
ρ_{spar} (kg/m^3)	1600	1600
E_{spar} (GPa)	200	200
TS_{spar} (MPa)	1600	1600
SF_{spar}	4	4
MBL_{LW} (MPa)	1570	1570
SF_{LW}	4	4
d_{LW} (mm)	18	25

4.6. Results

The results of both Design of Experiments are given in Table 5. For each airfoil type, the geometrical and structural data of the optimal design is given. In every optimal design, the wing is found to be tapered, in which the optimal tip chord length corresponds to its lower boundary. The wings are somewhat more tapered in the dual-pilot case, the taper ratio λ being smaller compared to the single-pilot case. The higher lift needed in the dual-pilot case, results in a larger optimal wing span b, a larger angle of attack AoA when comparing the optimal designs with the same airfoil and a heavier spar (m_{spar}). The optimal wall thicknesses of the spar at root and tip (t_{root} , t_{tip}) are seen to be identical in each optimal wing design. Note that all designs make use of a lift wire (LW), in which most of the lift wires are exploited to their maximum allowable stress. The maximal stress occurring within the main spar (σ_{spar}) is seen to be comparable in both cases. However, the most interesting result is the drag of the wing. Although the drag is larger in the dual-pilot cases, when dividing the corresponding required power over 2 pilots, there clearly seems to be an advantage. The reduction in required power per pilot is seen to range from 35 to 57 W. The most optimal wing is thus found to be for 2 pilots. Comparing the results of the different airfoils, the E395 is seen to be the most optimal. Using this most optimal wing, our HPA will now be further constructed and designed for 2 pilots.

Table 5. Geometrical and structural data of optimal designs (upper table: single-pilot, lower table: dual-pilot)

Single-Pilot Airfoil	b (m)	c_{tip} (m)	λ –	Γ (°)	t_{root} (mm)	t_{tip} (mm)	m_{spar} (kg)	σ_{spar} (MPa)	σ_{LW} (MPa)	AoA (°)	D (N)	P/pilot (W)
DAE11	20.75	0.35	0.58	6	0.80	0.80	3.53	249	334	3.38	16.85	202
DAE21	21.00	0.35	0.58	6	0.81	0.81	3.31	298	367	3.11	15.58	187
DAE31	20.25	0.35	0.62	6	1.09	1.09	3.83	274	359	3.20	15.22	183
E395	22.00	0.35	0.64	6	1.00	1.00	4.18	273	388	2.21	14.18	170
E396	22.50	0.35	0.62	6	0.81	0.81	3.77	287	392	1.79	14.62	175
E397	22.75	0.35	0.63	6	0.80	0.80	3.89	277	391	1.92	14.92	179
E398	23.25	0.35	0.64	6	0.80	0.80	4.13	264	392	1.95	15.05	181
E399	23.50	0.35	0.66	6	0.80	0.80	4.30	252	391	2.00	15.44	185
FX63-137	23.50	0.35	0.60	6	0.80	0.80	4.18	264	392	-0.49	14.65	176
FX76MP120	18.75	0.35	0.70	6	0.89	0.89	3.00	295	342	1.35	17.10	205
FX76MP140	19.50	0.35	0.70	6	0.80	0.80	3.28	250	329	-2.22	17.15	206
L7769	20.25	0.35	0.58	6	0.98	0.98	3.52	285	355	7.00	16.93	203

Dual-Pilot Airfoil	b (m)	c_{tip} (m)	λ –	Γ (°)	t_{root} (mm)	t_{tip} (mm)	m_{spar} (kg)	σ_{spar} (MPa)	σ_{LW} (MPa)	AoA (°)	D (N)	P/pilot (W)
DAE11	27.50	0.35	0.47	6	1.21	1.21	8.01	284	388	4.50	25.72	154
DAE21	27.75	0.35	0.46	6	1.62	1.62	9.94	255	392	4.27	24.15	145
DAE31	27.25	0.35	0.46	6	1.89	1.89	10.52	253	392	3.79	23.42	141
E395	**28.75**	**0.35**	**0.46**	**6**	**1.65**	**1.65**	**10.94**	**239**	**388**	**2.88**	**22.47**	**135**
E396	28.75	0.35	0.46	6	1.36	1.36	9.68	250	392	2.79	23.04	138
E397	28.50	0.35	0.48	6	1.32	1.32	9.38	253	392	3.27	23.35	140
E398	29.25	0.35	0.47	6	1.20	1.20	9.32	250	392	2.98	23.86	143
E399	28.75	0.35	0.46	6	0.90	0.90	7.33	284	392	2.86	24.26	146
FX63-137	29.50	0.35	0.42	6	1.03	1.03	8.38	265	392	0.12	23.35	140
FX76MP120	26.25	0.35	0.55	6	1.93	1.93	10.20	255	392	2.17	24.99	150
FX76MP140	27.00	0.35	0.57	6	1.46	1.46	9.22	258	392	-1.17	24.75	149
L7769	27.25	0.35	0.43	6	1.64	1.64	9.45	266	391	7.49	26.72	160

4.7. Complete Optimized Design

The idea consists in taking the Daedalus and replacing its wing by our own optimized wing and to adjust its fuselage to fit a second pilot. The incidence of the wing with respect to the aircraft was taken as the angle of attack determined in Table 5 and its position along the aircraft followed from a small optimization. The optimized wing was further given a twist of 1 degree, found to slightly increase its performance. The fuselage was extended by 1.5 m, assuring sufficient space for the second pilot. Concerning the stability, both the Daedalus and our optimized HPA were found to be statically stable in AVL. The CAD model of the wing and fuselage of our optimized HPA is shown in Figure 16 together with the Daedalus for comparison.

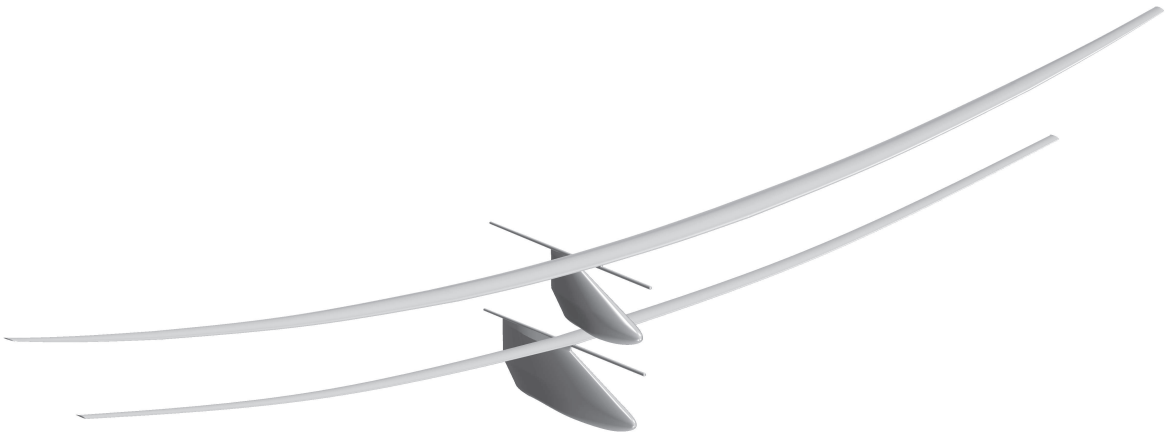

Figure 16. Comparison of wing and fuselage (upper: Daedalus, lower: optimized dual-HPA)

The optimized HPA is now simulated in STAR-CCM+, being the final simulation. As for the Daedalus, the CFD simulation was performed steady, in which the flight velocity was set to 12 m/s and the angle of attack of that aircraft to 1.30 degrees. The results of the CFD simulation are given in Table 6 and are compared with the CFD results of the Daedalus. So, in case of our optimized HPA, each pilot should generate a power of 215 W, in order to obtain a flight velocity of 12 m/s. Note that this flight velocity is 80% higher compared to the Daedalus while the corresponding pilot power has only increased by 10%. An interesting result is that the total drag of the optimized wing is smaller compared to the Daedalus. However, the parasite drag has substantially increased. The drag of the fuselage has increased with a factor 4, which is due to the higher frictional surface. Further note that the generated lift is somewhat larger than the total weight, which is a small safety and allows to carry an additional 2.4 kg. The final step now consists of measuring the physical performance of our 2 pilots.

Table 6. Comparison performance Daedalus versus optimized dual-HPA in STAR-CCM+

	Daedalus	**Optimized Dual-HPA**
Total Mass (kg)	105.4	147.0
Flight Velocity (m/s)	6.7	12
AoA Aircraft (°)	2.76	1.30
Gliding Drag (N)	26.2	32.3
Wing (N)	23.67	22.76
Fuselage (N)	1.05	4.24
Elevator (N)	0.44	2.36
Rudder (N)	0.53	1.60
Tailboom (N)	0.47	1.32
Lift (N)	1034.8	1465.5
Propulsive Efficiency	0.90	0.90
Total Power (W)	195	430
Pilot Power (W)	195	215

5. Final Test

The physical performance was measured using a bicycle trainer with an adaptive resistive power. Starting at a low resistive power of 60 W, the power was gradually increased every 2 minutes by 20 W until the pilot reached total fatigue. The results of the Power Test are shown in Figure 17, in which the heart rates (HR) of both pilots are given as a function of time together with the resistive power. Pilot 1 is seen to produce a maximal power output of 260 W, compared to 240 W for pilot 2. The maximal power output of both pilot together (500W) is definitely larger than the theoretical required

power of 430 W. As such, the pilots can surely reach the design flight velocity of 12 m/s with our optimized dual-HPA. However, in order to win the Kremer International Marathon Competition, the pilots must sustain the aircraft at this 12 m/s during 1 hour. Dividing the theoretical required power over the 2 pilots based on their maximal power output, results in respectively 223.6 W for pilot 1 and 206.4 W for pilot 2. These values correspond with 86% of their maximal physical performance.

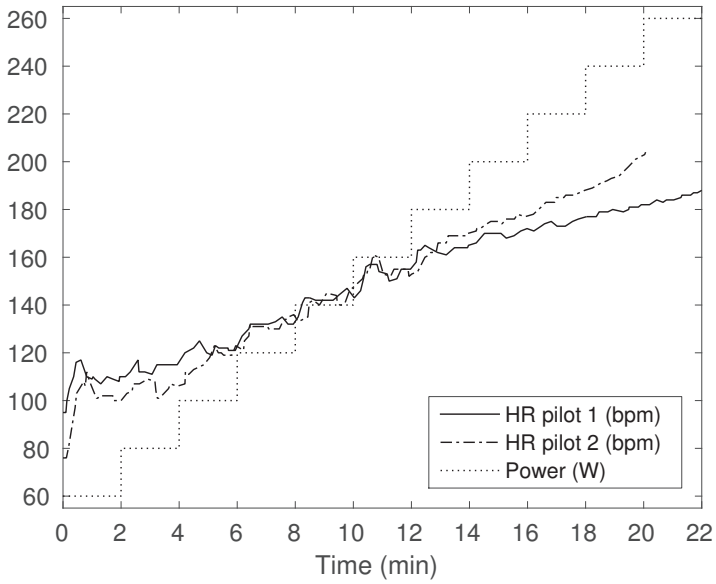

Figure 17. Power test of pilots

6. Conclusions

The two-dimensional CFD simulations proved that the γ-Re$_\theta$ transition model provides accurate results at low Reynolds numbers, while the simulations with only the k-ω SST turbulence model were seen to overpredict the drag by more than 50%. As such, the Daedalus was simulated in CFD using this transition model and resulted in a predicted pilot power within 3% of the value provided by MIT. The AVL simulation of the Daedalus underpredicted the pilot power by 18%, which is partly explained by the lower profile drag in the drag polars of XFOIL, but showed the major advantage of very short calculation times (order of seconds).

For the optimization of our own HPA, a full parametric model was constructed, allowing to generate any wing geometry. To verify the feasibility of every geometric design, AVL and MATLAB were coupled, allowing to perform FSI simulations. Using these simulations, the mechanical structure of the wing was further optimized when feasible, resulting in a minimal mass of the wing while assuring sufficient strength and the desired tip deflection.

Adding a second pilot on board of the aircraft was found to be beneficial compared to a single-pilot design. For the optimized dual-HPA, the maximal power output of both pilots was found sufficient to reach the required flight velocity of 12 m/s in order to win the Kremer International Marathon Competition. However, to really find out if the pilots can sustain the required flight velocity and complete the course within time, the optimized dual-HPA would have to be constructed. An important aspect which will have to be considered then is the steering of the aircraft in order to make the 180° turns present in the course.

Acknowledgments: The authors would like to thank Mark Drela for providing the links to all necessary data of the Daedalus, making this work possible and for helping out with the software AVL.

References

1. McIntyre, J. Man's Greatest Flight. *AeroModeller* **1988**
2. AVL (Athena Vortex Lattice). http://web.mit.edu/drela/Public/web/avl/ (archived on February 2016).
3. Regulations and Conditions for the Kremer International Marathon Competition. http://aerosociety.com/About-Us/specgroups/Human-Powered/Kremer (archived on February 2016).
4. Fazzolari, A.; Gauger, N.R.; Brezillon, J. Efficient aerodynamic shape optimization in MDO context. *Journal of Computational and Applied Mathematics* **2007**, *203*, 548-560.
5. Kenway, G.K.W.; Kennedy, G.J.; Martins, J.R.R.A. Scalable Parallel Approach for High-Fidelity Steady-State Aeroelastic Analysis and Adjoint Derivative Computations . *AIAA Journal* **2014**, *52(5)*, 935-951.
6. Tang, D.; Dowell, E.H. Experimental Aeroelastic Models Design and Wind Tunnel Testing for Correlation with New Theory. *Aerospace* **2016**, *3(2)*, 12.
7. Guo, S.; De Los Monteros, J.E.; Liu, Y. Gust Alleviation of a Large Aircraft with a Passive Twist Wingtip. *Aerospace* **2015**, *2(2)*, 135-154.
8. ASWING: Configuration Development System for Flexible Aircraft. http://web.mit.edu/drela/Public/web/aswing/ (archived on February 2016).
9. Drela., M. Low-Reynolds-Number Airfoil Design for the MIT Daedalus Prototype: A Case Study. *Journal of Aircraft* **1988**, *25*, 724-732.
10. Cruz, J.R.; Drela, M. and M. Drela. Structural Design Conditions for Human Powered Aircraft. OSTIV Conference, **1989**.
11. Katz, J.; Plotkin, A. *Low-Speed Aerodynamics, 2nd ed.; Cambridge University Press*, **2001**.
12. *XFOIL: Subsonic Airfoil Development System. http://web.mit.edu/drela/Public/web/xfoil/ (archived on February 2016).*
13. *Hansen, T. Modeling the Performance of the Standard Cirrus Glider using Navier-Stokes CFD.* Technical Soaring **2014**, 38, *5-14.*
14. *Morgado, J.; Vizinho, R.; Silvestre, M.A.R.; Páscoa, J.C. XFOIL vs CFD performance predictions for high lift low Reynolds number airfoils.* Aerospace Science and Technology **2016**, 52, *207-214.*
15. *Drela, M. Aerodynamics of Human-Powered Flight.* Annual Review of Fluid Mechanics **1990**, 22, *93-110.*

A.2 Detailed Overview Drawings

The following pages contain the detailed overview drawings of the Gossamer Condor, Gossamer Albatross and the Daedalus.

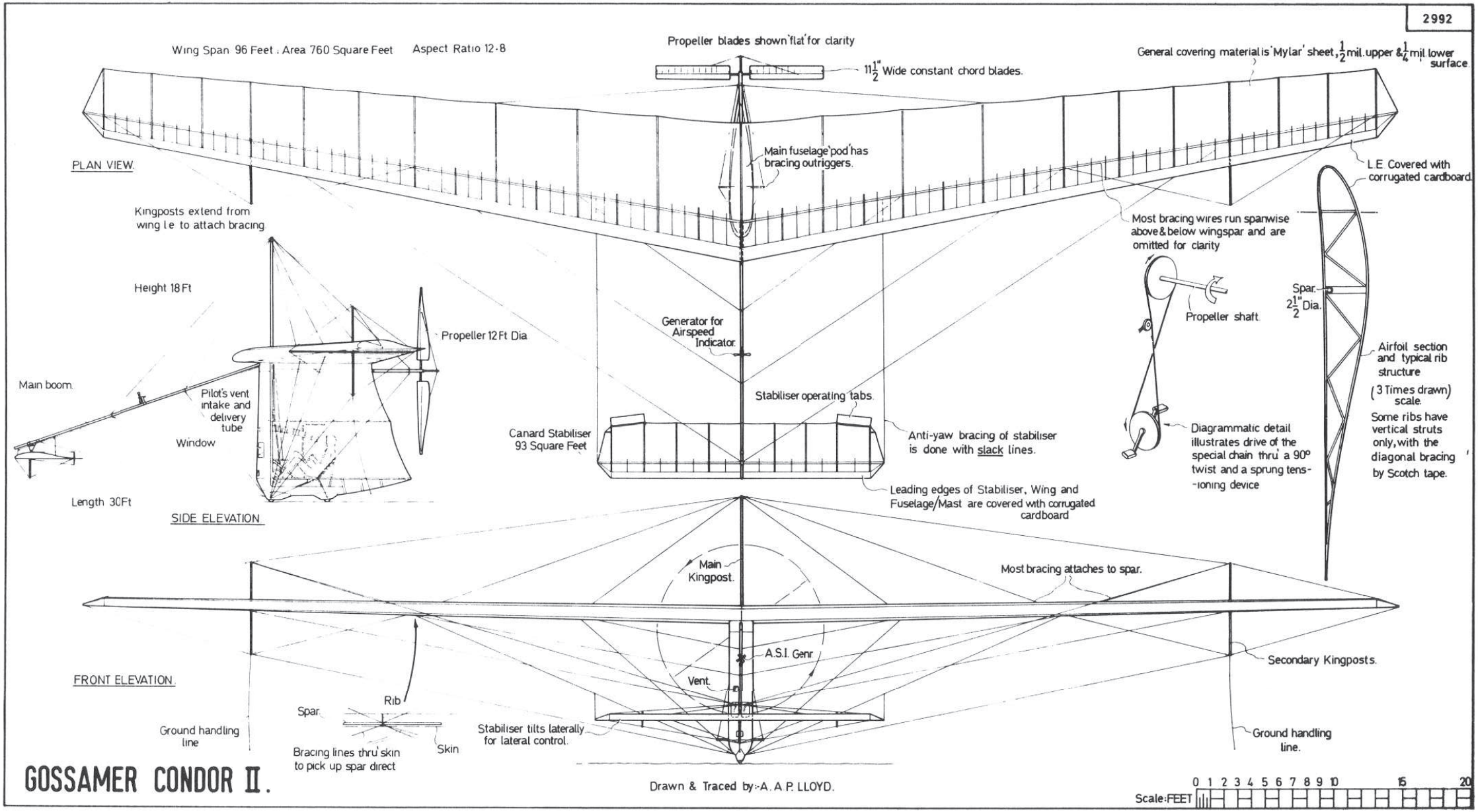

GOSSAMER CONDOR II.

Drawn & Traced by:- A. A. P. LLOYD.

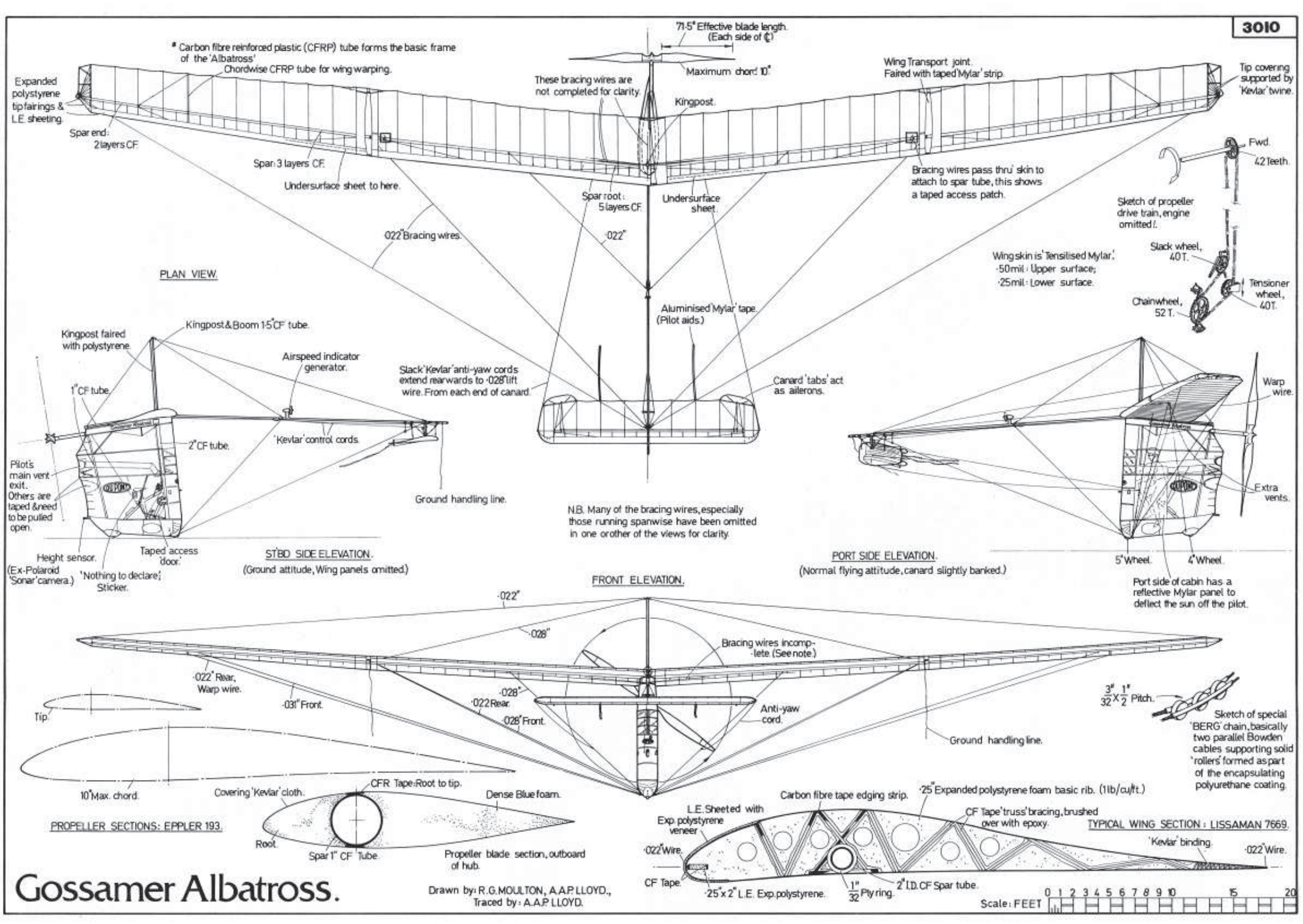

Gossamer Albatross.

Drawn by: R.G. MOULTON, A.A.P. LLOYD.,
Traced by: A.A.P. LLOYD.

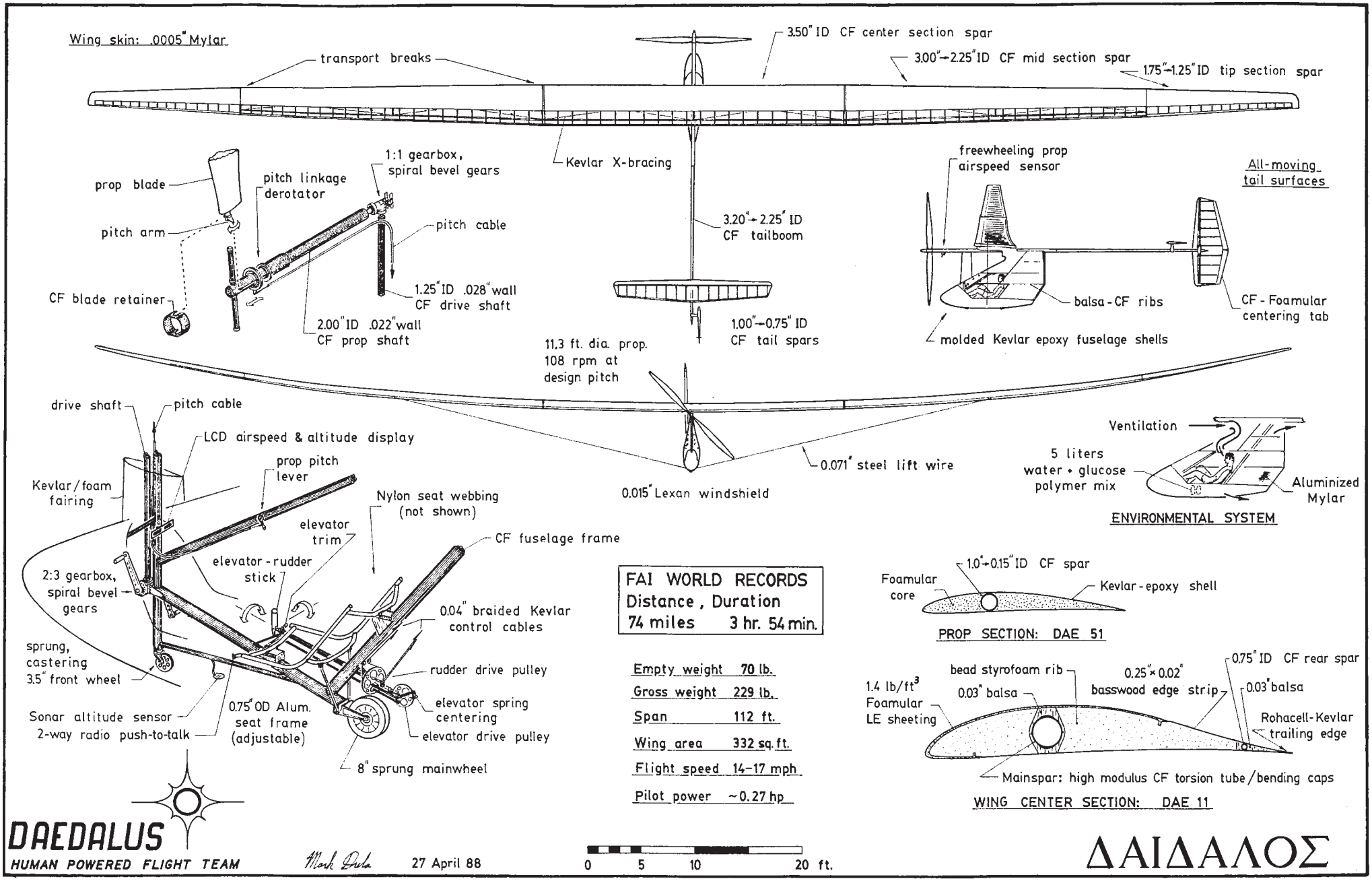
Wing skin: .0005" Mylar
transport breaks
3.50" ID CF center section spar
3.00"→2.25" ID CF mid section spar
1.75"→1.25" ID tip section spar
Kevlar X-bracing
prop blade
pitch arm
CF blade retainer
pitch linkage derotator
1:1 gearbox, spiral bevel gears
pitch cable
1.25" ID .028" wall CF drive shaft
2.00" ID .022" wall CF prop shaft
3.20"→2.25" ID CF tailboom
1.00"→0.75" ID CF tail spars
freewheeling prop airspeed sensor
All-moving tail surfaces
balsa-CF ribs
CF-Foamular centering tab
molded Kevlar epoxy fuselage shells
11.3 ft. dia. prop. 108 rpm at design pitch
drive shaft
pitch cable
LCD airspeed & altitude display
prop pitch lever
Kevlar/foam fairing
Nylon seat webbing (not shown)
elevator trim
CF fuselage frame
elevator-rudder stick
2:3 gearbox, spiral bevel gears
0.04" braided Kevlar control cables
sprung, castering 3.5" front wheel
rudder drive pulley
elevator spring centering
Sonar altitude sensor
2-way radio push-to-talk
0.75" OD Alum. seat frame (adjustable)
elevator drive pulley
8" sprung mainwheel
0.071" steel lift wire
0.015" Lexan windshield
Ventilation
5 liters water + glucose polymer mix
Aluminized Mylar
ENVIRONMENTAL SYSTEM
1.0"→0.15" ID CF spar
Foamular core
Kevlar-epoxy shell
PROP SECTION: DAE 51
bead styrofoam rib
0.25" × 0.02" basswood edge strip
0.75" ID CF rear spar
0.03" balsa
1.4 lb/ft³ Foamular LE sheeting
0.03" balsa
Rohacell-Kevlar trailing edge
Mainspar: high modulus CF torsion tube/bending caps
WING CENTER SECTION: DAE 11
FAI WORLD RECORDS
Distance, Duration
74 miles 3 hr. 54 min.
Empty weight 70 lb.
Gross weight 229 lb.
Span 112 ft.
Wing area 332 sq.ft.
Flight speed 14-17 mph
Pilot power ~0.27 hp
0 5 10 20 ft.
DAEDALUS
HUMAN POWERED FLIGHT TEAM
Mark Drela
27 April 88
ΔΑΙΔΑΛΟΣ

A.3 Structural Data of the Daedalus

Linear density distributions

Wing

s (ft)	s (m)	λ (lb/ft)	λ (kg/m)
0	0	0.610	0.9078
2	0.6096	0.495	0.7366
4	1.2192	0.465	0.6920
6	1.8288	0.462	0.6875
8	2.4384	0.445	0.6622
10	3.0480	0.432	0.6429
12	3.6576	0.434	0.6459
16	4.8768	0.424	0.6310
18	5.4864	0.428	0.6369
20	6.0960	0.432	0.6429
22	6.7056	0.438	0.6518
24	7.3152	0.438	0.6518
26	7.9248	0.444	0.6607
28	8.5344	0.435	0.6473
30	9.1440	0.408	0.6072
31	9.4488	0.361	0.5372
32	9.7536	0.350	0.5209
33	10.0584	0.329	0.4896
34	10.3632	0.317	0.4717
35	10.6680	0.305	0.4539
36	10.9728	0.294	0.4375
38	11.5824	0.285	0.4241
40	12.1920	0.273	0.4063
42	12.8016	0.215	0.3200
44	13.4112	0.165	0.2455
46	14.0208	0.152	0.2262
48	14.6304	0.138	0.2054
50	15.2400	0.105	0.1563
52	15.8496	0.099	0.1473
54	16.4592	0.094	0.1399
56	17.0688	0.090	0.1339

Fuselage

s (ft)	s (m)	λ (lb/ft)	λ (kg/m)
-5.6	-1.7069	0.75	1.1161
-3.2	-0.9754	0.75	1.1161
0	0	0.75	1.1161

Stab

s (ft)	s (m)	λ (lb/ft)	λ (kg/m)
0	0	0.95	1.4137
1.0	0.3048	0.95	1.4137
7.5	2.2860	0.50	0.7441

Rudder

s (ft)	s (m)	λ (lb/ft)	λ (kg/m)
-3.5	-1.0668	0.40	0.5953
0	0	0.95	1.4137
1.0	0.3048	0.95	1.4137
5.0	1.5240	0.55	0.8185

Tailboom

s (ft)	s (m)	λ (lb/ft)	λ (kg/m)
-6.5	-1.9812	0.15	0.2232
4.0	1.2192	0.15	0.2232
12.0	3.6576	0.11	0.1637
20.0	6.0960	0.06	0.0893

A.4 AVL files of the Daedalus

To model the Daedalus in AVL, two specific files are needed; the geometry file and the mass & inertia file. These two files are given in the following pages.

```
!============================================================
! Daedalus - AVL Model
! Geometrical Data
!============================================================

Daedalus
0                                       ! Mach
0           0           0               ! iYsym iZsym Zsym
30.8438     0.9035      34.1376         ! Sref Cref Bref
0           0           0               ! Xref Yref Zref
0                                       ! CDp

!========================= Wing ============================

SURFACE
Wing
10 1.0      ! Nchord Cspace Nspan Sspace
YDUPLICATE
0           ! mirror wing about y=0 plane

!-------------------- Center section ------------------------
SECTION
! Xle Yle Zle Chord Ainc Nspan Sspace
-0.3809  0.0000  0.1189  1.1430 3.52 6 0.0
AFIL
DAE11.dat
CDCL
0.4160  0.0131  0.8761  0.0092  1.5621  0.0119

SECTION
! Xle Yle Zle Chord Ainc Nspan Sspace
-0.3764  2.1366  0.1499  1.1430 3.52 6 0.0
AFIL
DAE11.dat
CDCL
0.4160  0.0131  0.8761  0.0092  1.5621  0.0119

SECTION
! Xle Yle Zle Chord Ainc Nspan Sspace
-0.3631  4.2732  0.2427  1.1430 3.52 10 0.0
AFIL
DAE11.dat
CDCL
0.4160  0.0131  0.8761  0.0092  1.5621  0.0119

!---------------------- Mid section -------------------------
SECTION
! Xle Yle Zle Chord Ainc Nspan Sspace
-0.2463  8.5443  0.6207  0.9525 3.52 10 0.0
AFIL
DAE1121.dat
CDCL
0.3887  0.0168  0.8041  0.0104  1.5729  0.0139

SECTION
! Xle Yle Zle Chord Ainc Nspan Sspace
-0.0949 12.8133  1.2388  0.7620 3.52 6 0.0
AFIL
DAE21.dat
```

```
CDCL
0.4128  0.0208  0.9297  0.0118  1.5536  0.0153

!---------------------- Tip section -------------------------
SECTION
! Xle Yle Zle Chord Ainc Nspan Sspace
-0.0125 14.2603  1.5037  0.6272 3.52 6 0.0
AFIL
DAE2131.dat
CDCL
0.5138  0.0188  0.9526  0.0125  1.4625  0.0143

SECTION
! Xle Yle Zle Chord Ainc Nspan Sspace
0.0737 15.7065  1.7965  0.4923 3.52 4 0.0
AFIL
DAE31.dat
CDCL
0.5365  0.0222  1.1599  0.0138  1.4744  0.0165

!----------------------- Wing tip -------------------------
SECTION
! Xle Yle Zle Chord Ainc Nspan Sspace
0.1484 16.8969  2.0698  0.3810 3.52 2 0.0
AFIL
DAE41.dat
CDCL
-0.0885  0.0179  0.4500  0.0121  1.0330  0.0147

SECTION
! Xle Yle Zle Chord Ainc Nspan Sspace
0.1609 16.9881  2.0900  0.3658 3.52 2 0.0
AFIL
DAE41.dat
CDCL
-0.0896  0.0183  0.4497  0.0124  1.0387  0.0151

SECTION
! Xle Yle Zle Chord Ainc Nspan Sspace
0.2502 17.0560  2.1028  0.2743 3.52 0 0.0
AFIL
DAE41.dat
CDCL
-0.1602  0.0232  0.3752  0.0162  1.0703  0.0181

!====================== Fuselage ==========================

SURFACE
Fuselage
20 1.0       ! Nchord Cspace [Nspan Sspace]
TRANSLATE
! dX dY dZ
 0.1524  0.0000  0.0000

SECTION
! Xle Yle Zle Chord Ainc Nspan Sspace
0.4411  0.0000  0.0000  0.9305 0.00 2 0.0
AFIL
N654021.dat
```

```
CDCL
-0.4696  0.0140  0.0000  0.0135  0.4696  0.0140

SECTION
! Xle Yle Zle Chord Ainc Nspan Sspace
0.4411  0.0000 -0.1500  0.9305 0.00 10 0.0
AFIL
N654021.dat
CDCL
-0.4696  0.0140  0.0000  0.0135  0.4696  0.0140

SECTION
! Xle Yle Zle Chord Ainc Nspan Sspace
-1.3246  0.0000 -0.9754  2.6962 0.00 2 0.0
AFIL
N654021.dat
CDCL
-0.5287  0.0069  0.0000  0.0067  0.5287  0.0069

SECTION
! Xle Yle Zle Chord Ainc Nspan Sspace
-1.6246  0.0000 -1.1156  2.8754 0.00 2 0.0
AFIL
N654021.dat
CDCL
-0.5289  0.0068  0.0000  0.0066  0.5289  0.0068

SECTION
! Xle Yle Zle Chord Ainc Nspan Sspace
-1.7599  0.0000 -1.1973  2.9404 0.00 2 0.0
AFIL
N654021.dat
CDCL
-0.5289  0.0067  0.0000  0.0065  0.5289  0.0067

SECTION
! Xle Yle Zle Chord Ainc Nspan Sspace
-1.8290  0.0000 -1.2789  2.9392 0.00 2 0.0
AFIL
N654021.dat
CDCL
-0.5289  0.0067  0.0000  0.0065  0.5289  0.0067

SECTION
! Xle Yle Zle Chord Ainc Nspan Sspace
-1.8233  0.0000 -1.3606  2.8632 0.00 2 0.0
AFIL
N654021.dat
CDCL
-0.5289  0.0068  0.0000  0.0066  0.5289  0.0068

SECTION
! Xle Yle Zle Chord Ainc Nspan Sspace
-1.7346  0.0000 -1.4423  2.7041 0.00 2 0.0
AFIL
N654021.dat
CDCL
-0.5288  0.0069  0.0000  0.0067  0.5288  0.0069
```

```
SECTION
! Xle Yle Zle Chord Ainc Nspan Sspace
-1.5545  0.0000 -1.5240  2.4536 0.00 2 0.0
AFIL
N654021.dat
CDCL
-0.5273  0.0072  0.0000  0.0071  0.5273  0.0072

SECTION
! Xle Yle Zle Chord Ainc Nspan Sspace
-1.0973  0.0000 -1.6459  1.8915 0.00 0 0.0
AFIL
N654021.dat
CDCL
-0.5241  0.0080  0.0000  0.0081  0.5241  0.0080

!======================== Stab ============================

SURFACE
Stab
10 1.0 5 1.0 ! Nchord Cspace Nspan Sspace
YDUPLICATE
0            ! mirror surface about y=0 plane

SECTION
! Xle Yle Zle Chord Ainc [Nspan Sspace]
5.1930  0.0000  0.3048  0.5639 0.00
NACA
0010
CDCL
-0.7608  0.0184  0.0000  0.0086  0.7608  0.0184
CONTROL
! name gain Xhinge XYZhvec SgnDup
stab 1 0 0 1 0 1

SECTION
! Xle Yle Zle Chord Ainc [Nspan Sspace]
 5.2540  2.2860  0.3048  0.3200 0.00
NACA
0010
CDCL
-0.6681  0.0187 -0.0000  0.0120  0.6681  0.0187
CONTROL
! name gain Xhinge XYZhvec SgnDup
stab 1 0 0 1 0 1

!======================== Rudder ===========================

SURFACE
Rudder
10 1.0 10 1.0      ! Nchord Cspace Nspan Sspace

SECTION
! Xle Yle Zle Chord Ainc [Nspan Sspace]
5.9284  0.0000 -1.0668  0.6706 0.00
NACA
0010
CDCL
-0.7801  0.0182  0.0000  0.0080  0.7801  0.0182
```

```
CONTROL
! name gain Xhinge XYZhvec SgnDup
rudder 1 0 0 0 1

SECTION
! Xle Yle Zle Chord Ainc [Nspan Sspace]
5.8293  0.0000  0.0000  1.0668 0.00
NACA
0010
CDCL
-0.8518  0.0173  0.0000  0.0056  0.8518  0.0173
CONTROL
! name gain Xhinge XYZhvec SgnDup
rudder 1 0 0 0 1

SECTION
! Xle Yle Zle Chord Ainc [Nspan Sspace]
5.9817  0.0000  1.5240  0.4572 0.00
NACA
0010
CDCL
-0.7215  0.0184  0.0000  0.0100  0.7215  0.0184
CONTROL
! name gain Xhinge XYZhvec SgnDup
rudder 1 0 0 0 1
```

```
!============================================================
! Daedalus - AVL Model
! Dimensional Units, Mass & Inertia Breakdown
!============================================================

Lunit = 1 m
Munit = 1 kg
Tunit = 1 s
g = 9.81
rho = 1.225

!------------------------------------------------------------

! mass x y z Ixx Iyy Izz [ Ixy  Ixz  Iyz ]
 8.5495 0 6.6180  0.9431 156.9227 2.1253 154.7974 0 0 -18.1381  ! wing - R part
 8.5495 0 -6.6180 0.9431 156.9227 2.1253 154.7974 0 0 -18.1381  ! wing - L part
 0.2568 5.3340  1.0184 0.3048 0.1068 0 0.1068 0 0 0             ! stab - R part
 0.2568 5.3340 -1.0184 0.3048 0.1068 0 0.1068 0 0 0             ! stab - L part
 1.9051 0.7620 0 -0.8534 0.4625 0.4625 0 0 0 0                  ! fuselage
 0.5154 6.0960 0  0.2592 0.2369 0.2369 0 0 0 0                  ! rudder
 1.4946 1.5496 0  0 0 7.1485 7.1485 0 0 0                       ! tailboom
74.8423  0.0000  0 -1.2192 0 0 0 0 0 0                         ! pilot
 5.4431 -0.0610  0 -1.6764 0 0 0 0 0 0                         ! water
 1.3608 -1.9812  0  0.0000 0 0 0 0 0 0                         ! prop
 0.9072 -0.9144  0  0.0000 0 0 0 0 0 0                         ! top gearbox
 1.3608 -0.9144  0 -1.5240 0 0 0 0 0 0                         ! crankset
```

Bibliography

[1] D.A. Reay. *The History of Man-Powered Flight*. Pergamon, 1977.

[2] J.D. Burke. *The Gossamer Condor and Albatross: A Case Study in Aircraft Design*. AeroVironment, 1980.

[3] M. Drela. Aerodynamics of human-powered flight. *Annual Review of Fluid Mechanics*, 22(1):93–110, 1990.

[4] J. McIntyre. *Man's Greatest Flight*. AeroModeller, 1988.

[5] RAeS. *Regulations and Conditions for the Kremer International Marathon Competition*. `http://aerosociety.com/About-Us/specgroups/Human-Powered/Kremer`.

[6] J. Katz and A. Plotkin. *Low-Speed Aerodynamics*. Cambridge University Press, second edition, 2001.

[7] J. Anderson. *Fundamentals of Aerodynamics*. McGraw-Hill, third edition, 2010.

[8] M. Drela and H. Youngren. *AVL (Athena Vortex Lattice)*. `http://web.mit.edu/drela/Public/web/avl/`.

[9] B. Etkin and L.D. Reid. *Dynamics of Flight: Stability and Control*. Wiley, third edition, 1995.

[10] R.C. Nelson. *Flight Stability and Automatic Control*. WCB/McGraw-Hill, second edition, 1998.

[11] M. Drela. *ASWING: Configuration Development System for Flexible Aircraft*. `http://web.mit.edu/drela/Public/web/aswing/`.

[12] M. Drela. Method for simultaneous wing aerodynamic and structural load prediction. *Journal of Aircraft*, 27(8):692–699, 1990.

[13] J.R. Cruz and M. Drela. Structural design conditions for human powered aircraft. *OSTIV Conference*, 1989.

[14] J. Peraire and S. Widnall. *Lecture 26 - 3D Rigid Body Dynamics: The Inertia Tensor*.

[15] Prop Designer. *Library on human powered flight*. `http://library.propdesigner.co.uk/html/naca_65-4--021.html`.

[16] T. Hansen. Modeling the performance of the standard cirrus glider using navier-stokes cfd. *Technical Soaring*, 38(1):5–14, 2014.

[17] M. Drela. Low-reynolds-number airfoil design for the mit daedalus prototype: A case study. *Journal of Aircraft*, 25(8):724–732, 1988.

[18] MIT. *The Feasibility of A Human-Powered Flight Between Creet and the Mainland of Greece, Vol.II* - daedalus airfoils. 1986.

[19] MIT. *The Feasibility of A Human-Powered Flight Between Creet and the Mainland of Greece, Vol.I* - advanced airfoil. 1986.

[20] M. Drela and H. Youngren. *XFOIL: Subsonic Airfoil Development System.* `http://web.mit.edu/drela/Public/web/xfoil/`.

[21] T. Hansen. *Wind Turbine Simulations using Navier-Stokes CFD.* Master's Thesis, Royal Institute of Technology, 2010.

[22] J. Morgado, R. Vizinho, M.A.R. Silvestre, and J.C. Páscoa. Xfoil vs cfd performance predictions for high lift low reynolds number airfoils. *Aerospace Science and Technology*, 52:207–214, 2016.